Experimentally validated multi-scale fracture modelling scheme of cementitious materials

Zhang, Hongzhi

DOI
10.4233/uuid:9a74f4ee-62e9-4117-bcb0-26c5a1a52cb9

Publication date
2019

Document Version
Final published version

Citation (APA)
Zhang, H. (2019). *Experimentally validated multi-scale fracture modelling scheme of cementitious materials*. [Dissertation (TU Delft), Delft University of Technology]. https://doi.org/10.4233/uuid:9a74f4ee-62e9-4117-bcb0-26c5a1a52cb9

Experimentally validated multi-scale fracture modelling scheme of cementitious materials

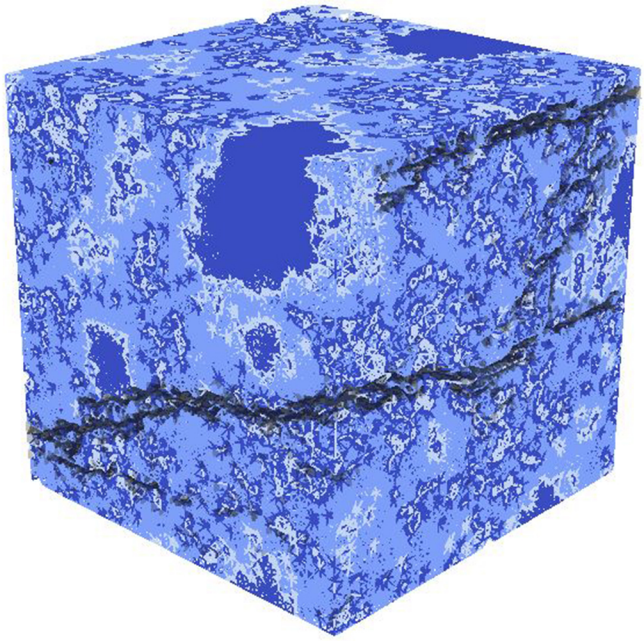

Hongzhi Zhang
张洪智

EXPERIMENTALLY VALIDATED MULTI-SCALE FRACTURE MODELLING SCHEME OF CEMENTITIOUS MATERIALS

EXPERIMENTALLY VALIDATED MULTI-SCALE FRACTURE MODELLING SCHEME OF CEMENTITIOUS MATERIALS

Dissertation

for the purpose of obtaining the degree of doctor
at Delft University of Technology
by the authority of the Rector Magnificus Prof. dr. ir. T. H. J. J. van der Hagen
chair of the Board for Doctorates
to be defended publicly on
Monday 28 October 2019 at 10:00 o'clock

by

Hongzhi ZHANG

Master of Engineering in architecture and Civil Engineering,
Harbin Institute of Technology, P.R. China,
born in Shandong, P.R. China.

This dissertation has been approved by the promotors

promotor: Prof. dr. ir. E. Schlangen
copromotor: Dr. B. Šavija

Composition of the doctoral committee:

Rector Magnificus,	chairperson
Prof. dr. ir. E. Schlangen,	Delft University of Technology
Dr. B. Šavija,	Delft University of Technology

Independent Members:

Prof. dr. ir. J. G. Rots,	Delft University of Technology
Prof. dr. Z. Li,	Delft University of Technology
Prof. dr. E . Landis,	University of Maine, United States of America
Dr. B. Pichler,	Vienna University of Technology, Austria

Keywords: Cementitious materials, Cement paste, Mortar, Micromechanics, Multi-scale modelling, Lattice fracture model, X-ray computed tomography, Size effect, Nanoindenter

Printed by: Ipskamp Printing, The Netherlands
Cover design: Hongzhi Zhang and Yu Chen

ISBN 978-94-6384-071-2

An electronic version of this dissertation is available at
http://repository.tudelft.nl/.

CONTENTS

List of Figures

LIST OF TABLES

SUMMARY

Cementitious materials are heterogeneous on mutliple length scales, from nanometres to metres. Consequently, their macroscopic mechanical properties are affected by material structures at all length scales. In pursuit of fundamental understanding the relationship between their multiscale heterogeneous material structure and mechanical properties, testing and modelling are required at all length scales.

In this thesis, a series of experimental and modelling techniques for cementitious materials on multiple length scales (micrometre to millimetre) has been developed. This forms an experimentally validated modelling scheme in which experimental results are used to provide input and validation for numerical model at each length scale.

The approach on micro-scale sized specimen preparation has been developed by combining thin-sectioning and micro-dicing techniques. Mechanical measurements on the prepared micro-scale sized specimens were performed using a nanoindenter under various test configurations. The micromechanical model has been developed by combining the micro X-ray computed tomography and discrete lattice fracture model.

In terms of hardened cement paste (HCP), the micro-cube indentation splitting test technique offers experimental results for the calibration of the micromechanical model. The one-sided micro-cube splitting test was used to validate the calibrated model. Moreover, the one-sided splitting test can offer the nominal splitting strength of HCP. The micro-cube compression test was developed to validate the modelling results and to provide the compressive strength and Young's modulus measurements of HCP at the micro-scale. The experimentally validated micromechanical model was further used to predict the uniaxial tensile fracture behaviour of HCP at the micro-scale. It is confirmed by both numerical modelling and experimental measurements that the micromechanical properties (such as compressive strength, tensile strength) of HCP are much higher than at the meso-scale properties. With respect to the interfacial transition zone (ITZ), micro-scale sized HCP-aggregate cantilever beams were fabricated and loaded by the nanoindenter. The measured load-displacement response was used to calibrate the microstructure informed lattice fracture model. This model was further used to predict the fracture behaviour of the ITZ under uniaxial tension.

The volume averaging up-scaling approach has been adopted as a tool to pass the outcome from the micro-scale to the higher scale as input. The micro-beam three-point bending test has been developed to validate this modelling scheme on HCP. The good agreement between modelling and testing shows that this modelling approach can reproduce the experimental results in terms of fracture pattern, strength and elasticity well. This up-scaling approach was further validated by comparing the modelling and testing results of the 10 mm cubic mortar under uniaxial tension. As strength and fracture properties of cementitious materials are size dependent, a size effect study on HCP has been carried out using both one-sided splitting test configurations and the multi-

scale modelling approach. The size range of specimens that can be experimentally measured and numerically simulated are significantly improved by using these techniques.

The experimentally validated multi-scale modelling scheme developed in this thesis is fully quantitatively predictable at the meso-scale. This modelling scheme is generic. It can be used in the same or similar way for studying systems utilizing other binders or aggregates.

SAMENVATTING

Cementgebonden materialen zijn heterogeen op verschillende lengteschalen, van nanometers tot meters. De consequentie is dat de macroscopische mechanische eigenschappen beïnvloed worden door materiaalstructuren op alle lengteschalen. Om de relatie tussen de heterogene materiaalstructuur en mechanische eigenschappen fundamenteel te begrijpen, zijn experimenten en modellen op alle lengteschalen nodig.

In dit proefschrift is een reeks experimentele en modelleringstechnieken ontwikkeld voor cementgebonden materialen op meerdere lengteschalen (micrometer tot millimeter). Dit vormt een experimenteel gevalideerd modelleringsschema waarin experimentele resultaten worden gebruikt om input en validatie te leveren voor een numeriek model op elke lengteschaal. De aanpak voor de preparatie van microschaalsproefstukken is ontwikkeld door het combineren van technieken voor het maken van dunne doorsneden en micro-dicing. Mechanische metingen op de geprepareerde microschaal formaat proefstukken werden uitgevoerd met behulp van een nanoindenter onder verschillende testconfiguraties. Het micromechanisch model is ontwikkeld door het combineren van de micro X-ray tomografie en het discrete lattice-breukmodel.

Op het gebied van verharde cementpasta (HCP) biedt de splijtproef door middel van nano-indentatie op een microkubus experimentele resultaten voor de kalibratie van het micro-mechanisch model. De eenzijdige splijtproef op een microkubus werd gebruikt om het gekalibreerde model te valideren. Bovendien geeft de eenzijdige splijtproef de nominale splijtsterkte van HCP. De microkubus drukproef is ontwikkeld om de resultaten van de simulaties te valideren en om de druksterkte en Young's modulus metingen van HCP op microschaal te bepalen. Het experimenteel gevalideerde micromechanisch model werd verder gebruikt om het uniaxiale trekgedrag van HCP op microschaal te voorspellen. Het wordt bevestigd door zowel numerieke modellering als experimentele metingen dat de micromechanische eigenschappen (zoals druksterkte, treksterkte) van HCP veel hoger zijn dan de eigenschappen op mesoschaal. Met betrekking tot hechtzone tussen HCP en toelagmateriaal (ITZ) werden microschaalgrote HCP-toeslag proefstukken (uitkragende balkjes) gefabriceerd en belast door de nanoindenter. Het gemeten kracht-verplaatsing-diagram werd gebruikt om het microstructuur gebaseerd lattice-breukmodel te kalibreren. Dit model werd verder gebruikt om het breukgedrag van de hechtzone (ITZ) onder een eenassige spanning te voorspellen.

De "volume averaging up-scaling" methodeis gekozen als een instrument om het resultaat van de microschaal door te geven als input voor de hogere schaalverdeling. De driepuntsbuigtest voor micro-balkjes is ontwikkeld om dit modelleringsschema op HCP te valideren. De goede overeenkomst tussen modellering en testen toont aan dat deze modelleringsbenadering de experimentele resultaten in termen van breukpatroon, sterkte en elasticiteit goed kan reproduceren. Deze opschalingmethode werd verder gevalideerd door het vergelijken van de modelleer- en testresultaten van de 10 mm3 mortel proefstukken belast op eenassige trek. Aangezien de sterkte en breukeigenschappen van

cementachtige materialen afhankelijk zijn van de grootte, is een studie naar het afmeting afhankelijk effect van HCP uitgevoerd met behulp van zowel eenzijdige splijtproeven alsook multi-schaal modellering. De range van afmetingen van de proefstukken die experimenteel gemeten en numeriek gesimuleerd kunnen worden, zijn aanzienlijk verbeterd door het gebruik van deze technieken.

Het in dit proefschrift ontwikkelde experimenteel gevalideerde multischaalmodelleringsschema is maakt het mogelijk om volledig kwantitatieve voorspellingen te doen op mesoschaal. Dit modelleringsschema is generiek. Het kan op dezelfde of een vergelijkbare manier gebruikt worden voor het bestuderen van systemen die gebruik maken van andere bindmiddelen of toeslagkorrels.

To my parents

I

General Introduction

1

General Introduction

This chapter illustrates the background and motivation of the current research. The framework of multi-scale modelling approach is briefly summarised. Furthermore, together with the layout of the thesis, objectives, methodology and scope of the research are given.

1

1.1. BACKGROUND

BEING the most widely used for construction in the world, cementitious materials have generated considerable research interest [1]. Such materials contain heterogeneities on scales ranging from nanometres to millimetres. Therefore, their mechanical properties are affected by various factors at all scales [2]. As the multi-scale model [3–11] is capable of coupling mechanics at different length scales, it has become an essential tool for fundamental understanding how the microstructure influences macroscopic mechanical performance.

In the multi-scale model, the behaviour of materials and structures can be analysed at several different length scales. Commonly, three scales can be considered for cementitious materials, namely micro-, meso- and macro-scales. The three scales, as defined by Wittmann [12], are shown schematically in Figure 1.1. At micro-scale, the internal structure of hardened cement paste is the most important structural feature, comprising various phases: i.e. the hydration products (e.g. inner and outer hydration products which are mainly the calcium silicate hydrate, calcium hydroxide and ettringite, etc.), anhydrous cement particles and capillary pores [13]. At meso-scale, the material structure consists of cement paste matrix, aggregates with different particle sizes and air voids. At macro-scale, no internal material structure is recognised. It is considered as homogeneous, isotropic and continuum from an engineering perspective.

Through a so-called up-scaling approach, the multi-scale model can capture the origin and evolution of the targeted physical processes at a lower scale (i.e. micro-scale) and their impact at a higher scale (i.e. macro-scale) of observation. Due to its inherently complex material structure, multi-scale analysis of cementitious materials requires experimental validation at each length scale. To date, most of the mechanical measurements are performed at meso- and macro- scales. In terms of the micro-scale, especially for the strength properties, studies are mostly carried out by simulations[4, 6, 14–19] and the predicted strengths are significantly different depending on the model used. Furthermore, since the mechanical properties of cementitious materials are size dependent [20, 21], micromechanical properties cannot directly be compared to macroscopic measurements. Therefore, it is highly desirable to perform mechanical tests at the micro-scale for the calibration and validation of the micromechanical models.

Mechanical testing of cementitious materials at the micro-scale has long be recognized as a challenging task. For other types of materials, micro and even nano scale tests have been performed and reported in the literature. This is mainly because cementitious materials are tested in the laboratory with sizes in the range of a few centimetres. The equipment is not possible of testing specimens smaller than a few millimeters in size. The instrument that can handle the small sized specimen and record accurately the load-displacement response during the test is still rare.Furthermore, preparation of micro-scale sized cementitious specimens is challenging as such materials are highly sensitive to changes in environmental conditions. Therefore, to accomplish the experimentally validated multi-scale modelling scheme, there is an essential need of developing advanced techniques for preparation and mechanical measurements of the micro-scale sized specimens.

To this end, this thesis proposes novel approaches to prepare and load the small sized specimens at micro-scale. On the basis of the proposed mechanical tests, the microme-

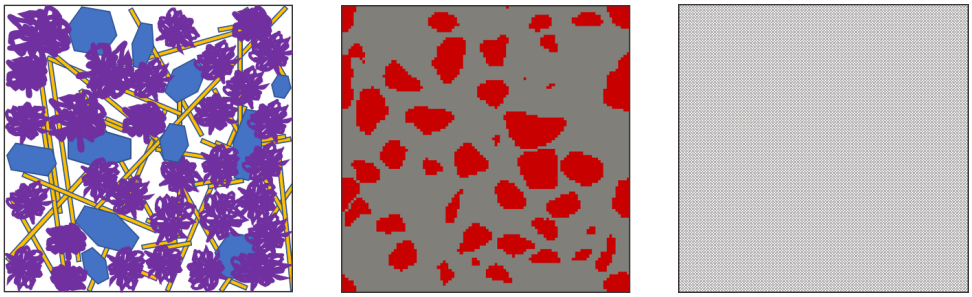

(a) (b) (c)

Figure 1.1: Three-scale approach after Wittmann: (a) micro-scale ($10^{-6} - 10^{-4}$ m); (b) meso-scale ($10^{-4} - 10^{-1}$ m) and (c) macro-scale ($10^{-1} - 10^{+}$ m) [12].

chanical models can be calibrated and validated experimentally. Under a multi-scale modelling scheme, the predicted results can be further up-scaled to serve as input parameters in the meso-scale models, which can be validated by the conventional fracture measurements. An experimentally validated multi-scale modelling scheme is therefore formed.

1.2. OBJECTIVES AND SCOPE

THE objective of this investigation is to develop an experimentally validated multi-scale modelling scheme of deformation and fracture for cementitious materials. Two length scales are considered in this work, i.e. the micro- and meso-scales. The main objective is achieved through following tasks:

- To develop a set of novel techniques for micromechanical properties characterization of cementitious materials. This consists of preparation and testing of micro-scale sized specimens.
- To assess proper input parameters for the micromechanical modelling on the basis of the observed experimental fracture mechanism. At the micro-scale, multiple hydration products and capillary pores can be observed in the cement paste matrix. Therefore, a multi-phase microstructure should be considered. The micromechanical properties of these phases are needed to be determined from the experiments. This requires a calibration and validation procedure using the experimental results.
- To up-scale the results from the micromechanical modelling as input for fracture modelling at a coarse scale, e.g. meso-scale and an intermedia scale termed sub-meso-scale. Experimental fracture tests at these scales are required as validation for the adopted multi-scale modelling scheme and up-scaling approach.
- To apply the developed testing and modelling approaches for fundamental understanding of how the featured microstructures at different length scales influence the macroscopic properties of cementitious materials.

In this research, the binder of the investigated cementitious materials, i.e. hardened cement paste and mortar, is limited to the ordinary Portland cement CEM I 42.5 N, as

the focus of this this research is on developing of the testing and modelling approaches and a rich knowledge base is available in the literature for ordinary Portland cement. However, approaches developed in this work are generic, and can be successfully used on systems which utilize other binders as well.

1.3. STRATEGY OF THE RESEARCH

IN order to accomplish the aforementioned objectives, the following strategies are developed and applied:

The micro-scale sized specimens, e.g. micro-cubes (100 μm × 100 μm × 100 μm) are produced using a micro-dicing technique which is commonly used in the semiconductor industry. The mechanical test at micro-scale is performed using a nanoindenter. Several test configurations are conducted for calibration and validation of the micromechanical models.

A discrete lattice fracture model is used to simulate the fracture behaviour of cementitious materials at different length scales. The model allows a straightforward implementation of the material heterogeneity at various levels of observation. On the basis of X-ray computed tomography images, multi-phase material structures of cement paste are obtained at different length scales. At micro-scale, the material structure of cement paste consists of capillary pores, anhydrous cement grains and inner and outer hydration products. At meso-scale and an intermediate scale termed sub-meso-scale, cement paste is considered as a matrix containing homogenised cement paste and air voids. In terms of mortar, a geometrical model is implemented to generate and add the "realistic" shaped sand particles into the matrix.

For upscaling of mechanical properties, an uncoupled volume averaging technique is adopted. By properly choosing a volume of material structure at small scale which matches the smallest feature of the larger scale observation, the global mechanical behaviour (i.e., load-displacement response under uniaxial tension) of smaller scale simulation can be used as input local mechanical properties for the fracture modelling at larger scale. The upscaling approach is validated using a three-point bending test concept of prismatic cement paste beam with a cross-section of 500 μm × 500 μm.

Based on the above modelling strategies, the behaviour of cementitious material at micro- and meso-scales can be properly simulated. Starting from the micro-scale, an integrated multi-scale testing and modelling scheme of cementitious materials is formed. This can help understand the multi-scale fracture mechanism of such materials and design material with desired properties.

1.4. OUTLINE OF THE THESIS

THE thesis is composed of four parts including 11 Chapters. The outline is presented in Figure 1.2.

In Chapter 1, the background, objectives, scope and strategies of the research are given. Chapter 2 reviews four aspects that are related with the micromechanical modelling. These aspects are techniques for microstructure characterisation, mechanical properties assessment of individual phases, micromechanical modelling approaches and up-scaling procedures.

The second part presents the developed testing and modelling techniques for cementitious materials at micro-scale. In Chapter 3, an approach to produce the micro-scale sized specimens is described. A so-called indentation splitting test was performed on the produced specimens and used to calibrate the micromechanical model. Chapter 4 presents the validation of the micromechanical model on the basis of a so-called one-sided splitting test. Based on the calibrated micromechanical model, Chapter 5 studies the stochastic micromechanical properties (tensile strength and elastic modulus) of cement paste and correlates them with the porosity present in the material structure. Chapter 6 focuses on the testing and modelling of the deformation and fracture of cement paste under uniaxial compression at micro-scale. Chapter 7 presents a procedure for the micromechanical modelling and testing of the interfacial transition zone (ITZ). The micro-scale sized aggregate-cement specimen is produced and tested. The experimental results are used to build a model to predict the micromechanical properties of ITZ. The predicted micromechanical properties of cement paste and ITZ are further used as input for the fracture modelling of cementitious material.

In the third part, the multi-scale modelling scheme is proposed and validated by experimental testing. Chapter 8 describes the multi-scale modelling approach and the validation procedure. The up-scaling approach i.e. the uncoupled volume averaging technique is introduced to transfer the results from the fine scale to the coarse scale. For the purpose of validation, a three-point bending test at the sub-meso-scale is developed. Chapter 9 deals with the size effect on strength of cement paste. based on the techniques developed in Chapter 4 and Chapter 8, the size range of specimens in both experimental test and numerical model are broadly increased respectively. In Chapter 10, a benchmark test of mortar is carried out for the validation of the multi-scale modelling scheme in which the micromechanical properties of cement paste and ITZ are transferred from the micromechanical modelling using the uncoupled upscaling approach.

The fourth part, i.e. Chapter 11 summarises the work in this thesis and gives conclusions and prospects. Remarks and recommendations for the further research are presented in this chapter.

1

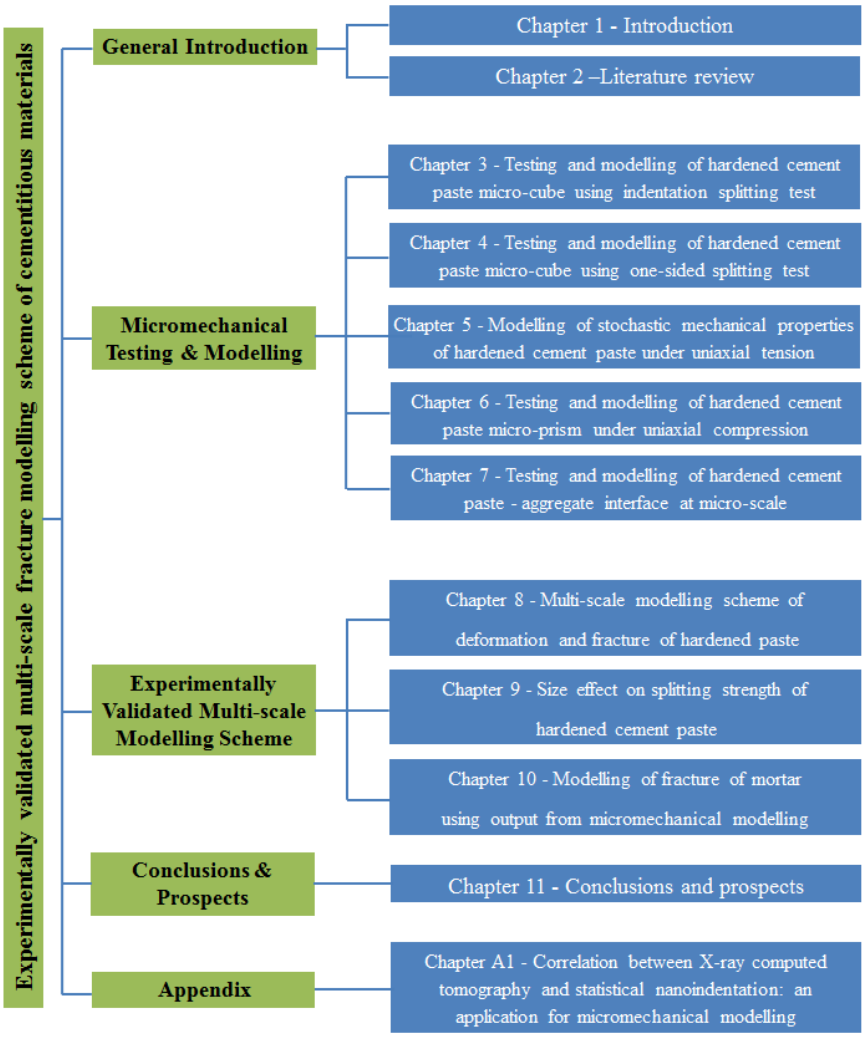

Figure 1.2: Outline of the thesis.

2

LITERATURE REVIEW

This chapter gives a critical review of techniques related with the micromehcanical modelling and up-scaling approaches that pass the micromechanical modelling results to the models at higher scale. On the basis of the review, knowledge gaps that are going to be bridged in this thesis are outlined.

2.1. INTRODUCTION

CEMENTITIOUS materials are heterogeneous at length scales ranging from metres to sub-nanometres. Consequently, their mechanical properties are affected by various factors at all scales [2]. To cope with its multi-scale nature, multi-scale modelling schemes are commonly applied [3–11].

In the multi-scale modelling scheme, it is generally assumed that the behaviour observed at one level can be explained in terms of the material structure at a lower level. For example, the creep and shrinkage phenomena in concrete are attributed to the changing of internal structure of the cement paste at micro-scale. In this way, the knowledge about the relationship between microstructure of cement paste (basic binding component in the cementitious materials) and its micromechanical behaviour helps to explain failure and degradation mechanism observed at the concrete level. In pursuit of fundamental understanding of this relationship and using it to explain the behaviours observed at mortar or concrete scale, the following four steps should be considered:

1. The first step is to obtain a realistic microstructure, which is the basis for determining the properties of a material. This can be achieved with the aid of either experimental techniques (e.g. scanning electron microscopy (SEM) [22] and X-ray computed tomography (XCT) [23]) or numerical models (e.g. Hymostruc [24–26], μic [27, 28] and CemHyd3D [29]).

2. The second step is to determine the local micromechanical properties of different phases. Usually micromechanical properties of different phases are derived from nano-indentation measurements [16, 30–32]. An alternative is to apply atomistic simulations [33, 34].

3. Once the microstructure and the local micromechanical properties are available, the micromechanical modelling approaches can be applied. Using such models, mechanical properties of the material at the micro-scale can be determined.

4. The last step is related with up-scaling the predicated properties to a higher level (meso/macro-scale) model using a certain multi-scale modelling scheme. Concurrent approach or hierarchical approach is commonly adopted.

This chapter provides an overview of the micromechanical modelling of cement paste and how the resulting micromechanical properties can be up-scaled to the meso-scale models. This review addresses the techniques that are related to the aforementioned four aspects. On the basis of the review, knowledge gaps that are going to be bridged in this thesis are outlined.

2.2. MICROSTRUCTURE CHARACTERIZATION

2.2.1. EXPERIMENTAL APPROACH

IN terms of visualisation of cement paste, several techniques including SEM [22], XCT [23], scanning laser scanning confocal microscopy [35, 36], focused ion beam nano-otomography [37, 38], scanning transmission X-ray microscopy [39, 40] can be applied.

Among those, SEM and XCT are perhaps the most popular techniques. The initial outcomes from both of these approaches are greyscale level images. Using image segmentation and thresholding techniques, the morphology and spatial distribution of individual phases can be derived. These play a crucial role for the micromechanical modelling.

SCANNING ELECTRON MICROSCOPY (SEM)

In the last 30 years, scanning electron microscope has become a general and versatile instrument for studying the microstructure of hardened cement paste. SEM technique produces images of a sample by scanning the surface with a focused beam of electrons and collecting the signals from the interaction between electrons and atoms on the material surface. As shown in Figure 2.1, the following three modes can be classified in terms of the type of the signal that used for the imaging:

- The secondary electron (SE) mode collects low-energy secondary electrons originating within a few nanometers from the sample surface [41]. This mode results in images with a well-defined, three-dimensional appearance, which is commonly used to observe the morphology of individual particles, fracture surfaces or hydrate surface.
- Backscattered electrons (BSE) consist of high-energy electrons originating in the electron beam. The detection of such electrons allows visualization of contrast between areas with different chemical compositions [41]. This is because the heavy elements (high atomic number) backscatter electrons more strongly than light elements (low atomic number), and thus appear brighter in an image. The BSE image can be used for quantification of spatial distribution and amount of different microstructural constituents in hardened cement paste matrix.
- The analysis of characteristic X-rays generated throughout the interaction volume energy-dispersive gives the chemical composition of the local area [41]. Energy dispersive spectroscopy (EDS) or wavelength dispersive spectroscopy (WDS) are generally used for this purpose.

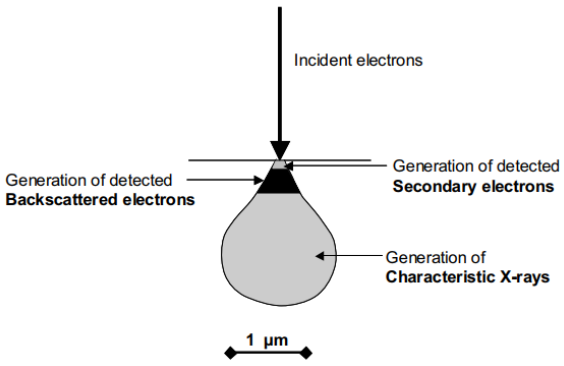

Figure 2.1: Schematic view of signal generation in the SEM [22].

In order to build the microstructure-property relationships, it is necessary to quantify microstructural features. For this purpose, BSE imaging is combined with image segmentation techniques or EDS mapping. Prior to the BSE imaging, the cement paste sample is impregnated with epoxy and well-polished. A typical BSE image of a cement paste surface is shown in Figure 2.2. The anhydrous cement clinker particles are the brightest; the calcium hydroxide (CH) looks lighter grey and other hydration products (i.e. calcium-silicate-hydrate, C-S-H) are as various shades of darker grey. Due to the low average atomic number of the epoxy that is filling the pores, the pores do not scatter electrons and appear black. Such contrast between different features offers an opportunity for image segmentation, see Figure 2.3. A typical greyscale level histogram of hardened cement paste is shown in Figure 2.4. In the histogram, several peaks can be observed. From right to left, these peaks correspond to anhydrous cement particles, CH and C-S-H respectively. It needs to be emphasized that no distinct peak for porosity occurs in the histogram. This is partly due to the resolution of the BSE technique and partly due to the limited pore boundary resolution [22]. Several strategies have been proposed to determine the threshold between pore and C-S-H reproducible. Depending on whether the histogram (Figure 2.4) or cumulative curve of the greyscale level (Figure 2.5) is used, the tangent-slope method [42] or the "overflow" pore segmentation method [43], respectively, is commonly applied. Although reasonable correlation with other measures of porosity and pore size distribution can be obtained [26], it should be noticed that when these strategies are used, the areas containing solid intermixed pores could be merged as solid or pore phases depending on the internal porosity of the local area. Furthermore, it is worth noticing that drying and specimen preparation for the BSE examination could introduce irreversible changes in the pore structure [23]. An environmental electron scanning microscope (ESEM) is generally used to overcome the drying process. However, polishing is still required.

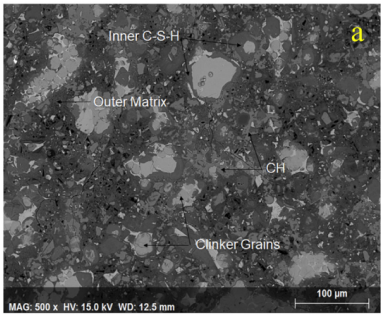

Figure 2.2: An example of an SEM image of cement paste after [44].

As mentioned above, because of the limitation of the resolution, a single pixel in a BSE image can contain signals from several phases, the relatively broad single peaks are usually observed in the histogram (Figure 2.4). EDS mapping can be coupled with the BSE technique to get the detailed chemical quantification of the hydrated matrix. In terms of identifying the hydration products, Al-Si-Ca system is of main interest.

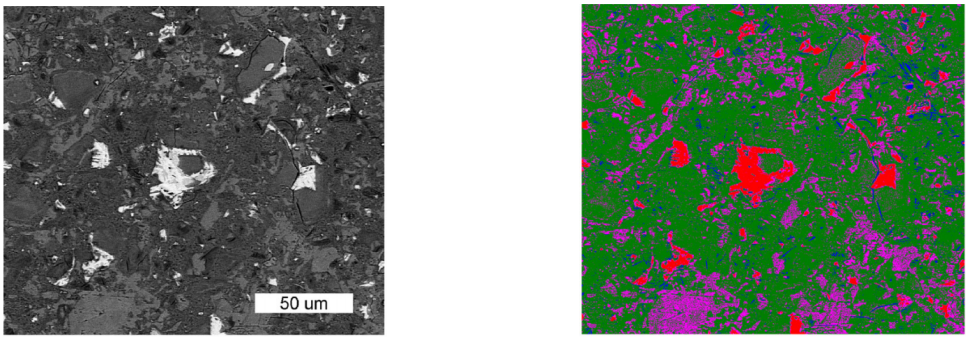

(a) (b)

Figure 2.3: An example of a segmented SEM image of hydrated cement paste: (a) Original SEM-BSE image. (b) Segmented image (blue - pores; green + violet = hydrates (violet - large CH crystals as a part of hydrates); red - anhydrous cement particles) after [45].

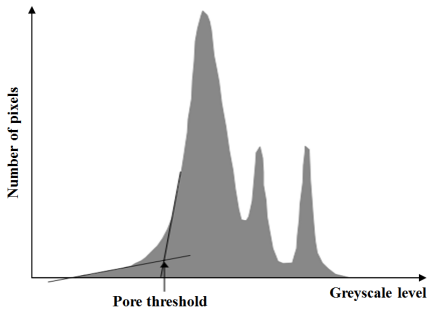

Figure 2.4: Typical greyscale level histogram of hardened cement paste. From the right (highest grey levels) the peaks correspond to anhydrous cement particles, CH and C-S-H respectively. No discrete peak for the porosity is observed [22].

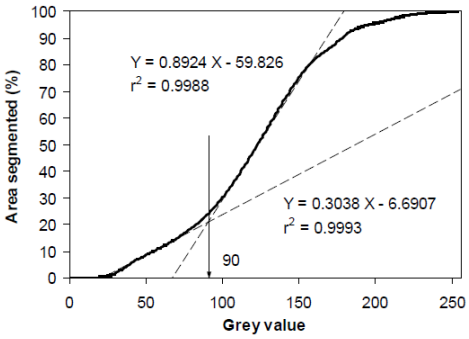

Figure 2.5: Determination of the "overflow" point for the pore segmentation using the cumulative greyscale histogram after [43].

Although BSE technique has offered a lot of valuable knowledge for understanding the features of cementitious materials at the micro-scale, it should be kept in mind that it can only offer two-dimensional (2D) section observations of a three-dimensional (3D) microstructure. This leads the challenge to techniques for transforming 2D information to the 3D. For example, quantitative parameters, such as overall volume fractions of a phase can be well estimated from 2D sections, but parameters like pore connectivity is difficult to be accessed.

X-RAY COMPUTED TOMOGRAPHY (XCT)

Due to the ease of sample preparation and non-destructive character, X-ray computed tomography has become an attractive technique for acquiring a 3D microstructure of cementitious materials. As schematically shown in Figure 2.6, an object is placed between an X-ray source and a detector. By rotating the sample, a series of 2D projections is created on the basis of measuring transmitted intensities by the detector. These projections are then used for the reconstruction of 3D material structure. The detected intensity I during X-ray irradiation is related to the integral attenuation of the various materials found inside the object following Lambert-Beer Law [46]:

$$I = I_0 e^{-\mu_a t} \tag{2.1}$$

where I_0 is the intensity of the incident radiation, t the thickness of the object and μ_a the attenuation coefficient of the object, in which the attenuation coefficient is a function of the density and the atomic number of the scanned object. After reconstruction, a stack of greyscale level based cross-section images of the physical object can be obtained.

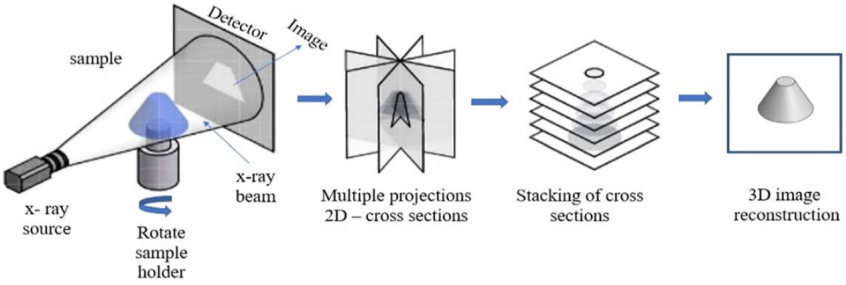

Figure 2.6: Schematic illustration of the image acquisition sequence for the 3D reconstruction of the samples analysed by x-ray computed tomography [47].

In 1990-2000, pioneering works have been conducted on construction materials using the conventional X-ray tomography [48–51]. The resolution is limited, thus only large scale features can be observed. With application of the synchrotron microtomography technique, the capabilities of the tomography systems have increased, making it possible to obtain a 3D material structure of hardened cement paste with a resolution better than 0.5 µm [14, 52, 53]. This resolution allows a direct observation of the material features of cementitious materials at the micro-scale. First tomographic scans of cement pastes were reported by Bentz et al. [54].Various microstructures of hardened cement

paste with high spatial resolution (0.95 µm/voxel) are available on the Visible Cement Data Set website (https://visiblecement.nist.gov/). Further work was done by Gallucci et al. [23], who compared a reconstructed slice from XCT with a BSE image acquired at an equivalent magnification, see Figure 2.7. They concluded that similar phase contrast is made for these two techniques, although the beam-matter interactions are fundamentally different. The anhydrous cement particles (A) appear as the brightest phase; "inner" C-S-H and undifferentiated hydration products (B) are grey; CH shows (C) light grey and pore (D) the darkest phase.

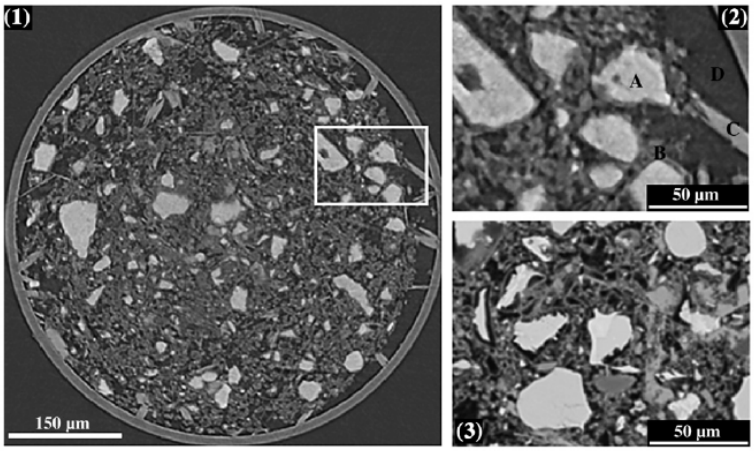

Figure 2.7: (1) Reconstructed slice of a 1-day old cement paste. (2) zoomed part of rectangle in (1). (3) comparison with similar specimen in SEM. A-anhydrous cement grains, B-inner C-S-H, C-CH, D-unfilled spaces (air or water filled porosity) [23].

To analyse the reconstructed microstructure quantitatively, an image thresholding procedure is required to segment the material into individual phases. Similar strategies used for BSE images are generally adopted. As shown in Figure 2.8, because no discrete peak for the pore can be observed, the aforementioned tangent-slope method [42] or the "overflow" pore segmentation method [43] are generally used to determine the threshold between the pore and solid phases. Furthermore, due to the limited resolution and the fact that hydration products such as C-S-H, CH, ettringite and monosulfate have a similar density, hydration products cannot be differentiated from the greyscale level histogram. As a consequence, they are generally considered together as a single phase. An example of a segmented 3D material structure consisting of pore, hydration products and anhydrous cement grains is shown in Figure 2.9, the tangent-slope approach [22] is used to isolate the pore from the solid matrix, while the tangent slope between HP and AN is considered as hydration products/anhydrous cement grain phase threshold value. Once the microstructure is available, a variety of computational tools exist to directly calculate the properties of the extracted digitalized microstructure, e.g. pore connectivity [52], transport [53, 55] and mechanical [17] properties, based on which the microstructure-property relationships can be quantified.

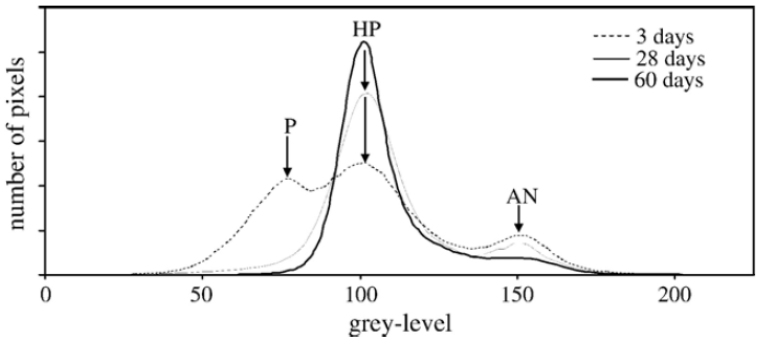

Figure 2.8: Greyscale level histograms of hardened cement paste at different curing time. From the right (highest grey levels) the peaks correspond to anhydrous cement particles, hydration products. The discrete peak for the porosity disappears with the hydration going on [23].

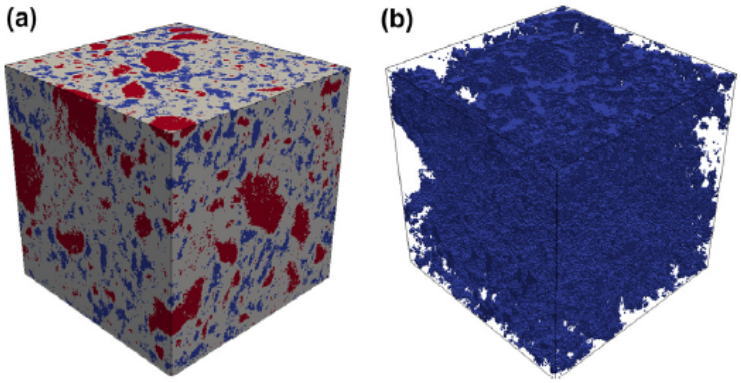

Figure 2.9: Spatial phase distribution obtained from XCT scanning and pore structure after thresholding (blue - pores; grey - hydration products; red - anhydrous cement grain) [53].

2.2.2. COMPUTER-GENERATED MATERIAL STRUCTURE

A number of models have been proposed to simulate the hydration process of cement paste and thus offering its microstructure for further investigations. Reviews on these models can be found in references [26, 56–59]. The most important assumptions for these models involve the kinetics of hydration, initial cement particle packing and spatial distribution of products.

According to the adopted algorithm to describe the microstructure, two types of models can be distinguished: vector (also termed as continuum) and digital microstructural models. Commonly used models are summarized in Table 2.1. In vector models, cement particles are commonly stored as centroid and radii of shells. The hydration process is essentially simulated as particle growth with overlaps. On the other hand, digital microstructural models represent the microstructure using cubic voxels. Each voxel is occupied by a single phase (e.g. anhydrous cement particle, pore or a hydration product).

Table 2.1: Categories of main integrated kinetic cement hydration models [60].

Category	Name
Vector model	Model of Jennings and Johnson [61] HYMOSTRUC3D [24–26] Model of Navi and and Pignat [62] Model of Nothnagel and Budelmann [63] µic [27, 28] Model of Wang et al. [64] Ducom [65]
Digital microstructural model	CEMHYD3D [29] HydraticCA [66, 67]

VECTOR MODELS

HYMOSTRUC3D and µic are perhaps the most widely used vector models. In HYMOSTRUC3D, the initial cement particle size is distributed on the basis of Rosin-Ramler distribution. The largest particle is placed in the centre of a representative volume. The others are packed around it and a periodic boundary is applied during the packing process. The hydration is controlled by the chemical composition and particle size distribution of the cement clinker, the water content and the temperature. With ongoing hydration, particles gradually dissolve and a porous shell of hydration products consisting of inner and outer hydration products forms around the particle. A 2D slice extracted from the simulated microstructure with size of 100 µm × 100 µm × 100 µm is shown in Figure 2.10. It should be noticed that the latest development of this model allows taking the deposition of CH into account [60]. Up to now, many mechanical performances, e.g. autogenous shrinkage [25], drying shrinkage [68] and fracture [4] of cement paste has been predicted on the basis of the microstructure obtained by HYMOSTRUC3D.

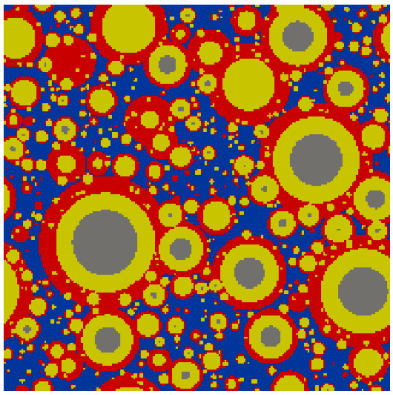

Figure 2.10: A 2D slice from 3D microstructure of cement paste simulated by HYMOSTRUC3D (grey - anhydrous cement particles; yellow - inner hydration products; red - outer hydration products; blue - pores).

µic is another widely used numerical model for study of microstructure-property relationships of cement paste. It was developed by Bishnoi et al. [27, 28] on the basis of work presented by Navi and Pignat [62]. In order to efficiently calculate overlap of spherical grains, several key algorithms involving grid subdivisions and point sampling

are introduced to the model [27, 28]. Figure 2.11 shows a 2D slice from μic simulated 3D microstructure of cement paste. One of the advantages of this model is that it offers flexibility to set several parameters defining the reactions, which facilities the understanding of the driving mechanisms of cement hydration. Elastic properties [69], creep and shrinkage behaviour [70] of cement paste have been predicted based on this model.

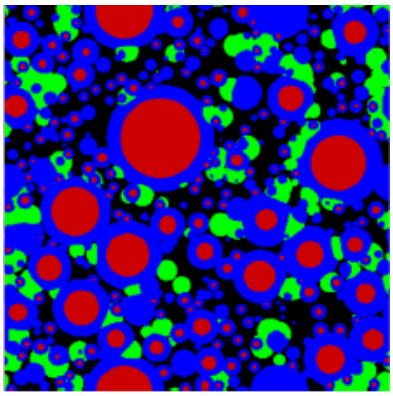

Figure 2.11: A 2D slice from 3D microstructure of cement paste simulated by μic platform [71] (red - anhydrous cement particles; blue - C-S-H; green - CH; black - pore).

Although vector models are more computationally effective, the assumption of the spherical shapes of cement particles has a significant effect on the simulated hydration progress [72]. Furthermore, it is reported that the assumed morphology of hydrates in the simulated microstructure significantly influences micromechanics-based elastic stiffness estimates of cement paste, particularly at very early age [73].

DIGITAL MODELS

CEMHYD3D [29] is the most used digital microstructural model in cement science today. It permits a direct representation of multi-phase, multi-size and non-spherical cement particles using SEM images see Figure 2.12. In the current version, the irregular particles are generated on the basis of the results from XCT [74]. As the output from the model is already in a discretized form, finite element approach can be easily applied to calculate its mechanical properties [75–78]. Although this approach is simple and effective in terms of application for finite element modelling of mechanical properties , the model requires a trade-off between accuracy and speed [27]. Another criticism of this model is the time scale in the model is not defined as the physical time because of the cellular-automata scheme [79] used for the hydration simulation. Essential calibrations are therefore required [59]. To overcome the aforementioned limitations, a new model named HydratiCA has recently being proposed on the basis of more fundamental principles of reaction kinetics and thermodynamics [66, 67]. Although a lot can be expected from this model, it is still under development.

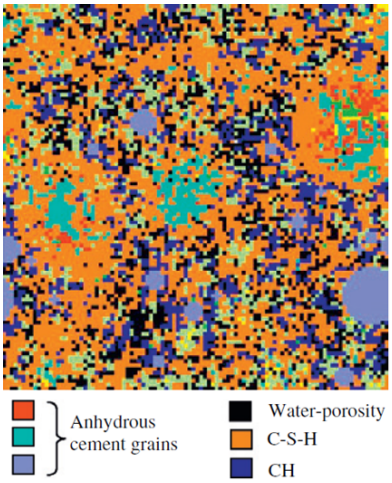

Figure 2.12: A 2D slice from 3D microstructure of cement paste simulated by CEMHYD3D after [80].

2.3. MECHANICAL PROPERTIES CHARACTERIZATION OF INDIVIDUAL PHASES

2.3.1. NANOINDENTATION TECHNIQUE

NANOINDENTATION has become a general tool for the purpose of assessment of micromechanical properties, i.e. elastic modulus and hardness of individual constituents, of hardened cement paste. As such, it is commonly used for providing input for micromechanical models. This section reviews its principle, testing strategies and newly developed test configurations for the strength properties measurements.

PRINCIPLE

The basic idea of nanoindentation is simple: push a very sharp hard tip with known geometry and mechanical properties into the surface of a material and investigate the bulk elastic behaviour of the material from the recorded load-displacement curve. For this purpose, a three sided pyramid Berkovich tip is commonly used. A typical load-displacement curve and the deformation pattern of an elastic-plastic sample during and after indentation are shown in Figure 2.13. The indenter is first pressed into a flat surface under a constant loading rate. To avoid plastic effects, the indenter is held for a few seconds at the prescribed maximum load (indentation depth), after which the specimen is unloaded. This allows a direct measurement of the hardness and the elastic modulus using the method proposed by Oliver and Pharr [81] on the basis of analytical solutions applicable to homogeneous and isotropic half-space with a flat surface. The hardness H can be obtained at the peak load P or maximum depth $h_{\max}$ as:

$$H = \left(\frac{P}{A}\right)\Big|_{h=h_{\max}} \tag{2.2}$$

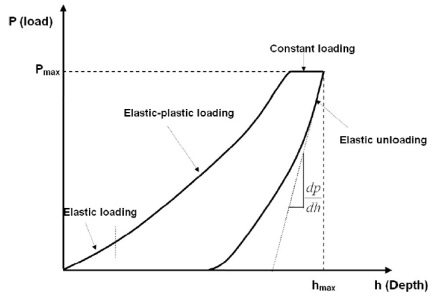

(a)

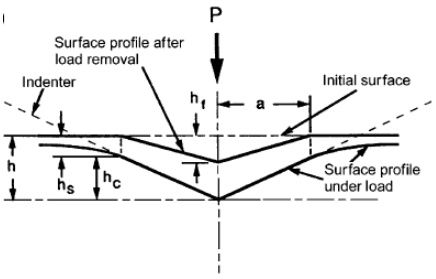

(b)

Figure 2.13: (a) A typical load-displacement curve [83] and (b) the deformation pattern of an elastic-plastic sample during and after indentation [81].

where h is the displacement relative to the initial surface, A the projected area which is a function of the contact depth h_c for an indenter tip with a known geometry. In terms of assessment of the elastic modulus, it is assumed that during the unloading phase only elastic displacements are recovered and that the reduced elastic modulus, also known as indentation modulus M, can be determined using the slope of the unloading curve:

$$S = \left(\frac{dP}{dh}\right)\Big|_{h=h_{\max}} = \frac{2}{\sqrt{\pi}} M\sqrt{A} \tag{2.3}$$

where S is the elastic unloading stiffness defined as the slope of the upper portion of the unloading curve during the initial stage of unloading. Because M accounts for the deformation which occurs in both the indented material and the indenter, a correction is made following Hertz's contact solution [82]:

$$M = \frac{1-\upsilon_s{}^2}{E_s} + \frac{1-\upsilon_i{}^2}{E_i} \tag{2.4}$$

where υ_i and E_i refer to indenter's Poisson's ratio and Young's modulus (0.07 and 1140 GPa, respectively, for a diamond indenter), and υ_s, E_s are the corresponding properties for the tested material.

NANOINDENTATION OF HYDRATED CEMENT PASTE

As mentioned above, nanoindention is naturally designed for assessing mechanical properties of homogenous materials, e.g. ceramics [84] and glass [85]. In terms of heterogeneous materials, like cement paste, the nanoindentation measurements encompass mechanical properties of the local (indented) material microstructure but also the microstructure around the indent (generally termed as the interaction volume [86]) with the length scale around 3-5 $h_{\max}$ [87, 88].

In order to derive the mechanical properties of individual constituents in cement paste, several strategies have been developed. Basically, two strategies can be summarized in terms of whether additional instruments are required. The first one is the so-called statistical nano-indentation. It is based on a combination of grid indentation and

deconvolution approach with no need of known details (e.g. chemical compositions, phase deification) of the indented location for each test. As schematically shown in Figure 2.14, a large number of indents (≥ 400, in general) are performed on the matrix surface. According to the scale separation theory, when the grid size and indentation depth are chosen properly (a general rule-of-thumb is that $h_{max} \leq D_c/10$, where D_c is the characteristic size of the phases [89, 90]), each indentation test may be treated as an independent statistical event, and a subsequent statistical deconvolution of the indentation results can be applied. Briefly, the deconvolution approach involves fitting n Gaussian distributions to the experimental probability density function (PDF, see Figure 2.15) or cumulative distribution function (CDF, see Figure 2.16) and generating the theoretical PDF for the grid nanoindentation data. More details about the deconvolution approach can be found in [83, 89] for the PDF and in [91, 92] for fitting the CDF. Furthermore, it is worth mentioning that, because generation of the experimental PDF requires a choice of bin-size for histogram construction, it is analytically more convenient to deconvolute the CDF rather than the PDF [91, 92]. However, it should be noted that the scatter in the resulting mechanical properties of individual cement phases is high and it is debated in literature whether this method can be used at all for heterogeneous materials like cement paste [19, 93–96]. A reason for this is that, although the tip-radius is very small (in case of the typically used Berkovich tip), it is almost impossible to probe a single phase; in fact, a composite made up of different phases is probed by indenting the material with a diamond tip [93].

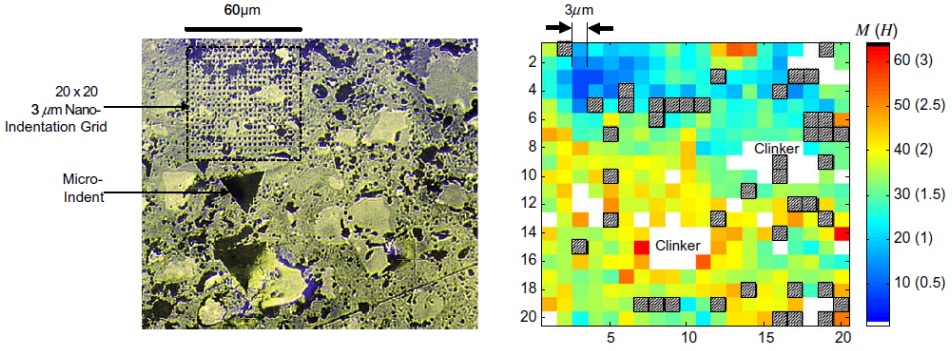

Figure 2.14: A schematic view of grid indentation technique applied on cement paste (left) and maps of the derived mechanical properties of the test area [95].

The second strategy relies on the knowledge about the indented microstructure with aid of SEM. In this strategy, the indents are performed to a material phase with indentation depth smaller than the characteristic dimension of the tested phase. As shown in Figure 2.17, BSE technique is adopted to visualize and characterize the microstructures where nanoindentation tests were performed. The intrinsic properties of these indistinct phases (still intrinsic phase porosity underneath h cannot be excluded) can be obtained separately. However, it should be noticed that when dealing with cement paste, which is a 3D heterogeneous material, the indentation outcome is always influenced by the underlying material, which can be stiffer and harder than the indented phase or just

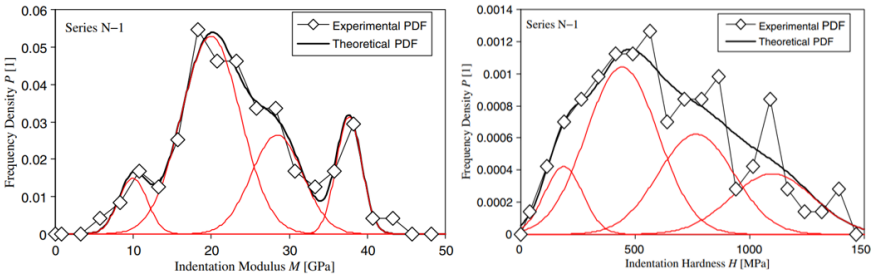

Figure 2.15: Example of statistical deconvolution of PDF after [89].

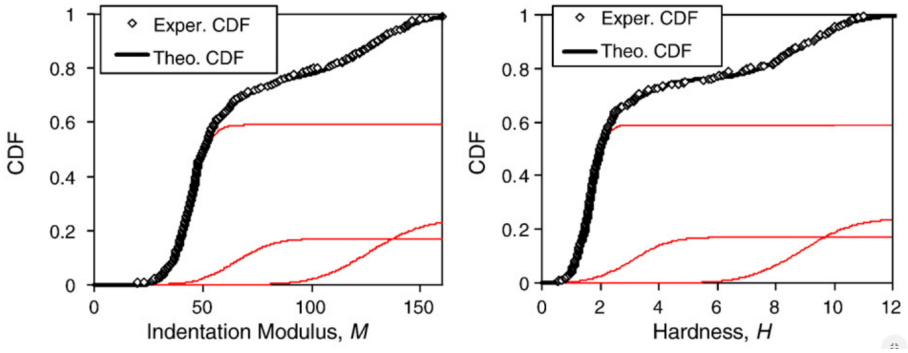

Figure 2.16: Example of statistical deconvolution of CDF after [92].

the opposite [19]. A possibility to determine whether the local indentation response was a result of a single- or a multi-phase response, is to couple the grid-indentation with ex situ scanning electron microscope-energy-dispersive X-ray (SEM-EDS) [88]. As shown in Figure 2.18, by properly choosing the indentation depth and set up of EDS (accelerating voltage, beam current and working distance), the interaction volumes probed by each method match a comparable size. The mechanical information provided by nanoindentation can be therefore correlated with the chemical information provided by SEM-EDS (Figure 2.19).

Using the grid indentation technique, elastic properties of clinker phases, i.e. C_3A, C_2S, C_3A and C_4AF have been tested and reported in [97]. With respect to C-S-H, numerous indentation tests have been conduced. A comprehensive review can be found in [83]. For the low-density C-S-H, the average indentation modulus varies from 18.1 to 26.84 GPa, while a range between 29.1 and 36.1 GPa is found for the high-density C-S-H [16, 17, 89, 98–101]. Note that these reported properties include the effect of porosity and embedded monocrystalline CH or minor compounds present at smaller scales. The other hydration product e.g., CH, has been characterised as 38 ± 5 GPa, which is similar to the high density C-S-H [16].

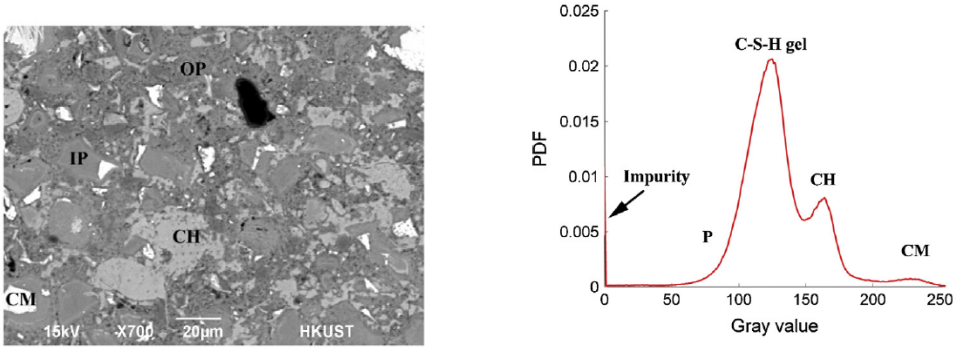

(a) (b)

Figure 2.17: BSE image of the indented area to identify the microstructure structure information of each indent (left) by using the image segmentation on the right side [30].

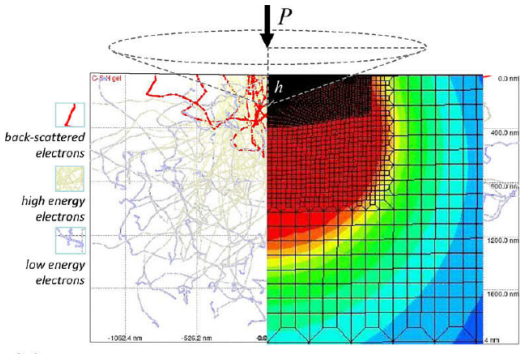

Figure 2.18: Interaction volumes probed respectively chemically by Wavelength Dispersive Spectroscopy and mechanically by nanoindentation (right): the left-half of the figure displays results of Monte Carlo simulation of electron beam penetration of C–S–H gel. The right-half represents finite element results of Von-Mises stresses below the indenter, after [95].

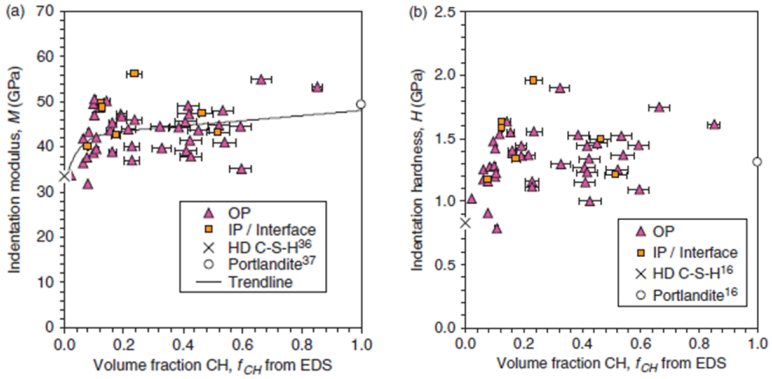

Figure 2.19: (a) Indentation modulus M and (b) indentation hardness H plotted as a function of the volume fraction of CH in micro-volumes containing CH and C-S-H [88].

UNIVERSAL TESTING USING NANOINDENTER

While nanoindentation may be considered appropriate for measuring the elastic properties of cement paste and its individual phases, more complex procedures are needed for measuring strength properties at the micro-scale. This is because no relation between the indentation hardness and strength has been found so far for cement based materials [19]. Therefore, more advanced procedures need to be used.

Recently, use of a nanoindenter has been proposed by several researchers to measure the tensile strength of cement paste [102] and individual hydration phases [45] using micro-cantilever bending tests. This technique consists of specimen preparation using a focused Ga-ion beam milling. With this procedure, micro-cantilevers with a triangular (Figure 2.20) or rectangular cross-section (Figure 2.21) can be created by milling the solid matrix. Typically, the length of these micro-cantilevers is up to 10 µm. These cantilevers are subsequently subjected to bending by applying a load at the free end of the cantilever using the nanoindenter or atomic force microscope. This provides a measure of the elastic modulus and the flexural strength of the micro-volume. Similarly, a micro-pillar compression technique involving focused ion milling of a micro-pillar in the material (Figure 2.22) and a compression test using the nanoindenter has been performed by Shahrin and Bobko [103] to measure the compressive strength and modulus of the C-S-H particles in the cement paste matrix. When the in-situ test is applied, special attention should be paid to the unavoidable influence of vacuum and heat which appear during specimen preparation and in-situ test on the micromechanical performance of cement pastes. It is reported that both application of vacuum in SEM and high energy milling for specimen preparation increase elastic moduli of inner and outer products as well as the tensile strength [104]. Furthermore, a major drawback of this approach is the time-consuming specimen preparation. Consequently, a relatively small number of specimens can be prepared and analysed [105]. At small length scales (i.e., micro-scale), a high scatter of measured mechanical properties is expected [106]. Therefore, a large number of tests need to be performed for the measurements to be statistically reliable.

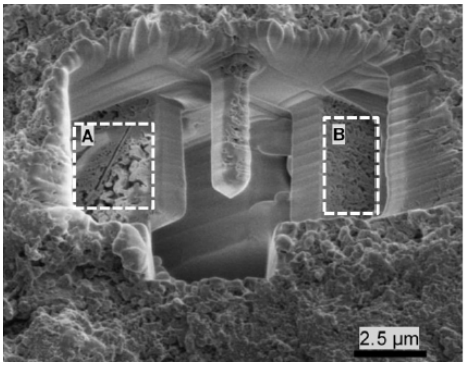

Figure 2.20: ESEM image of the micro-cantilever with a rectangular cross-section after [102].

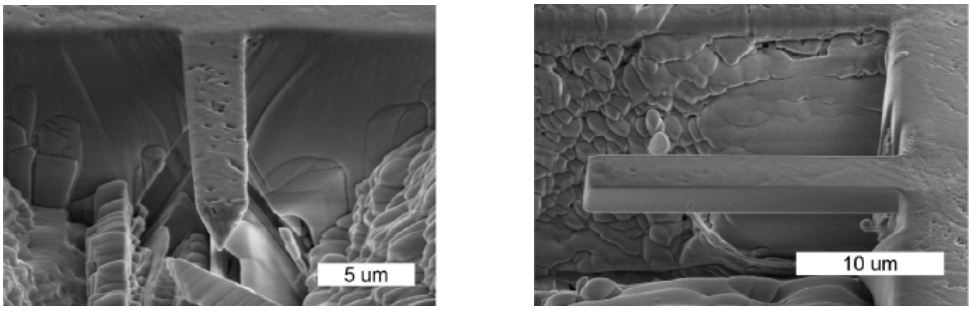

(a) (b)

Figure 2.21: ESEM image of the micro-cantilever with a triangular cross-section after [45]: (a) front view; (b) side view.

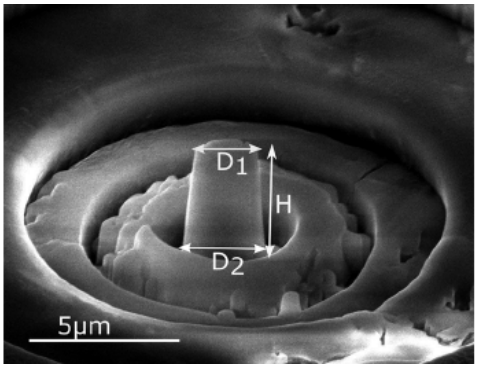

Figure 2.22: SEM image of a micro-pillar after [103].

2.3.2. ATOMISTIC SIMULATIONS

An alternative way to derive the mechanical properties of individual phases present in the cementitious materials is by using atomistic simulations, e.g. ab-initio, Monte Carlo and Molecular Dynamics, etc. On the basis of these techniques, the elastic response of the crystalline phases has been analysed. Dolado and van Breguel [58] compared these computed elastic properties with the experimental measurements reported in the literature. In terms of the clinker phases, a good agreement can be found for C_3S [107, 108], C_2S [107, 108] and C_3A [107–109], while a big dispersion occurs for ferrite. No clear explanation is available for this disagreement. With respect to the crystalline hydrates, the atomistic simulations reproduce well the experimental values of CH (35-48 GPa) [107], while the complex structure of ettringite introduces a mismatch between the simulation and measurement [107, 110].

The real challenge for atomistic simulations is the description of C-S-H gel. This is due to its amorphous structure and lack of direct observations at the atomistic level. Thus, much of the actual knowledge on C-S-H gel is derived on the basis of simulations of its mineral analogues (tobermorite and jennite) or different morphological features presented in both layered models [111–116]. Prediction of the elastic properties of these crystalline minerals can be found in [33, 107, 116, 117]. On the basis of some basic char-

acteristics of C-S-H gel measured by nanoscale techniques, a “realistic C-S-H model” as shown in Figure 2.23 has been proposed by Pellenq et al. [34] using Molecular Dynamic and the Grand Canonical Monte Carlo. The predicted anisotropic Young’s modulus (55 GPa along y direction, 66-68 GPa along the x-z plane) is in accordance with the value derived by the nanoindention(65 GPa) [89]. On the basis of the presented C-S-H model, the tensile strength of the atomistic structure is estimated from 1 to 3 GPa depending on the relative humidity. Hou et al. [118] implemented a uniaxial tensile test on this model to study the influence of the size of gel voids on the fracture response of a 138 Å × 138 Å × 138 Å C-S-H unit, see Figure 2.24. In their study, a significant decrease in terms of the stiffness and strength is observed due to the presence of the gel pores. This indicates that the gel porosity at nano-scale is detrimental to the mechanical properties of the C-S-H gel.

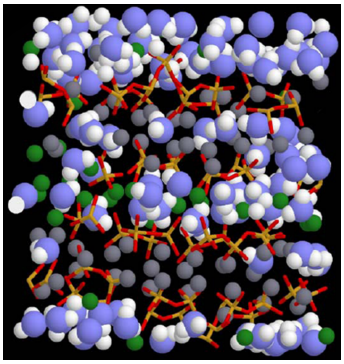

Figure 2.23: A molecular model of C-S-H from [34]: the blue and white spheres are oxygen and hydrogen atoms of water molecules, respectively; the green and grey spheres are inter and intra-layer calcium ions, respectively; yellow and red sticks are silicon and oxygen atoms in silica tetrahedral.

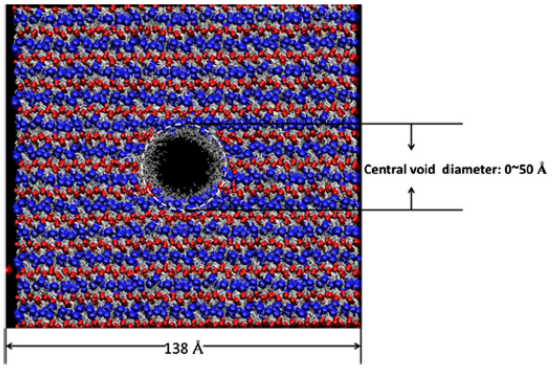

Figure 2.24: Configuration of the C-S-H gel with the central void for the uniaxial tension test after [118]: White thick chain is silicate bond; short thin chain is water molecule; large blue ball represents interlayer calcium atoms and; small red ball represents calcium atoms in the sheet.

Although atomistic simulations are promising, this is still a new field of research in

terms of cementitious materials. Furthermore, due to the current computational capacities, the atomistic simulation can only be performed on a very small piece of material (up to 10 nm) [58]. In a typical micromechanical model, the resolution is generally around 0.5-2.0 μm. As a consequence, the large distance between the micro-scale and nano-scale is present and cannot be bridged by the atomistic simulation only. Thus, an intermediate level, termed as sub-micro level, has been proposed to computationally describe C-S-H gel on the scale ranging from tens to hundreds of nanometres. At this scale, the high-density and low-density C-S-H can be assembled by these small C-S-H bricks obtained from the nano-scale on the basis of a packing factor [119, 120]. Although several pioneering works have been done [121–125], additional research is required in the development of relations bridging the nano- and micro-scale [126].

2.4. MICROMECHANICAL MODELLING

2.4.1. EFFECTIVE MECHANICAL PROPERTIES

Based on the assumptions of the existence of a representative volume element (RVE), homogenization techniques derive the definitive effective properties of a heterogonous material by "averaging" the detailed fields in the RVE. Specifically, for the known stress field σ_{ij} and ε_{ij} under certain applied load, the averaged stresses and strains over the RVE are normally defined as [127]:

$$\bar{\sigma}_{ij} = \frac{1}{V}\int_V \sigma_{ij} dV \tag{2.5}$$

$$\bar{\varepsilon}_{ij} = \frac{1}{V}\int_V \varepsilon_{ij} dV \tag{2.6}$$

where V is the volume of the RVE. When linear elasticity is assumed, Hooke's law can be applied as [127]:

$$\bar{\sigma}_{ij} = C_{ijkl}\bar{\varepsilon}_{kl} dV \tag{2.7}$$

here C_{ijkl} is defined as the effective stiffness tensor for the homogenized heterogonous material structure. Thus, in order to calculate the homogenized properties of a material, the exact solutions of the stress and strain fields at each point are needed. To obtain these exact solutions, several techniques have been proposed. These techniques can be divided into two categories: analytical and numerical.

Analytical approaches require idealized geometric models. Mori-Tanaka [128] and Self-Consistent [129] are commonly used to link the composite geometrical structure with its effective properties. The basic assumptions in these two schemes are matrix-inclusion morphology and mechanical interactions in between particles. As shown in Figure 2.25, at the micro-scale, cement paste matrix is represented by the C-S-H matrix, together with anhydrous cement particles, aluminates, and capillary pores. Since they are largely disordered and in contact with each other, Self-Consistent scheme is generally used. However, this approach cannot deal with the clustered structures or microstructures with large differences between properties of the phases. When big difference occurs in the stiffness between matrix and inclusions (see Figure 2.26), the Mori-Tanaka approach should be adopted to consider the mechanical interactions between inclusions [3, 16]. Due to its high computational efficiency, the application of analytical homogenization is mainly focused on the predicting the evolution of elastic properties

of cementitious materials [3, 73, 76, 130]. The influence of the shape of the individual phases on the predicted effective elastic properties has been reported [73, 130]. Furthermore, the compressive strength of cement paste can be estimated by calculating the deviatoric stress peak from the elastic energy stored in the RVE [15, 73, 131].

As mentioned above, analytical approaches are only applicable for idealised material microstructures. When dealing with more realistic and complex material structure as mentioned in Section 2.2, numerical approaches have to be used. The finite element method (FEM) has been extensively used to analyse the elastic properties of complex microstructure of cement paste obtained from CEMHYD3D [132, 133], XCT [75, 134] and µic [69] through the homogenization technique. As an alternative to FEM, Fast Fourier Transform (FFT) has been adopted by Šmilauer and Bittnar to model the evolution of elastic properties of the hydrating cement paste [135]. A comparison between analytical and numerical approaches seems to favour the utilization of FEM for microstructure at early ages where higher porosity exists. Stora et al. [136] concluded that when capillary porosity is above 35 %, the analytical schemes fail to account for the interactions between inclusions. Although comparable results were found for the numerical and analytical schemes for sound hydrated paste where spherical and prismatic inclusions exist in the matrix [137], the volume fraction of inclusion should not exceed 30 % when the Mori-Tanaka approach is applied.

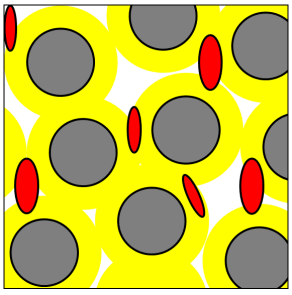

Figure 2.25: Polycrystalline RVE of "cement paste" built up of C-S-H (yellow), aluminates (red), anhydrous cement particles (grey) and capillary pores (white) modelled by Self-Consistent scheme, after [16].

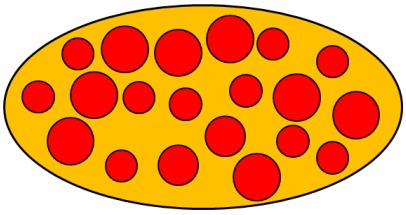

Figure 2.26: RVE of matrix-inclusion composite "cement paste" where a spherical clinker phase is embedded in a hydrate foam matrix (modelled by Mori-Tanaka scheme), after, after [15].

2.4.2. STRESS-STRAIN RESPONSE

As the failure of cementitious materials at the meso or macro-scale is mostly governed by the local tensile stress [2], the fracture behaviour of cement paste under uniaxial tension loading is very important at micro-scale. One of the most important outputs from such computational uniaxial tension modelling is the stress-strain response, from where the tensile stress, elastic modulus and fracture energy can be derived. Bernard et al. [6] incorporated the digitalized microstructure from CEMHYD3D to finite element software Abaqus for a fracture analysis. In their work, 3D solid linear finite elements are used. A Rankine criterion is adopted to model the failure of the different phases. Zhang and Jivkov [17, 18] applied a site-bond model to predict the micromechanical properties of cement paste. In the site-bond model, the material volume is represented by an assembly of truncated octahedral cells, each of which consists of six square and eight regular hexagonal faces, as shown in Figure 2.27. A homogenization approach is applied to obtain the mechanical parameters of each cell on the basis of the features, i.e. size distribution of anhydrous particles and capillary pores obtained from the segmented XCT images. An energy-based failure criterion is used to determine the failure of the bond between two cells. The fracture process is modelled by continuously increasing the strain and removing the failed bond until the prescribed strain is reached. Similar like the site-bond model, discrete lattice model [138] discretises the material volume as a set of beam elements with linear elastic behaviour, see Figure 2.28. The crack growth is simulated by using a sequentially-linear solution procedure [139]. This procedure implies performing a linear elastic analysis in every step; then, a single element with the highest stress/strength ratio is identified and removed from the mesh, thereby introducing a discontinuity; this procedure is then repeated until a global failure criterion is reached. On the basis of such model, the fracture process of micro cement paste cubes under uniaxial tension has been reported by Qian [4] and Luković et al. [19] respectively. Recently, a crack phase field model has been utilized by Han et al. [14] to analyse the XCT generated material structure. Such model requires Young's modulus and Poisson's ratio for the solid phase and two key modelling parameters for material degradation, namely the fracture energy and the diffusive length parameter.

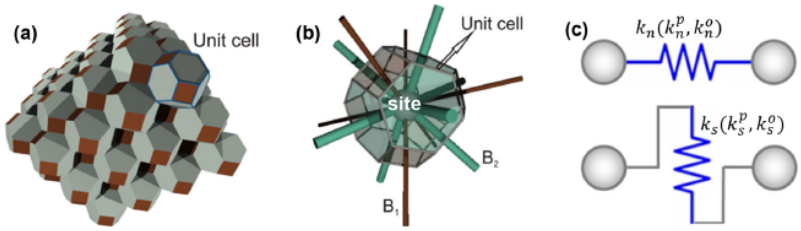

Figure 2.27: Schematic view of a site-bond model: (a) site-bond assembly; (b) unit cell with bonds; (c) normal and shear springs [17, 18].

The simulated stress-strain curves of the aforementioned works are compared in Figure 2.29. Although comparable results are found for the stiffness, a large difference in terms of the strength (peak stress) is observed for these models. This is mainly because the elastic properties of each phase they considered in the model are more or less the

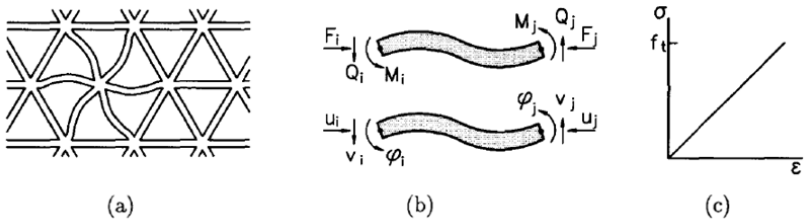

Figure 2.28: Schematic view of a discrete lattice model in 2D: (a) regular triangular lattice of beams; (b) external forces and deformations on a single beam element (c); pure elastic constitutive law for an element [138].

same (normally taken from nanoindention), while other parameters which govern the crack development, e.g. strength and fracture energy, are difficult to be determined. At such small length scales, there are no experimental measurements reported in the literature. The result from Bernard et al. [6] shows the lowest strength. This mostly attributes to the fact that, in their model, the tensile strength of each phase is assumed as 1/1000 of its elastic modulus. Although this ratio is in accordance with the phenomena observed at macro-scale, it has been shown in [45, 140, 141] that this ratio increases with the observed scale decreasing. Luković et al. [19] assumed the tensile strength as 1/30 of the material hardness measured from nanoindentation, resulting in a much higher strength. Han et al. [14] used the modelling results from [19] to calibrate their model. This is the reason why comparable strengths are obtained for [19] and [14]. Although identical model and material structure features were used by Zhang and Jivkov [17, 18], the predicted strength from their earlier work [17] is much higher compared with the latter [18]. This is because different approaches are applied to homogenise the mechanical properties of each cell. Such homogenization procedure would also decrease the heterogeneity that could be explicitly present in the model. This leads to a much more brittle post-peak behaviour compared with the lattice model in which similar strategy is implemented for the crack development.

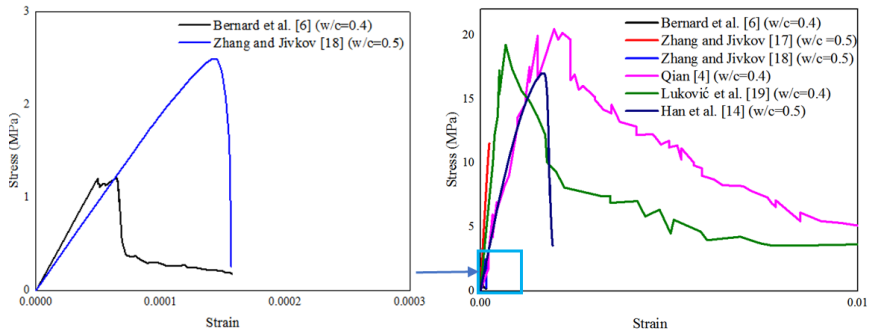

Figure 2.29: Comparison of the simulated stress-strain responses of cement paste under uniaxial tension in the literature.

Furthermore, it is worth mentioning that, although the same fracture model is applied, different elastic properties were obtained from Qian [4] and Luković et al. [19]

due to different material heterogeneities that have been implemented. Qian [4] used the microstructure obtained from HYMOSTRUC3D. On the other hand, Luković et al. [19] overlapped the spatial distribution of mechanical properties from grid nanoindention measurements directly to the lattice network. In this approach, defects larger than the interaction volume of indentation test cannot be considered. Consequentially, the lattice system in Luković et al. [19] is stiffer than the one reported by Qian [4]. Thus, the approach to consider the original heterogeneity in the discrete model also plays an important role on the predicted mechanical performance.

It is therefore important to note that, apart from the material structure, the predicted mechanical properties strongly depend on the assigned value of each model parameters. As the predicted results are going to be up-scaled for the models at meso- or even macro-scale, it is essential to validate these results at micro-scale. Therefore, mechanical tests at the micro-scale are highly desired to be conducted to calibrate the input parameters for the model. In this way, reliable results from the micromechanical modelling can be obtained, which facilities the multi-scale modelling and the understanding of multi-scale mechanical behaviour of cementitious materials.

2.5. MULTI-SCALE MODELLING STRATEGIES

Multi-scale methods are a collection of different strategies to establish a coupling of mechanics at different length scales. In this way, origin and evolution of the targeted physical processes at a fine scale and their impact at a coarse scale of observation can be captured. Depending on the tackled problems in which the scales are separated or coupled, there exist two types of multi-scale modelling schemes: hierarchical and concurrent. These methods were initially based on two main concepts: scale separation and RVE [7, 142–144].

In general, hierarchical multi-scale strategies attempt to piece together a hierarchy of computational approaches where large scale models use the coarse-grained representations with constitutive relations obtained from fine scale models [145]. In these strategies, the relevant cause-effect relations at the lower scale and its relevant effects for the next higher scale are distinguished on the basis of statistical analysis methods, homogenization techniques, or optimization methods. In light of Wittmann's three independent scales (i.e. macro, meso and micro) [146], the hierarchical multi-scale modelling scheme of cementitious martials has now been extended to five levels so far. At the nano-scale, individual atoms can be observed, thus atomistic simulations are generally implemented. Up to the sub-micro-scale, the main focus is on the recognition of colloidal and gel-like properties of C-S-H gel. The next level is the micro-scale level where different constituents are explicitly differentiated in the cement paste. The meso-scale corresponds to the level where the aggregates are embedded in the cement paste matrix. Finally, when it comes to the macro-scale, the material is generally considered as homogeneous continuum.

Most of the hierarchical multi-scale modelling crossing more than two scales has been done using the analytical homogenization approach due to its low computational demands. A simple three-step analytical homogenization scheme for determining the elastic properties of hardened cement paste can be found in [147, 148]. As shown in Figure 2.30, the solid cement paste is represented by a single three-phase composite sphere.

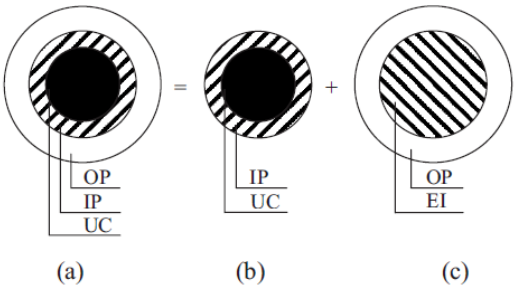

Figure 2.30: (a) Three-phase composite sphere model for solid cement paste; (b) two-phase composite sphere for UC and IP; and (c) two phase composite sphere for EI and OP (UC - unhydrated cement; IP - inner product; OP - outer product; EI - equivalent inclusion [147].

More complicated schemes using analytical homogenization can be found in [3, 15, 16, 130], see Figure 2.31. In these models, different assumptions on matrix-inclusion morphology and mechanical interactions in between these inclusions can be made at different length scale [3, 73, 76, 130]. For example, as shown in Figure 2.31, the Mori-Tanaka scheme is applied at level I, level III and level IV, where strong matrix-inclusion morphology and mechanical interactions in between particles are assumed, while at level II, a self-consistent scheme is adopted to consider the polycrystalline shaped inclusions [3]. Another alternative approach is to apply the discrete modelling at each scale and the solutions at lower scale are then translated into effective constitutive behaviours of single discrete element at the upper scale. As shown in Figure 2.32, a multi-scale modelling framework starting from the microstructure has been proposed on the basis of the discrete lattice fracture model and computer-generated characteristic material structures at corresponding length scales [4, 5]. A similar scheme can be found in [6] where a two-scale (micro and meso correspond to cement paste and mortar respectively) multi-scale modelling framework has been proposed. A scheme combining discrete modelling and analytical homogenization can be found in [131], showing the flexibility of the hierarchical multi-scale modelling schemes.

Concurrent approaches attempt to link methods at different scales together in a combined model. In this approach, different scales of the system are considered simultaneously and communicate with some type of hand-shaking procedure [145]. Behaviour of system at each scale depends strongly on what happens at the other scales. This interaction characterizes the trans-scale process, where the nonlinear behaviour occurring in the finer-scale controls the coarser-scale response at the same time. The coupling between micro/meso and macro scales is generally accounted by considering displacement comparability and momentum balance across the whole structure. In order to handle the coupling between the coarse scale mesh and the fine scale mesh, domain decomposition methods [149] and vibrational multi-scale methods [150] are generally applied. Although concurrent multi-scale methods are advantageous in many applications, especially studies of material failure, a challenge inherent to the concurrent approach lies in the efficient algorithms for adaptive addition of fine scale features to the coarse scale. At present, most of the concurrent simulations of the fracture of concrete are limited in the two-scale models [8–11, 151]. Nguyen et al. [7] has proposed a three-

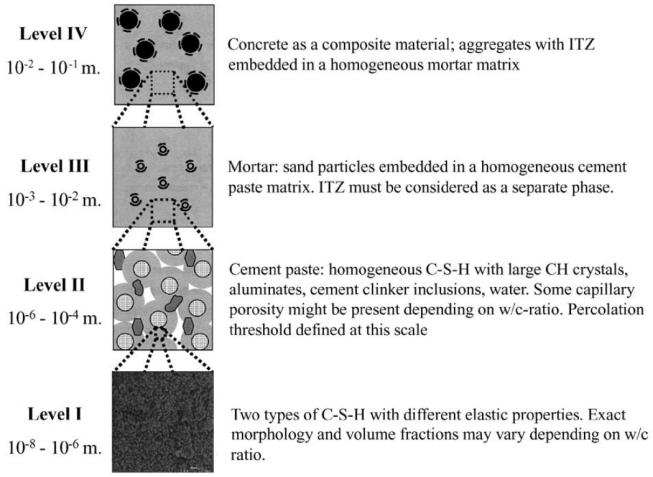

Figure 2.31: Analytical homogenization scheme of cementitious materials, after [3, 16].

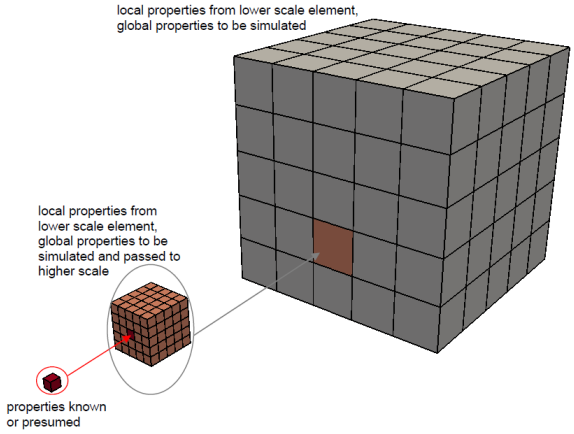

Figure 2.32: Parameter-passing multi-scale modelling scheme, after [4].

scale based concurrent modelling approach (Figure 2.33). However, because of the high computational demands, it has not been implemented yet. On the other hand, the hierarchical scheme allows investigating the material behaviour at each scale independently. It is therefore more popular for the characterization of the material properties at different length scales.

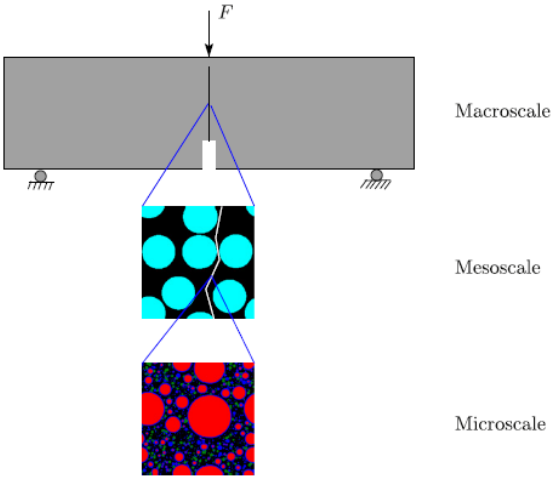

Figure 2.33: A macro-meso-micro three-scale concurrent model for concrete fracture modelling proposed by Nguyen et al. [7].

2.6. SUMMARY AND REMARKS

This chapter provides an overview of the multi-scale modelling schemes and aspects that relate to the micromechanical modelling of cementitious materials. Based on the above discussion, the following conclusions can be drawn:

- Prediction of micromechanical behaviour of cementitious material requires well-characterised material structures, proper input parameters and advanced fracture modelling approaches.

- For the material structure characterisation, numerical cement hydration models have clear advantages in terms of the efficiency, while the experimental approach is more "realistic". With micro CT techniques, it is possible to obtain a 3D microstructure of cementitious materials with a high resolution for modelling of fracture performance of cementitious material at the micro-scale.

- Mechanical properties of individual phases are essential for the prediction of mechanical response of cement paste at the micro-scale. The elastic properties of these phases can be derived from the nanoindentation test or atomistic simulations. However, dealing with the strength characterization remains a challenge. Although pioneering work has been conducted, there remains significant research

need in the prediction and measuring of the fracture properties of these phases.

- Several models have been proposed and implemented for the prediction of micromechanical properties of cement paste. The homogenization approach shows advantages when predicting the evolution of elastic properties along hydrating, but this approach cannot be used for the fracture analysis. Discrete model is therefore introduced. However, a comparison of the existing predicted stress-strain response of the cement paste shows large diverge. Thus, mechanical tests at the micro-scale should be conducted to calibrate the input parameters and validate the predicted micromechanical properties.

- Compared with the concurrent multi-scale scheme, the hierarchical scheme allows investigating the material behaviour at each scale independently, which is more suitable for understanding the structure-property relationship of a material that behaves differently at each separate length scale.

Therefore, an experimentally validated multi-scale modelling scheme is required for fundamental understanding and reliable prediction of the multi-scale mechanical properties of cementitious materials. To achieve this, advanced techniques in different fields need to be carefully selected and combined. Further work is needed in the part of experimental calibration and validation of the micromechanical models through advanced micromechanical measurements.

II

Micromechanical Testing and Modelling

3

TESTING AND MODELLING OF HARDENED CEMENT PASTE MICRO-CUBE USING INDENTATION SPLITTING TEST

This chapter provides a method for numerically and experimentally investigating the fracture mechanism of hardened cement paste (HCP) at the micro-scale. A new procedure was proposed to prepare micro-scale sized HCP cubes (100 µm × 100 µm × 100 µm) and beams with a square cross section of 400 µm × 400 µm. By loading the cubes to failure with a Berkovich tip, the global mechanical properties of HCP were obtained with the aid of a nanoindenter. Simultaneously, the 3D images of HCP were generated by applying X-ray computed tomography (XCT) to a micro-beam. After image segmentation, a cubic volume with the same size as the experimental tested specimen was extracted from the segmented images and used as input in the lattice model to simulate the fracture process of this heterogeneous microstructure under indenter loading. The input parameters for lattice elements are local mechanical properties of different phases. These properties were calibrated from experimental measured load displacement diagrams. With the method presented in this chapter the framework for fitting of the modelling at micro-scale was created, which forms a basis for multi-scale analysis of cementitious materials.

Parts of this chapter have been published in Materials **9** (11), 907 (2016) [152].

3.1. INTRODUCTION

MICROMECHANICAL modelling of cement paste requires experimental measurements at the same length scale for calibration and validation. However, mechanical testing of cement paste at micro-scale is still an challenging task [2]. To this end, this chapter provides a newly developed method for the micro-scale sized specimen preparation and mechanical measurements. The same size virtual specimen was generated by XCT scanning and image segmentation techniques. Discrete lattice model was used to model the fracture process of specimens under the indenter loading. Through inverse analysis, inputs of the lattice model were calibrated by the experimental measurements. These input parameters would be consistently used in the thesis. This forms the basis for multi-scale modelling of cementitious materials.

3.2. EXPERIMENTAL

3.2.1. SAMPLE PREPARATION

HEREIN, a new technique for preparing micro-cubes (100 µm × 100 µm × 100 µm) and micro-beams with a cross section of 400 µm × 400 µm. The micro-cubes are used for global mechanical performance test, while the micro-beams are for the XCT scanning. Standard grade ordinary Portland cement (OPC) CEM I 42.5 N cement pastes with w/c ratio of 0.3, 0.40 and 0.5 were cast in PVC cylinders (diameter: 24 mm, height: 39 mm) in sealed condition. After 24 h rotation and curing 28 days at room temperature (20 °C), specimens were demoulded and two discs with the thickness of 2 mm were cut from the middle part. One of the pieces was used to create the micro-cubes, while the other was used to create the micro-beams. The hydration was arrested by solvent exchange method using isopropanol [153]. In order to enable faster water-solvent exchange, samples were immerged five times and taken out for a period of one minute. Afterwards, they were placed for 3 days in isopropanol and subsequently taken out, and solvent was removed by evaporation at ambient conditions.

To create micro-cubes and micro-beams, the following procedure is followed: The first step is to make the thickness of the specimens even and equal to 100 µm and 400 µm (for micro-cube and micro-beam creation, respectively) using a Struers Labopol-5 thin-sectioning machine; afterwards, the micro-cubes and micro-beams are generated by running a precise diamond saw for semiconductor wafers (MicroAce Series 3 Dicing Saw, with a 260 µm wide blade) in two directions over the thin-section as schematically shown in Figure 3.1. To prevent chipping of the edges of the micro-cubes and micro-beams while cutting, a thin layer of soluble glue was applied on the surface of the thin section, which was later removed by soaking the specimen for a short time in acetone. The final cubes are at the dimension of 100 µm × 100 µm × 100 µm and beams are with a cross-section of 400 µm × 400 µm as shown in Figure 3.2.

3.2.2. GLOBAL MICRO-MECHANICAL PERFORMANCE USING MICRO-CUBE INDENTATION

In order to obtain the global mechanical properties, the micro-cubical HCP samples were placed in an KLA-Tencor G200 nanoindenter and loaded using a Berkovich tip (Figure 3.3). A displacement controlled test was performed by using the continuous stiff-

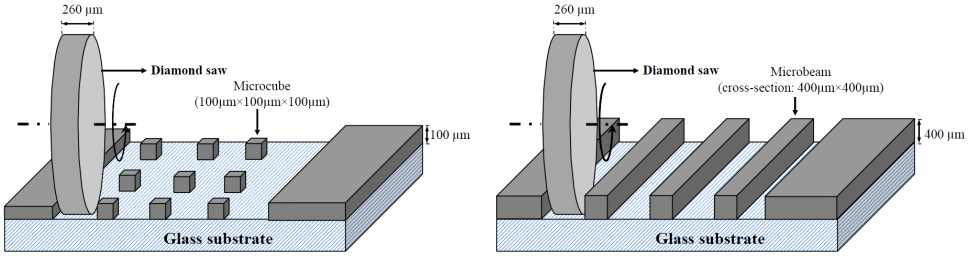

(a) (b)

Figure 3.1: Schematic view of sample generation: (a) micro-cube; (b) micro-beam.

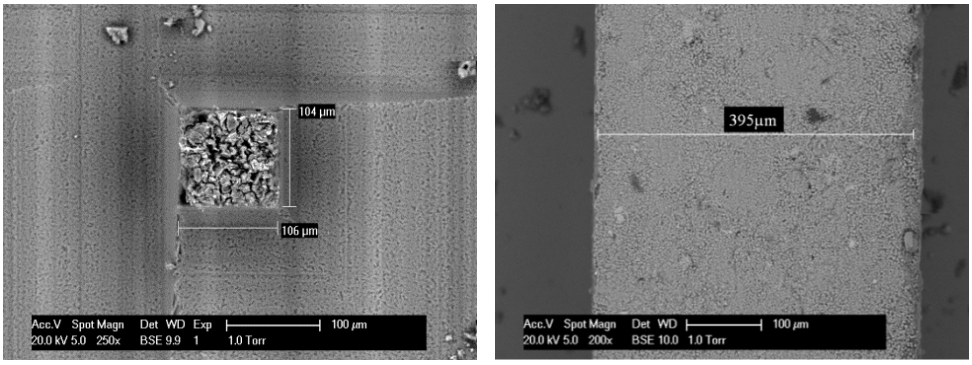

(a) (b)

Figure 3.2: SEM images of prepared specimens: (a) micro-cube; (b) micro-beam.

ness method (CSM) [154]. This method relies on applying a small harmonic load with frequency on the nominal load. The CSM settings applied in this study were: 2 nm amplitude, 45 Hz frequency and a displacement rate of 50 nm/s. The load-displacement response up until failure of the micro-cube is shown in Figure 3.4. In total, 8 load-displacements were measured in the experiments for HCP with a w/c ratio 0.4. Multiple measurements on different cubes show a high degree of repeatability. Two regimes can be distinguished from the graph. In regime (I), the load on sample increases monotonically for increasing indenting depth until reaches the peak load. The maximum load that can be applied before the micro-cube collapses is between 350 mN and 450 mN at a critical displacement between 10 µm to 15 µm. Once this load is exceeded, the system transitions from a stable regime (I) towards an unstable regime (II) with rapid displacement bursts. The horizontal line in regime (II) indicates structural collapse of the micro-cube, which results in an overshoot of the indenter tip towards the substrate. Since displacement control of the nanoindenter is not fast enough, it is not possible at present to capture the post-peak behaviour of the specimen. Furthermore, the behaviour might be brittle, and the system cannot capture a snap-back. Therefore, the calibration of the numerical model was carried out only in regime (I). It is observed that the test results still show variability which is induced by the inherent heterogeneity of the material.

The failure mechanism of the specimen under tip loading is observed in previous work [155], where different loading depths were applied. Crack patterns at various depths were obtained using environmental scanning electron microscope (ESEM). As shown in Figure 3.5, the typical failure mechanism obtained is the splitting of the material under the tip and three main cracks running to the sides of the cubes, starting from the three edges of the Berkovich tip. Complete crushing of the sample was achieved by indenting the tip further into the specimen.

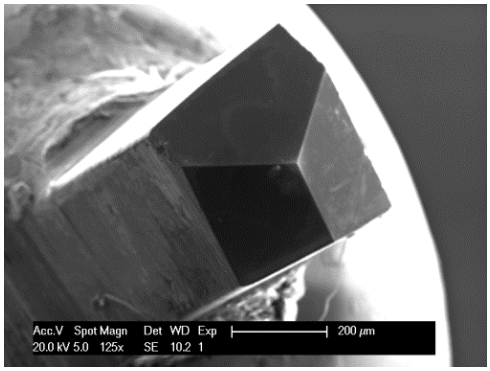

Figure 3.3: SEM image of the diamond Berkovich tip.

3.2.3. MICROSTRUCTURE CHARACTERIZATION USING XCT

In order to obtain the microstructure of the micro-cube, a generated micro-beam is scanned using a micro CT-scanner (Phoenix Nanotom). The micro-beam was fixed on a holder (see Figure 3.6a) and then put on the rotatable stage. The X-ray source tube worked at 120 kev/60 µA. 2800 images with an exposure of 6 s were acquired on a digital

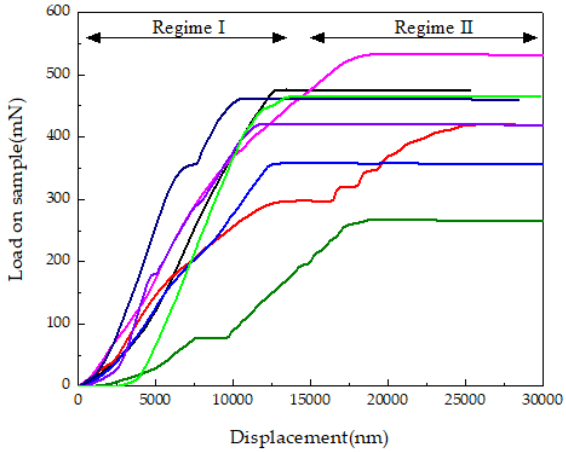

Figure 3.4: Measured global mechanical response of HCP micro-cubes prepared with w/c ratio of 0.4: load versus displacement response.

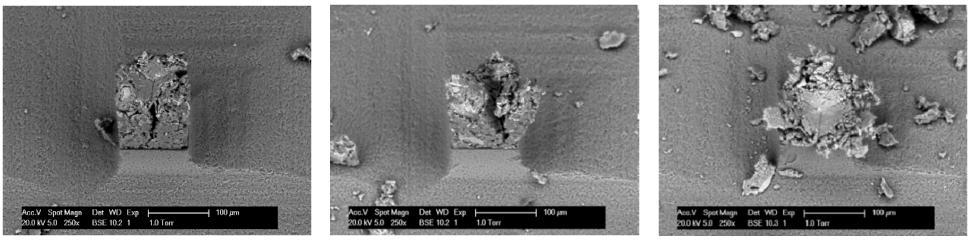

(a) (b) (c)

Figure 3.5: Three stages in the nano-indentation loading process of micro-cubes observed in SEM: (a) initial stage of loading; (b) three main cracks running to the sides of the cubes; (c) complete crushing of the sample (adapted from [155]).

GE DXR detector (3072 × 2400 pixels). The voxel resolution under these conditions was 0.5 µm × 0.5 µm × 0.5 µm. To reduce the influence of beam hardening in the XCT experiment, a cuboid region of interest (ROI) with a cross-section of 200 µm × 200 µm and length of 500 µm was extracted from the middle region of the specimen for the analysis (Figure 3.6b). The mesh discretization in the fracture model is correlated with the voxel size from the material structure, and a large number of simulations (more than 100) are required to be performed in the thesis, which means a huge computational effort were needed. For this reason, the resolution was reduced to 2 µm/voxel through a "median method" implemented in the X-ray reconstruction software. Finally, a 3D stack of 8-bit cross-section images were generated.

Image segmentation was performed using a so-called global threshold approach [17, 22, 23, 53]. In this method, phases were isolated from the original grey-scale map by choosing corresponding threshold step by step as shown in Figure 3.7. Firstly, two threshold grey values are defined on the basis of grey-level histogram as shown in Figure 3.8: T_1, pore/solid phase threshold, is assumed as the grey value at the inflection point in the

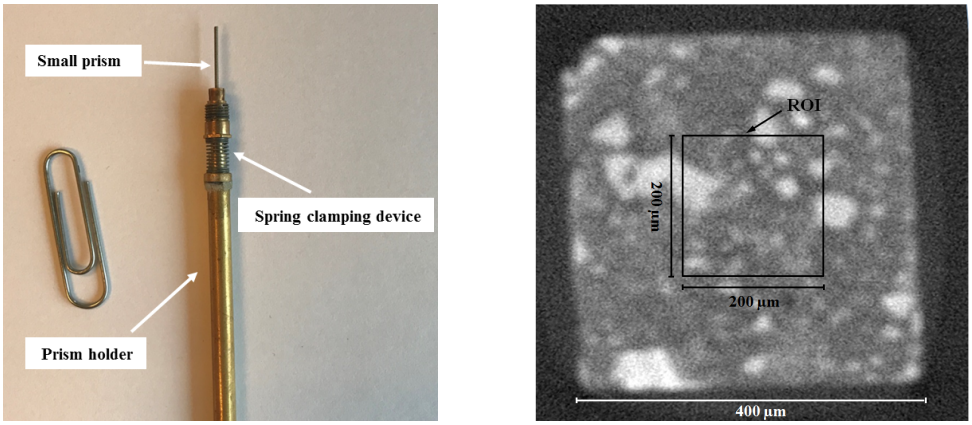

(a) (b)

Figure 3.6: (a) Small prism clamped on the special holder for CT scanning; (b) an example cross sectional XCT image of ROI.

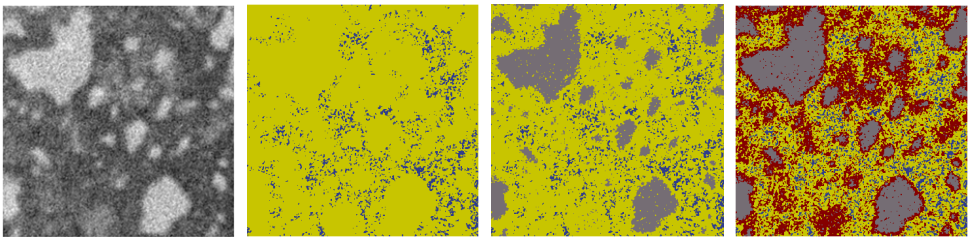

(a) (b) (c) (d)

Figure 3.7: 2D schematic view of image segmentation process:(a) original grey-scale map; (b) pore (blue) and solid phases (yellow) are isolated from the grey-scale map; (c) anhydrous cement (grey) and hydration product (yellow) are isolated form solid phases; (d) outer product (yellow) and inner product (red) are segmented from hydration product.

cumulative fraction curve of the histogram; T_2, hydration products/anhydrous cement phase threshold, is a critical point at which the tangent slope of histogram changes suddenly. So far three phases: pore, anhydrous cement and hydration product are isolated. More details about this approach can be found in [17, 53]. However, it is well known that at least three types of hydration product with different mechanical properties [16, 30–32] exist: low density C-S-H_{LD} (outer hydration product), high density C-S-H_{HD} (inner hydration product) and CH. In order to simplify the procedure, CH was not considered as a separate phase, and therefore was not explicitly modelled. This simplification is considered not to significantly affect the results of mechanical properties simulation [4]. However, in further work, CH as a separated phase should be considered.

A so called J-T model [156] on the basis of specific surface measurements was introduced here to calculate the volume fraction of C-S-H_{LD} and C-S-H_{HD}. As shown in Figure 3.9, the inputs for this model are w/c ratio and degree of hydration which can be estimated on the basis of volume fraction of anhydrous cement $V_{anhydrous}$ and hydration

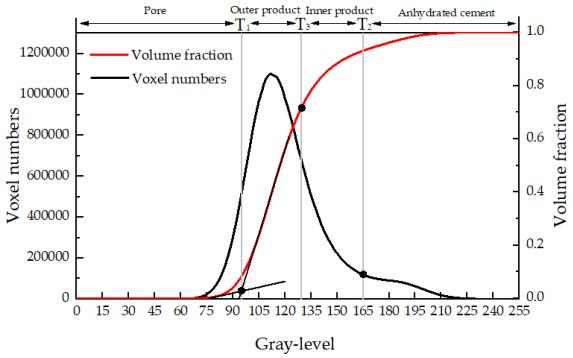

Figure 3.8: Phases evolution through greyscale level histogram of CT images.

products $V_{hydrated}$ according to equation:

$$\alpha = \frac{\frac{V_{hydrated}}{\nu}}{\frac{V_{hydrated}}{\nu} + V_{anhydrous}} \tag{3.1}$$

where ν is defined as volume reaction product /volume reactant ratio and assumed as 2.2 for OPC [24]. Once the volume fraction of those two products are obtained, the threshold value can be determined on the basis of greyscale level histogram. Finally, a cubical region of interest with 100 µm (50 voxels) in length was extracted from the segmented microstructure for lattice fracture analysis.

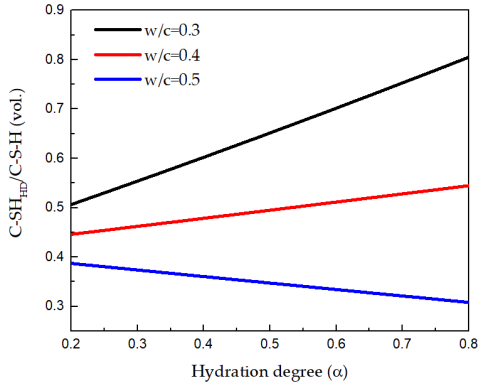

Figure 3.9: C-S-H_{HD} evolution based on the J-T model [156].

For each w/c ratio (i.e. 0.3, 0.4 and 0.5), one prism was scanned. Based on the described procedure, the segmented volume fraction of pore, anhydrous cement grains and hydration degree of each scanned prism are listed in Table 3.1. The hydration degree is quite close to the one reported by Haecker et al. [77] using non-evaporable water content method (for w/c =0.3: 63.0 %, w/c=0.4: 80.6 % and w/c= 0.5: 88.4 %). One should

Table 3.1: Details of segmented microstructures.

W/c	Porosity (%)	Anhydrous cement grains (%))	Hydration degree (%)
0.3	8.44	15.30	69.65
0.4	11.84	10.64	74.99
0.5	17.50	8.02	80.85

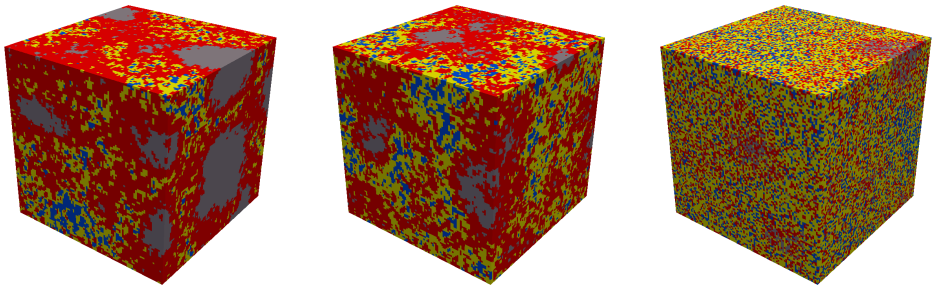

(a) (b) (c)

Figure 3.10: 3D segmented microstructure (100 µm ×100 µm × 100 µm) of HCPs with different w/c ratios: (grey-anhydrous cement; red-inner product; yellow-outer product; blue-pore).

keep in mind that, owing to the limitation of image resolution, pores smaller than 2 µm are not detectable and are mixed within the segmented solid phases [157, 158]. Therefore, the total porosity derived from CT images is significantly lower than the theoretical total porosity predicted by Powers model (for w/c=0.3: 17.80 %, w/c=0.4: 23.3 % and w/c=0.5: 29.2 %) [159] and mercury intrusion porosimetry (MIP) test performed on similar pastes (for w/c=0.3: 17 %, w/c=0.4: w/c=23 % and 0.5: 31 %) [160] which include the capillary pores smaller than 2 µm as well as part of gel pores. A virtual cubic specimen with size of 100 µm for each w/c ratio was shown in Figure 3.10). In this chapter, only the virtual specimen with w/c ratio of 0.4 was used for the mechanical simulations. Use of the other virtual specimens were shown later.

3.3. MODELLING

3.3.1. MODELLING APPROACH

AGAIN the aim in this chapter is mainly to determine the micromechanical properties of local phases in lattice model by fitting the experimental results. The lattice model is applied in this study to model the observed fracture behaviour of the tested micro-cubes. In the model, the material is schematized as a grid of beam elements connected at the ends and all individual elements are defined having linear elastic behaviour. Due to the low ratio of length and height of beam elements in the network, a Timoshenko beam element is used to take shear deformation into account [4]. A set of linear elastic analyses is then performed by calculating the stress distribution at each element for an imposed particular external boundary condition. Normal force and bending moments in lattice beam elements are both taken into account by the following general relation:

$$\alpha = \alpha_N \frac{N}{A} + \alpha_M \frac{\max(M_x, M_y)}{W} \tag{3.2}$$

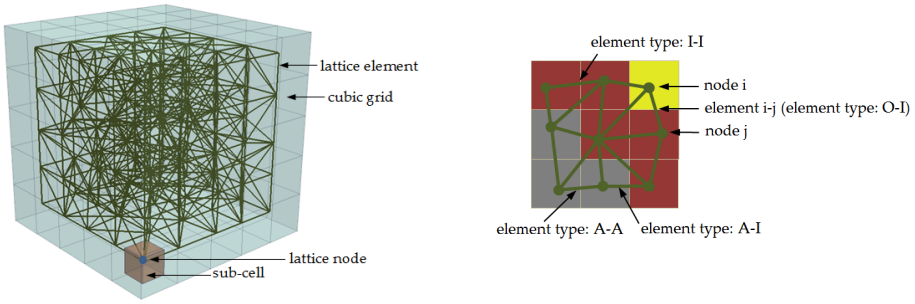

(a) Lattice network construction(5×5×5) (b)

Figure 3.11: Schematic view of lattice model generation: (a) lattice network construction (5 × 5 × 5); (b) overlay procedure for a 2D lattice mesh (yellow-outer product; red-inner product; grey-anhydrous cement).

where A denotes the beam cross-sectional area, W is the cross-sectional moment of resistance; N is the normal force along the element. M_x and M_y are the bending movements in the local coordinate system. α_N and α_M represent the normal force influence factor and the bending influence factor. Their values are commonly adopted as 1.0 and 0.05, respectively [161]. These values were also adopted herein. The influence of different values of these parameters on the concrete fracture response is discussed elsewhere[162]. For simplicity,torsion is not included in the fracture law in the current study. In every analysis step, loading is increased until exactly one beam in the mesh has a stress/strength ratio equal to one. This beam is then removed from the mesh. The mesh is then updated and relaxed. This loading procedure is repeated until a predefined stopping criterion (e.g. load or displacement). Consequently, the fracture pattern of the investigated material volume at each step can be obtained as well as their load-displacement response. The "Berkovich tip loading" test is simulated by applying a vertical displacement in four nodes in the centre of the top surface. The lattice element can fail either in tension or compression. The procedure to generate the lattice mesh and assign mechanical properties of elements is as follows.

The 3D mesh generation is described in Figure 3.11. First, a cubic domain (100 µm × 100 µm × 100 µm) is divided into a cubic grid with a cell size of 2 µm. Then, a sub-cell was defined within each cell in which a node is randomly positioned. The ratio between the length of sub-cell and cell is defined as randomness. As shown in a previous study [138], the choice of randomness affects the simulated the fracture behaviour of materials, because the simulated crack shape is affected by the orientation of elements in the mesh. In order to avoid big variations in length of elements and introduce geometry disorder of material texture, a randomness of 0.5 is adopted. Then, Delaunay triangulation is performed to connect the four nodes that are closest to each other with lattice elements.

The overlay procedure is applied to realize the heterogeneity of this material, see 3.11b. In this procedure, different micromechanical properties are assigned to corresponding phases. For this purpose, the microstructure of HCP with w/c ratio 0.4 obtained in Section 3.2.3 is used here. Each node is assigned a local phase based on the

voxel value it belongs to and the lattice element is determined by the locations of its two nodes. No lattice node is generated in the voxels which represent pore phases, as it does not contribute global mechanical performance of the specimen. Three solid phases in the microstructure in six types of lattice elements as listed in Table 3.2. The shear modulus and Young's modulus of element i–j connecting phase i and phase j are determined as [4]:

$$\frac{2}{E_{ij}} = \frac{1}{E_i} + \frac{1}{E_j} \tag{3.3}$$

where E_i, E_j and E_{ij}, are the Young's modulus or shear modulus for phase i, phase j and element which connects phase i and phase j, respectively. The compressive strength and tensile strength take the lower value of the connected two phases, which can be expressed as [4]:

$$f_{ij} = \min(f_i, f_j) \tag{3.4}$$

where f_i, f_j and f_{ij}, are the compressive strength or tensile strength for phase i, phase j and element which connects phase i and phase j, respectively. The mechanical properties of these pure phases was preferred to be measured in laboratory test, but in the case of a lack of experimental data, properties of these phases are commonly derived from the nano-indentation measurements [4, 19]. However, no data is available defining the relationship between the model parameters (tensile and compressive strength) and nano-indentation results (indentation hardness). Herein, in order to work out this relationship, the simulated fracture performance is compared with the experimental results to find out the best simulation. In the calibration, tensile strength (and compressive strength) of each phase is assumed proportional to the measured hardness.

Table 3.2: Classification of lattice element types.

Element type	Phase 1	Phase 2
A–A	Anhydrous cement	Anhydrous cement
I–I	Inner product	Inner product
O–O	Outer product	Outer product
A–I	Anhydrous cement	Inner product
I–O	Inner product	Outer product
A–O	Anhydrous cement	Outer product

Table 3.3 summarizes the assigned mechanical properties of relevant phases in the model. The Poisson's ration follows directly from the origin of the discrete element mesh. The mesh configuration that is chosen has a Poisson's ratio of about 0.18. For elasticity modulus, mean values reported in [30] were used in the current work in which SEM is adopted to visualize and characterize the microstructures where nanoindentation tests were performed, more reliable results are therefore expected. Hu and Li [30] report a lower elastic modulus of anhydrous cement particles than those reported by Velez et al. [97] in which nanoindentation is performed on different synthesized pure clinker phases. This is due to the fact that the residual cement particles in HCPs are more porous [163]. Although the results from Velez et al. [97] have been successfully used in different micromechanical models [3, 15, 73, 164–167], for the sake of more reasonable input model parameters, the more recent outcome [30] was adopted in the current work.

Table 3.3: Measured mechanical properties of individual local phases from [30].

Phase	Modulus of elasticity (GPa)	Hardness (GPa)
Anhydrous cement	99.2	8.24
Inner product	31.6	1.14
Outer product	25.2	0.75

3.3.2. CALIBRATION AND DISCUSSION

During the calibration of mechanical properties of local phases, three sets of parameters as listed in Table 3.4 were evaluated to study their influence on the simulated fracture performance. The simulated load displacement diagrams are compared with the experimental results as shown in Figure 3.12. A descending branch is observed in regime (II) for the simulated results, which is missed in the micro-cube indentation measurement. Their corresponding damaged patterns in the final stage are presented in Figure 3.13.

Table 3.4: Assumed local mechanical properties of individual local phases in HCP.

Set	Anhydrous cement			Inner products			Outer products		
	E(GPa)	f_t(GPa)	f_c(GPa)	E(GPa)	f_t(GPa)	f_c(GPa)	E(GPa)	f_t(GPa)	f_c(GPa)
S1	99.2	0.683	6.830	31.6	0.092	0.92	25.2	0.0583	0.58
S2	99.2	0.683	68.3	31.6	0.092	9.2	25.2	0.0583	5.8
S3	99.2	0.683	∞	31.6	0.092	∞	25.2	0.058	∞

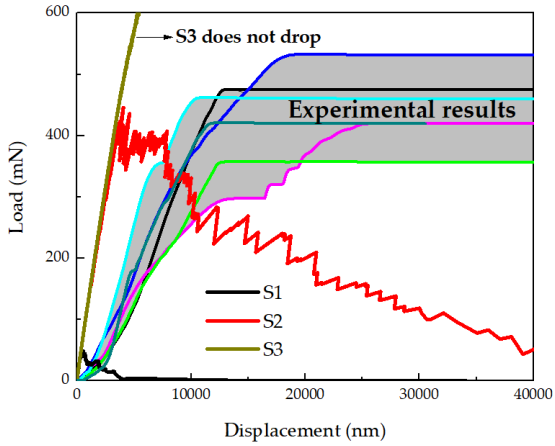

Figure 3.12: Comparison between simulated load-displacement diagrams and experimental results.

The adopted compressive strength/tensile strength ratio of local elements has significant influence on simulated load displacement diagram and damage evolution. Figure 3.13a shows the damage evolution of S1 in which the compressive strength is taken as 10 times higher than the tensile strength (similar with the assumption in [131]). A few microcracks are initiated around the loading points causing local crushing of the indented area, thus inducing an unrealistically low load response. On the contrary, in the simulation of S3, no softening branch is found in the simulated load-displacement diagram

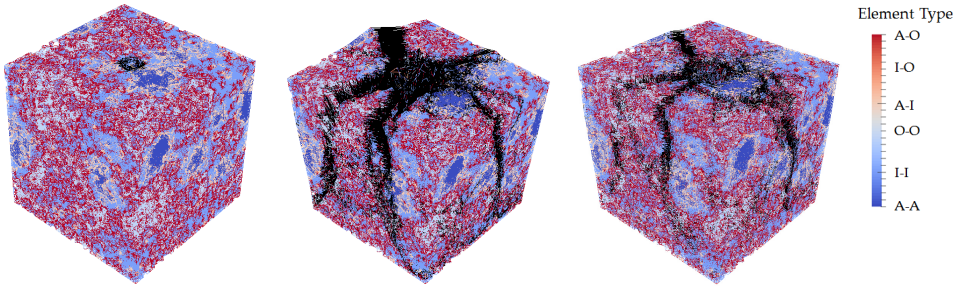

(a) S1 (b) S2 (c) S3

Figure 3.13: Crack patterns in the final failure state: (a) S1; (b) S2; (c) S3; (d) element type (black-damaged element).

Table 3.5: Lattice element types and their mechanical properties.

Element type	Young's modulus (GPa)	Tensile strength (MPa)
A-A	99	683
I-I	31	92
O-O	25	58
A-I	47	92
I-O	28	58
A-O	40	58

even when the "indenter" reaches the bottom of the micro-cube specimen. This is because no compressive failure is allowed for local elements in this particular case. In the fracture model, the loading points starts out dragging the upper surface down, and apparent load that can be withstood by the specimen becomes unrealistically high.

Simulation of S2 and "measured" curves show a very high degree of consistency on the peak load and stiffness(slope of the load displacement curve). Due to the fact that some slip occurs at the beginning of the experiments, the measurements are slightly shifted, but the slope is similar to the linear part of simulated load displacement curve of S2. In S2, the assumed tensile strength is 12 times lower than the measured hardness, in accordance with [131], while the ratio between compressive strength and tensile strength (100) is much higher than in [131]. This may be because of the different resolutions and theories applied in these two models. Parameters in S2 is therefore continuously used in the following chapters for the micromechanical modelling. The resulting mechanical properties of six element types are listed in Table 3.5.

3.4. CONCLUSIONS

THIS chapter presents an approach for determining the micromechanical properties of individual HCP phases. A procedure for micro-scale sized specimen preparation and testing of global performance using nanoindenter was developed and employed. As a result, fracture patterns under different loading depth and load displacement diagrams were obtained. Two regimes were observed experimentally in the load displace-

ment diagram. Since the displacement control of the nanoindenter equipment is not fast enough to capture the fast decrease in load when the specimen fails, a horizontal line existed in regime (II). Thus, the ascending branch in regime (I) was applied to calibrate the microstructure-informed lattice model.

The 3D lattice model was built up based on a microstructure of HCP obtained from XCT. The mechanical properties of local phases were calibrated by validating the simulated results with the experimental results. It is showed in this chapter that the adopted mechanical properties of local phases are critical for the investigate in terms of load displacement response and failure mechanism. Therefore, it is of great importance to fit these parameters by designing experiments on the specimens in the same size as well as under well-controlled boundary condition. As a result, parameters in Table 3.5 is suggested as proper input for mechanical properties of each phase presented in the microstructure.

4

TESTING AND MODELLING OF HARDENED CEMENT PASTE MICRO-CUBE USING ONE-SIDED SPLITTING TEST

This chapter presents the investigation of micromechanical properties by both numerical modelling and experimental testing. Micro-cubes with length of 100 µm were split by a wedge tip mounted on the nanoindenter. A nominal splitting tensile strength was derived from the maximum load of the recorded load-displacement diagram to represent the global fracture performance of the fractured micro-cube. To achieve this, an analogy was made between the one-sided splitting test and the standard Brazilian splitting test. To cope with the inherent heterogeneity of this material at micro-scale, for cement paste with each water/cement (w/c) ratio (0.3 ,0.4 and 0.5), more than hundred micro-cube specimens were fabricated, tested and analysed using Weibull statistics. The analysis shows that the splitting tensile strength of cement paste on the micro-scale is much higher than on the macroscopic scale but lower than tensile strength of distinct hydrated cement phases measured at micro-scale. The experimental results were then used to validate the micromechanical model which has been calibrated in Chapter 3. A good consistency in terms of the load-displacement curve and fracture pattern is found between the simulations and experiments.

Parts of this chapter have been published in Engineering Fracture Mechanics **199**, 773-789 (2018) [168].

4.1. INTRODUCTION

RECENT studies, both experiments and simulations, found that the tensile strength of components in cement paste at small scale is much higher than the macroscopic value of concrete (a few MPa). For example, in molecular dynamics models, tensile strength of pure C-S-H globules is predicted from 1 GPa to 3 GPa depending on dry or wet conditions [34], while low and high density C-S-H phases are predicted to have tensile strengths of 66 MPa and 320 MPa, respectively, by means of inverse analysis using a multi-scale model [131]. In addition, micro-cantilever experimental measurements (length scale of several μm) show that the tensile strengths are around 264 MPa, 700 MPa and 655 MPa for outer products, inner hydration products, and calcium hydroxide, respectively [45]. Therefore, it is expected that the studies on cement paste at micro-scale could fill the gap between nano scale and meso scale.

At the micrometre length scale high scatter of measured mechanical properties can be expected [106, 169] and that a large number of tests need to be performed for the measurements to be statistically reliable. To this end, the precision micro-dicing technique developed in Chapter 3 is adopted for micro-scale specimen preparation. In this way, a large number of micro-cubes can be fabricated in a short period of time. These cubes are split by applying a line force at centre of the top surface using a wedge tip mounted on a nanoindenter. Splitting tensile strength is derived from the recorded maximum load using an analogy with the analytical solution of a classic Brazilian splitting test. Hardened cement pastes with different w/c ratios (0.3, 0.4 and 0.5) were investigated. Considering the heterogeneous nature of this material at micro-scale, at least one hundred specimens for each w/c ratio were tested and the so-called Weibull statistics was adopted to conduct the statistical analysis of measured strength.

In addition to the experiments, a microstructure informed lattice fracture model was used to study the fracture process of the micro-cube under the one-sided splitting. Such fracture model requires digitalized microstructure and mechanical properties of individual phases. The input mechanical properties of individual phases are calibrated in Chapter 3 using the experimental data from where the same size micro-cube was fractured by a Berkovich tip. It is therefore expected that a validation procedure can be conducted in the current work by applying different boundary conditions on the micro-cube and compared with the experimental results. In this way, an integrated system for fitting and validating micro-scale fracture simulation can be completed.

4.2. MICRO-CUBE ONE-SIDED SPLITTING TEST

4.2.1. MATERIALS AND EXPERIMENTS

THE same raw materials (Standard grade OPC CEM I 42.5 N and deionized water) and preparation procedure as described in Section 3.2.1. were used to prepare the 100 μm micro-cubes with w/c ratio 0.3, 0.4 and 0.5.

The micro-cube one-sided splitting test was conducted by applying a line load at the centre on top surface of the specimen as schematically shown in Figure 4.1, which was achieved by the KLA-Tencor G200 nanoindenter equipped with a diamond wedge indenter tip (Figure 4.2). Length and radius of the cylindrical edge are 200 μm and 9.6 μm, respectively. The micro-cube was progressively loaded with a constant displace-

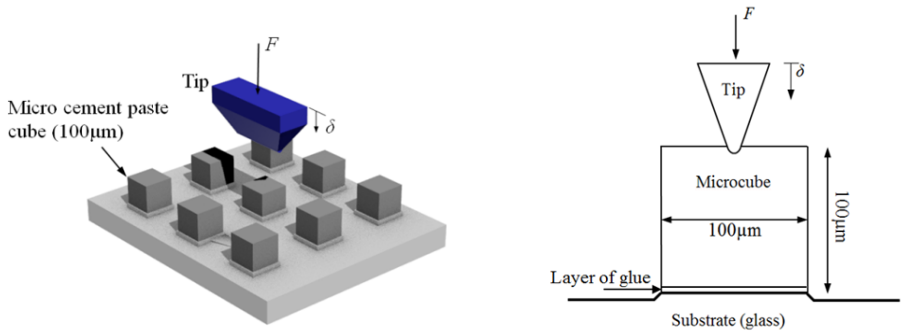

(a) (b)

Figure 4.1: Schematic illustration of (a) the micro-cube splitting procedure; (b) The contact mechanics between indenter tip, micro-cube and substrate.

ment increment of 50 nm/s until failure. Force and displacement data were acquired using the continuous stiffness measurement (CSM) technique [154] and the applied CSM settings were: 2 nm amplitude, 45 Hz frequency and 100 N/m surface detection. The maximum load capacity of the instrumented nanoindenter is around 635 mN[1]. A typical load-displacement curve recorded by the nanoindenter is shown in Figure 4.3. Clearly two regimes as well as the maximum load point at failure stage can be distinguished from this curve. In regime (I), the load on sample increases monotonically until reaching the critical splitting load (maximum load) P_u. Once the load exceeds P_u, the system transitions from a stable regime (I) towards an unstable regime (II). The horizontal line in regime (II) indicates an overshoot behaviour of the wedge indenter tip towards the substrate because of the structural collapse of the micro-cube. As explained in Chapter 3, displacement control of the nanoindenter is not fast enough so it is not possible at present to capture the post-peak behaviour of the specimen, or the behaviour of the material might be so brittle that the system cannot capture a snap-back.

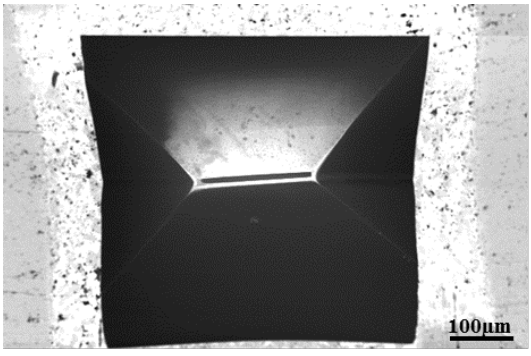

Figure 4.2: Top view of the diamond wedge tip with 200 μmm in length and a round apex with a radius of 9.6 μm

[1] In Chapter 6, a high load device is installed to increase load capacity of the nanoindenter.

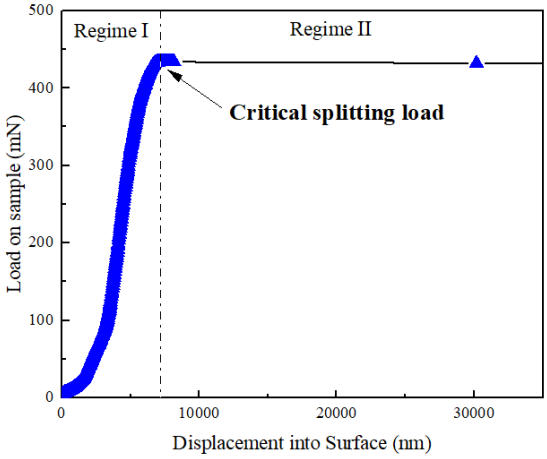

Figure 4.3: A typical load versus displacement response measured in the micro-cube splitting test.

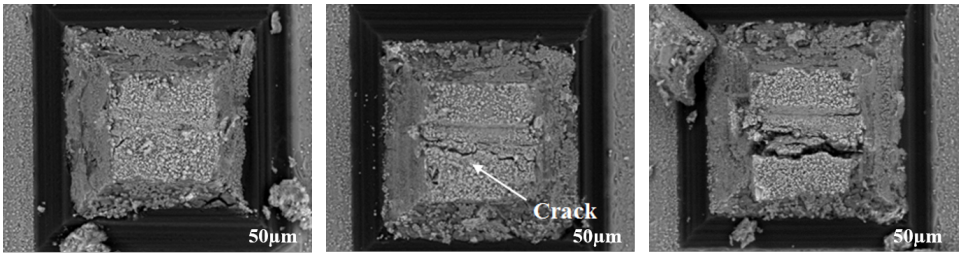

(a) (b) (c)

Figure 4.4: Three stages in the micro-cube splitting process: (a) initial stage of the loading; (b) crack starts to propagate next to the tip; (c) splitting failure of the micro-cube.

Additionally, in order to visually observe the fracture mechanism of this test, different loading depths were applied. After test, the fractured specimens were examined using ESEM and the micrographs are presented in Figure 4.4. Since the indented specimen is small enough, the structural damage occurs under a relatively low force and the typical failure mechanism is splitting of the material in which the main cracks extend and propagate under the tip until the specimen is split in two halves across the plane of loading.

4.2.2. SPLITTING TENSILE STRENGTH ASSESSMENT USING FEM

As a structural collapse happens to the micro-cube once a critical load is reached during testing, a parameter (i.e. strength) that could represent the global mechanical performance can be derived from the critical load. This enables a quantitative study of the micromechanical performance. Since the boundary conditions of micro-cube splitting test are similar to a standard Brazilian splitting test (BS-EN 12390-6 [170]) for splitting tensile strength assessment of cementitious materials, it is expected that the tensile strength can be predicted in a similar way. An analogy between these two tests was made by as-

sessing the stress distributions of specimens under corresponding loading conditions using linear elastic, homogeneous, and isotropic finite element modelling (FEM). It has to be noted that, although the micro-cube paste specimens clearly cannot be considered as homogeneous and isotropic on this length scale, these assumptions were made in order to enable a relatively simple conversion of measured values to splitting strength by comparing it to a standard test (i.e. the Brazilian test). The influence of heterogeneity in the mechanical behaviour of paste on this length scale is discussed later.

In the Brazilian test, a pair of symmetrical line loads are applied by compressing two parallel bearing strips at the centre of both top and bottom surfaces of cubic specimen, as schematically shown in Figure 4.5. This geometry and loading conditions lead to a nearly uniform tensile stress state in the central plane of the specimen and the stress becomes more uniform as the strips become narrower. Therefore, the expected failure mode of this test is the splitting of specimens in two halves (similar to the observation in micro-cube splitting test). According to elastic theory, the maximum stress is a measure of the splitting tensile strength which is defined as [171, 172]:

$$f_{st} = \frac{2P_s}{\pi D^2} \tag{4.1}$$

where P_s is the maximum load, D is the length of cube. Simultaneously, a commercial FEM software package FEMMASSE [173] was used for simulation of stress distribution in which materials properties were set as homogeneous, isotropic, and linear elastic. For simplicity, only half of the specimen with 50 × 100 FE grid mesh was simulated. The loading was simplified as a concentred point load and a vertical displacement support at symmetry axis as shown in Figure 4.6a. Figure 4.6b presents the simulated contours of equal principal tensile stress. Clearly the numerical simulated maximum stress is consistent with the analytical solution in Equation 4.1. Afterwards, the numerical modelling for micro-cube splitting was achieved by clamping the bottom surface as shown in Figure 4.7a, while other parameters remained unchanged. The results are shown in Figure 4.7b. It is found that the maximum tensile stress for both simulations appear in the central plane and the ratio between micro-cube splitting and Brazilian splitting is around 0.73. Although the tension zone is smaller and moved upwards, it is expected that to break the same brittle-elastic specimen the Brazilian test needs 0.73 load of the micro-cube splitting test. Therefore, a reduction factor α=0.73 is added in Equation 4.1 to derive the splitting tensile strength from measured maximum load in the current test:

$$f_{st} = \alpha \frac{2P_s}{\pi D^2} \tag{4.2}$$

Equation 4.2 was therefore used to convert the maximum load to splitting strength in the following sections.

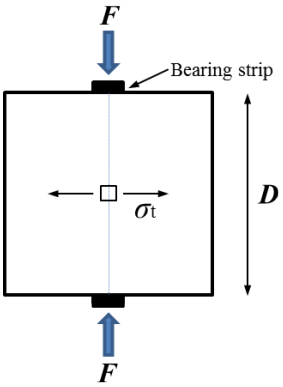

Figure 4.5: Load configuration of Brazilian test on cubic specimen.

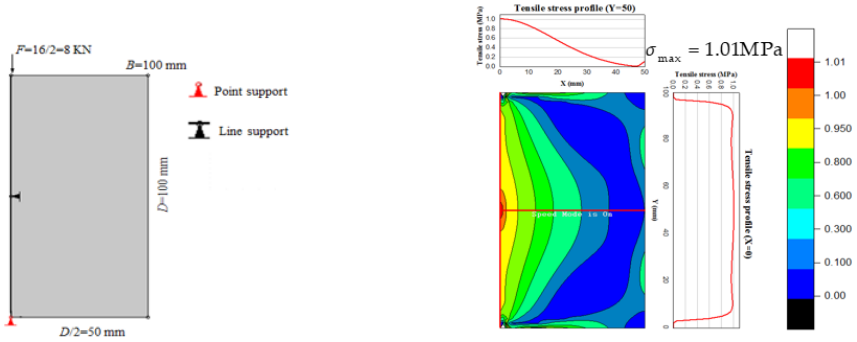

(a) (b)

Figure 4.6: 2D FEM computations of Brazilian test:(a)boundary conditions; (b) contours of equal principal tensile stress.

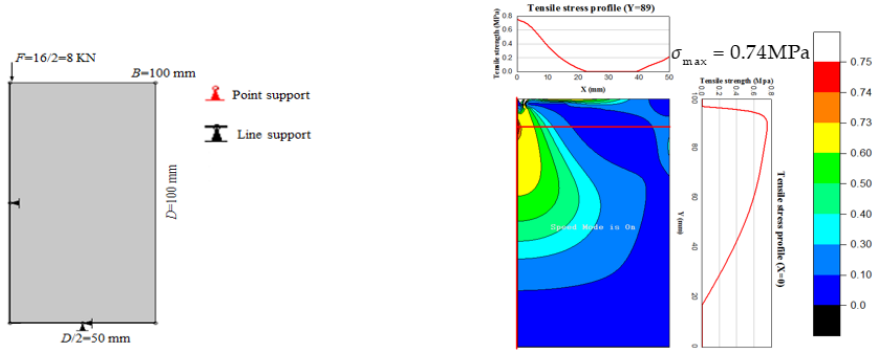

(a) (b)

Figure 4.7: 2D FEM computations of indentation splitting test: (a) boundary conditions; (b) contours of equal principal tensile stress.

4.2.3. ELASTIC PROPERTIES MEASUREMENTS OF ADHESIVE LAYER:

As a two-component epoxy adhesive (Araldite 2020) was adopted for bonding glass substrate and cement for micro-cube fabrication. In order to get the micromechanical properties of the adhesive as input for fracture simulation, grid nanoindentation tests were performed. The two components were mixed uniformly and dropped on the glass substrate to form a hardened film with a thickness of around 1 mm. Prior to testing, the adhesive film was ground using sandpaper to reach a relative flat and smooth surface. After grinding, the film was polished with 6 µm (5 min), 3 µm (5 min), 1 µm (10 min), and 0.25 µm (30 min) diamond paste on a lapping table. Each suspension was used for 30 min and after each polishing step, samples were soaked into an ultrasonic bath to remove any residue.

A series of 10 × 10 indents was performed on the polished surface with a spacing of 20 µm between each indent using the Agilent Nanoindenter G200 (Keysight, Santa Rosa, CA, USA) equipped with a diamond Berkovich tip. The Continuous Stiffness Method (CSM) proposed by Oliver and Pharr [81], which provides continuous measurements of elastic modulus as a function of indentation depth, was used to analyse the results. Indentation depth was set to 1000 nm and the average E modulus was determined in the loading range between 800-900 nm. For the calculation, Poisson's ratio of the indented material was estimated as 0.3. An average value of 3.06 MPa with a standard deviation of 0.42 MPa was derived from 100 indents indicating that a deterministic value can be used for the simulation. As the adhesive element in the simulation is not allowed to fail, it has no contribution to the predicted strength in the modelling. Therefore, there is no demand for the strength of this element in the simulation.

4.3. MODELLING

THE modelling approach presented in Chapter 3 was used herein. In order to show the deviation of the material properties introduced by the heterogeneity of the microstructure, 10 virtual specimens with w/c 0.4 were randomly from the segmented material structures in Section 3.2.3. The discrete lattice model was implemented to model the virtual specimens under the one-sided splitting. In order to validate the modelling approach proposed in Chapter 3, the mechanical properties of S2 as listed in Table 3.5 were used. Six types of lattice elements were determined by the three solid phases. Elastic modulus of a beam element was estimated as a harmonic average of the connected two phases (Equation 3.3), while the lower value of the two phases was considered as tensile strength (Equation 3.4).

The boundary conditions are shown in Figure 4.8. The nodes at bottom surface were clamped to represent the glued sample on the glass plate. A vertical displacement was applied on nodes in the two lines closed to the middle axis of the top surface to mimic the indenter load. It is emphasized that in order to show a more realistic elastic fracture behaviour of micro-cube under indentation, the lattice elements (coloured grey in figure) located up to 20 µm from the bottom were set as adhesive elements with a low elastic modulus of 3 GPa to represent the adhesive layer (AL) between cement paste and glass substrate. The AL was set to be linear elastic.

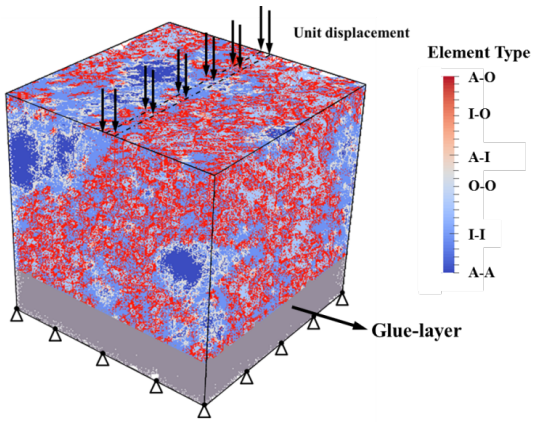

Figure 4.8: Fracture modelling of micro-cube under one-sided splitting.

4.4. RESULTS AND DISCUSSION

4.4.1. EXPERIMENTAL RESULTS AND DISCUSSION

FOR each w/c ratio, at least one hundred micro-cube specimens were fabricated and tested. Histograms of measured splitting tensile strengths are shown in Figure 4.9. The results exhibit great dispersion owing to the heterogeneous nature of the material at this scale. Thus, it is preferable to analyse the experimental data by Weibull statistics. For samples which have the same volume, the probability of failure P_f can be written as [174]:

$$P_f = 1 - \exp\left[-\left(\frac{\sigma_f}{\sigma_0}\right)^m\right] \tag{4.3}$$

where P_f is the cumulative probability of failure, m is the Weibull modulus (shape parameter) used to describe variability in measured material strength of brittle materials, σ_f is the fracture strength and σ_0 is the scaling parameter (characteristic strength). At the characteristic strength, the value of P_f equals 0.63 indicating that 63 % of specimens will fail at or below σ_0. In the absence of specific requirements, a general rule-of-thumb is that approximately 30 test specimens provide adequate Weibull strength distribution parameters, with more test specimens contributing little towards better uncertainty estimates [175, 176]. Therefore, considering the number of specimens tested in each group, a good regression can be expected if the strength of cement paste at micro-scale can be represented by the two-parameter Weibull statics. As shown in Figure 4.10, the splitting tensile strengths are plotted in a Weibull coordinate system. A least-squares method was used to fit m and σ_0, where m is the slope of the least-squares fit and σ_0 can be calculated from the x-intercept of this fit. Note that if the strength values of the specimens in the group have an infinite scatter, then the fitted line in Figure 4.10 would be vertical and the Weibull modulus would approach zero. Conversely, a Weibull modulus approaching infinity would correspond to a group with specimens have exactly the same strength with each other and a horizontal line can be expected in Figure 4.10 for this case. The fitted results are given in Table 4.1. Although some deviation from the best-fit line oc-

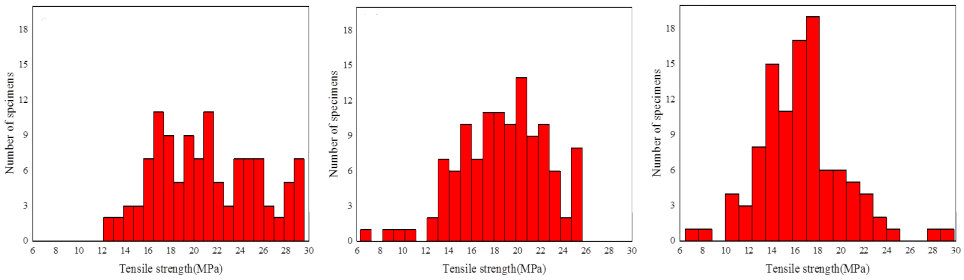

Figure 4.9: Measured splitting tensile strength of cement paste micro-cubes with different w/c ratios:(a) 0.3; (b) 0.4; (c) 0.5.

curred at the high strength extreme of cement paste with a w/c ratio of 0.3, a reasonable agreement is demonstrated between the best straight-line fit and the experimental data points with a high coefficient of determination (R^2). This difference is introduced because of the limited load capacity of the instrumented nanoindenter, which is around 635 mN corresponding to a strength limitation of 29.5 MPa. Once the response of the load reached this value, the test was stopped, and this value was recorded as the maximum load leading to a sharp increase of the cumulative probability at the high strength extreme.

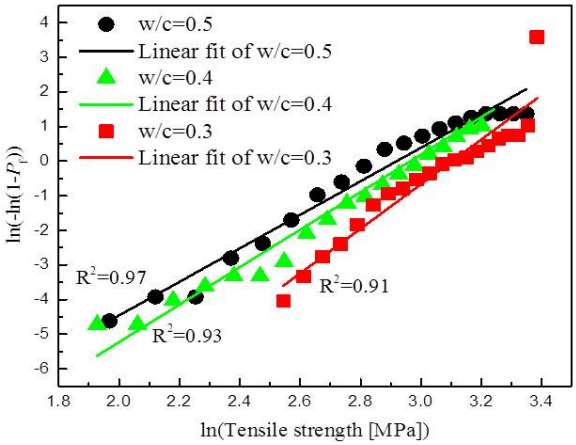

Figure 4.10: Weibull plot for measured splitting tensile strength of cement paste micro-cubes with different w/c ratios.

Table 4.1: Weibull parameters for the measured splitting tensile strength.

W/c ratio	Number of specimens	m	σ_0 (MPa)	Average results (MPa)
0.3	115	6.45	22.27	21.28 ± 4.29
0.4	117	5.14	19.48	18.72 ± 3.85
0.5	105	4.86	18.54	16.54 ± 3.71

Table 4.1 shows that m and σ_0 increase with the decrease of w/c ratio of the cement

pastes. It indicates that the cement paste with a lower w/c ratio yields a higher fracture strength and less varying mechanical properties. This can be mainly explained by the decreased volume and varied size distribution of capillary pores in specimens where the capillary pore works as the initial defect and introduce local stress concentration upon loading [177]. Similar observations are also reported in concrete at a higher scale [178].

The present work has, for the first time, shown the values of stochastic tensile strength of cement paste at micro-scale. These values are much higher than the macroscopic strengths of cement paste or concrete and one order of magnitude lower than the microscopic values of distinct hydrated cement phases [45]. This agrees with the scaling law for quasi-brittle materials: according to this, the strength increases as the sample size or scale decreases [179], and indicates that different levels defects exist in cementitious materials. On one hand, capillary pores would have a large effect on the decrease of strength at micro-scale. On the other hand, unavoidable micro-cracks, large capillary pores and entrapped air voids introduce decrease on strength at a upper scale [2]. To the author's best knowledge, the only other reported experimental tensile strength of cement paste at this scale is from measurements of a single focused ion beam machined micro-cantilever with rhomboidal cross section (3.5 μm in with, 5 μm in length) and identified to be 2.67 MPa [102], which is in contradiction to scaling law of strength to micrometres in quasi-brittle materials [2]. Furthermore, the Young's modulus of these tested micro-cantilever is reproduced from the recorded load-displacement curve and seems to be unrealistically low (less than 0.13 GPa). Therefore, it is not possible to use this test for comparison. Furthermore, it is worth mentioning that a statistical distribution of mechanical properties should be provided by the modelling instead of deterministic value due to the inherent heterogeneous microstructure and quasi-brittle properties of this material. This could be done by means of an e.g. random fields model [180].

It is emphasized that, although the way to derive the nominal splitting strength considers the material as perfectly isotropic and linear elastic, the aim of this method is to set a proper parameter which can be used to represent the global mechanical properties of the tested material, so that the influence of the change of the microstructure on the yield strength at this scale can be quantified and compared to each other. In the current research, it was shown the influence of initial w/c ratio on the micromechanical properties and it is expected that the influence of other factors, i.e. hydration time and degradation on the micromechanical properties can be investigated quantitatively by the method proposed in this study.

4.4.2. NUMERICAL RESULTS AND DISCUSSION

Figure 4.11 presents a comparison between simulated load-displacement curves of one micro-cube under one-sided splitting and those measured experimentally. For comparison, the experimental load-displacement curve for 10 specimens were plotted. As described above, the horizontal line represents the overshoot behaviour of the indenter. The influence of AL on the fracture performance of cement paste is investigated by comparing the simulations with and without the AL. As the post-peak behaviour cannot be captured experimentally at present, only the ascending branch was used for the comparison. Clearly, the simulation considering the AL shows a good agreement with the experimentally measured curves in terms of the maximum load and slope of load-

displacement curve (stiffness). Due to the fact that local imprinting of the indenter into the micro-cube occurs at the beginning of the experiments, the measurements are slightly shifted, but the slope remains similar to the one in simulated load displacement curve. In addition, it can be seen from the simulation that the stiffness is significantly decreased by adding the AL at the bottom, while the peak load is slightly increased. It is also clear that, in the simulations, a post-peak response can be observed, which is impossible to observe in the experiment due to limitations of the equipment described previously. Note that the behaviour in the simulation with glue layer is brittle with several snap-backs. This can be captured by the model, but not in the experiments. As this is one of the first attempts at directly testing cement paste specimens at the micrometre length scale, this is not seen as a problem at the moment. In fact, it should be noted that, even on the macro-scale, observing of the post-peak behaviour remains a challenge for certain types of materials, and for such cases it is also necessary to design specific test setups [181]. The simulated crack pattern of these two cases corresponding to the peak load point are compared in Figure 4.12. It is evident that, in both cases, the micro-cube was split in half as the maximum tensile stress always exists in the middle axis below the tip, although some local cracks are observed along the tip edge and around defects (pores) because of the stress concentration, which is in accordance with the experimental observation as shown in Figure 4.4. Furthermore, it is observed that a straighter vertical main crack exists in the micro-cube without AL, while the crack pattern in the simulation considering the AL is more inclined to one side because of the bottom is confined by the AL. Therefore, a higher load capacity is expected for the one with the AL.

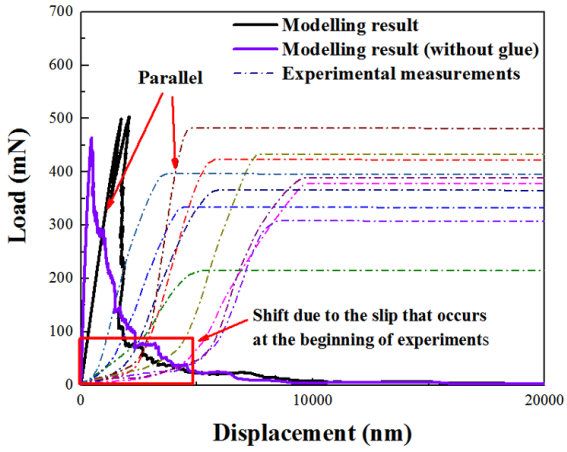

Figure 4.11: Comparison between the simulated load-displacement curve of micro-cube under one-sided splitting

It is emphasized that the input mechanical properties of individual phases in cement (e.g. anhydrous cement, inner hydration products and outer hydration products) are calibrated in Chapter 3 using experimental data from where the same size micro-cubes were fractured by a Berkovich tip using nanoindenter. It is showed that these input local mechanical properties can be applied to lattice fracture simulations under different

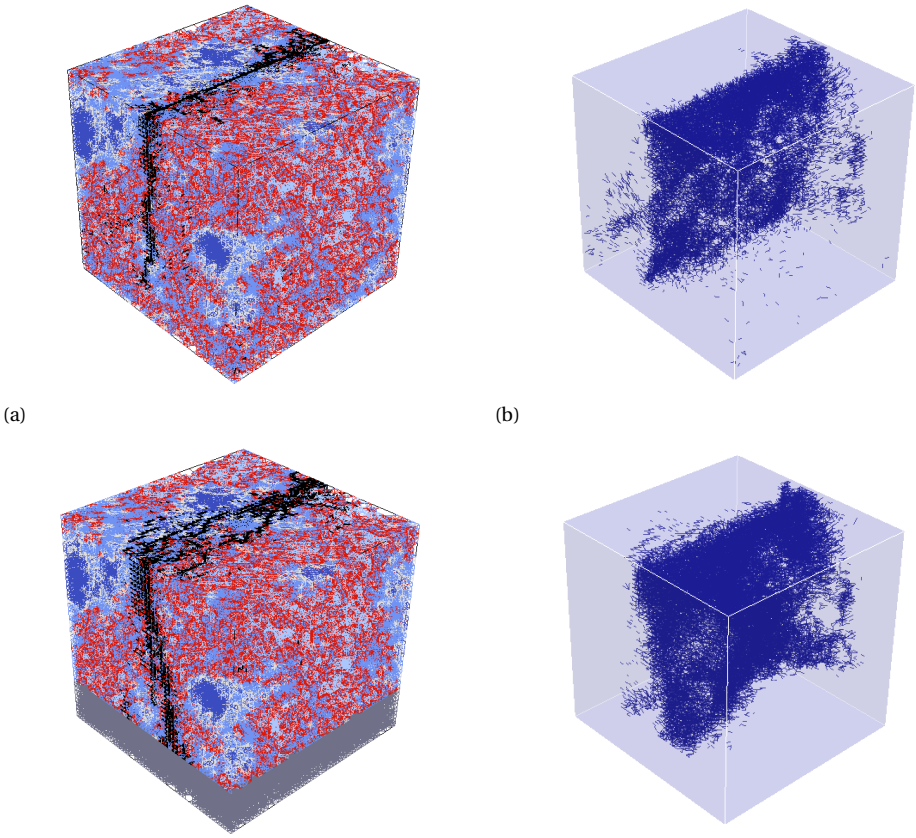

(a) (b)

(c) (d)

Figure 4.12: Simulated crack pattern of one cement paste micro-cube under one-sided splitting: (a) showing the microstructural features, without the glue layer; (b) showing only the crack, without the glue layer; (c) showing the microstructural features, with the glue layer; (d) showing only the crack, with the glue layer.

boundary conditions and have satisfactory results. Together with the method presented in Chapter 3 the framework for fitting and validation of the modelling results at micro-scale is created. The crack patterns at different test stages are plotted in Figure 4.13. It shows that the crack first initiates around the tip and the middle axis beneath the tip. After localising, a relatively straight vertical crack forms in the upper part and propagates to the bottom and turns to lean to the right-hand side because of the AL.

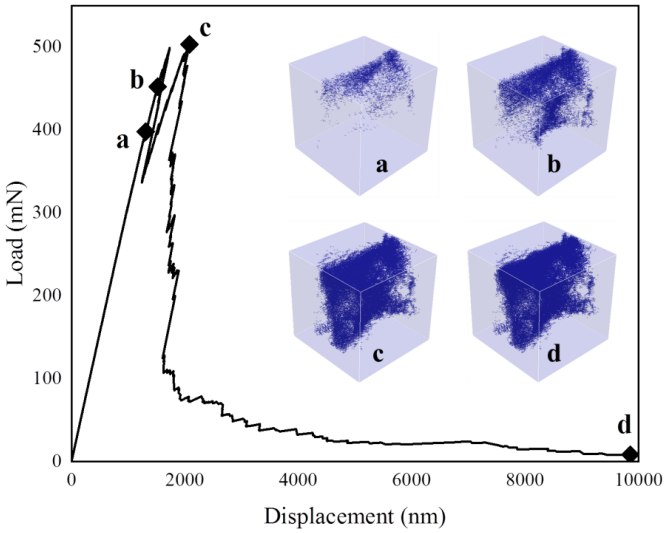

Figure 4.13: Simulated fracture patterns of micro-cube (considering the AL) under different loading state: (a) initial state which has 5000 broken elements with a response of 398 mN of load and 1.3 µm of indentation depth; (b) crack pattern with 20000 broken elements, 1.7 µm indentation depth, and responses for 452 mN (c) crack pattern at peak load of 503 mN with 44988 broken elements under indentation depth of 2.1 µm (d) failure state at indentation depth of 10 µm with 50780 broken elements.

It is worth mentioning that the test results show a high variability which is introduced by the inherent heterogeneity of this material at this length scale. Therefore, 10 voxel-based digital specimens are generated and tested. The simulated load-displacement curves are shown in Figure 4.14. Clearly, the stochastic nature of the mechanical properties can be successfully reproduced numerically by choosing the same size volume (100 µm × 100 µm × 100 µm) from different locations in the XCT characterised material structure. The average nominal splitting strength of these 10 cubes is 21.43 MPa which slightly higher than the experimentally measured value (18.72 MPa). This can be attributed to the deviation of the statistics as the number of the investigated digital specimens might not be large enough to represent the stochastic nature of cement paste at this scale. However, the number of simulations was limited due to the large computational efforts. Nevertheless, as simulation requires detailed material information from where porosity can be obtained, the strength-porosity relationship was studied. Figure 4.15 presents the correlation relationship between the predicted splitting strength and porosity. It is found that the splitting strength decreases with porosity following an exponential decay. A similar trend is observed experimentally in recent studies on a model gypsum plaster material [182].

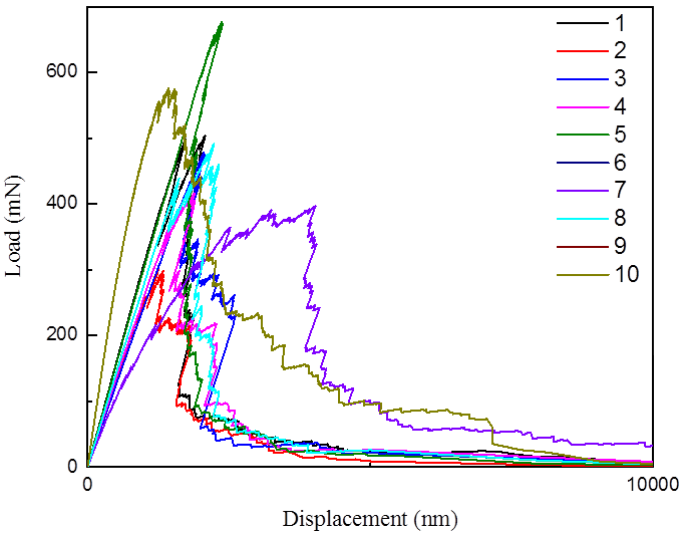

Figure 4.14: Simulated load-displacement curve of micro-cubes under one-sided splitting.

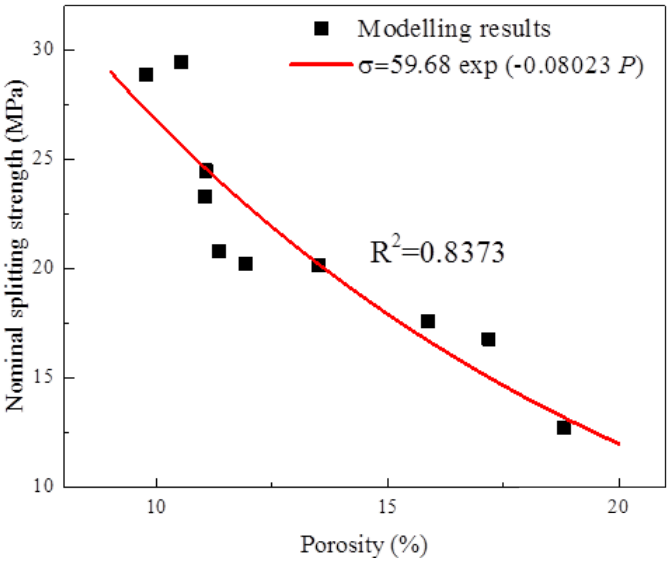

Figure 4.15: Simulated load-displacement curve of micro-cubes under one-sided splitting.

4.5. CONCLUSIONS

BASES on an analogy with Brazilian splitting test, nominal splitting tensile strength of micro-cube was derived from the measured maximum load. To deal with the heterogeneity of this material at micro-scale, large amount of data was obtained from specimens with different w/c ratios and analysed using Weibull statistics. The experimentally measured splitting tensile strength fills the gap between meso-scale and nano-scale. In parallel with the experiments, the fracture performance of micro-cubes under the one-sided splitting was simulated using the microstructure informed lattice fracture model, and a good agreement was found between the simulation and experiment except the post-peak results which cannot be captured experimentally due to the instrumental limitation. The following conclusions can be drawn:

- The tensile strength of cement paste at micro-scale is found to be an order of magnitude lower than the values of individual cement hydrated phases, but an order of magnitude higher than the macroscopic strengths of cement paste or concrete.

- The influence of initial w/c ratio of mixture on the nominal splitting strength is studied and it is found that with an increasing w/c ratio, the micro-scale specimens are more likely to yield a lower strength and have higher deviation.

- Since the measured displacements also include deformation of the supporting AL and local imprinting of the indenter into the micro-cube, the stiffness or elasticity of tested micro-cubes cannot directly be obtained from the recorded load-displacement curves, further investigations are expected to solve this limitation.

- The recorded load-displacement curve is successfully used as a validation for the micro-scale fracture modelling. Together with the method presented in Chapter 3, the framework for fitting and validation of the modelling results at micro-scale is created. This method forms also a basis for validation of multi-scale modelling results at every scale.

5

MODELLING OF STOCHASTIC MECHANICAL PROPERTIES OF HARDENED CEMENT PASTE UNDER UNIAXIAL TENSION

This work presents a study of stochastic fracture properties of hardened cement paste (HCP) at the micro length scale based on a combination of X-ray computed tomography (XCT) technique and discrete lattice fracture model. Thirty virtual specimens consisting of porosity, outer hydration products, inner hydration products and anhydrous cement particles were extracted from 3D images obtained through XCT from real HCP samples. These virtual specimens were subjected to a computational uniaxial tension test to calculate their tensile strengths and elastic moduli. The predicted stochastic strengths were analysed using Weibull statistics, showing that specimens with lower w/c ratio yield higher strength and less variability. The strength-porosity and modulus-porosity relations were investigated based on existing empirical models. It was shown that existing models can predict the properties in the studied porosity range quite accurately, with the exponential model having the highest determination coefficient among all the models for both relations. Finally, by comparing with measurements reported in published literature, it is found that the smaller HCP specimens have higher modulus/tensile strength ratio than concrete, which indicates that they are able to have more strain at the peak load.

Parts of this chapter have been published in Construction and Building Materials **183**,(2018) [183].

5.1. INTRODUCTION

ALTHOUGH a lot of valuable micromechanical information was obtained to set a basis for understanding and improving the macroscopic mechanical performances, stochastic micromechanical properties of HCP have been rarely studied due to the complex and time-consuming modelling procedure. Furthermore, for a number of reasons that include problems with producing and measuring miniaturized mechanical samples, the predicted mechanical properties are difficult to verify experimentally at the micro scale. As reported in Chapter 4, micro scale sized specimens with a cubic dimension of 100 µm were produced by a micro dicing saw and ruptured by a diamond wedge tip mounted on a nano-indentation system. The splitting tensile strength of the tested specimens was derived from the recorded critical load and the test results show a large dispersion, as expected for a highly heterogeneous material at this scale. For a specific ruptured specimen, detailed microstructure information cannot be obtained due to technical and instrumental limitations. Therefore, it is hard to correlate the fracture properties with its microstructure for quantitative assessment at the micro scale. Instead, application of microstructure-informed numerical model that has been calibrated and validated respectively in Chpter 3 and 4 offers an opportunity to achieve this. Therefore, the aim of this chapter is to utilize this calibrated numerical model to study the stochastic mechanical properties of HCP at micro-scale and correlate them with the features of microstructures.

5

5.2. METHODOLOGY

IN order to show the stochastic mechanical properties of HCP at micro-scale, for each w/c ratio (0.3, 0.4 and 0.5), 10 microstructures with a cubic dimension of 100 µm × 100 µm × 100 µm were sliced from XCT images (characterised in Chapter 3) of HCP specimens cured for 28-days. These microstructures were then used as input for fracture simulations performed using the discrete lattice model. Considering the heterogeneity of this material, computational uniaxial tension test is performed on three different loading directions for each cubic specimen, resulting in 30 simulations for each w/c. As shown in Figure 5.1, The test was achieved by applying a nodal displacement at one side and fixing the deformation of nodes at the opposite side. For tensile strength and elastic modulus of each phase, values in S2 of Table 3.4 were adopted. Because these values have been validated, reasonable modelling results can be expected.

5.3. RESULTS AND DISCUSSION

5.3.1. MODELLING RESULTS

AS an example, the simulated stress-strain diagrams of uniaxial tension tests of a specimen tested in different directions are shown in Figure 5.2. The Young's modulus E can be computed from the initial slope of the curve, while tensile strength σ_f corresponds to the peak point. Fracture energy G_f is calculated from the post-peak part of the stress-strain curve as [184]:

$$G_f = \int_{u_1}^{u_2} \sigma \, du \tag{5.1}$$

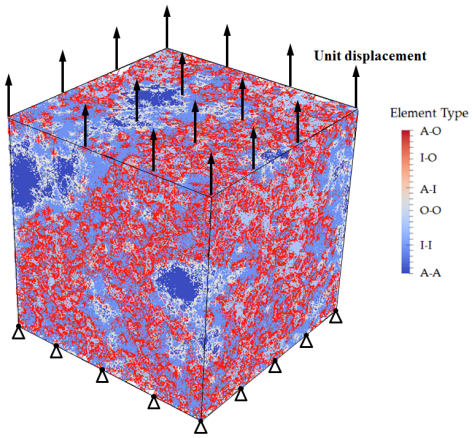

Figure 5.1: Schematic view of computational uniaxial tension test.

where σ is the stress and u the displacement; u_1 corresponds to the displacement at peak stress; u_2 denotes displacement at failure state and is regarded as 5 µm in this study. Note that the calculated fracture energy would be somewhat different if a different "cut-off" displacement was selected, but the main purpose of this work was to compare the fracture energy between different specimens. Results of all 90 simulations are listed in Table 5.1. Clearly, the strengths obtained at the micro-scale are relatively high compared with conventional laboratory centimetre sized samples (3 - 6 MPa) [185]. A similar trend was observed in other quasi-brittle materials such as nuclear graphite both experimentally [186] and numerically [106]. This is attributed to the fact that at micro-scale, samples are free from air voids or defects larger than the sample size. However, large scatter is present in the simulated data as a result of the small volume of material sampled.

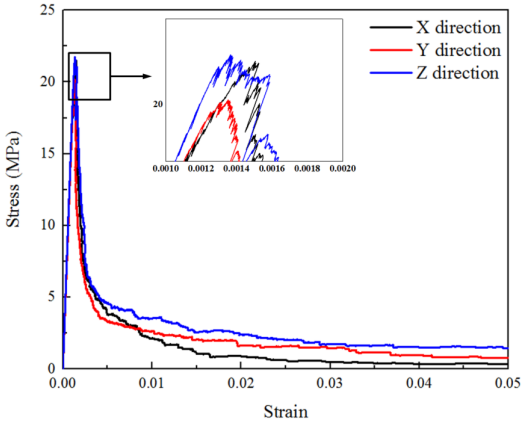

Figure 5.2: Comparison of simulated stress strain curves of one specimen with w/c ratio of 0.4 under uniaxial tension from three directions.

Table 5.1: Outcome of computational uniaxial tension tests.

W/c ratio	Sample	Porosity (%)	Young's modulus (GPa)			Tensile strength (MPa)			Fracture energy (J/m^2)		
			X	Y	Z	X	Y	Z	X	Y	Z
0.3	S1	7.00	28.51	28.15	28.14	28.19	27.07	27.68	9.02	9.45	6.16
	S2	6.26	28.9	28.37	28.77	30.19	25.67	27.69	7.70	7.20	11.50
	S3	4.77	32.13	31.63	30.34	31.5	29.30	29.73	8.10	15.41	11.20
	S4	6.95	28.42	28.22	28.45	26.53	25.55	25.54	13.08	11.68	9.88
	S5	6.86	26.11	26.63	27.05	26.99	22.68	26.11	9.01	8.66	9.61
	S6	6.99	26.70	25.11	25.42	22.43	25.34	26.70	13.88	9.96	7.52
	S7	12.56	23.1	22.49	22.17	20.80	21.21	18.43	10.49	9.40	7.77
	S8	8.54	31.43	28.33	26.46	23.89	24.38	19.60	8.77	9.49	7.52
	S9	5.10	33.69	32.34	30.34	32.13	28.07	24.16	13.25	10.09	14.51
	S10	9.79	25.07	24.67	24.82	26.40	24.67	24.65	9.87	9.41	8.67
0.4	S1	11.04	21.73	21.44	21.25	21.50	20.15	21.73	6.11	8.75	12.46
	S2	15.86	21.75	18.12	17.72	17.85	15.91	16.40	7.22	7.87	8.94
	S3	11.92	23.36	22.92	23.12	18.91	17.45	20.20	10.99	9.48	6.72
	S4	11.07	21.20	22.86	22.54	21.33	19.90	21.20	8.25	12.60	9.71
	S5	17.18	19.30	19.25	18.48	15.67	15.96	13.93	5.57	5.89	5.82
	S6	11.53	22.60	20.64	19.86	19.98	15.76	22.60	8.76	8.78	7.69
	S7	11.35	24.98	25.31	22.42	20.57	20.88	18.92	8.26	11.54	7.83
	S8	13.50	21.83	19.08	19.20	17.65	18.01	16.53	9.69	6.08	6.26
	S9	9.76	21.66	22.61	22.52	24.40	20.02	21.66	10.63	9.83	5.33
	S10	18.82	19.31	19.19	15.80	16.44	17.69	9.76	4.93	5.89	4.17
0.5	S1	18.85	17.13	16.88	15.23	15.13	15.18	10.50	5.70	4.47	5.28
	S2	12.32	21.24	20.84	21.02	21.73	20.15	20.98	6.29	6.80	5.83
	S3	25.01	13.09	12.61	11.20	8.71	10.21	8.49	3.54	4.57	3.73
	S4	14.76	19.43	21.42	17.06	16.86	19.03	16.31	6.20	5.96	7.05
	S5	23.88	15.49	13.10	12.57	13.66	9.55	8.76	8.64	3.41	4.26
	S6	20.85	15.51	15.28	13.13	12.44	13.07	9.47	2.96	4.42	4.90
	S7	7.77	27.44	29.49	25.95	20.08	25.62	20.21	7.16	4.98	5.96
	S8	12.68	20.08	22.18	19.61	18.14	20.43	14.49	5.94	7.30	5.80
	S9	11.29	23.67	24.61	21.86	20.15	20.06	17.26	8.90	8.90	7.43
	S10	9.55	24.93	26.33	22.45	22.00	23.19	15.63	5.78	7.64	6.16

The average results of each w/c ratio are summarized in Table 5.2. Such high tensile strengths were experimentally observed by rupturing the same size specimens through the nanoindentation system in Chapter 4. Furthermore, even higher strength is expected for samples at smaller length scale (few microns) [45], where distinct cement hydration phases like inner and outer hydration products containing capillary and gel pores can be sampled as micro cantilever beams. The final fracture pattern of one of the specimens is presented in Figure 5.3. More than one main crack is observed in the final failure mode, which was attributed to the distributed pores which act as initial defects and anhydrous cement grains existing as "stiff inclusions" in the material and thereby deflecting the cracks. As the crack patterns are not identical, the strength property varies more than Young's modulus which is mostly influenced by the components and their relative amounts. Figure 5.4 shows the fracture propagation of the presented specimen under Z direction loading. As can be seen, micro-cracks initiate around the middle part of the specimen and spread further until the final failure. In addition, an outline of an anhydrous cement grain is clearly observed in Figure 5.4, similar to the observation in conventional concrete, in which the micro-cracks always outline the aggregates

[187, 188]. In addition, as expected, the predicted mechanical properties decrease and become more variable with increasing w/c ratio. As presented in Figure 5.5, the predicted average Young's moduli of HCPs with different w/c ratios almost coincide with the experimental values from elastic resonance measurements [77] and show a good agreement with those from other micromechanical models [3, 15, 16, 18, 76]. The only exception is the predicted modulus of HCP with w/c ratio 0.3 from [76], which is higher compared with the result in this work, but similar to the result of S9 at X direction (33.69 GPa, see Table 5.1). Therefore, the difference between the predicted modulus in the literature can be attributed the stochastic nature of this material. One should note that, to make the data from literature comparable to the current work, the corresponding hydration degree was used to extract results from references [3, 15, 76]. A Poisson's ratio of 0.24 (the same as assumed in [15]) was used to convert bulk modulus from their work to Young's modulus.

Table 5.2: Summary of simulated micromechanical properties.

W/c ratio	Porosity (%)	Anhydrous cement grains (%)	Young's modulus (GPa)	Tensile strength (MPa)	Fracture energy (J/ m^2)
0.3	7.48±2.18	14.70±2.86	27.73±2.91	25.78±3.29	9.94±1.50
0.4	13.20±2.89	9.91±2.44	21.067±3.01	18.63±2.99	8.07± 1.62
0.5	15.70±5.76	7.24±1.42	19.36 ±5.03	15.97±5.02	5.86±1.30

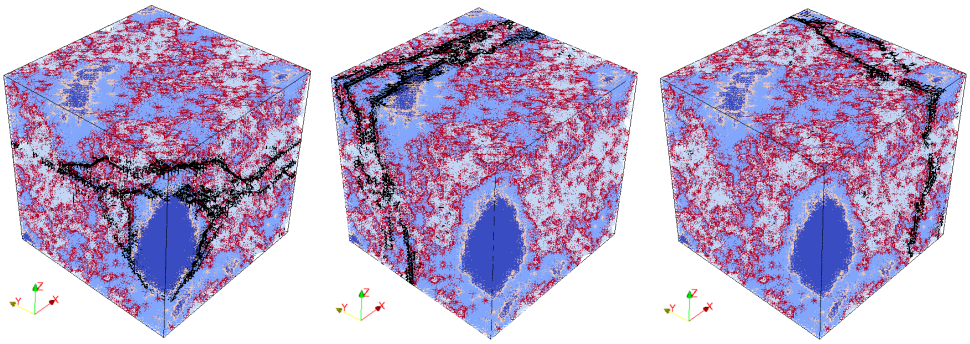

(a) (b) (c)

Figure 5.3: One cracked and deformed specimen with w/c ratio of 0.4 under uniaxial tension in three directions: (a) Z (b) Y and (c) X at failure stage. (black-cracked element; Deformations have been scaled for clarity).

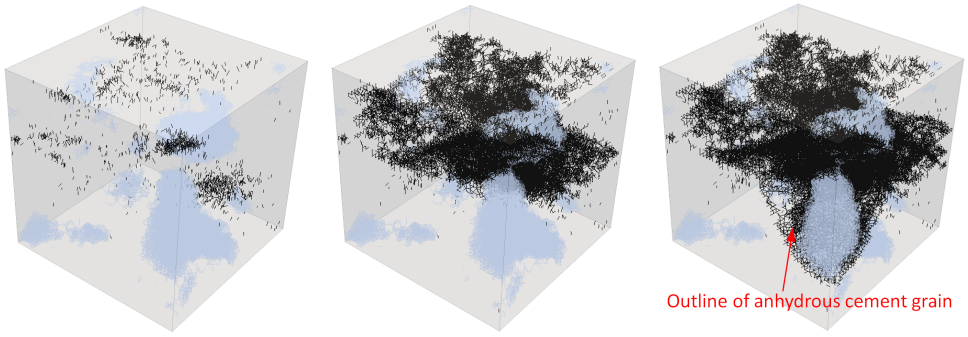

(a) (b) (c)

Figure 5.4: Fracture pattern of one specimen with w/c ratio of 0.4 under unaxial tension in direction Z at different stage: (a) fracture pattern at peak load; (b) fracture pattern at 1 % strain deformation; (c) fracture pattern at final stage having an outline out line of anhydrous cement particles (the anhydrous cement particles are represented by the blue colour and semi-transparent for clarity).

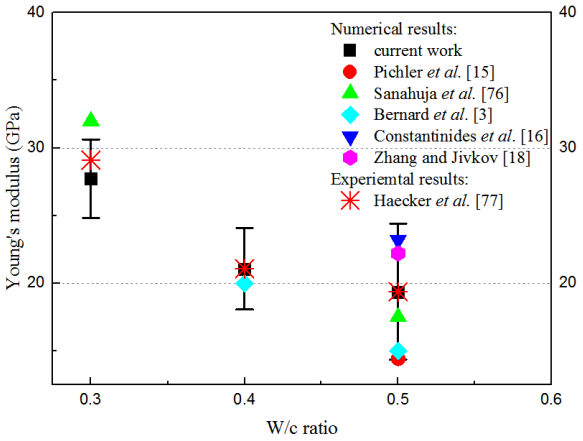

Figure 5.5: Comparison of predicted Young's modulus with other micromechanics models together with experimental results.

5.3.2. WEIBULL ANALYSIS OF STRENGTH

Weibull analysis has been widely used for characterising the scatter in measured fracture strength (which is mostly governed by the weakest link in the system) of a group of specimens that are nominally identical. Herein, the two-parameter Weibull analysis (Equation 4.3) was used to analyse the 30 simulated strengths in each group with identical w/c ratio. The tensile strengths are plotted in a Weibull coordinate system in Figure 5.6. The fitted results are given in Table 5.3. A determination coefficient (R^2) higher than 0.95 is observed for all three groups, which means a strong linear relationship between $\ln\ln(1/1\text{-}P_f)$ and $\ln\sigma_f$ exists and indicates that the fracture process is mostly dominated by one type of flaw. From Table 5.3, it can be seen that, with the increase of w/c ratio, the strength decreases and becomes more variable. Consequently, both m and σ_0 in terms of strengths in each group decrease with w/c ratio increasing. This is in accordance with the experimental observations in Chapter 4. To have further insight into this issue, the typical fracture pattern of specimens with each w/c ratio are presented in Figure 5.7. It is apparent that micro-cracks are less localized in the paste with lower w/c ratio due to the higher amount of anhydrous cement grains and lower porosity in its microstructure, which results in a more stable crack propagation and branching and therefore higher and less varied strength is expected, and more fracture energy is released during the crack propagation. This is opposite to the results from [4] in which the material structure is generated based on modelling. As cement clinkers are assumed as spheres for hydration simulation, different material structures, especially the pore structures are expected [4]. It is important to comment on the nature of the characteristic strength. The characteristic strength is akin to the median strength below which 50 % of the fractures would fall. In general, the median and the mean of a distribution are similar but the difference between the median and the mean depends on the details of the distribution. Likewise, the characteristic strength and the mean strength are typically similar but not equal and with respect to this study the characteristic strength is higher than the mean strength.

Table 5.3: Weibull parameters for the simulated tensile strength.

w/c ratio	Weibull modulus m	Scaling parameter σ_0	Determination coefficient R^2
0.3	8.85	26.96	0.99
0.4	6.11	19.42	0.98
0.5	3.17	17.10	0.96

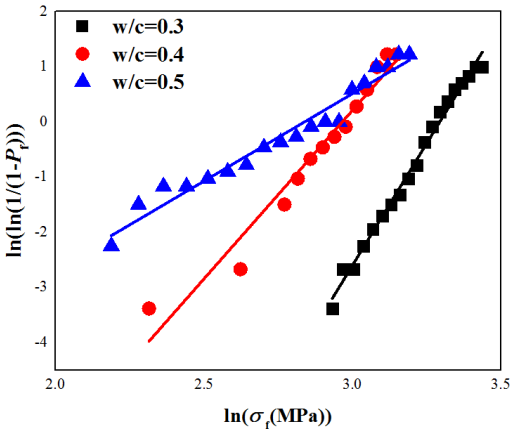

Figure 5.6: Weibull plot of for simulated tensile strength of HCP with different w/c ratios.

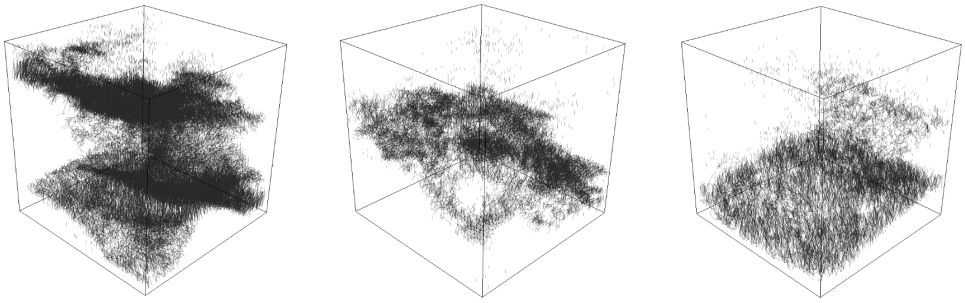

(a) (b) (c)

Figure 5.7: Typical crack patterns in the final failure state of HCP with w/c ratio: (a) 0.3; (b) 0.4; (c) 0.5.

5.3.3. RELATIONSHIP BETWEEN POROSITY AND SIMULATED MECHANICAL PROPERTIES

In the matrix, pores act as stress concentration sites and promote failure under loading by introducing micro-cracks. Hence, an increase in pore volume reduces the elastic modulus, fracture energy, and strength of the material [182]. The shapes, sizes and locations of pores are all parameters affecting the deformation and fracture properties [189]. Among these, porosity is regarded as the governing parameter for mechanical properties of porous materials [190]. Although many efforts have been made to correlate mechanical properties with porosity for cementitious materials [177, 178, 191–195], few of them have focused on the micro metre scale. In order to study the micromechanical properties-porosity relation of cementitious materials, the predicted mean strength and Young's modulus of specimens are plotted against their porosity in Figure 5.8. It is observed that, regardless of the w/c ratio, these two key mechanical properties decrease continuously with porosity increasing. Therefore, data of HCP with different w/c ratio was combined for a micromechanical properties-porosity empirical relation study.

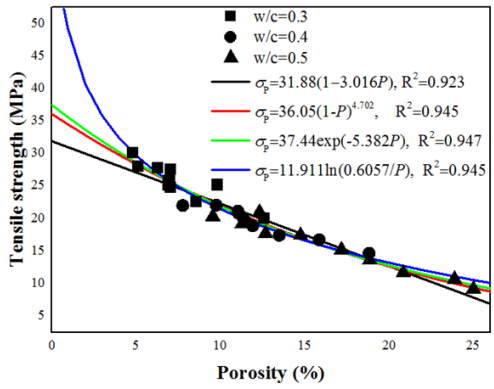

(a)

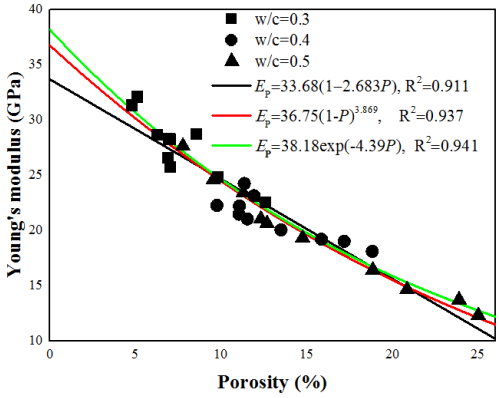

(b)

Figure 5.8: Relationship between predicted mechanical properties and porosity: (a) strength-porosity relation; (b) elastic modulus-porosity relation.

With respect to porous materials, quite a few equations have been proposed and developed for expressing the effect of porosity on strength and on Young's modulus in literature [196–201]. For strength, typically four types of relationships in form of linear ($\sigma_P = \sigma_{p0}(1-kP)$) [196], power exponent ($\sigma_P = \sigma_{p0}(1-P)^k$) [197], exponential (($\sigma_P = \sigma_{p0}e^{-kP}$) [198] and logarithmic ($\sigma_P = ln(P_0/P)$) [199], are most widely used. In all these relationships, σ_P stands for tensile strength at porosity P, σ_{p0} stands for tensile strength at zero porosity, P_0 stands for porosity at zero strength, k is an empirical constant which can be fit from the experimental results. In analogy to expression for porosity-strength relationships, the Young's modulus-porosity relationship can be expressed as $E_P = E_{p0}(1-kP)$ [196], ($E_P = E_{p0}(1-P)^k$) [200] and $E_P = E_{p0}e^{-kP}$ [201]. Analogously, E_P denotes elasticity modulus at porosity P, E_{p0} is the elasticity modulus at zero porosity. Results of fitting mentioned models of strength–porosity and modulus–porosity relations are given in Figure 5.8. All these empirical equations show a good agreement with the simulated results, while exponential curve yields the highest determination coefficient values in both

strength–porosity and modulus–porosity fitting (0.947 for strength and 0.941 for modulus). It should be kept in mind that this exponential equation does not satisfy the boundary condition that σ_P or E_P goes to zero as P approaches 1, demonstrating that these empirically developed equations are valid for a limited porosity range. The predicted results in forms of exponential and power are quite close to each other and it is reported in [202] that these results can be made to approximate each other and can be used with satisfactory results. According to these two equations, uniaxial tensile strength of non-porous HCP is estimated to be around 36 and 37 MPa, while the modulus is around 36 and 38 GPa. Furthermore, it is also important to notice that the k in the power equation for modulus-porosity relation indicates the irregularity degree of a pore structure and it is concluded that, in polycrystalline materials [203], for closed spherical pores k=2 and for random orientated pores k=4. Therefore, a highly random orientated pore structure is expected for the investigated material structure at micro-scale according to k=3.87 in this study. The Logarithmic model determines a percolation threshold as 60.57 % at which porosity the material yields zero strength. However, as shown in Figure 5.8a when P approaches 0, an infinite strength is predicted, which is of course not possible. As all empirical models in Figure 5.8a and 5.8b give good fitting results within the tested porosity range, to determine which model predict more realistic results, it is essential to broaden the modelling results of specimens with porosity lower than 5 % and higher than 25 %. This can be done by applying the computational uniaxial tension tests on the specimens with lower and higher w/c ratios, respectively.

Furthermore, it should be emphasized that the estimated values of the parameter σ_{p0}, P_0 and E_{p0} may not always provide a reliable estimate due to the limited resolution of the digitalised material structure and size effect. For example, the sub-micron features in HCP [157, 158], especially the porosity, cannot be takin into account in the current work. Therefore, the estimated σ_{p0}, P_0 and E_{p0} involve microstructural details lower than the current resolution, like density of cement grains, hydration products and defects [193–195]. Hence, one should be careful with how these fitted parameters are used in practical applications.

5.3.4. RELATION BETWEEN TENSILE STRENGTH AND YOUNG'S MODULUS

As key mechanical properties of porous materials, the ratio between tensile strength and modulus is of great interest from which the deformation ability of the material can be obtained. As shown in Figure 5.9, this ratio is found to be between 800 and 1600 in this study, although a higher value of modulus/strength (10000) is expected at the concrete scale [138]. Recent micro-cantilever measurements of individual components in HCP matrix show even lower values (outer hydration product: around 90, inner hydration products: around 48) [45]. This is because less defects are involved in the material on small length scales [106]. Griffith concluded from measuring glass fibres with small diameter that this ratio can approach 9 when no defect is present in the tested material [204]. Recent measurements of the elastic properties and intrinsic strength of free-standing monolayer graphene membranes reveal that the intrinsic strength can be as even high as $E/8$ [205]. Therefore, the results obtained in this research are regarded reasonable and it can be concluded that the modulus/strength ratio decreases with the investigated length-scale decreasing. This indicates that, with respect to HCP, smaller

specimens will have more strain at the failure stress compared to the larger specimens.

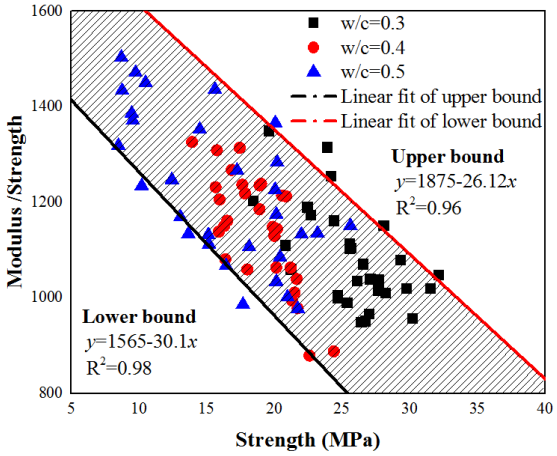

Figure 5.9: Relationship between predicted modulus/strength ratio and strength.

Furthermore, a general trend that the modulus/strength ratio decreases with the increasing of strength (decreasing of porosity) is observed, which means that the strength is more sensitive to defects compared to elastic stiffness. This can be explained by a theory proposed by Hasselam [196] as shown in Figure 5.10. While a material is under loading, a stress-free zone exists above and below the defects in the direction of the applied stress. Because neither the pore nor the material in the stress-free zone is stressed, they do not contribute to the strength. Consequently, with increasing porosity, the material of load-bearing area oriented perpendicularly to the applied stress would be reduced not only by the intersected pore but also the additional stress-free zone. Therefore, the effect of porosity on strength is expected to be more significant than on elastic stiffness. As a specimen with lower w/c ratio always has a lower porosity than the one with higher w/c ratio, its modulus/strength ratio is lower. Additionally, two linear bounds were fitted by the data at the edge (Figure 5.9). The area within the bonds covers 92.2 % results. Note that these bounds are based on data fitting only and should not be confused with analytical bounds existing for elastic modulus (e.g. Hashin-Shtrikhman or Voigt-Reuss).

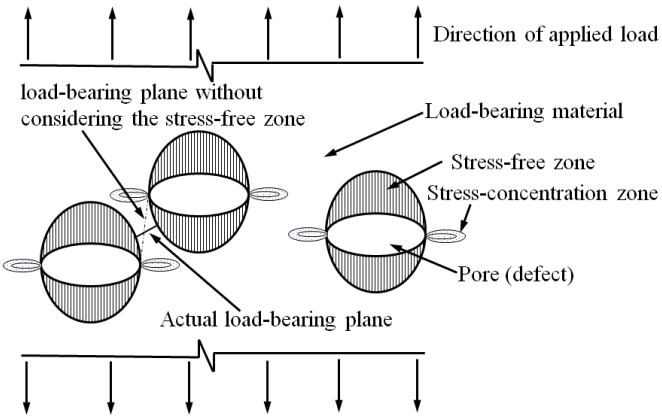

Figure 5.10: Schematic view of the model for the effect of porosity on strength.

5.4. CONCLUSIONS

BASED on the material structure informed micromechanical modelling approch developed in Chapter 3 and 4, a comprehensive study on fracture behaviour of HCP at micro-scale was carried out. The stochastic micromechanical properties of HCP were successfully predicted by lattice fracture model using microstructures randomly extracted from XCT images. From the presented numerical simulations, the following conclusions can be reached:

- The micromechanical properties of HCP vary a lot due to the heterogeneous nature of its material structure. It is found that most of the predicted moduli at micro-scale fall into the range of the current work, which indicates that the difference between their predicted results can be mainly explained by the heterogeneous nature of this material. Therefore, those who are studying the micromechanical properties of HCP should be careful with the stochastic nature of such material.

- A two-parameter Weibull statistic formula is able to describe the stochastic strength of HCP prepared with the identical w/c ratio. It is found that Weibull modulus and characteristic strength of specimens decrease with their w/c ratio increasing. This reveals that specimens prepared with lower initial w/c ratio have higher and less variable strength value.

- Over the examined porosity, ranging from 5 % to 25 %, all the tested empirical equations can be regarded as good representations for both strength–porosity and modulus–porosity relationships. It is estimated that the micromechanical properties of HCP can be increased to around 36-37 MPa for strength and 36 -38 GPa for Young's modulus, if initial flaws (i.e. pore) larger than 2 μm can be eliminated from the material structure.

- The modulus/strength ratio falls in the range between 800 and 1600 at the in-

vestigated length scale, which is larger than the one at molecular scale (8-9) but smaller than one at meso scale (around 10000). the predicted results are therefore regarded reasonable and proves that a size effect exists in the modulus/strength ratio.

6

TESTING AND MODELLING OF HARDENED CEMENT PASTE MICRO-PRISM UNDER UNIAXIAL COMPRESSION

The aim of this chapter is to investigate the mechanical performance of hardened cement paste (HCP) under compression at the micrometre length scale. In order to achieve this, both experimental and numerical approaches were applied. In the experimental part, micro-scale sized HCP specimens were fabricated and subjected to uniaxial compression by a flat end tip using nanoindenter. The recorded load-displacement curves were further used to calculate the compressive strength and the elastic modulus of tested specimens. In the modelling part, virtual micro-scale sized specimens were created from digital material structures obtained by X-ray computed tomography. A computational compression test was then performed on these virtual specimens by a discrete lattice fracture model using the local mechanical properties calibrated in Chapter 3. A good agreement, in terms of the load-displacement curve and fracture pattern, is found between the experimental and numerical results. The approach proposed in this work forms a general framework for testing and modelling the compression behaviour of cementitious material at the micrometre length scale.

6.1. INTRODUCTION

WITH respect to the compressive failure, which is one of the most studied loading cases in the field of cementitious materials, the measurement and understanding at the micrometre length scale is still missing. With recent advances in multi-scale modelling, the micromechanical properties of cement paste under uniaxial compression are modelled [15, 131, 164], showing much higher strength compared with the macroscopic results [206]. Unfortunately, these findings have not been experimentally validated so far. Therefore, the aim of this work is to develop an approach to conduct the uniaxial compression test on cement paste at the micrometre length scale.

The procedure developed in Chapter 3 for producing 100 µm-sized hardened cement paste (HCP) cubes offers an unprecedented opportunity for experimental investigation of compressive failure performance of HCP at the micrometre length-scale. In this chapter, a flat end tip was mounted on the nanoindenter instrument to apply a uniformly distributed compressive load on the 100 µm-sized HPC specimens. In order to explain fracture process of HCP during the experiment, the discrete lattice model was used to simulate the uniaxial compression test. The X-ray computed tomography (XCT) generated microstructure in Chapter 4 was used. The elastic-brittle fracture behaviour of local phases are derived from the previous Chapters. It is believed that with the presented experimental measuring and numerical modelling, improved insight of the compressive failure performance of HCP at the micro-scale is provided.

6.2. EXPERIMENTAL

THREE 28 days cured HCPs with different water to cement (w/c) ratios (0.3, 0.4 and 0.5) were prepared. Following the procedure developed in Chapter 3, micro-scale sized specimens were fabricated. As shown in Figure 6.1, three types specimens were prepared for HCP with each w/c ratio: two types of micro-cubes with size of 100 µm and 200 µm, and one prism with the height of 400 µm and cross-section of 200 µm × 200 µm. With these three types of specimens, the influence of specimen's size and slenderness ratio, respectively, on the measured micromechanical properties could be investigated.

6.2.1. UNIAXIAL COMPRESSION TEST

The KLA-Tencor G200 nanoindenter was used to conduct the uniaxial compression test on the prepared micro-scale sized specimens. A diamond flat end tip with a diameter of 330 µm (Figure 6.2) was mounted on the XP head to apply a uniformly distributed load on the top surface of the specimen as schematically shown in Figure 6.3. The diameter of the tip allows an overall cover of the specimens' surface but avoids touching the other pillar during the test. To ensure only normal force is transmitted to the specimen, the tip was aligned with the centre of the specimen. The positioning accuracy was ensured by an indenter to microscope calibration procedure prior to the test. The compression test was applied to each specimen under load control with a constant loading increment i.e. 10 mN/s. Prior to the experiments, the indenter was calibrated against a fused silica standard. A typical load-displacement curve of the compression test is shown in Figure 6.4. It is evident that three stages can be distinguished. First, the load increases monotonically until reaching a critical load P_c (stage I). This is followed by a rapid burst of displacement

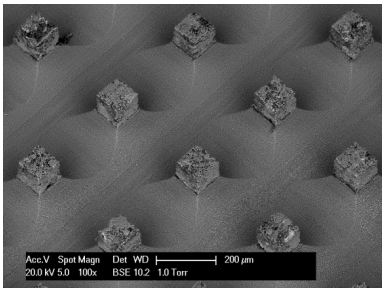

(a)

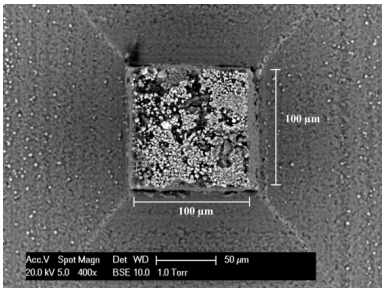

(b)

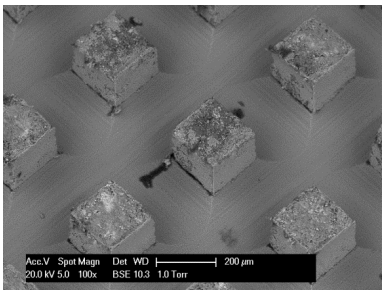

(c)

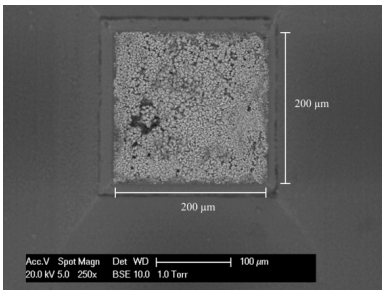

(d)

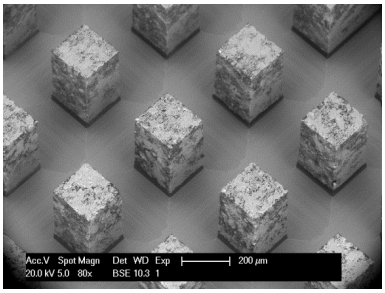

(e)

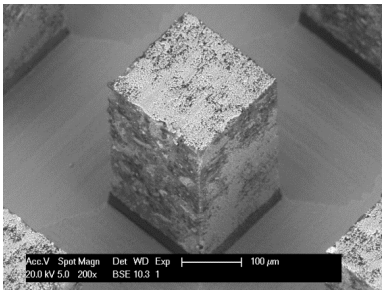

(f)

Figure 6.1: ESEM images of the fabricated micro-scale sized HCP specimens: (a) an array of 100µm-sized HCP cubes; (b) top view of one 100µm-sized HCP cube with dimensions; (c) an array of 200 µm-sized HCP cubes; (d) top view of one 200 µm-sized HCP cube with dimensions; (e) an array of HCP prisms with 400 µm height and 200 µm square cross-section; (f) a zoomed-in image of one prism on the glass substrate.

in the second stage, which indicates that catastrophic failure of the specimen occurs. As the test is performed under load control, the indenter overshoots towards the substrate until it hits the crushed specimen or substrate and continues to load to the prescribed maximum load (stage III) which is required by the test method. Furthermore, non-linear behaviour is observed just prior to catastrophic failure. This allows a forecast for the catastrophic failure. In order to visualise the cracked specimen prior to the failure, the test was manually terminated in several cases when the aforementioned behaviour was observed. Note that this procedure was only performed for several specimens for image acquiring. The critical load P_c was used to calculate the compressive strength f_c of test specimens:

$$f_{\mathrm{c}} = \frac{P_{\mathrm{c}}}{D^2} \tag{6.1}$$

where D is the dimension of the square cross-section. From the load displacement diagram, the Young's modulus was determined by the slope in the range between 50 % and 80 % of the critical load. It is calculated as:

$$E_{\mathrm{m}} = S\frac{h_{\mathrm{m}}}{D^2} \tag{6.2}$$

where S is the average slope; h_{m} is the height of specimen measured by the length gauge. Note that the E_{m} directly derived from the load-displacement curve cannot be used to represent the elasticity of the HCP as the recorded displacement includes also the deformation from the underlying materials (AL and glass substrate) which should be eliminated for evaluation of the stiffness of the HCP. Compared with the AL, the glass substrate has a limited contribution to the measured displacement. If it is assumed that all the materials behave linear-elastic in this region, the following equation can be obtained:

$$\frac{h_m}{E_m} = \frac{h_c}{E_c} + \frac{h_{AL}}{E_{AL}} \tag{6.3}$$

where h_c is the real height of the specimen and $h_c = h_m - h_{AL}$. E_c is the Young's modulus of the HCP; E_{AL} represents the elastic modulus of the AL. This equation was used in Section 6.4.1 to calculate the Young's modulus of tested HCP specimens.

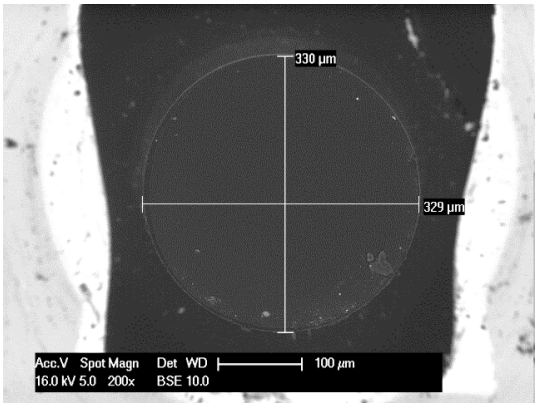

Figure 6.2: Top view of the diamond flat end tip with 330 µm in diameter.

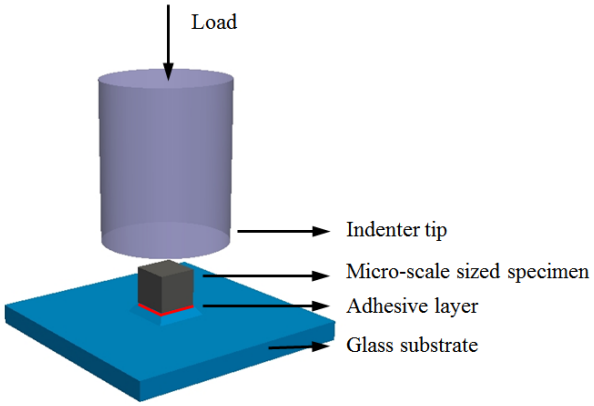

Figure 6.3: Schematic illustration of compression test instrumented by the nanoindenter.

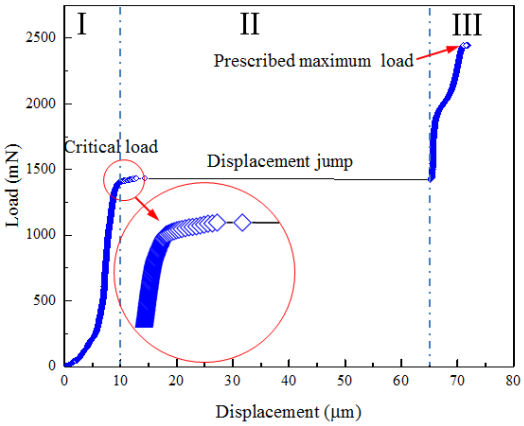

Figure 6.4: A typical load-displacement curve of the load-controlled compression test.

6.3. MODELLING

6.3.1. DIGITIAL SPECIMENS

ON the base of the segmented microstructure in Chapter 3, two types of virtual specimens were created with respect to each w/c ratio mixture. The first is one having a cubic shape with size of 100 µm × 100 µm × 100 µm which was extracted from the segmented microstructure (Figure 6.5). The second one is formed by replacing the volume at bottom up to 20 µm by the adhesive layer (AL) that occurs in the experiments (Figure 6.6). This allows a comparison between experimental measurements and numerical modelling.

6.3.2. DEFORMATION AND FRACTURE MODEL

The discrete lattice model was used for the fracture analysis. Values in Table 3.5 were constantly used in this chapter. The compressive strength of each element was then assumed as 10 times higher than the tensile strength considering the fact that cementitious materials have a higher resistance to the compressive loading than tensile. In terms of AL, its elastic modulus is measured by the nanoindention test (3 GPa, same as Chaper 4). Elements that connect AL phase maintain linear elastic during the simulation.

The compressive boundary conditions were applied as shown in Figure 6.7. In each analysis step, displacement was applied on the one end and the other end was clamped. A set of linear elastic analyses was then performed by calculating the stress within each lattice element using Equation 3.2. As mentioned above, for a system that fails under tension, a small value (i.e. 0.05) is generally adopted mainly because of the fact that all beam elements fail in pure mode-I crack [188]. On the other hand, in case of the compression test, the failure process is a combination of several fracture mechanisms, thus a large α_M (i.e. 0.5) is recommended to depict the failure introduced by bending [207, 208]. In order to keep the model parameters consistent, the α_M is taken as 0.05 when the local lattice element is under tension, while 0.5 is adopted for the compressed elements. In every analysis step, only one element with the highest stress/strength ratio is marked. This is followed by one of the two actions: 1) if it is the first time that a beam element is marked, it degrades from a Timoshenko beam element into a truss element

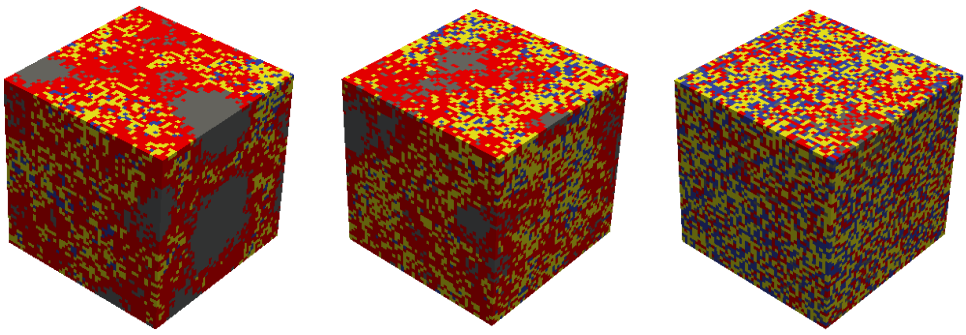

(a) (b) (c)

Figure 6.5: 3D cubic specimen (100 µm ×100 µm ×100 µm) of HCPs with w/c ratio (a) 0.3; (b) 0.4; (c) 0.5.

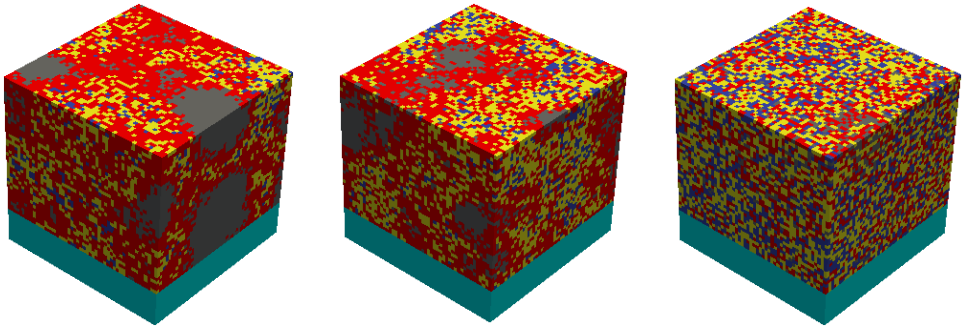

(a) (b) (c)

Figure 6.6: 3D cubic specimen (100 µm ×100 µm ×100 µm) of HCPs considering adhesive layer (AL) with w/c ratio (a) 0.3; (b) 0.4; (c) 0.5.

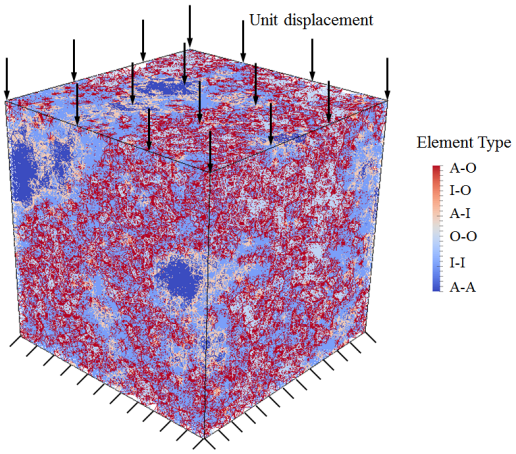

Figure 6.7: An example of boundary conditions used for uniaxial compression modelling.

for which only the axial stiffness remains (see Figure 6.8); 2) if it is the second time that an element is marked in a subsequent calculation (using the same failure criteria), the truss element is removed and a small crack is introduced. The second step simulates the friction of crack faces in a way. Note that in order to avoid the overlapping of the neighbouring nodes and to account for the sliding that happened in between the two surfaces of a crack, the truss element was allowed to fail only in tension. The mesh is then updated and relaxed. The calculation procedure is repeated until a predefined stopping criterion (in terms of, e.g., load or displacement) is met.

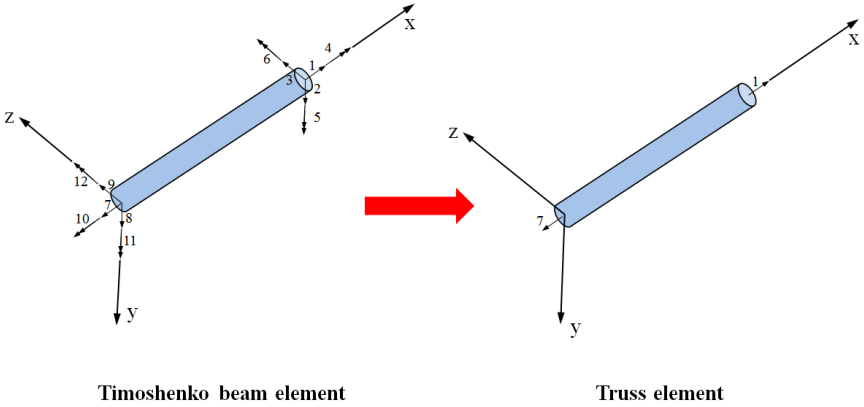

Figure 6.8: Schematic view of the element degradation at first step.

6.4. RESULTS AND DISCUSSION

6.4.1. EXPERIMENTAL RESULTS AND DISCUSSION

CONSIDERING the heterogeneity of HCP and its influence on the deformation and fracture performance at the micrometre length scale, for each type specimen, more than 100 specimens were produced and tested. Table 6.1 summaries the calculated strength and elastic modulus using Equation 6.1 and 6.3. The number in the parentheses is the variation coefficient. From this table, the following trends can be observed:

As expected, for the same type of specimen, the mean value of compressive strength decreases with the initial w/c ratio, while its coefficient of variation increases. The same trend was observed for the elastic modulus. This is mainly because of the fact that a mixture with a higher w/c ratio always has a more porous and heterogeneous microstructure. Note that the compressive strength is measured at equal age, not at equal degree of hydration, for the three w/c ratios (see Table 3.1).

The size of specimens influences the measured compressive strength and elastic modulus. The smaller cubes have a higher strength and elastic modulus compared with the larger cubes, as large defects (i.e. capillary pores > 100 μm) are not sampled in the smaller specimen. Compared with the elasticity, the size effect has more influence on the strength, since strength is more sensitive to defects compared to elastic stiffness.

Cubic specimens have higher strength compared with prismatic specimens of the same cross section, which have a slenderness ratio of 2. As a rigid flat end indenter was used for loading and the bottom of the specimen is fixed on the glass substrate, a relatively high frictional restrained boundary condition is expected for the current uniaxial compression test, although the bottom is less confined compared to the top of the specimen because of the low stiffness of the AL. As explained in the literature [208–211], a shear stress between the loading platen and the specimen occurs because of the mismatch in their lateral expansion and stiffness. Consequently, an area of triaxial compression occurs due to confinement at the two ends of the specimen as schematically shown in Figure 6.9. It is evident that a specimen with small slenderness has a larger relative restrained area. Thus, a higher strength is expected to be measured from a low

slenderness specimen mainly because cementitious material has higher resistance to the triaxial compressive stress than the uniaxial compressive stress. Unlike the compressive strength, the measured elastic moduli are less influenced by the slenderness of specimens as shown in Table 6.1. Fracture patterns of specimens prior to the catastrophic failure (Figure 6.10 and Figure 6.11) were captured as mentioned in Section 6.2.1. Clearly, because of the restraint on the ends of the specimen, different crack patterns are observed. For cubic specimens, typically, an hourglass-shape main crack is formed. On the other hand, more straight and vertical cracks are observed for the slenderer specimens. This is in accordance with macroscopic observations [2].

Table 6.1: Summary of test results of each type specimen.

W/c ratio	quantity	Sample size (µm)	Young's modulus (GPa)	Compressive strength (MPa)
0.3	131	100 × 100 × 100	22.21 (0.15)	159.52 (0.20)
	113	200 × 200 × 200	21.81 (0.19)	124.79 (0.13)
	105	400 × 200 × 200	20.34 (0.19)	107.05 (0.20)
0.4	125	100 × 100 × 100	17.16 (0.17)	124.97 (0.28)
	111	200 × 200 × 200	16.95 (0.20)	112.40 (0.20)
	104	400 × 200 × 200	16.53 (0.19)	99.79 (0.31)
0.5	106	100 × 100 × 100	14.34 (0.26)	110.24 (0.37)
	176	200 × 200 × 200	13.78 (0.23)	103.19 (0.32)
	111	400 × 200 × 200	13.31 (0.25)	76.71 (0.32)

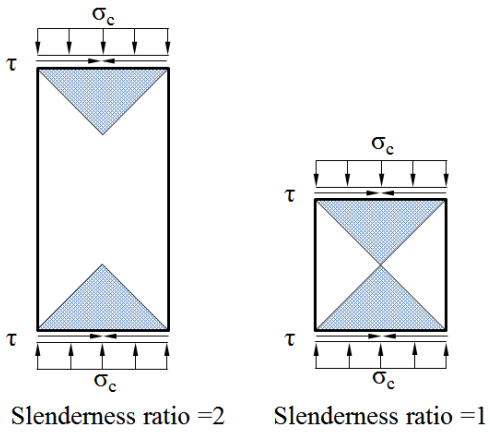

Figure 6.9: Confined zones due to frictional restraint for specimens of different slenderness (shaded areas indicate parts of the specimen under triaxial compression).

As more than one hundred specimens were tested for each specimen type, it was possible to analyse the measured micromechanical properties statistically. For cementitious materials, normal distribution and two-parameter Weibull statistics are commonly used to describe the statistical distribution of mechanical properties. Their applicability for the micromechanical properties were investigated using the data from the 100 µm cubes. As construction of the experimental probability density function largely depends on the choice of the bin size which would further disturb the fitting results, the approach considering cumulative distribution function (CDF) was adopted. The CDF of a normal

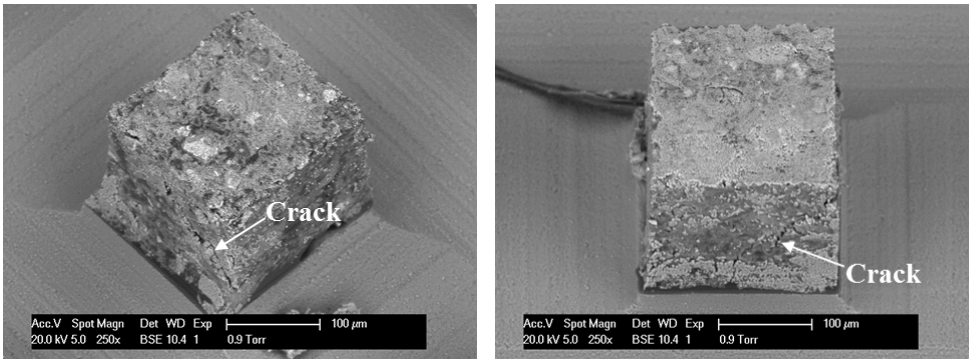

(a) (b)

Figure 6.10: Characteristic fracture patterns of cubic specimens prior to the catastrophic failure.

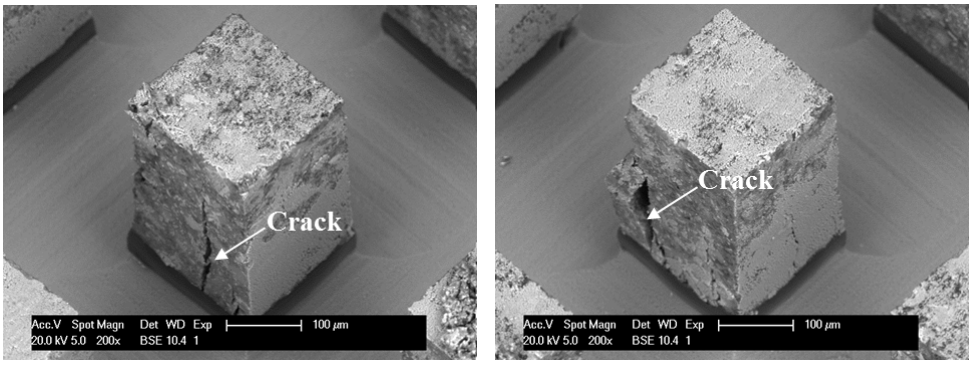

(a) (b)

Figure 6.11: Characteristic fracture patterns of prismatic specimens prior to the catastrophic failure.

Table 6.2: Fitting results of normal distribution.

W/c ratio	Data sample	μ	σ	p
0.3	Elastic modulus	22.21	3.33	0.29
	Compressive strength	159.52	31.82	0.19
0.4	Elastic modulus	17.16	2.90	0.57
	Compressive strength	124.97	34.70	0.75
0.5	Elastic modulus	14.34	3.78	0.32
	Compressive strength	110.24	40.23	0.10

distribution can be written as [212]:

$$F(x) = \Phi(\frac{x-\mu}{s}) \tag{6.4}$$

where μ is the mean value, s is the standard deviation, and Φ is the error function. For the two-parameter Weibull distribution, its CDF is given by Equation 4.3. Note that the Weibull distribution is derived from the weakest link theory [213], and has been widely applied for characterisation the strength of brittle or quasi-brittle materials, e.g. concrete [212, 214], rocks [215] and ceramics [175]. As the purpose of this study is to see whether these two distributions can be applied for the measured mechanical properties, these two distribution functions were used to fit both experimental measured elastic modulus and compressive strength. The fitting results are shown in Figure 6.12. It is observed that, the theoretical CDF curves from different probability functions are closer to each other. The goodness of fitting was checked by a Chi-square goodness-of-fit test. This test determines if a data sample comes from a specified probability distribution. The test groups the data into bins and calculates the observed and expected counts for those bins, and computes the chi-square test statistic [216]:

$$\chi^2 = \sum_{i=1}^{N} (O_i - E_i)^2 / E_i \tag{6.5}$$

where O_i are the observed counts and E_i are the expected counts based on the hypothesized distribution. The test statistic has an approximate chi-square distribution when the counts are sufficiently large. The fitting results are listed in Table 6.2 and Table 6.3 for normal distribution and Weibull distribution, respectively. It is shown that, for all three materials, the Chi-square test does not reject the null hypothesis (the sample data comes from the tested distribution with determined parameters) at 5 % significance level, which indicates that both distributions can be applied for the compressive strength and the elastic modulus. However, different p values are found. p is the probability of observing a test statistic as extreme as, or more extreme than, the observed value under the null hypothesis. It is a scalar value in the range [0, 1] and small values of p cast doubt on the validity of the null hypothesis. By comprising p value, it is suggested that the normal distribution is superior to Weibull distribution for the elastic modulus, while the opposite is found for the compressive strength. This is expected, as the elastic modulus is more influenced by the properties of material components and their relative amounts, while the (fracture) strength is also governed by the weakest link in the system.

The mechanical properties of HCP with size of a few hundred micrometres have been rarely measured by experiments. It is the first time that the compressive strength of

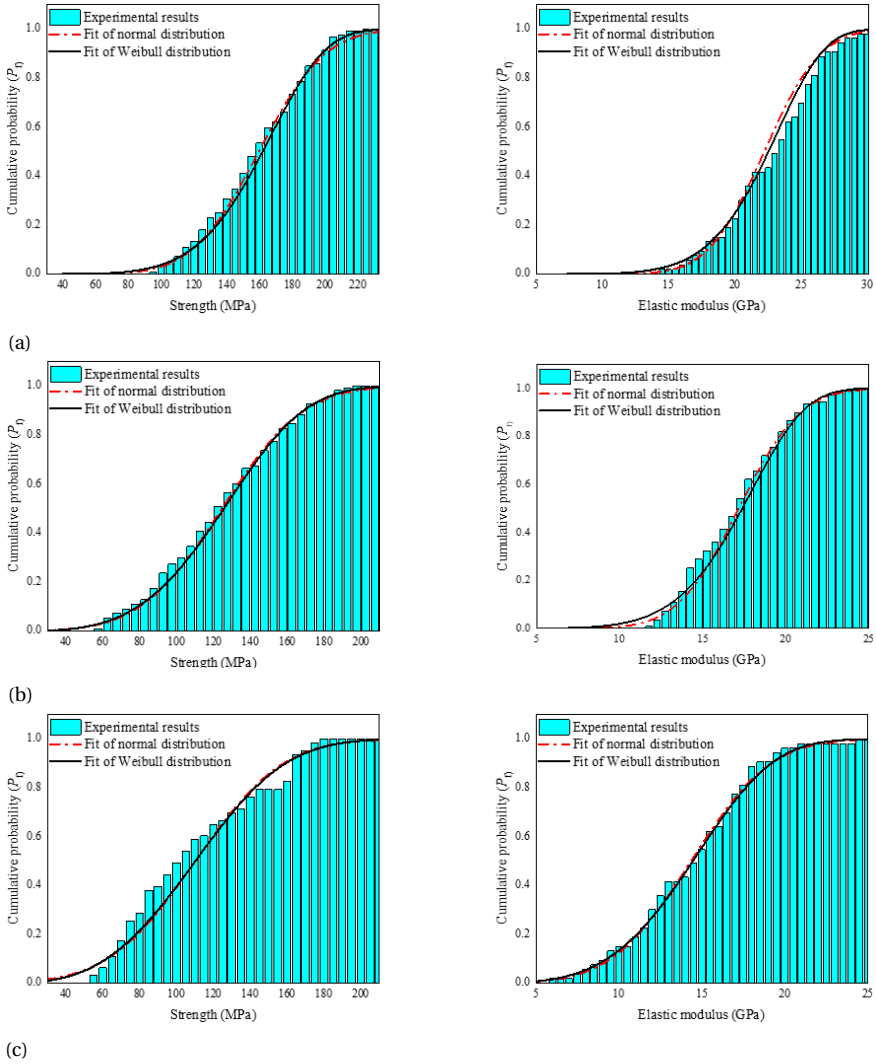

Figure 6.12: Cumulative probability of 100 µm-sized HCP cube with w/c ratio of (a) 0.3, (b) 0.4 and (c) 0.5 (left: strength; right: elastic modulus).

Table 6.3: Fitting results of Weibull distribution.

W/c ratio	Data sample	σ_0	m	p
0.3	Elastic modulus	23.66	7.44	0.23
	Compressive strength	172.13	5.98	0.30
0.4	Elastic modulus	18.39	6.46	0.35
	Compressive strength	137.93	4.08	0.79
0.5	Elastic modulus	15.76	4.25	0.30
	Compressive strength	123.30	3.27	0.14

HCP with such size is tested. Compared with the macroscopic compressive strength of such material or normal concrete [217], the strength measured at the micro-scale is significantly higher. Even for the specimen prepared with high w/c ratio (i.e. 0.5), a mean value of 110.24 MPa was measured. Likewise, similar trend has been found in terms of the splitting tensile strength measured in Chapter 4 and the simulated uniaxial tensile strength in Chapter 5. This is mainly because of the fact the micro-scale sized samples are free from air voids or defects larger than the sample size, which could create more stress concentration spots, thus significantly reducing its material strength [182, 186]. On the other hand, a large scatter is observed as a result of the heterogeneity of such material and small volume of material sampled. Recently, Shahrin et al. [103] prepared micro-pillar of C-S-H specimens (around a few micrometres) using FIB technique and measured their compressive strengths. The measured compressive strength of 10 C-S-H specimens varies from 225 MPa to 606 MPa. As expected, the measured strength from smaller scale shows higher value and a lager variation compared with current work. However, in their work, a sphero-conical indenter is mounted on the nanoindenter to apply the load on the top of the micro-pillar. Consequentially, some of the compressed micro-pillars are split in half, thus the measurements failed to provide the uniaxial compressive strength but a combination of the splitting and compression. Therefore, a somewhat lower value of the C-S-H strength is obtained in their work compared with the assumptions in the current work, where low and high hydration products have a compressive strength of 580 MPa and 920 MPa, respectively (see Table 3.5). Furthermore, it is important to notice that the splitting strengths for the same size specimens measured in Chapter 4 are 21.28 MPa, 18.72 MPa and 16.5 MPa for w/c ratio 0.3, 0.4 and 0.5, which is around one-eighth of the compressive strength. Considering that the splitting strength is generally about 1.1-1.2 time higher than the uniaxial tensile strength, it is estimated that the uniaxial compressive strength is around 10 times of the uniaxial tensile strength at this scale. This is in accordance with the centimetre sized concrete specimens [217].

Based on the multi-scale modelling, Hlobil et al. [131] give an estimation of compressive strength of HCP at 28 days with w/c ratio 0.297, which equals 147.985 MPa; for w/c ratio 0.51, its compressive strength is estimated as 52.119 MPa. The former prediction is close to the mean value and the latter approximates the lower bound of the current measurements. It is therefore advised that for the mechanical properties of HCP at smaller scale, stochastic results are needed rather than the deterministic results due to the heterogeneous material structure. On the other hand, Pichler et al. [15] calculated the deviatoric strength of a representative volume element of HCP composite with size of 0.7 mm. In order to make their results comparable with the current study, the hydration degree presented in Table 1 was used. It is estimated that, for w/c ratio 0.5, HCP with hydration degree of 0.8 has a compressive strength of 37.5 MPa, while the compressive of HCP with w/c ratio 0.35 and hydration degree of 0.6 is calculated as 60 MPa. Their prediction is much lower compared with the current results, suggesting that a strong size effect probably exists for such a heterogeneous material. The calculated elastic moduli of 100 µm-sized HCP cubes using Eq. 3 are compared with available data in the literature [3, 15, 16, 18, 76, 133], as shown in Figure 6.13.The reported moduli in the current work are comparable with the results presented in the literature, but seem relatively lower.

This mainly attributes to the fact that the deformation of the substrate glass is not considered.

It is worth mentioning that the reported compressive strength in the current work is limited under a loading rate of 10 mN/s. As reported in [218, 219], the loading rate has considerable influence on the measured strength, it is therefore expected that various loading rates would be carried out in the future. This way, the loading rate-compressive strength relationship at the micrometre length can be quantified. Additionally, both linear and nonlinear creep behaviours have been observed for the compression test of concrete [220, 221], which have a considerable influence on the failure of the tested material. With respect to the micrometre length scale, the influence of creep on the nanoindentation test has been studied by applying multiple loading cycles on the cement paste [222]. As a sharp tip (Berkovich tip) was used in the test, a high stress concentration occurs below the indenter during the test, leading to a significant creep strain. The magnitude of creep in concrete has been found to be proportional to the intensity of applied stress [217]. A stress concentration occurring underneath a Berkovich indender should, accordingly, result in high local creep. In uniaxial compression, as tested herein, it is expected that creep is less pronounced, and is therefore not considered herein. Nevertheless, there is a need for quantifying this effect.

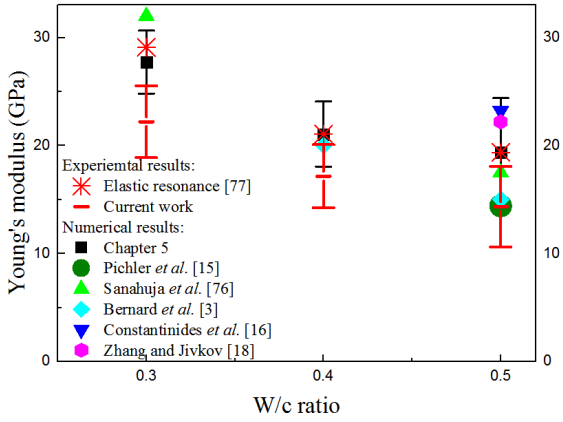

Figure 6.13: Comparison of elastic moduli reported in the literature (reference number in the Figure would be updated in the final version of the thesis).

6.4.2. MODELLING RESULTS AND DISCUSSION

In order to validate the adopted discrete lattice model, the computational uniaxial compression test was first conducted on the virtual specimens containing AL which is comparable with the experimental set up. In Figure 6.14, the simulated load-displacement curve is compared with the experiments for each w/c ratio. Clearly, a descending branch after the peak load is obtained from the modelling. However, such post-peak behaviour cannot be captured by the experimental measuring as the test is run under a load control model. Consequently, a load plateau is observed as a result of the overshoot of the indenter. Therefore, the comparison is limited to the pre-peak regime from which the

compressive strength and elastic modulus are obtained. It is observed that the slope and peak load from the model are in the range of the experiments, although dispersion remains in the experimental measurements. Figure 6.15 presents the simulated crack pattern of 100 µm-sized HPC cube consisting AL at stage of peak load and failure for each w/c ratio. It is evident that diagonal main cracks form at the side of the cube at the final crack stage, which agrees with the experimental observations. The comparison proves that the adopted discrete lattice model can simulate the conducted experimental compressive measurement and give a reasonable prediction in terms of the compressive strength and elastic modulus.

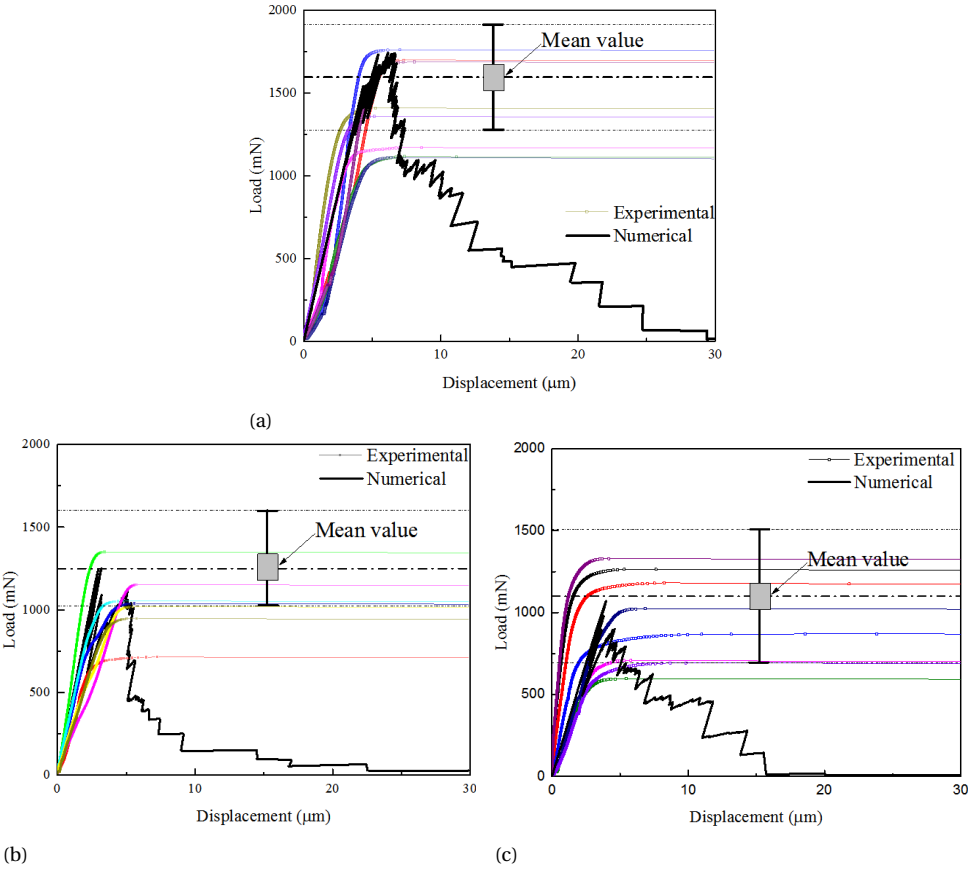

Figure 6.14: Comparison of simulated results of 100 µm-sized cubes (having 20 µm AL) with experimental measured results: (a) w/c= 0.3; w/c=0.4; w/c=0.5.

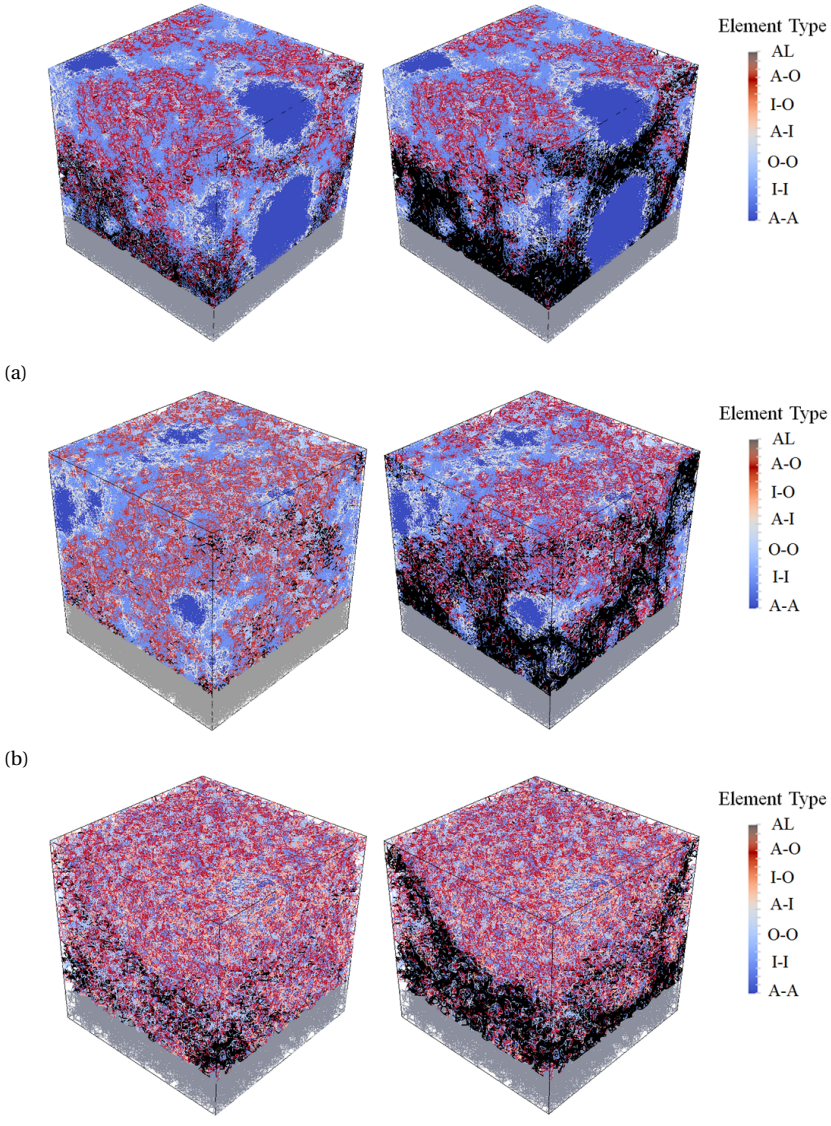

Figure 6.15: Simulated crack pattern of 100 µm-sized HCP cubes consisting of AL with w/c ratio (a) 0.3, (b) 0.4 and (c) 0.5 at two stages (left: peak load; right: final failure state. black denotes the crack).

After validation, the compressive fracture performance of HCP was modelled using the 100 µm-sized virtual cubes without the AL. The used local mechanical properties of lattice element remain unchanged as aforementioned. Herein, a high friction compression boundary condition was applied by restraining deformation of horizontal displacement of the nodes at two ends. Figure 6.16 presents the simulated stress-strain curve of HCP cube with different w/c ratios. The elastic modulus and compressive strength were derived from the stress-strain curve and listed in Table 6.4 together with the tensile strength that obtained in [152]. As expected, HCP with lower w/c ratio has a higher strength and elastic modulus. The ratio of compressive/tensile strength ranges from 7.91 to 9.66, which is in accordance with concrete [2]. Furthermore, it is observed that a higher strength would be obtained once the AL is removed as the AL has a relatively low stiffness which reduces the ability to restrain the deformation of the bottom surface of HPC. The simulated moduli are also higher than those measured from the experiments due to the fact that Equation 6.3 does not consider the deformation of the substrate glass and the possible creep of the micro-cubes. Nevertheless, the numerical and experimental results are comparable. As shown in Figure 6.17, the simulated fracture patterns at peak load and the final failure stages are presented. Typical inclined fracture pattern is observed more pronounced in the HPC cube prepared with higher w/c ratio, in which fewer stiff inclusions, i.e. anhydrous cement particles remain in the microstructure. As these inclined cracks are distributed by the anhydrous cement particles leading to more crack branches and stable crack propagation, the cement paste with lower w/c ratio has a higher load bearing capacity (higher strength).

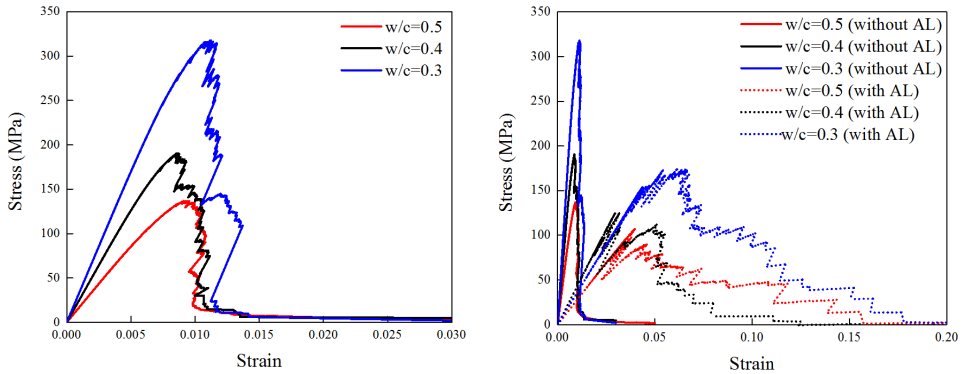

Figure 6.16: (a) Simulated stress-strain diagrams of 100 µm-sized HCP cube (without AL) with various w/c ratios; (b) comparison between stress-strain diagrams of 100 µm-sized HCP cube with and without AL.

In the end, it is worth mentioning that, for each w/c ratio, only one virtual specimen was tested using the developed discrete model. To have a more comprehensive understanding of compressive failure of HPC at the micrometre length scale, more virtual specimens need to be created and tested like Chapter 4 and 5 to have a stochastic-based results. Furthermore, the influence of the size and shape of specimens on their fracture performance as listed in Table 6.1 should also be investigated using the developed

Table 6.4: Calculated global mechanical properties, compared with tensile strength in the literature [152].

W/c ratio	Young's modulus (GPa)	Compressive strength (MPa)	Tensile strength [152] (MPa)	Compressive strength / tensile strength
0.3	33.27	317.72	32.9	9.66
0.4	25.40	190.52	22.3	8.54
0.5	16.97	136.81	17.3	7.91

model following the approach as discussed in Chapter 9 and [223]. However, compared with the computational uniaxial tensile test, the compression test requires significantly more computational time as compressive failure process is more complex and more (micro) cracks form before the specimen fails. It is expected that the mentioned limitations would be overcome with more powerful computational facilities and a more efficient numerical algorithm in the future.

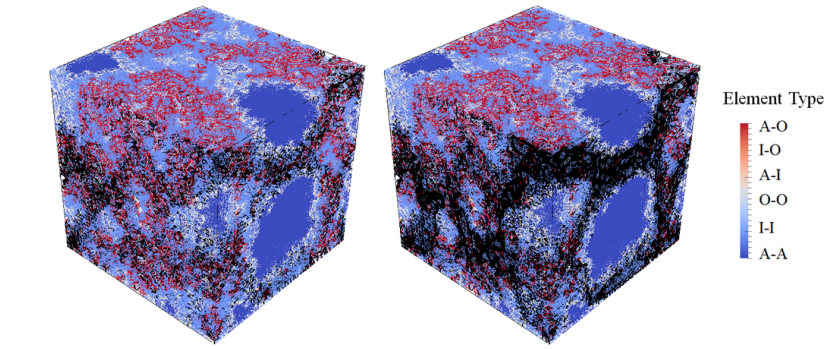

(a)

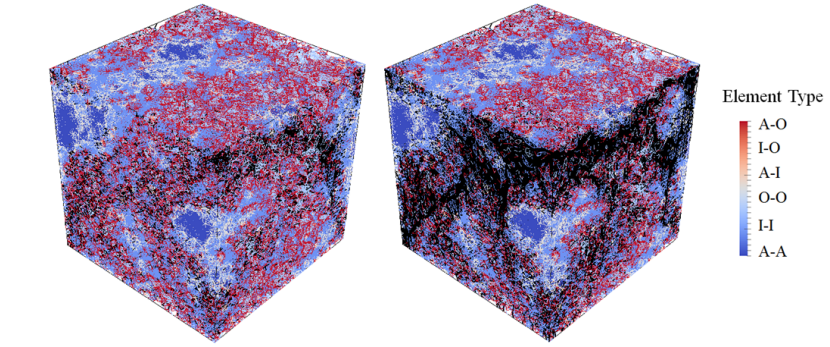

(b)

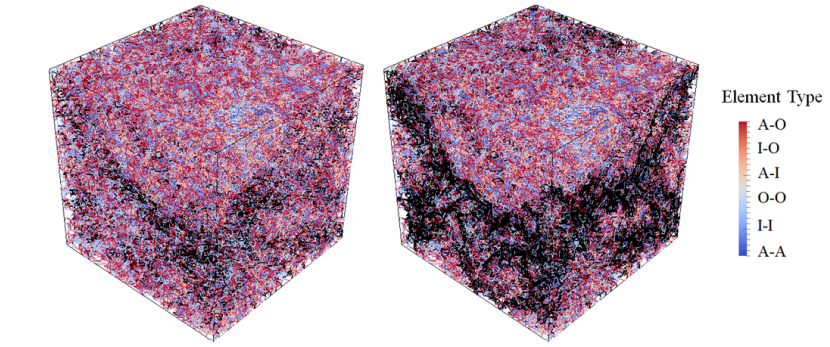

(c)

Figure 6.17: 18 Simulated crack pattern of 100 µm-sized HCP cubes with w/c ratio (a) 0.3, (b) 0.4 and (c) 0.5 at two stages (left: peak load; right: final failure state. black denotes the crack) when no AL is considered.

6.5. CONCLUSIONS

IN this chapter, a new approach has been developed to study the compressive failure of micro-scale sized HCP specimens. The discrete lattice model was used to mimic the failure process of specimens under compression. Although a stable measuring of post-peak stage is missing in the experiments because of the limitation of instruments, a good agreement between modelling (considering the AL) and experiment is found in the pre-peak stage in terms of the load-displacement curve and crack pattern. Based on the current study, the following conclusions can be drawn:

- Although slenderness and w/c ratio play a significant role on the compressive fracture performance of HCP, the experimental measured strength in this work is much higher than the strength measured from centimetre sized specimens and lower than the one for smaller sized specimens.

- Both normal distribution and Weibull distribution are applicable to describe the experimental probability distribution of compressive strength and elastic modulus. While the normal distribution is more suitable for the elastic modulus and Weibull distribution is better for the compressive strength.

- The input local mechanical properties for the discrete lattice model are calibrated from the previous chapter, and results in satisfactory modelling results when compared with the experimental measurements. Together with Chapter 5, the lattice model is capable of simulating both tensile and compressive fracture behaviours of HCP at the micrometre length scale, which forms the basis for the multi-scale modelling of cementitious material.

- From both modelling and testing, the compressive strength is almost 10 times of the tensile strength which is in accordance with the phenomenon that observed for the centimetre sized concrete specimens.

In the end, it is important to notice the limitations of the current experimental set up. First, the influence of AL and substrate underneath the HCP on the measured displacement is not considered. Thus, the estimated elastic modulus based on the linear elastic assumption is relatively low. This is expected to be solved by monitoring the deformation at two ends of HCP using a high magnification camera during the mechanical test. The other is that the stable post-peak cannot be captured by the nanoindenter. Therefore, a more advanced instrument with adequate high-resolution system for displacement control and measurements is needed.

7

TESTING AND MODELLING OF HARDENED CEMENT PASTE - AGGREGATE INTERFACE AT MICRO-SCALE

The aim of this chapter is to predict the micromechanical properties of interfacial transition zone (ITZ) by combining experimental and numerical approaches. In the experimental part, hardened cement paste (HCP) cantilevers (200 µm × 100 µm × 100 µm) attached to a quartzite aggregate were fabricated and tested using micro-dicing saw and nanoindenter, respectively. In the modelling, comparable digital specimens were produced by the X-ray computed tomography (XCT) and tested by the discrete lattice model. The fracture model was calibrated by the experimental load-displacement curves and can reproduce the experimental observations well. In the end, the calibrated model was used to predict the mechanical behaviour of ITZ under uniaxial tension, which can be further used as input for the meso-scale analysis of concrete.

Parts of this chapter have been published in Cement and Concrete Composites **104** (2019) [224].

7.1. INTRODUCTION

CONCRETE is a composite material consisting of cement paste and aggregate inclusions with various particle sizes. A well-known fact is that, a thin layer of cement paste with a thickness between generally 30 and 80 µm, having different features, e.g. morphology, composition and density, with the bulk cement paste matrix occurs around aggregates [225–229]. This thin layer is the so-called interfacial transition zone (ITZ). Numerous experiments and simulations have established that the ITZ is more penetrable by fluids and gases [229–232], and appears to be the weakest region [233–235] in conventional concrete. Therefore, it plays a dominant role in determining the overall performance of this composite material.

Concrete is generally considered to be a three-phase material composed of aggregate, cement paste matrix and the ITZ at meso-scale [161, 236–241]. In order to offer fundamental insight into the fracture mechanisms of such composite material and give a proper prediction, the input parameters of each phase are required to be calibrated separately. The behaviour of the matrix phase and the aggregate can be studied in a rather straightforward manner because these materials can be prepared and tested individually. Unfortunately, this does not apply to the ITZ, because this zone is an integral part of the whole microstructure together with the bulk cement paste and the aggregate [242]. Over the past decades, various test configurations have been developed to study the interface fracture at the meso-scale. The specimens are generally made by casting the cementitious matrix against a flat block of aggregate. Load is then applied to split these two materials along the interface to quantify the bonding strength. Mode I and mode II are the mostly adopted loading conditions for the mechanical properties measurements. The mode I loading types include the uniaxial tensile test [243–245], wedge splitting [246, 247], flexure test (i.e. cantilever bending [248, 249] and three-point bending [250–252]) and Brazilian splitting test [251], while mode II experiments contain mainly push-out test [253, 254] and slant shear test [255]. Based on these aforementioned techniques, a lot of knowledge about the influence of ITZ on the mechanical performance of concrete has been gained. However, almost all fracture experiments are carried out at the scales larger than that of real aggregate in concrete. A clear understanding about the micromechanical properties of the ITZ is still missing, as it is a special material feature at the micro-scale. At this scale, studies are mostly carried out by simulations [256–258] due to the technical and instrumental limitations. Consequently, these models cannot be validated due to the mismatch in terms of the investigated scale length. Therefore, there is a need for experimental measurements at the micro-scale, which can be used for the calibration and validation of the micromechanical modelling of the ITZ.

Recent reports document the utilization of nanoindenter as a versatile instrument for loading micrometre sized specimens [45, 102, 103, 259]. The micro-dicing technique developed in the previous chapters has proved to be able to produce specimens with a size of a few hundred micrometres with shape of cube, prism and cantilever beam. This technique is therefore adopted to produce small HCP cantilevers having one end bonded to the aggregate. To test the fracture performance of aggregate-cement interface, a load was applied at the free end of the cantilever by the nanoindenter. To the authors' best knowledge, it is the first time that fracture of aggregate-cement interface has been successfully tested at the micro-scale. This offers valuable experimental data

for the calibration and validation of the micromechanical modelling of the ITZ.

In addition to experiments, a micromechanical model of ITZ is proposed. The model is built up on the basis of a combination of X-ray computed tomography and discrete lattice fracture model. It is first calibrated by the experimental results and further used to predict the micromechanical properties of the pure ITZ. This work presents a fundamental study of the fracture testing and modelling of the aggregate-cement interface at the micrometre length scale. The predicted micromechanical properties of ITZ can be further used to determine the interface properties between aggregate and HCP in the discrete fracture modelling of concrete or mortar at the meso-scale.

7.2. EXPERIMENTAL

7.2.1. MATERIALS AND SAMPLE PREPARATION

FOR the sample preparation, standard CEM I 42.5 N Portland cement, quartzite aggregate and deionized water were used. A flat aggregate slice having thickness of 1 mm was made by cutting and thin-sectioning. The thin-sectioning was conducted by grinding using a Struers Labopol-5 thin sectioning machine. To obtain smooth and parallel surfaces and to eliminate the effect of different surface roughness, both sides were ground using discs with grit sizes of 135 µm and 35 µm in a descending order. The slice was placed at the bottom of a plastic mould. Fresh cement paste with w/c ratio of 0.3 was mixed following EN-BS 196-3:2005+A1:2008 [260] using a Hobart mixer and cast on the top of the aggregate slice. After 28 days curing under sealed conditions, the HCP-aggregate specimen was demoulded. A thin-sectioning procedure was then conducted on the HCP surface to make the thickness of the whole specimens 1.2 mm (0.2 mm cement paste layer and 1 mm aggregate layer, see Figure 7.1a). To fabricate micrometre sized cement paste cantilever having one end attached to the aggregate, the following steps as shown in Figure 7.1 were conducted using the micro-dicing saw, which ensures the precision for preparing specimens with size of a few hundred micrometres. The blade was run in two perpendicular directions as shown in Figure 7.1b and 7.1c to fabricate the HCP beam with a square cross-section of 100 µm and a length of 200 µm on the aggregate. The dicing width was set as the sum of the length of the designed cross-section (100 µm) and the thickness of the blade (260 µm). The blade was cut 20 µm into the aggregate in order to have a clear boundary between HCP beam and the aggregate support. A strip of aggregate consisting of a row of HCP cantilevers was then cut off from the aggregate slice as shown in Figure 7.1d. Afterwards, the morphology of the produced cantilever beams were checked by an environmental scanning electronical microscope (ESEM) under the backscattered electrons (BSE) model, see Figure 7.2. A clear boundary with much higher porosity between the HCP beam and aggregate support can be clearly observed in Figure 7.2c, indicating a weak bound between the HCP and aggregate.

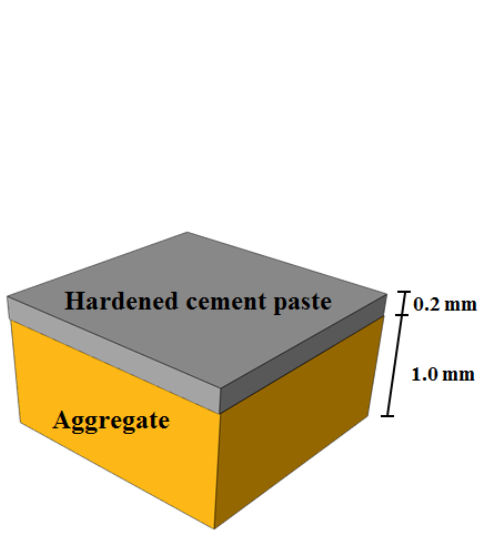

(a)

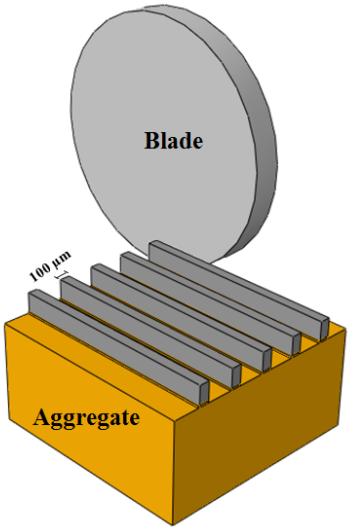

(b)

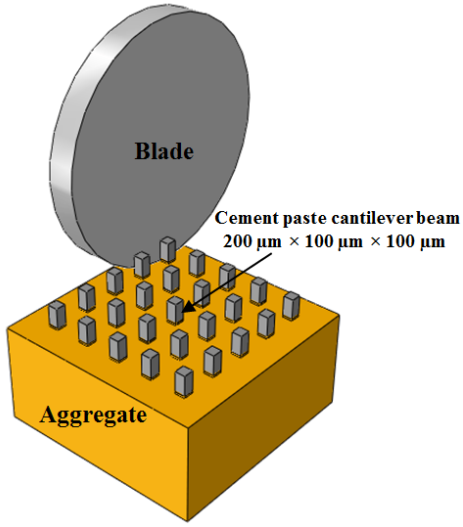

(c)

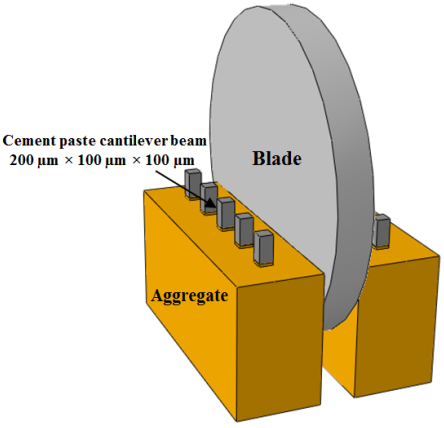

(d)

Figure 7.1: Schematic illustration of the sample preparation procedure: (a) preparing a HCP-aggregate slice; (b) cutting through HCP at one direction; (c) cutting through HCP at a perpendicular direction; (d) cutting one aggregate strip off.

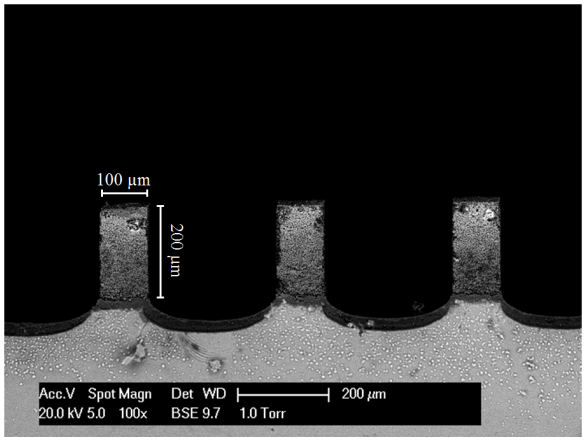

(a)

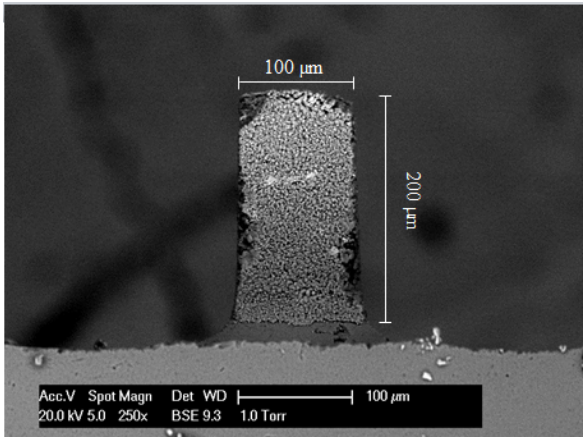

(b)

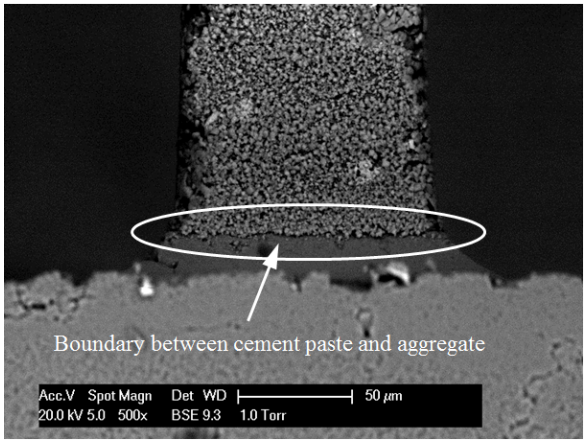

(c)

Figure 7.2: ESEM image of (a) a row of cantilever beams, (b) one cantilever beam with dimensions and (c) the interface between HCP beam and the aggregate.

7.2.2. MECHANICAL TEST USING NANOINDENTER

The test configuration is schematically shown in Figure 7.3. The aggregate strip was attached to a support vertically resulting in a row of HCP cantilevers standing horizontally. A nanoindenter was then instrumented for applying load at the free end of the cantilever. To eliminate the possible penetration of the indenter into the specimen, the flat end cylindrical tip with a diameter of 330 µm as presented in Figure 6.2 was adopted instead of a standard Berkovich tip. The tip was set to be aligned with the centre of the free end of the beam using the in-situ imaging system. To ensure the positioning accuracy, a microscope to indenter calibration procedure was conducted prior to the test. The test was run under a displacement-controlled method with a constant displacement increment of 50 nm per second. The cantilever beams were loaded until failure and the load-displacement curves were recorded by the nanoindenter for further analysis.

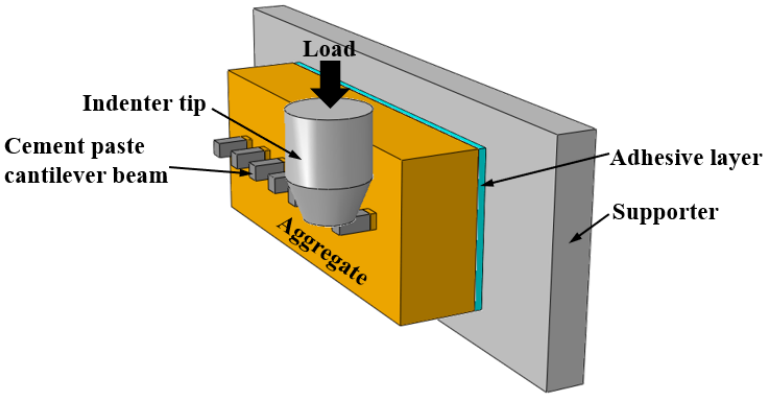

Figure 7.3: Schematic view of the test setup.

7.2.3. EXPERIMENTAL RESULTS

10 cantilever beams were tested. Figure 7.4 shows their load-displacement curves. A good repeatability can be found and, in general, these curves can be divided into two parts: ascending and plateau. In the ascending part, the load increases monotonically with the displacement until reaches a critical load. Afterwards, a displacement jump is observed. This is because the control of the nanoindenter is not fast enough to enable a stable post-peak behaviour measurement. Consequently, a catastrophic failure happens and the indenter overshoots downward. Thus, only the first regime was used for the calibration of the fracture model in Section 7.4.2. In this regime, the peak load ranging from 36.96 mN to 49.03 mN and its corresponding displacement (1103.6 - 1432.62 nm) can be derived. The fluctuation is mainly attributed to the heterogeneous nature of the material structure, especially the porous interface. Note that these values cannot be used to calculate the interface properties through simple analytical solutions for bending or shearing because of the complex boundary conditions at the interface introduced by the test configuration. In this case, the numerical approach shows advantages when dealing with such complex boundary conditions.

After the fracture test, the aggregate strip was checked by the ESEM. Figure 7.5 shows the remaining aggregate support. This means that the crack occurs along the interface between the aggregate and HCP. A top view of the fractured surface is shown in Figure 7.6. It can be distinguished from the texture of the surface that part of HCP remains on the aggregate surface, indicating a tortuous fracture surface. This agrees well with the macroscopic observations [2].

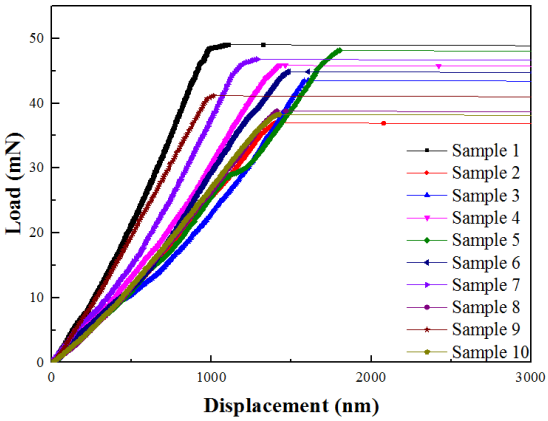

Figure 7.4: Experimental load-displacement diagrams of the cantilever bending test.

7.3. DIGITAL SPECIMENS

7.3.1. XCT EXPERIMENTS

THE fracture modelling requires virtual specimen with details of the featured material structure. In this work, X-ray computed tomography (XCT) and image segmentation techniques were used to characterize the material structure and build the digital

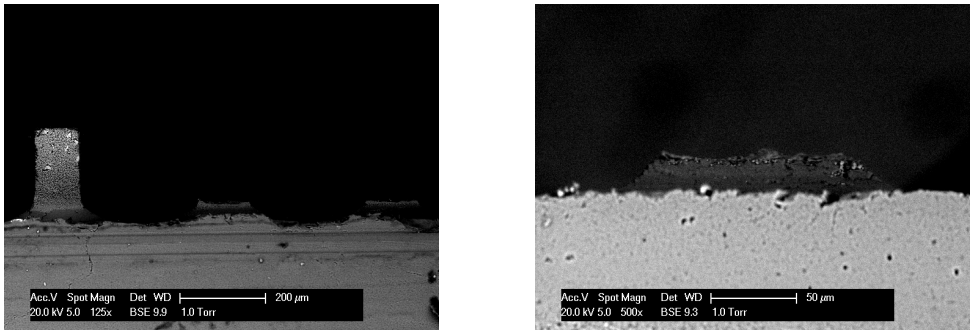

(a) (b)

Figure 7.5: ESEM micrographs of the ITZ cantilever beams after failure: (a) an intact cantilever and two fractured cantilevers (b) remains of the microcantilever after failure (higher magnification).

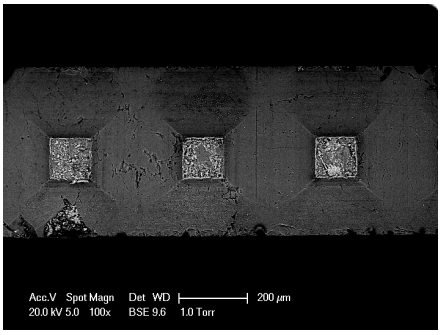

(a)

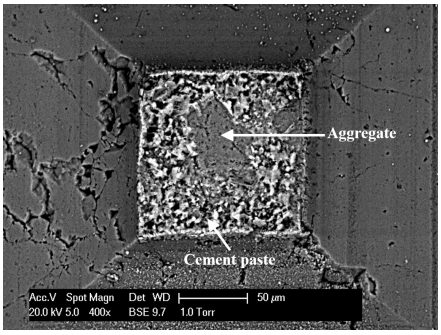

(b)

Figure 7.6: ESEM micrographs of the fracture surface after ITZ cantilever beam failure: (a) three fracture cantilevers (b) one cracked surface at higher magnification.

specimens which are comparable with the realistic specimen. As shown in Figure 7.7: a HCP-aggregate prism was created and clamped on a special holder for the scanning. A small drop of cyanoacrylate adhesive was added to the surface of the specimen to protect the sample from breaking during clamping. The prism has a square cross-section of 500 μm × 500 μm and a length of 3 mm. It was fabricated using a similar approach as proposed in Section 7.2.1. First, a 3 mm two-layer cement paste-aggregate material (2 mm aggregate substrate and 1 cement paste layer) was made by casting cement paste on a 2 mm aggregate slice and grinding after 28 days curing. The micro-dicing saw was then run two perpendicular directions over the slice to create the prisms. In order to separate these prisms, the saw was set to cut through the aggregate during the dicing.

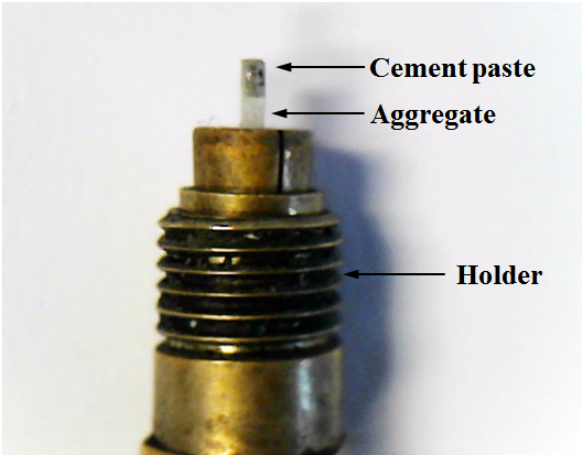

Figure 7.7: Cement paste-aggregate specimen clamped on the holder for CT scanning.

In the XCT experiment, the holder was fixed in the rotatable stage. The X-ray source tube was set as 120 Kev/60 μA for the scanning. 2800 projections were acquired using a digital GE DXR detector (3072 × 2400 pixels). This setup results in a greyscale level-based

material structure with a resolution of 1 µm × 1 µm × 1 µm. In order to reduce the noise in the reconstructed XCT images as well as the computational efforts in the discrete fracture modelling, a binning level of 2 was used in the reconstruction. The resulted final material structure has a resolution of 2 µm × 2 µm × 2 µm. Afterwards, a stack of 2D slices from the side view was exported for image segmentation and digital specimen generation. To reduce the influence of beam hardening in the XCT experiment, a region of interest (ROI) with a cross-section of 300 µm × 300 µm and length of 1000 µm was extracted from the central region of the scanned specimen.

7.3.2. MICROSTRUCTURE CHARACTERISATION

In general, aggregate particles are observed as relatively homogeneous in XCT images. On the other hand, cement paste shows significant heterogeneity due to presence of porosity and different hydration phases. Therefore, differences in relative grayscale levels can be used to distinguish between the aggregate and the paste phase in XCT images. This was also done in the current study. First, the fluctuation of the greyscale level along the height of the ROI was analysed by calculating the coefficient of variation (CoV) of greyscale level of voxels at each row using:

$$\mathrm{CoV_i} = \frac{S_\mathrm{i}}{\mu_\mathrm{i}} \tag{7.1}$$

where CoV_i is the CoV of greyscale level at height i, S_i the standard deviation greyscale level at height i, μ_i the mean greyscale level at height i. As shown in Figure 7.8, on the one hand, the CoV at the aggregate part is relatively low (below 0.1). On the other hand, HCP has a much higher CoV. It is therefore reasonable to consider the aggregate as a single-phase material in the model. Note that the CoV value at height i is averaged from the 3D ROI rather than a 2D slice. Additionally, a significant increase of CoV (from 0.05 to 0.25) is observed at the boundary between the aggregate and HCP, which was used to separate the two materials from the original greyscale level-based images.

To consider the heterogeneity of HCP at the micro-scale, both the multi-phase based material structure (Chapter 3) and continuous greyscale level based material structure (Appendix A) can be used. Herein, the global thresholding approach that developed in Chapter 3 was adopted to segment the HCP part into a 4-phase material consisting of capillary pore (CP), inner hydration product (IHP), outer hydration product (OHP) and anhydrous cement particle (ACP). This method determines the threshold value of greyscale value using both cumulative and histogram of the greyscale level in the ROI. In order to avoid the influence of the ITZ on the determination of the threshold value of different phases, the region away from the boundary of 150 µm was used, which can be regarded as the bulk cement paste. The information of the segmented material structure of bulk cement paste is listed in Table 7.1, which is similar to the results that obtained in Chapter 3 for a pure cement paste prepared with the identical w/c ratio (0.3, see Table 3.1). It should be note that, under the current resolution, the inner or outer product does not represent any single chemical composite in the HCP but a combination of several of them e.g. calcium-silicate-hydrate gel, calcium hydroxide, ettringite and monosulfate, etc. Figure 7.9 shows a comparison between segmented material structure and its corresponding greyscale level image. With the approach proposed in this section, a

Table 7.1: Information of the segmented bulk cement paste.

Porosity	Anhydrous cement particles	Hydration degree
8.35 %	16.96 %	66.69 %

multi-phase material structure can be segmented from these greyscale level based XCT images.

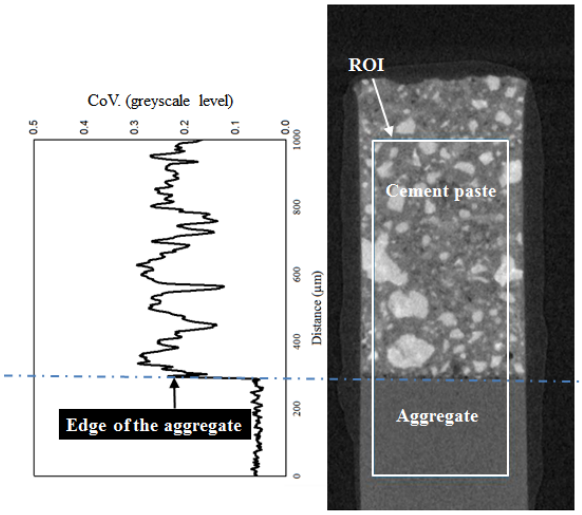

Figure 7.8: (left) CoV of the greyscale level along the ROI, clearly indicating a more homogeneous greyscale value distribution in the aggregate compared to paste; (right) A slice from the X-ray CT micrograph of the cement paste/aggregate specimen (Both shown in 2D for clarity).

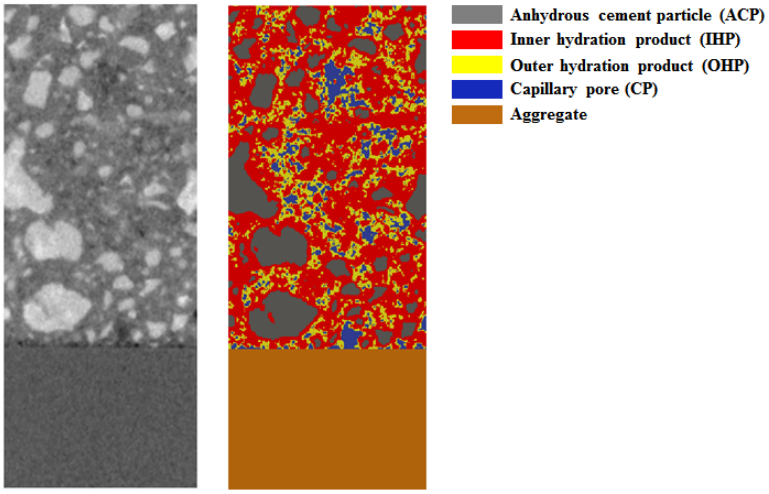

Figure 7.9: (Left) X-ray computed tomography of the ROI; (right) segmented microstructure of the ROI (Both shown in 2D for simplicity).

7.3.3. DIGITAL SPECIMEN GENERATION

Two types of digital specimens were extracted from the segmented voxel-based images for the fracture analysis. As shown in Figure 7.10, the first one (Type I) has a cross-section of 100 µm × 100 µm and length of 220 µm consisting of 20 µm length of aggregate and 200 µm length of HCP. The features of this type specimen are assumed to be the same as the cantilever beam that is fabricated in Section 7.2.1. This enables the calibration of the fracture modelling in Section 7.4.2. In order to study the deviation of the mechanical properties of the investigated material as shown in the experiments, 10 digital specimens were randomly extracted. The second (Type II) is a pure ITZ specimen which is obtained by "cutting" off the aggregate and bulk cement paste part from the Type I specimen. The thickness of this zone was determined by checking the porosity profile perpendicular to the interface in the ROI, see Figure 7.11. It is clearly that with the position keeping away from the aggregate surface, the porosity decreases dramatically until reaches the average porosity (8.35 %) of the bulk cement paste at around 50 µm. Therefore, 50 µm is regarded as the thickness of ITZ herein, which is in accordance with references [225, 227, 229]. The microstructure within this area was then extracted from Type I specimen to form the pure ITZ specimen as shown in Figure 7.12. 10 Type II specimens were created to consider the deviation of the modelled micromechanical properties.

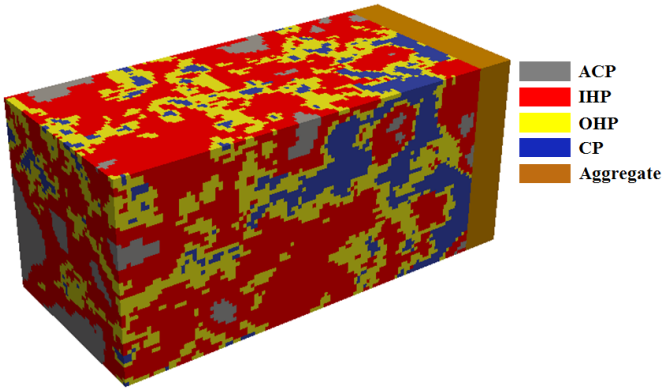

Figure 7.10: Type I specimen with size of 220 µm × 100 µm × 100 µm (110 voxel × 50 voxel × 50 voxel).

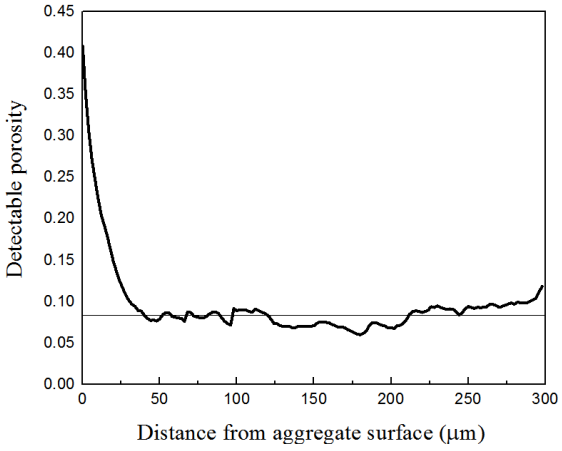

Figure 7.11: Porosity profile of cement paste part in the ROI.

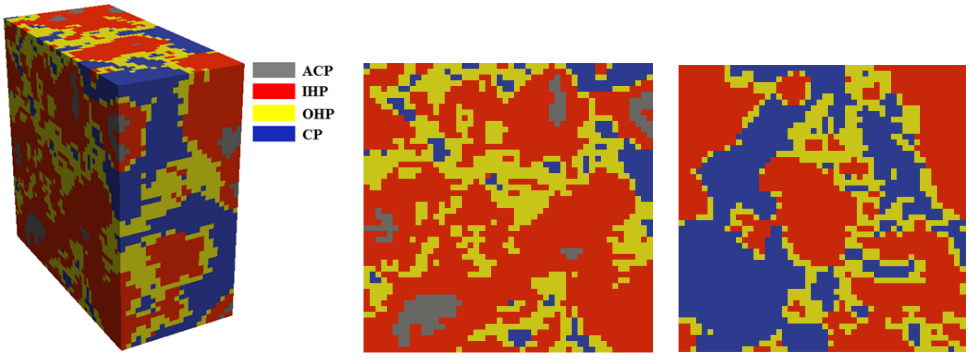

(a) (b) (c)

Figure 7.12: Type II specimen with size of 50 µm × 100 µm × 100 µm (25 voxel × 50 voxel × 50 voxel): (a) side view; (b) view from the bulk cement paste side; (c) view from the aggregate side.

7.4. DEFORMATION AND FRACTURE MODELLING

IN this section, the discrete lattice fracture model, as described in Chapter 3, was used to predict the mechanical performance of the generated specimens. The Type I specimen was used to calibrate the input local mechanical properties using the experimental measurements. After calibration, the fracture model was applied on Type II specimen to predict the mechanical properties of pure ITZ.

7.4.1. MODELLING APPROACH

Following the procedure developed in Chapter 3, the fracture process of digiatal specimens genereated in Section 7.3.3 can be analysed by the discrete lattice model. For the elements that exist in the cement matrix, their mechanical properties have been calibrated and validated in the previous chapters and listed in Table 3.5. With respect to the element within the aggregate, its elastic modulus is taken from [251], i.e. 70 GPa. Its tensile strength is assumed as 1/1000 of the modulus, i.e. 70 MPa. The adopted strength/modulus ratio is larger than the one commonly observed at the meso-scale in order to consider the size effect [261]. Furthermore, because fracture happens at the cement paste part, the strength of the aggregate has no contribution to the mechanical response.

It is well known that a rather thin layer forms directly on the aggregate surface, typically a micron or so in thickness, including the products from any reaction that may happen between the aggregate and cement paste. These products contain mainly calcium silicate hydrate, calcium hydroxide and ettringite depending on the specimen preparation and the size of the aggregate [226, 242, 262–266]. This layer cannot be distinguished from the XCT images due to limited resolution and segmentation techniques. In order to take this layer into account, the elements that connect the solid phases in cement paste and the aggregate are generated, which has a comparable dimension with the thickness of the layer. For simplification, the mechanical properties of these elements are assumed proportional to the phases they connect with in HCP. In this way, the elastic moduli and strengths of these elements can be calibrated through inverse analysis using experimental measured load-displacement curves. Furthermore, it should be noticed that the element that connects the anhydrous cement particle and aggregate is removed from the mesh, as negligible bonding strength is expected for these two solid phases. This results in two types of interface elements (i.e. Ag-I, Ag-O, see Table 7.2) that are needed for the calibration.

7.4.2. CALIBRATION AND DISCUSSION

In this section, the discrete lattice model was applied for the fracture analysis of the Type I specimen. As schematically shown in Figure 7.13, a Type I digital specimen has been mapped to a lattice mesh. The end of the aggregate part was clamped. In the experimen-

Table 7.2: Lattice element type that need to be calibrated in this chapter.

Element type	Phase 1	Phase 2
Ag-I	Aggregate	IHP
Ag-O	Aggregate	OHP

Table 7.3: Calibrated mechanical properties of the lattice elements connecting aggregate and HCP.

Case number	Boundary configuration	Element type	Young's modulus (GPa)	Tensile strength (MPa)	Compressive strength (MPa)
1	Fully contacted	Ag-I	0.2	3	30
		Ag-O	0.16	2.5	25
2	Edge contacted	Ag-I	0.17	5	50
		Ag-O	0.14	4.2	42

tal test, due to the rotation of the cantilever beam, the contact area between the flat end tip and the cantilever beam decreases gradually from fully contacted to only the edge of the indenter with the deformation of beam increasing. However, such dynamic boundary configuration could not be implemented in the modelling. Two extreme boundary conditions as shown in Figure 7.13 are therefore adopted herein for the purpose of calibration. The fully contacted loading boundary condition was modelled by adding unit displacement at nodes within the dash line marked zone (Figure 7.13a), while the edge contacted boundary condition is mimicked by applying unit displacement at the notes on the right side edge (Figure 7.13b). Through a trial-and-error approach, satisfactory load-displacement curves were obtained when the values in Table 7.3 were adopted. As the fracture pattern for the simulated two boundaries are almost identical and a linear-elastic constitutive law is implemented for the local beam elements, the simulated load-displacement curves have similar shapes. Furthermore, the mechanical properties listed in Table 7.3 are rather low compared with the phases connected by the element in HCP. This tends to confirm the weak bonding between cement paste and aggregate. Figure 7.14 presents the comparison between the simulated load displacement curve and the experimental ones. As mentioned above the experiments are not able to measure the post-peak behaviours, the comparison is only made in the pre-peak regime. Clearly, the simulation can reproduce the experimental measured results well in terms of the ascending slope and the peak load. The simulated fracture patterns at peak load and final stage are plotted in Figure 7.15. It is observed that, all the cracks happen in the interface (the weakest part of the specimen) until the peak load. At the failure stage, the HCP beam is debonded from the aggregate. It can be seen from Figure 7.15b that almost all the interface elements are broken. While, the small amount unbroken interface element and the crack occurring in the HCP proves that there are some residual HCP left on the aggregate after the debonding. This is in accordance with the experimental observation.

The identical boundary configurations and input mechanical parameters are used to model the fracture of other 9 Type I specimens. The simulated load-displacement curves are shown in Figure 18 for both boundary conditions. The load-displacement curves of all specimens consist of a linear ascending branch and a zig-zag descending branch. The zig-zag is a consequence of the use of a sequentially-linear procedure [139] in the model. After a beam element is removed from the lattice system, much less load is needed to break the next one(s) until an increasing load is required to continue further. This is comparable with a small propagation of a crack under a constant loading before the fracture process becomes stable again. Additionally, as expected, variations between individual specimens are observed due to the heterogeneity of the material structures.

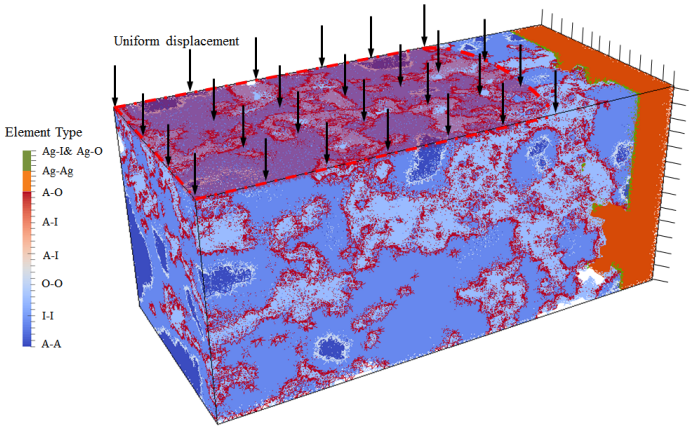

(a)

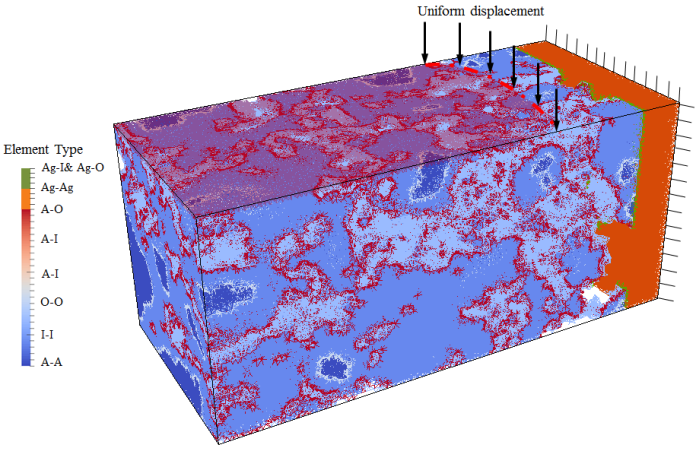

(b)

Figure 7.13: Schematic illustration of the boundary configurations for the modelling of the cantilever under loading: (a) fully contacted with the indenter surface; (b) contacted with the edge of indenter.

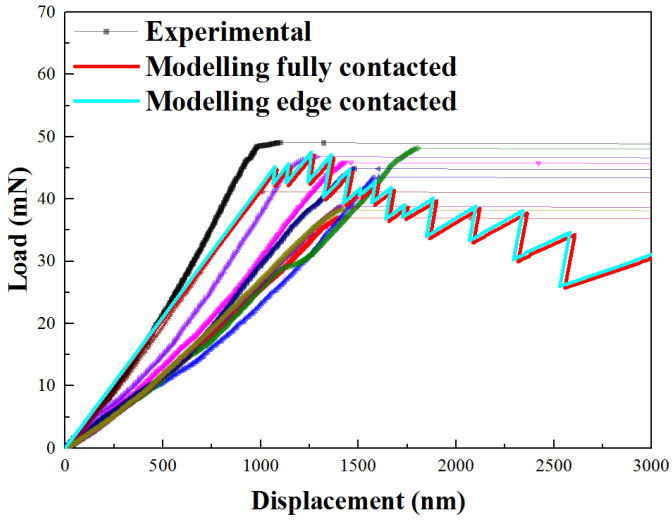

Figure 7.14: Fit back of the lattice fracture model.

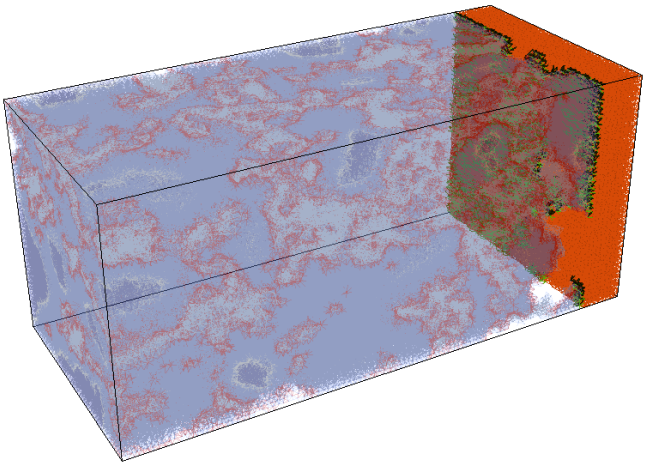

(a)

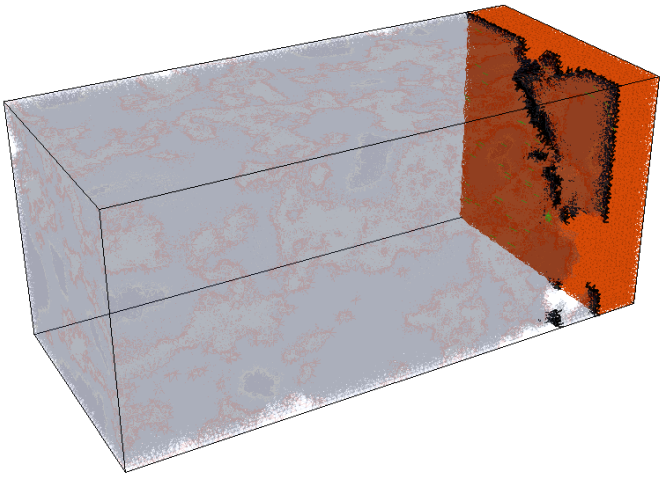

(b)

Figure 7.15: Simulated crack patterns at different stages: (a) peak load; (b) failure (black: crack, green: Ag-I and Ag-O).

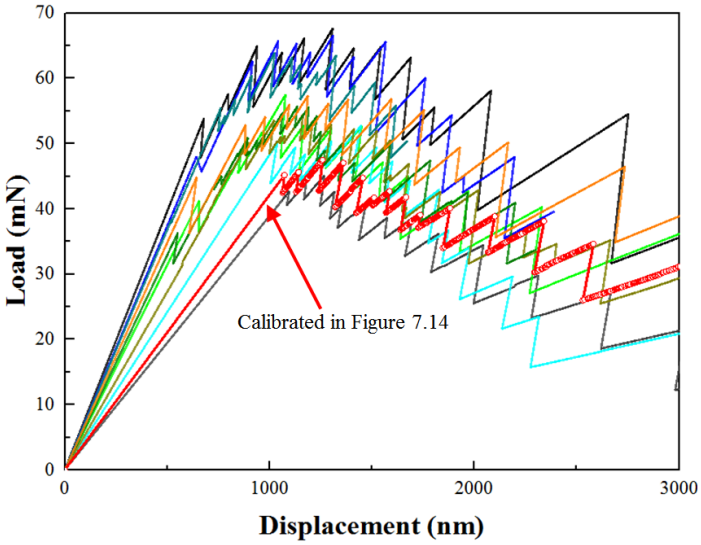

(a)

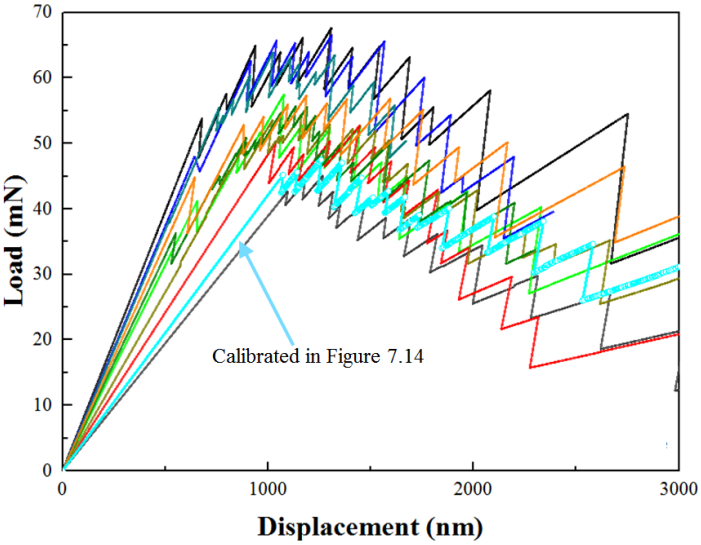

(b)

Figure 7.16: Modelling results of 10 specimens under: (a) fully contacted boundary conditions (b) edge contacted boundary conditions.

7.4.3. PREDICTION OF UNIAXIAL TENSILE STRENGTH OF ITZ

In order to predict the tensile strength and elastic modulus of the ITZ, microstructure of the pure ITZ as generated in Section 7.3.3 was used. A computational uniaxial tension test was conducted using the two sets calibrated input mechanical parameters. The boundary configuration is shown in Figure 7.17 that one end of the material is clamped, and the nodal displacement is applied on the other. The same crack pattern are obtained for the two sets input parameters (see Figure 7.18, all the interface elements are broken), as the interface elements are the weakest elements in the system. The simulated stress-strain curves are compared in Figure 7.19. As expected, stress-strain curves having similar shapes are observed for the two data sets. When implementing the calibrated results from case 2, higher stress and stiffness are obtained at the same strain level because they are proportional to the strength and strength/modulus ratio of the interface elements, respectively. As the two data sets were fitted from two extreme boundary conditions, the real response of the tested ITZ specimen under uniaxial tension probably lies in between these two curves. Additionally, it is clear that the stress-strain curves have two stress peaks, while the first peak is higher than the second. These two peaks could form because of the two main cracks [2] as shown in Figure 7.20 where the crack pattern at first, second peaks and the final stages are plotted together with the interface elements. Before crack happens (see Figure 7.20a), a large number of defects already exist in the interface layer due to the high effective w/c ratio and the weak bound between anhydrous cement particles and aggregate. At the first peak (Figure 7.20b), it seems like a crack starts localizing at the left side, while at the second peak (Figure 7.20c), another crack going through the middle is observed. In the end, all the interface elements are broken, the specimen fails entirely, see Figure 7.20d.

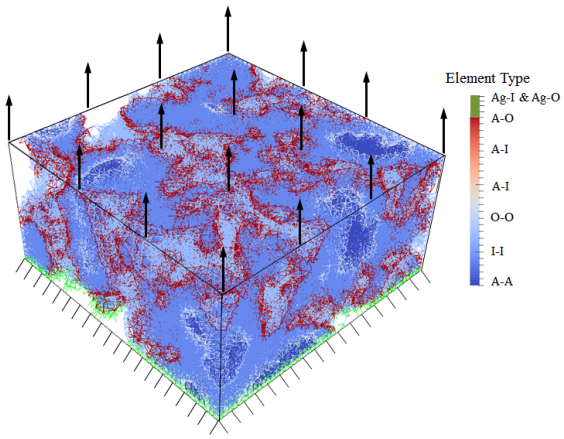

Figure 7.17: Boundary configuration of the uniaxial test of ITZ.

In order to show the variations of the mechanical properties of ITZ, 10 specimens were tested using both data sets. Their stress-strain curves are plotted in Figure 7.21. All the stress-strain curves have two stress peaks because of the aforementioned reasons. Furthermore, the peaks of different specimens align almost at the same strain level when

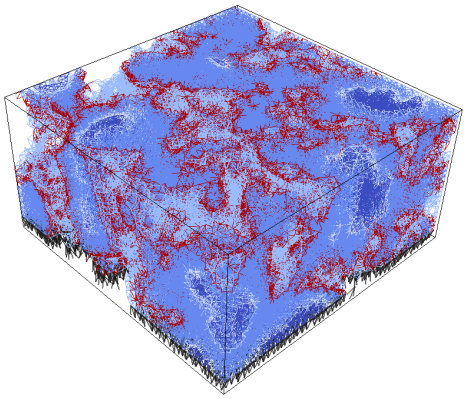

Figure 7.18: Deformed ITZ specimen at the final stage (black-crack element).

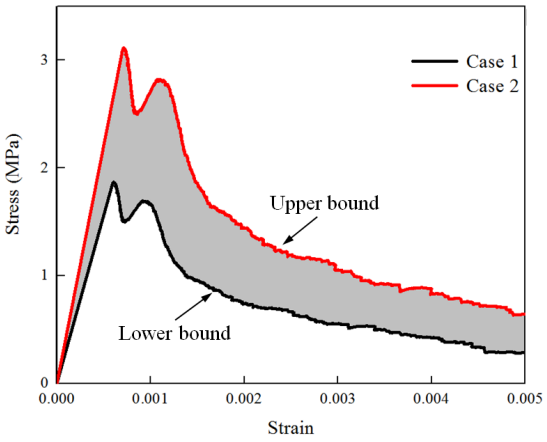

Figure 7.19: Comparison between the simulated stress-strain curves of the ITZ specimens under uniaxial tension.

the same set mechanical properties of local elements are used. In terms of case 1, the first peak aligns around 0.0005, while the second aligns at around 0.001. At the strain level of 0.005, the stress almost reaches 0. Therefore, it is regarded as the final failure stage.

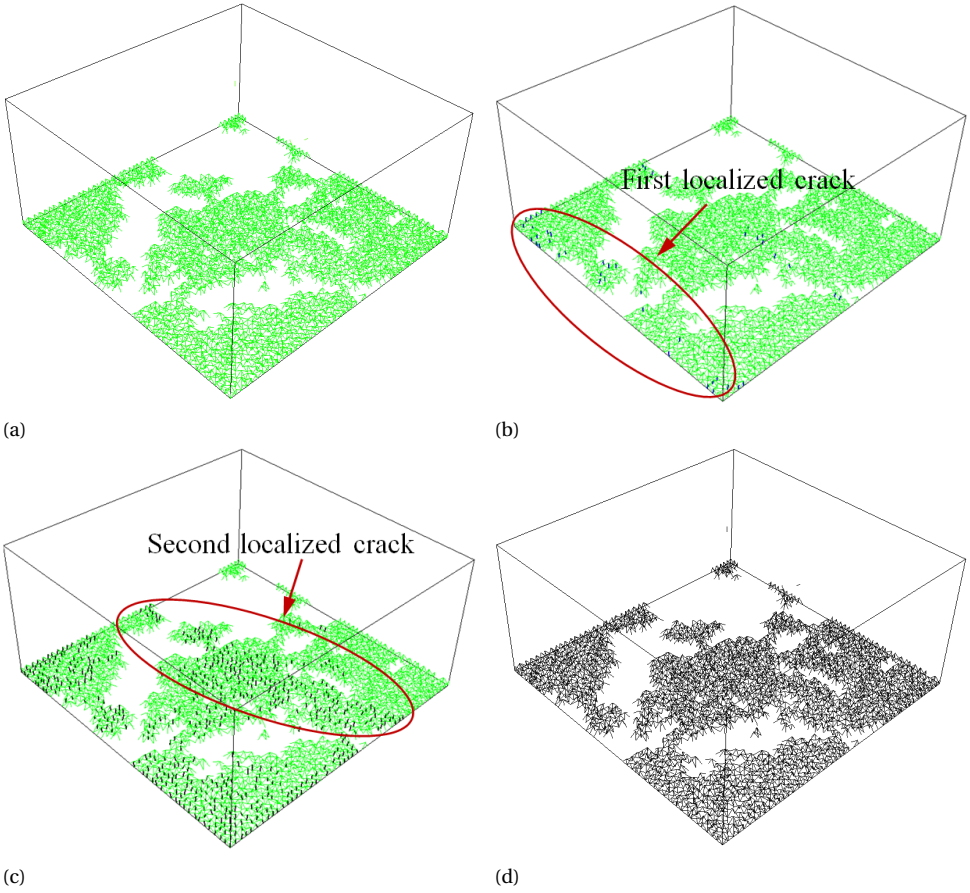

Figure 7.20: Crack pattern of type II specimens together with interface elements at different failure stage: (a) before loading; (b) first peak; (b) second peak; (c) final stage (black-crack, green-interface element).

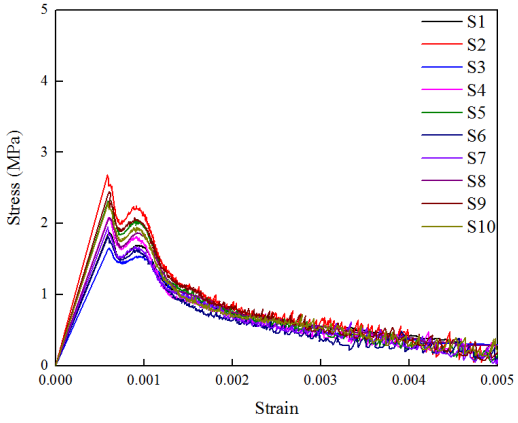

(a)

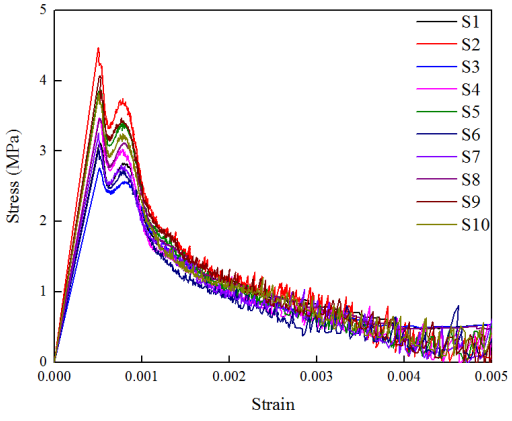

(b)

Figure 7.21: Variations of simulated load-displacement responses due to the material structure heterogeneity: (a) case 1; (b) case 2.

On the basis of the stress-strain curve, the strength, elastic modulus and fracture energy are derived and listed in Table 7.4 and 7.5. Note that the fracture energy G_f is calculated from the post-peak part of the stress-strain curve using Equation 5.1.As expected, these values are much lower compared with the bulk cement paste at the same length scale (strength: 25.78 MPa; elastic modulus 27.73 GPa; fracture energy: 9.94 J/m^2, see Chapter 5). When looking at the literature, the reported HCP-aggregate bonding strength varies a lot, even for the specified aggregate and w/c ratio of ordinary cement paste. For example, it is measured as 0.78 MPa by Zimbelmann [245] but reported by Ping and Beaudoin [267] as high as 4 MPa for the bonding strength between cement paste with 0.3 w/c ratio and "flat" quartzite surface at 28 days. This is partly because the bonding strength is significantly influenced by the geological properties of the aggregate, especially the surface roughness which is mainly determined by the pre-treatment process [268] and partly due to the specimen preparation method which has a considerable influence on internal stress in the boundary. Furthermore, it should be noted that a size effect occurs on the strength of cementitious material [261]. The most comparable experimental test that can be found in the literature is made by Jebli et al. [243] in which a uniaxial tension test has been conducted on a "sandwich" aggregate-cement-aggregate sample with a square cross-section of 10 mm, giving an estimation of the bonding strength as 1.6 MPa and an elastic modulus of 4.3 GPa for the composite. As the aggregate they used is limestone, lower bonding strength is expected for the quartz aggregate-cement at meso-scale [268]. The modulus reported in [243] is a homogenised value with the aggregate and bulk cement paste, thus it is higher than the results for the pure ITZ as reported in the current study. It is reported in [236] that the Young's modulus of cement paste at distance of 20 µm away from the aggregate is around 2.2 MPa after 3 days hydration, which tends to confirm the simulated Young's modulus falls in the reasonable range.

Table 7.4: Mechanical properties of the pure ITZ derived from the simulated stress-strain curves of case 1.

No.	Young's modulus(Gpa)	Tensile strength (MPa)	Fracture energy (J/m^2)
1	3.12	1.87	0.16
2	4.57	2.68	0.18
3	2.76	1.65	0.15
4	3.49	2.08	0.14
5	3.91	2.32	0.15
6	3.07	1.82	0.13
7	3.29	1.95	0.14
8	3.46	2.08	0.16
9	4.07	2.44	0.17
10	3.86	2.29	0.16
Average	3.560±0.515	2.118±0.298	0.154±0.014

Table 7.5: Mechanical properties of the pure ITZ derived from the simulated stress-strain curves of case 2.

No.	Young's modulus (GPa)	Tensile strength (MPa)	Fracture energy (J/m^2)
1	4.42	3.12	0.29
2	6.47	4.47	0.33
3	3.91	2.75	0.26
4	4.94	3.47	0.26
5	5.54	3.87	0.29
6	4.35	3.03	0.24
7	4.66	3.25	0.26
8	4.9	3.47	0.3
9	5.77	4.07	0.31
10	5.47	3.82	0.29
Average	5.040±0.730	3.530±0.498	0.283±0.026

7.5. CONCLUSIONS

This chapter proposes an approach for fracture testing and modelling of the ITZ at the micro-scale. The micro-scale sized HCP-aggregate cantilever beams were fabricated and tested both experimentally and numerically. The experimentally measured load-displacement responses were used as benchmark for the calibration of the numerical model. After the calibration, the model can reproduce the experimental observations well including the variation and explain the experiments in detail. The calibrated model was further used to predict the fracture properties of the ITZ under uniaxial tension. The following conclusions can be drawn:

- The model shows that the bonding between HCP and aggregate is weak and a high porosity exists at the interface layer. Therefore, the micromechanical properties of the ITZ are much lower compared with the HCP at the same length scale. On the other hand, they are higher than the properties measured at the meso-scale due to the size effect.

- The XCT scanning technique is able to capture porosity gradients of cement paste along the distance away from aggregate, which can be further used to distinguish the ITZ and bulk HCP from the matrix.

- In the end, this work contributes to the multi-scale modelling of the concrete. The interface properties between cement paste and aggregate in the meso-scale model can be determined on the basis of the results presented in the current work.

More comprehensive work can be conducted on the basis of the proposed approaches to investigate the influence of different factors on the micromechanical properties of the ITZ. Through a multi-scale modelling framework, these influences can be explicitly visualized at meso-scale.

III

Experimentally Validated Multi-scale Modelling Scheme

8

MULTI-SCALE MODELLING SCHEME OF DEFORMATION AND FRACTURE OF HARDENED CEMENT PASTE

This chapter presents a validation procedure of multi-scale modelling scheme by making, testing and modelling deformation and fracture of hardened cement paste (HCP) beam at sub-meso-scale (between micro- and meso-scale). Miniaturized three-point bending testing concepts were adopted. HCP beams with a cross-section of 500 µm × 500 µm were fabricated using the micro dicing saw and subjected to bending using nanoindenter. Simultaneously, fracture behaviour of the same size specimens was predicted by the microstructure informed multi-scale lattice fracture model in which input microstructures were obtained by X-ray computed tomography at two length scales (micro and sub-meso). Uncoupled volume averaging upscaling approach was used to relate the material's mechanical behaviour at sub-meso-scale with the microstructures at lower scale. A good agreement between experimental and numerical results was observed which shows that starting from micro-scale and with relatively simple mechanical considerations it is possible to correctly reproduce behaviour at upper scale.

Parts of this chapter have been published in Cement and Concrete Research **102**,(2017) [269].

8.1. INTRODUCTION

Under the hierarchical modelling scheme, a so-called uncoupled volume averaging upscaling method is commonly applied to bridge any two scales[3–6, 106, 135]. In this upscaling method, the simulated global mechanical performance of composites at lower scale are directly assigned as the local mechanical properties of the matrix in the upper scale models. This method is often criticized because of its simple mechanical considerations. Furthermore, it is not easy to be verified by experiments at scale where aggregates exit, because not only the matrix is regarded as a homogenous material but also the ITZ is introduced in the system, which is indeed another complex issue [227, 270]. Therefore, the main aim of this work is to verify the upscaling method through a relatively simple scheme. The verification scale is chosen in between micro-scale and meso-scale in which the cement paste matrix and air voids or big capillary pores are recognised. As the investigated length scale is much smaller than the typical laboratory sample size, the experimental challenges include producing and mechanical testing of such miniaturized samples.

As a high precision instrument that can record small load and displacement with high accuracy and precision, nanoindenter is becoming a general tool in small scale mechanical testing. Utilizing this technique for micromechanics provides a basis for the development of various miniaturized testing concepts, e.g. micro-beam bending test [45, 271], pillar compression test [154, 272]and pillar indentation splitting test [273]. Based on the recorded load and displacement data during the test, the basic deformation mechanisms and behaviour of small mechanical samples can be used to derive elastic, plastic and fracture material properties. Applications of micro dicing saw on preparation of small HCP specimens make it possible to prepare the small scale specimens such as cube and beam. In this chapter, miniaturized three-point bending testing concepts were adopted. HCP beams with a cross-section of 500 µm × 500 µm were fabricated using the micro dicing saw and subjected to bending using nanoindenter.

In parallel with the experiments, a multi-scale, lattice-based model is introduced here to simulate the deformation and fracture performance of these sub-meso-scale specimens under three-point bending. To consider the heterogeneous and multi-phase microstructure in the simulation, it is essential to have a well-characterised 3D material structure. Therefore, 3D X-ray computed tomography (XCT) has been adopted in the current study to characterize the microstructures of this material at two scales. The uncoupled upscaling method is then used in this paper to relate the material's mechanical behaviour at sub-meso-scale with the microstructures at lower scale. After validation, influence of porosity on the mechanical performance is studied based on the predicted results.

8.2. EXPERIMENTAL

8.2.1. MICRO-BEAM THREE-POINT BENDING

28 days cured HCPs (OPC CEM I 42.5 N) with w/c ratio of 0.3,0.4 and 0.5 were investigate in this study. Micro-beams with a square cross-section of 500 µm (see Figure 8.1) were fabricated using the approach developed in Chapter 3. Figure 8.2a schematically shows the setup of miniaturized three-point bending test. The test was instrumented by KLA-

Tencor G200 nanoindenter system equipped with a diamond cylindrical wedge indenter tip (radius 9.6 µm, length 700 µm, see Figure 8.2b). The micro-beams were placed in flutes of a 3D printed support with a span length of 12 mm (Figure 8.2c). A line load was then applied at the centre of the span by the indenter. To observe the fracture process during loading, an external camera was added. A video recording the fracture process is available online[1].

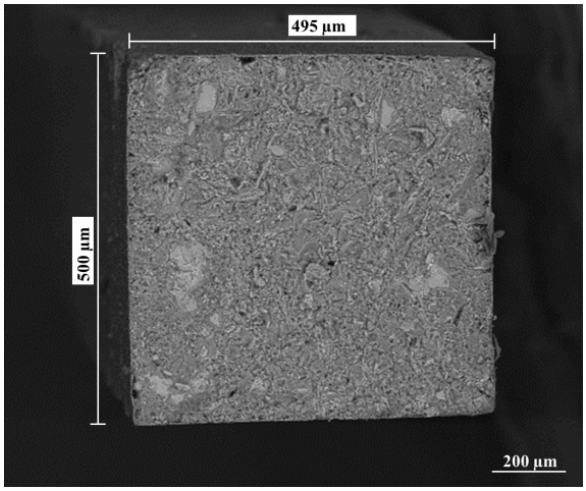

Figure 8.1: ESEM image of cross-section of micro-beam with dimensions.

The experiments were run using displacement control with a loading rate of 500 nm/s. Figure 8.3 shows the typical recorded load-displacement diagram in which the maximum reached force $F_{\max}$ was used for the flexural strength calculation using elastic beam theory [274]:

$$f_t = \frac{3F_{\max}L}{2d^3} \tag{8.1}$$

where L is the length of span and d is the cross-sectional dimension of the square. In the evaluation of Young's modulus of the HCP beams, data of recorded load displacements in the range between 50 % and 80 % of maximum load were used. The plots in this range are linear to the point of fracture. Young's modulus E is evaluated as:

$$E = \frac{L^3}{4d^4}S \tag{8.2}$$

where S is the average slope in the range between 50 % and 80 % of maximum load. Since the deflection of the beam cannot be measured directly in the current setup, the recorded vertical displacement of the indenter is used as an estimate, which may lead to a somewhat lower value of modulus since the local imprinting of the indenter into the beams is recorded as well.

[1] https://www.sciencedirect.com/science/article/pii/S0008884617308256

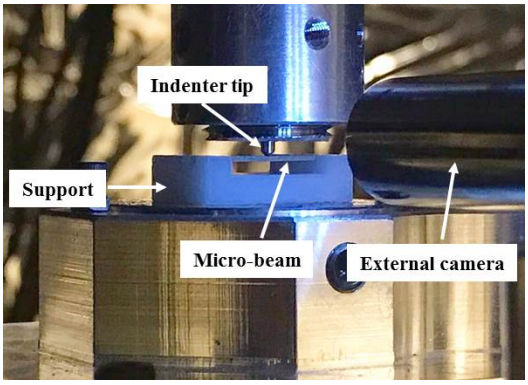

(a)

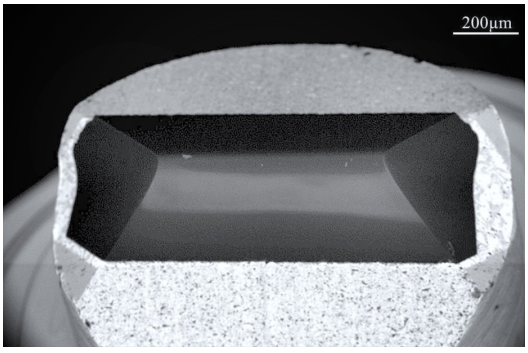

(b)

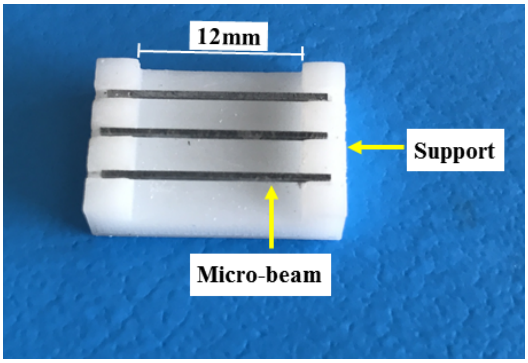

(c)

Figure 8.2: (a) Platform of miniaturized three point bending test. (b) diamond cylindrical wedge indenter tip (c) Miniaturized beam specimens on the support.

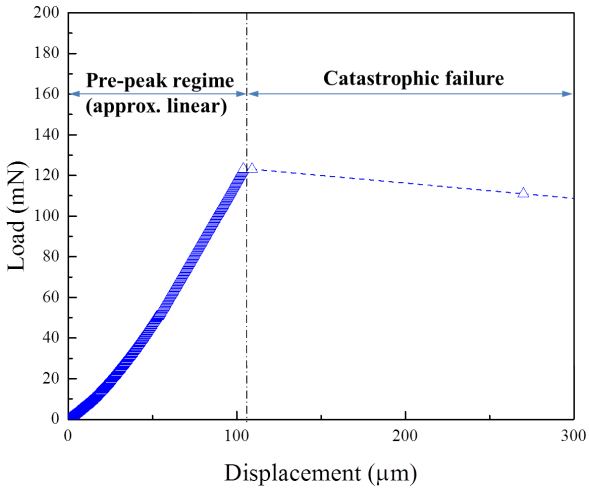

Figure 8.3: A typical load vs. displacement curve measured in the miniaturized three-point bending test.

8.2.2. FRACTURE PATTERN VISUALIZATION

After testing, one failure micro-beam with w/c ratio 0.4 on the support was bonded by dropping a tiny drop of transparent instant adhesive on the loading point. The micro-beam was then taken out of the support and clamped by the holder as shown in Figure 3.6a. The holder was then fixed on the rotatable stage in the Phoenix Nanotom micro-computed tomography system to visualize the fracture path in the cracked specimen. The setup for acquiring greyscale level based images and approach for image segmentation as described in Chapter 3 were used. Three 2D slices of the segmented microstructure are shown in Figure 8.4. Clearly, the main crack follows a tortuous path across the tensile surface, similar to the observations in [184, 275, 276]. In addition, it tends to propagate around the anhydrous cement phase. A possible explanation for this observation could be that, with the highest strength and elastic modulus, anhydrous cement particles work as local stiff inclusions in the matrix, deflecting the crack. Similar observations are reported in concrete, due to the influence of aggregates [187, 188].

8.3. METHOD VALIDATION

For validation of the tested method, a commercial objective glass, which is expected to be a homogenous and isotropic material, with a thickness of 1.6 mm was used. Five micro-beams with the same size as HCP (0.5 mm × 0.5 mm × 12 mm) were fabricated using the same procedure described in Chapter 3 and tested under three-point bending. The recorded load displacement diagrams are presented in Figure 8.5 and show a high degree of repeatability. The modulus and flexural strength were calculated and listed in Table 8.1.

Nanoindentation technique was conducted for modulus characterisation as the reference for the validation of the measured flexural modulus. This technique determines local mechanical properties of tested material from the indentation load displacement

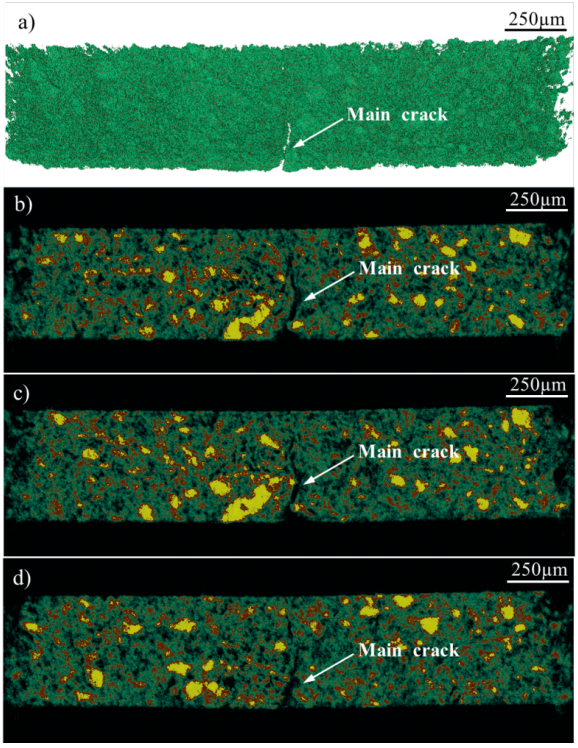

Figure 8.4: X-ray computed tomography of cracked beam with a main crack in the middle. (a) 3 D image. (b) (c) (d) 2D slices of cutaway view (green represents outer hydration products, red is the inner hydration products and yellow is the anhydrous cement particle).

curve. The analysis was performed with the same nanoindenter system equipped with a Berkovich tip (three-side pyramidal tip). A grid containing 5 × 5 indents with 100 μm separation between neighbouring indents was performed using Continuous Stiffness Method (CSM) proposed by Oliver and Pharr [81]. The indents were displacement controlled with a 0.05/s strain rate targeting the maximum depth of 1000 nm. The average E modulus was determined in the loading range between 800 - 1000 nm. For the calculation, Poisson's ratio of the indented material was taken as 0.25 (a common value of glass material) [277]. A mean value of indentation modulus 72.15 GPa with a standard deviation 2.34 GPa was obtained.

In terms of modulus, although the three-point bending measured values are somewhat lower than the indentation measurements, a reasonable agreement is found. The reason for the lower values of three-point bending measurements could be that the recorded displacement is not the actual deformation of the micro-beam, but of the loading indenter, and it therefore includes the local imprinting of the indenter into the beams. Good agreement between the methods shows that correct assumptions are used in this technique.

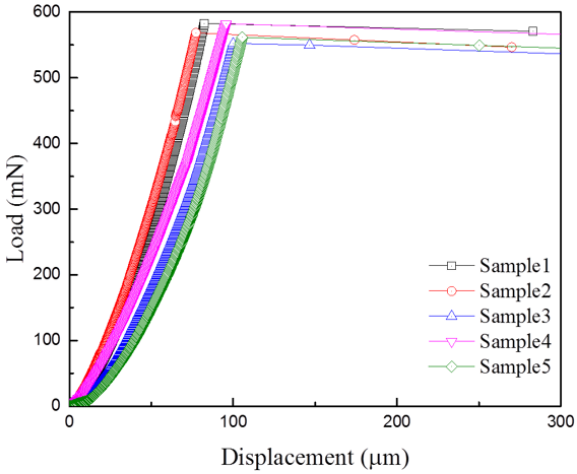

Figure 8.5: Load vs. displacement curves measured in the three-point bending test of miniaturized glass beams.

Table 8.1: Elastic properties, tensile strengths of miniaturized glass beams from three-point bending tests.

No.	Young's modulus (GPa)	Flexural strength (MPa)
1	69.30	83.91
2	66.86	81.85
3	58.32	79.52
4	58.08	83.87
5	62.25	80.90
Mean value ± standard deviation	62.96±5.03	82.00±1.91

8.4. MODELLING

To include the influence of microstructures at micro-scale, a multi-scale modelling approach combined with the experimental characterized microstructures is adopted, as illustrated in Figure 8.6. At the micro-scale, HCP specimens are in the shape of a cube, and the size length is 50 μm with mesh size 2 μm at meso-scale. At sub-meso-scale, the microstructures match the size of the test specimens (0.5 mm × 0.5 mm × 12 mm) with a resolution of 50 μm × 50 μm × 50 μm. Hence, the length 50 μm is the point which connects the meso-scale model to the sub-meso-scale model. An uncoupled volume averaging multi-scale modelling approach is adopted in which the simulated output properties of HCP from meso-scale modelling are used as the input properties for the sub-meso-scale modelling.

8.4.1. MICROSTRUCTURE

At micro-scale, 3D segmented digital microstructures of HCP were taken from Chapter 3. As presented in Figure 8.6, 4 phases are distinguished in the small cube: anhydrous cement, outer hydration products, inner hydration products and capillary pores. Owing to the current image resolution (2 μm/voxel), capillary pores smaller 2 μm and gel pores are not detectable and are not included in the segmented pores. Although it is reported that these pores have significant influence on the mechanical properties, especially at

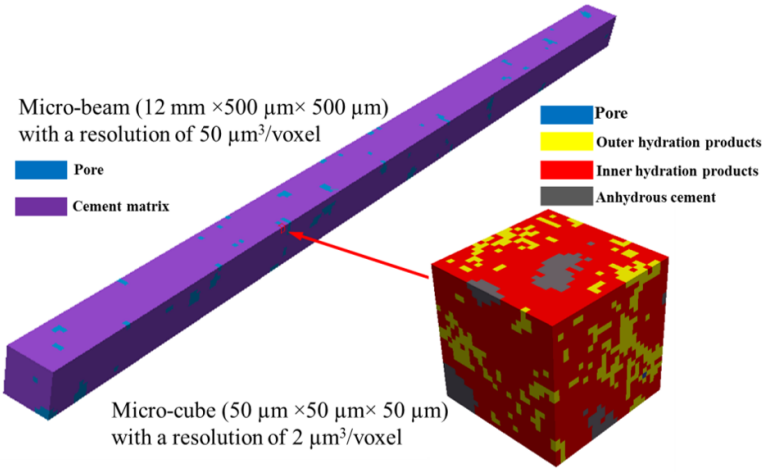

Figure 8.6: Schematic illustration of multi-scale modelling strategy.

early age [15, 164], again, the main aim of this research is verifying the upscaling method through a relatively simple scheme and therefore influence of microstructure at lower scale (smaller than the current resolution) is not taken into account. Considering the heterogeneous nature of this material, for each w/c ratio, 160 small cubes were randomly extracted from the segmented microstructures and used as input for the fracture model to provide a range of local mechanical behaviour at upper scale.

At sub-meso-scale, material structure was considered to consist of two phases: solid phase (cement paste matrix) and pores (large capillary pores and air voids), see Figure 8.6. The procedure for generating the binary microstructure of micro-beam is schematically shown in Figure 8.7. A cylindrical HCP specimen (diameter: 24 mm; height: 39 mm) was first scanned by the CT scanner to form a digitalized microstructure with a spatial resolution of 50 μm/voxel. The greyscale value at the first inflection point in its cumulative fraction curve was regarded as the threshold to convert the original grey images to binary imagines. The microstructure of full size micro-beam was then randomly extracted from the segmented CT images. For each w/c ratio, eight digital microstructures were investigated.

8.4.2. THREE-POINT BENDING MEASUREMENTS

A lattice type model, as described in Chapter 3, was used for the deformation and fracture analysis. In the lattice model, the material is discretised as a set of beam elements. In this Chpater, a regular cubical grid of beam elements with equal lengths was used for the sub-meso-scale specimens, while a random triangular mesh (same as the mesh used in Part II) was created for the micro-scale simulation.

At micro-scale, a computational tensile test is performed on each of the small cubes (Figure 8.8a). For these simulations, every beam element is assigned locally brittle behaviour on the basis of the extracted microstructure in which tensile strength and elas-

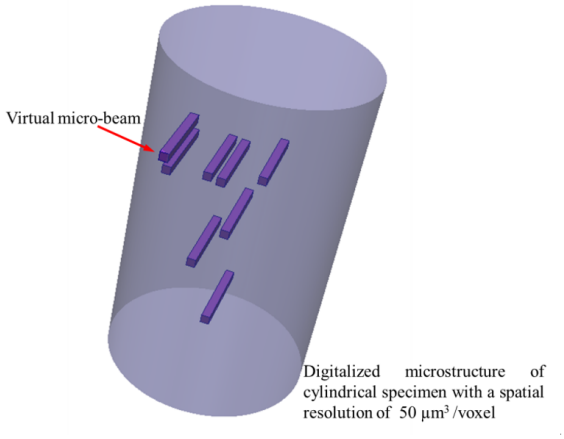

Figure 8.7: Schematic illustration on extraction of virtual micro-beam from cylindrical specimen.

tic modulus are required. The outcome of the simulation is load–displacement curve. These curves are then schematised as multi-linear curves, which are the input for elements in the upper scale system (see Figure 8.8b, the points are taken at: (1) origin; (2) peak load; (3) first point in response for which load is <75 % of the peak; (4) first point in response for which the load is <50 % of the peak; (5) first point in response for which the load is <25 % of the peak; (6) point after which the specimen is considered to be broken and the simulation is stopped with a displacement of 0.25 μm).

The tensile strengths and elastic moduli of local phases are taken from Table 3.5, which have been calibrated and validated in Part II. It needs to be emphasized that the assigned local mechanical properties are influenced by the discretization of digitalized microstructure: a lower resolution results in a coarser mesh, and lower local mechanical properties should be adopted since more larger pores and defects are homogenized in the domain represented by the element or voxel. Furthermore, it is reported a smaller element size results in smaller crack widths and a somewhat more brittle response when this type of model is used [138]. This is attributed to the fact that, in a lattice-type model, the cracked area localizes into the narrowest band permitted by the lattice discretization (which is, dependent on the structure of the lattice mesh, often one element wide) [278]. More complex approaches are available in the literature (e.g. the approach of Grassl and Jirásek [279]), in which an isotropic damage constitutive model is used (instead of the linear elastic-brittle, as used herein), and the resulting crack openings are independent of the length of the element. However, in these approaches, the simplicity of lattice models (i.e. simple constitutive laws and a small number of input parameters) is lost. Discretization also has effect on the fracture criterion (Equation 3.2). A coarser mesh makes the bending moment in beam elements higher compared to the normal force, and therefore has a higher contribution in the fracture criterion causing smaller beams to break faster. However, this effect is minimized by the selected value of α_m (0.05).

At sub-meso-scale, the larger beam specimen is subjected to a computational three-point bending test (Figure 8.8c). The local element behaviour was randomly assigned

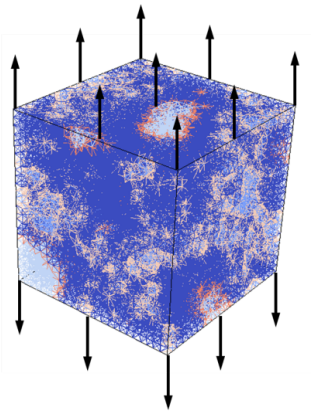

(a)

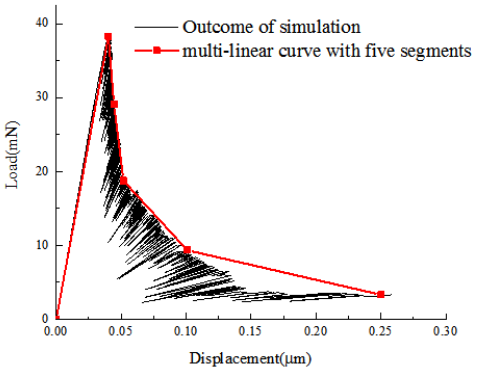

(b)

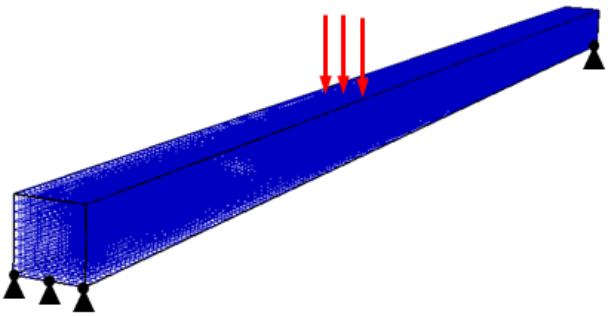

(c)

Figure 8.8: Multi-scale modelling concept: (a) a small cube under computational uniaxial tensile test; (b) simulated load displacement curve of a small cube (the red curve is a schematisation with 5 segmentations of the black); (c) boundary condition of full-size specimens under computational three-point bending.

from the lower scale simulations, which was indeed a multi-linear constitutive law (Figure 8.8b). As a consequence, the beam elements were not completely removed at each loading step, but if an element reached a maximum stress its stiffness and strength, it would change according to the specific constitutive relation. This means that the element would then adopt the properties of the next point in the local multi-linear load-displacement curve, as shown in Figure 8.8c.

8.5. RESULTS AND DISCUSSION

8.5.1. THREE-POINT BENDING MEASUREMENTS

The load response versus the vertical displacement of indenter diagrams for all HCP specimens are depicted in Figure 8.9. Based on measurements, the flexural strengths and elastic moduli are calculated and summarized in Table 8.2. Mean flexural tensile strength as well as the Young's modulus, as expected, decrease as the w/c ratio increases. The results for tensile strength are in the range between the measured tensile strength at micro-scale (mean values of 21.28 MPa, 18.72 MPa and 16.54 MPa for HCP prepared with w/c ratio 0.3, 0.4 and 0.5 respectively in Chapter 4 and meso-scale, typically lower than 10 MPa [185, 280]). This is in accordance with the size effect of quasi-brittle materials in which theoretical strength increases as the sample size or scale decreases [281].

Table 8.2: Elastic properties, tensile strengths of HCP from three-point bending tests.

W/c ratio	Young's modulus (GPa)	Flexural strength (MPa)
0.3	16.68±1.92	20.28±2.63
0.4	12.79±2.13	15.31±2.93
0.5	9.09±1.56	11.71±2.22

8.5.2. MODELLING RESULTS AND COMPARISON WITH EXPERIMENTS

RESULTS AT MICRO-SCALE

As stated, at micro-scale, 160 virtual small cubes with a size of 50 µm × 50 µm × 50 µm were extracted from microstructures for each w/c ratio (0.3, 0.4 and 0.5) at 28 days curing age. Each small cube consists of 25 × 25 × 25 voxels, with a voxel size of 2 µm. These small cubes were then subjected to computational uniaxial tensile test to simulate the load displacement curve from where the uniaxial tensile strength and Young's modulus can be derived. Distributions of strengths and Young's moduli of all microstructures are shown in Figure 8.10. The histogram of simulated results of modulus are less variable compared with the strength. The results are summarized in Table 8.3. The average elastic moduli are quite close to those predicted by other micromechanical models [15, 76]. Clearly, with increasing w/c ratio, a shift towards lower values is observed in the histograms of strengths and modulus. However, it should be noted that paste specimens with lower w/c ratios are stronger on average but there remains a chance to yield a weaker mechanical performance compared with specimens with higher w/c ratios. As the fracture is mostly governed by the weakest spot, i.e. pores, in the material, the probability of fracture was analysed using Weibull statistics (Equation 4.3).

The tensile strengths are plotted in a Weibull coordinate system (Figure 8.11). The least squares method was adopted to fit the Weibull modulus and the scaling parame-

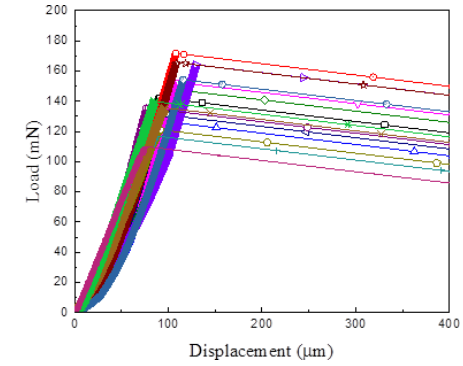

(a)

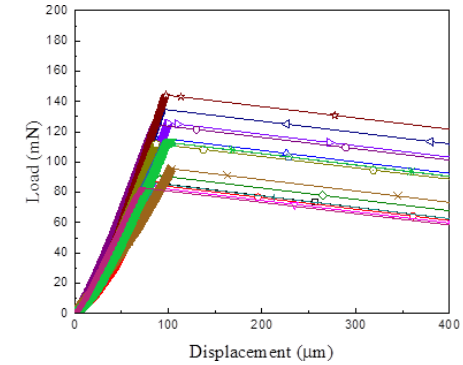

(b)

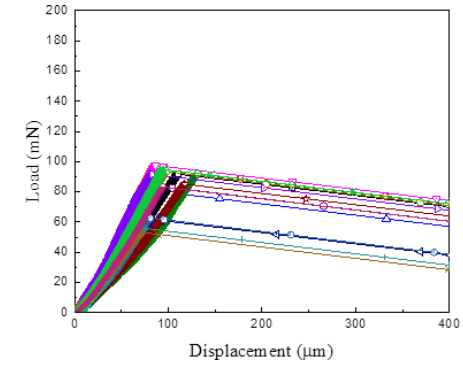

(c)

Figure 8.9: Experimental measured load-displacement curves of three-point bending test of HCP with w/c ratio: (a) 0.3, (b) 0.4, (c) 0.5.

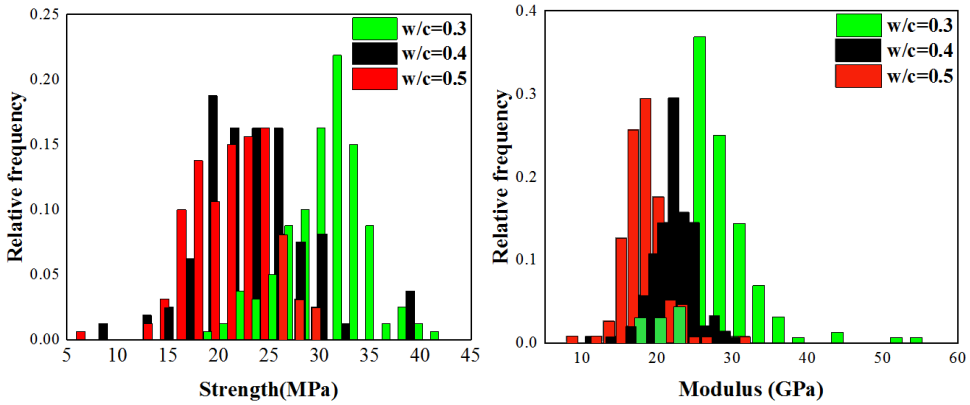

(a) (b)

Figure 8.10: Simulation results of small cubes at micro-scale under uniaxial tension: (a) distribution of uniaxial strength of small cubes; (b) distribution of Young's modulus of small cubes.

Table 8.3: Summary of the modelling results at micro-scale(Experimental measured splitting strengths from Chapter 4 are presented as a comparison).

W/c ratio	Porosity (%)	Young's modulus (GPa)	Tensile strength (MPa)	Splitting strength (MPa)
0.3	2.36±3.56	26.85±5.77	29.41±4.87	21.28±4.29
0.4	6.07±7.32	22.20±2.78	23.96±5.47	18.72±3.85
0.5	8.26±8.07	18.36±2.76	21.05±39.05	16.54±3.71

ter. The fitted results are given in Table 8.4. A coefficient of determination (R^2) higher than 0.9 is observed for all w/c ratios. Both the Weibull modulus and the scaling parameter decreases with the increase of w/c ratio, which indicates that pore structures are clustered more inconsistently in paste specimens with higher w/c ratios. A similar trend is observed experimentally in a micro-cube splitting test at the same scale (Chapter 4). In addition, although the obtained mechanical properties are of the same order of magnitude as the experimental results, the predicted tensile strengths are almost 30 % higher than the experimental measured values due to the fact that the experimental investigated cube specimens have a size of 100 µm (two times larger than cubes in current studies). Therefore, it is of great importance to perform validation of fracture models of heterogeneous materials on the same length scale, since size effect plays a considerable role in their mechanical performance.

Table 8.4: Weibull parameters for the simulated uniaxial tensile strength of small cubes.

W/c ratio	Weibull modulus, m	Scaling parameter, σ_0 (MPa)	R^2
0.3	8.81	43.36	0.986
0.4	5.03	25.03	0.946
0.5	5.00	22.66	0.904

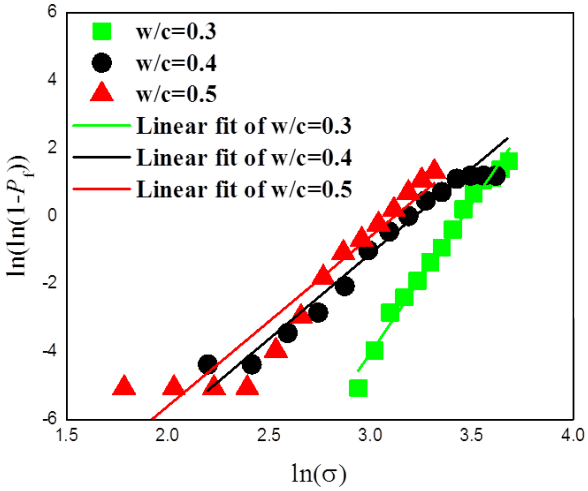

Figure 8.11: Weibull plot for uniaxial tensile strength of small cubes with different w/c ratios.

RESULTS AT SUB-MESO-SCALE

Outputs of small-scale simulations were simplified as multi-linear load-displacement curves and used as input for full-scale simulations as shown in Figure 8.8. Three-point bending modelling was performed on 8 beam specimens for each w/c ratio. Load vs. displacement diagrams for all simulations are shown in Figure 8.12. Similar to the experimental observation, mostly linear response till breaking point is found in the simulated curves. Furthermore, post-peak behaviour is observed in simulations, which could not be experimentally measured in current study due to the limitation of the equipment. On the basis of these diagrams, the strength and modulus were calculated and listed in Table 8.5. Figure 8.13 presents a deformed mesh resulting from a full-scale simulation at the final stage. In accordance with experimental observation, a tortuous main crack and localized small cracks are observed due to the distributed mechanical properties of local elements and existed initial flaws (pore).

In Figure 8.14, comparisons on flexural strength and modulus between simulated results and experimental values are given. A same trend is observed as experiments: flexural strength and modulus decrease with the increasing w/c ratio. On one hand, the simulated strengths are within the experimental scatters, which shows a good agreement between simulation and experiments. On the other hand, the simulated modulus is higher than the measured values, but still in a reasonable range. As explained previously, lower values obtained through experiments are due to the local imprinting of indenter into the

Table 8.5: Summary of three-point bending modelling results of full-size beam.

W/c ratio	Porosity (%)	Young's modulus (GPa)	Flexural strength (MPa)
0.3	2.36±3.56	19.76	21.89
0.4	6.07±7.32	16.00	16.69
0.5	8.26±8.07	11.98	12.97

specimens. The advantages of numerical simulations include that the full details of the used material microstructure are known. Therefore, more detailed investigation can be further explored such as the relationship between porosity and predicted mechanical properties.

The simulated flexural tensile strength and modulus of all beam specimens are plotted with their corresponding porosities in Figure 8.15. In Figure 8.15a and 8.15b, only pores which can be visualised under current resolution of 50 µm/voxel are considered. Although a clear decrease with increasing porosity is observed for specimens with the same w/c ratio, the values of strength and modulus are commonly lower for the specimens with higher w/c ratios. This is because the weaker and variable mechanical behaviour of local elements obtained from micro-scale. The mean porosity at the lower scale microstructures are then added in Figure 8.15c and 8.15d. As can be seen, the flexural strength decreases exponentially with increasing porosity, while elastic modulus shows a linear decrease. A similar trend is observed experimentally in recent studies on a model gypsum plaster material [182]. Regardless of the w/c ratio, porosity appears to be the main factor determining the strength and modulus properties of HCP. This is in accordance with experimental observations reported in the literature [177, 282].

When comprising with results at micro-scale, decreases in strength and modulus at bigger scale are observed on the specimens with the same w/c ratio, since large pores which act as initial flaws in the lattice system and heterogeneity are introduced in the big scale models. Both the flaws and heterogeneity then cause stress concentrations. Localised cracks are then formed prior to the main crack. The material's global performance therefore becomes weaker. The natural heterogeneity and initial flaws are suggested as the main factors that cause size effect in HCP based on the simulations.

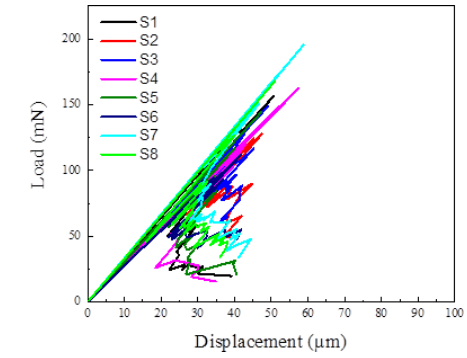

(a)

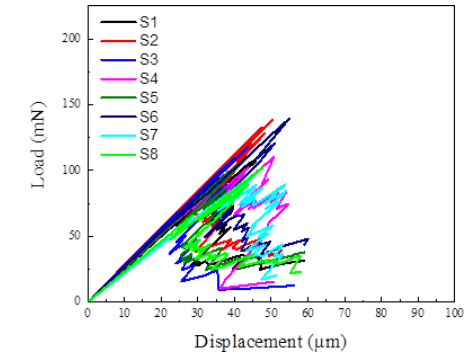

(b)

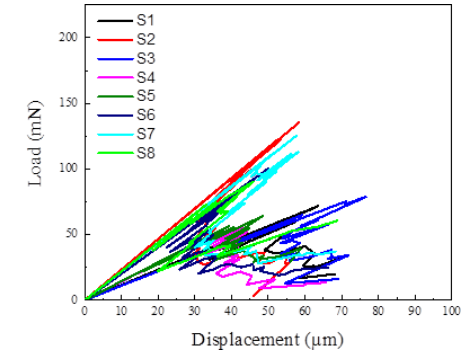

(c)

Figure 8.12: Modelling results of three-point bending test of full-size specimens with different w/c ratios: (a) 0.3, (b) 0.4, (c) 0.5.

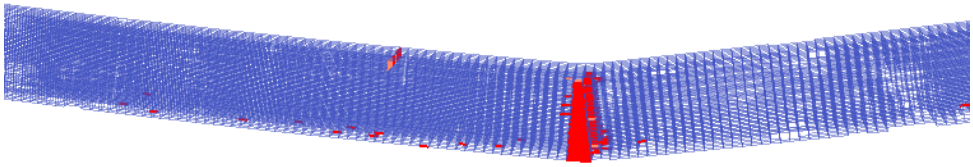

Figure 8.13: Deformed mesh at failure of one lattice modelling (Red colour denotes damaged lattice elements; deformations have been scaled for clarity).

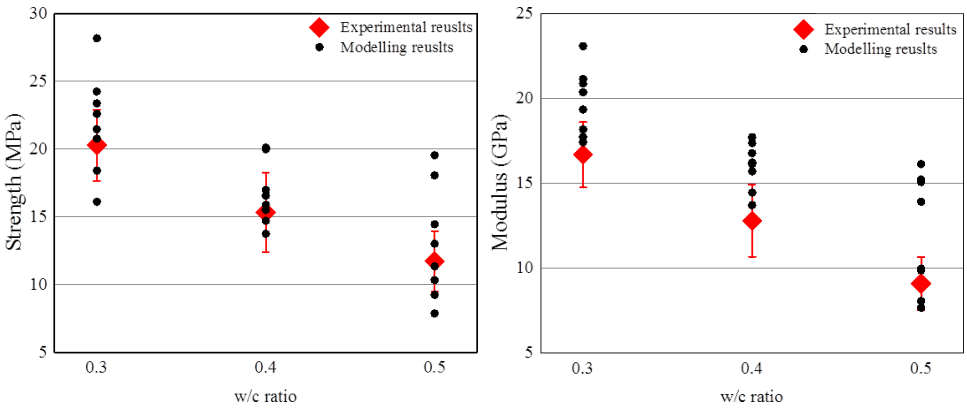

Figure 8.14: Comparison between modelling and experimental results in terms of (a) strength and (b) modulus.

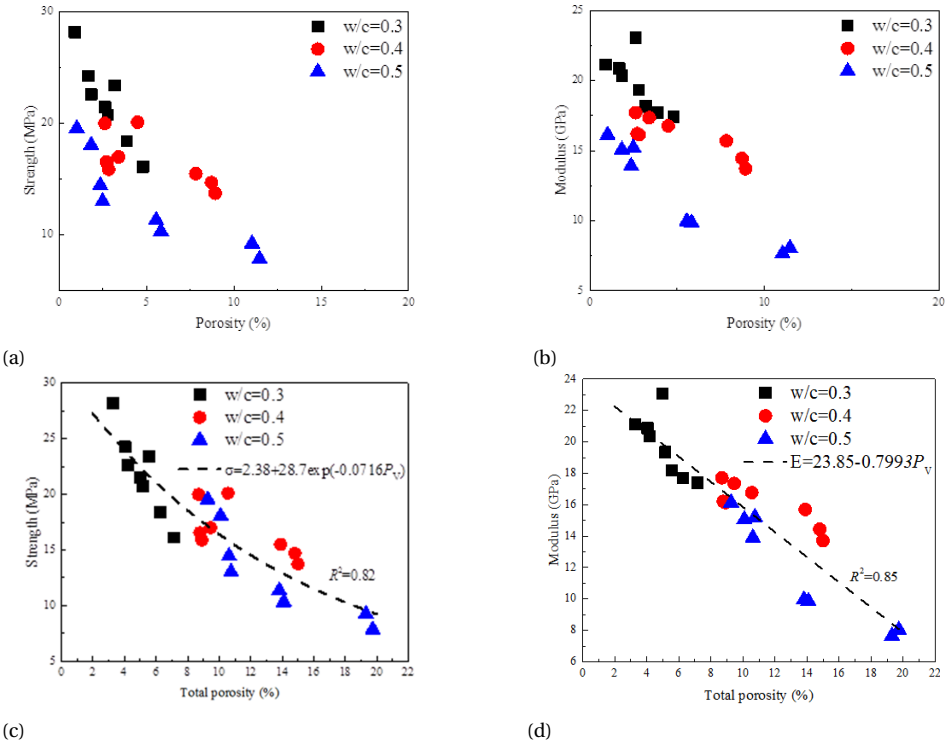

Figure 8.15: Mechanical properties vs. porosity: (a) strength vs. porosity (visualised under resolution of 50 µm/voxel); (b) modulus vs. porosity (visualised under resolution of 50 µm/voxel); (c) strength vs. total porosity including the mean porosity at lower scale; (d) modulus vs. total porosity including the mean porosity at lower scale.

8.6. CONCLUSIONS

In this chapter, a miniaturized three-point bending test combining micro dicing and nanoindenter was developed. The proposed procedures were tested and validated using an isotropic homogenous material (i.e. glass). The measured mechanical properties of HCP are in between of the values at micro- and meso-scale reported in the literature. A multi-scale modelling approach was generated based on the uncoupled volume averaging upscaling method and feature microstructures at two scales to mimic the fracture performance of same size specimens under loading. The good agreements between experimental and numerical results show that starting from micro-scale and with relatively simple mechanical considerations it is possible to correctly reproduce behaviour at upper scale. The following conclusions can be reached from the presented numerical simulations:

- Uncoupled upscaling method is a valid tool to bridge two scales. Making use of the combination of X-ray computed tomography and lattice fracture model, the fracture behaviours of HCP at different scales were successfully predicted. By further extending the proposed modelling approach to the mortar and concrete scale, an experimentally informed multi-scale modelling approach will be created.

- The predicted strengths at micro-scale of HCP were analysed using Weibull statistics. It shows that, with w/c ratio decreasing, the Weibull modulus and scaling parameter increases, which results generally in stronger and less variable mechanical performance of specimens with lower w/c ratio.

- Porosity appears to be the main factor determining the strength and modulus properties of HCP. With the increasing porosity, the strength decreases exponentially while elastic modulus follows a linearly decay.

- Lower strengths were observed at the sub-meso-scale specimens when compared with results at micro-scale. The results suggest that initial flaws (pores) at different level and heterogeneity are the key factors that determine the size effect of cement based material.

9

SIZE EFFECT ON SPLITTING STRENGTH OF HARDENED CEMENT PASTE

In this chapter, cubic specimens in a size range of 1: 400 were produced and tested by a one-sided splitting concept using different testing instruments. The smallest specimen with size of 0.1 mm showed a high nominal splitting strength (18.81 MPa), an order of magnitude higher than the measured strength of 40 mm specimen (1.80 MPa). The test results were used to fit existing analytical size effect models. Although a good fit can be found for the existing size effect models, special attention should be given to the physical meaning behind these empirical parameters. In addition, the multi-scale modelling strategy that considers microstructural features at different length scales was adopted to model the trend of decreasing strength with specimen size observed in experiments. A good agreement between experimental observations and modelling results indicates that the featured material structure dominates the observed size effect on measured strength in the considered size range.

Parts of this chapter have been published in Cement and Concrete Composites **94** (2018) [283].

9.1. INTRODUCTION

ALTHOUGH the fracture properties of hardened cement paste (HCP) have been studied extensively [284–287], a clear understanding of the deformation and fracture behaviour at different length scales is still lacking. This is because the overall material structure of cement paste covers multiple length-scales (ranging from sub-nanometres to metres) [158], and the fracture tests of laboratory sized samples (centimetre range in general) are not capable of investigating the influence of the material structure smaller than a few millimetres. Furthermore, it has been long known that strength and facture behaviour of quasi-brittle materials are size dependent [20]. The measured mechanical properties depend on the sample size and the featured material structures. Therefore, tests need to be performed at different length scales in order to understand the mechanical and fracture behaviour of such materials.

In practice, failure of HCP is caused by the local tension [2]. It is therefore important to investigate the tensile strength at different length scales. For the centimetre sized samples, tensile strength is measured using a variety of test methods: uniaxial tension, Brazilian splitting, 3-point bending and 4-point bending. However, these techniques are difficult to apply at the micro-scale, since the equipment is not suitable for manipulating components with sub-millimetre size [288]. Therefore, more suitable instruments and advanced test procedures need to be used.

In Chapter 4, a so-called one-sided splitting test has been developed and conducted on the micro-cubes (e.g. 100 μm × 100 μm × 100 μm). This technique provides an unprecedented opportunity for experimental investigation of fracture behaviour of HCP with a significantly improved size range, as the most conventional size of HCP specimen is around a few centimetres. In this work, HCP cubes of seven different sizes in a scale range of 1: 400 were produced and tested by this one-sided splitting concept with different test instruments.

During past decades, several analytical size effect models, such as Carpinteri's multifractal scaling law [289–291] and Bažant's size effect law [179, 261, 292], have been proposed to predict the strength decreasing with the structure size increasing. The first approach is based on considerations of the fractal geometry of the microcrack structure at peak stress [289], whereas the second method is established according to an energy balance relation [179]. Both models can give good estimations for the laboratory sized specimens and provide valuable input for the design of concrete structures. On the other hand, with the development of the advanced computer facilities and algorithms, numerical modelling has become a complementary approach to investigate the size effect. The use of an experimentally informed discrete model which takes the material structure into account provides an insight into the relation between material structures and fracture process [293, 294]. With recent advantages in parallel computing, a 3D lattice fracture model has been used for studying size effect in concrete [295, 296]. Although the approach is promising, the size range analysed so far is relatively small (1:8) due to (still) huge computational demands. In order to broaden the size range in which such discrete model can be used, the multi-scale modelling strategy reported in Chapter 8 has been adopted herein to simulate the fracture performance of specimens over two length scales. Microstructures at different length scales were captured by X-ray computed tomography (XCT) and used as input in the model. The modelling results were

compared with those obtained experimentally, showing a good agreement. With the large size range of fracture testing and multi-scale modelling of HCP cube under one-sided splitting, the existing analytical size effect models can be examined and a new insight into the influence of featured material structures at different length scale on the fracture performance is provided.

9.2. EXPERIMENTAL

9.2.1. MATERIALS AND SAMPLE PREPARATION

THE tested material was a 28-day-old standard grade OPC CEM I 42.5 N paste with 0.4 water-to-cement ratio. Cubic specimens of different sizes (0.1 mm, 0.2 mm, 0.5 mm, 5mm, 10 mm, 20 mm and 40 mm, see Figure 9.1) were prepared for the one-sided splitting test. Cement and deionized water were mixed for one minute at low speed and two minutes at high speed. The fresh mixtures were poured into two types of PVC cylinders: a cylinder with a diameter of 60 mm and a height of 120 mm was used to fabricate specimens larger than 20 mm, while smaller specimens were obtained from a cylinder with diameter of 24 mm and height of 39 mm. In order to minimize bleeding, the samples were rotated at a speed of 2.5 revolutions per minute for 24 hours. Afterwards, the HCP cylinders were stored for curing in sealed conditions at a temperature of 22±2 °C. After 28 days, they were demoulded and cut using a diamond saw into final cubic size at meso-scale (5 mm, 10 mm, 20 mm and 40 mm) as shown in Figure 9.1a, while the fabrication process reported in Chapter 3 was used for the preparation of micro-scale cubic specimens (0.1 mm, 0.2 mm, 0.5 mm). Environmental scanning electron microscope (ESEM) images of the 200 µm and 100 µm cube array are shown in Figure 9.1b and 9.1c. The images were taken in backscattered electron (BSE) mode using 20 kV accelerating voltage with 10 mm working distance and the magnification was 100 ×.

9.2.2. ONE-SIDED SPLITTING TEST

The setup of the one-sided splitting test is similar to the Brazilian test (NEN-EN 12390-6 Standard) for splitting tensile strength assessment of cementitious materials. As shown in 9.2, the difference is in the boundary condition at the bottom: in the standard Brazilian test, a linear support is used; for the micro-cube splitting test, the specimen is clamped (glued) to the bottom. In order to undertake this set of mechanical tests across several length-scales, three arrangements were used herein.

The first is an KLA-Tencor G200 Nanoindenter. A diamond cylindrical wedge tip (radius 9.6 µm) was used to apply the load across the middle axis of the micro-scale sized specimens glued on the glass. A tip with a length of 200 µm was adopted for testing the cubes of 100 µm and 200 µm, while cubes of 500 µm were split by a wedge tip with a radius of 50 µm and a length of 700 µm. The experiments were run using displacement control with a loading rate of 50 nm/s. Figure 9.3a presents the fractured specimens observed by the ESEM. Since large scatter is expected for the micro-scale sized specimens, 100, 60 and 30 specimens were fabricated and tested for 100 µm, 200 µm and 500 µm cubes, respectively. A typical load-displacement curve of the smallest sample is presented in Figure 9.3b. As stated in Chapter 4, the curve shows two distinct regimes. In regime I, a nearly linear load-displacement curve is observed until the peak. This is followed by

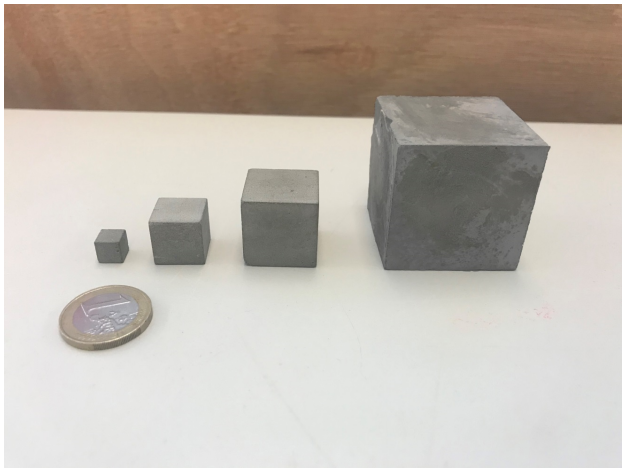

(a)

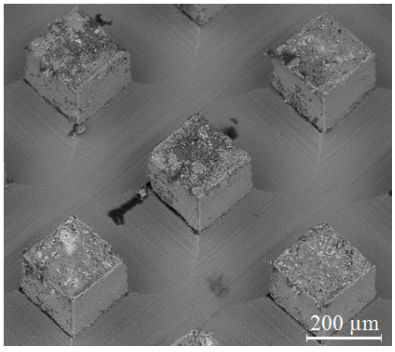

(b)

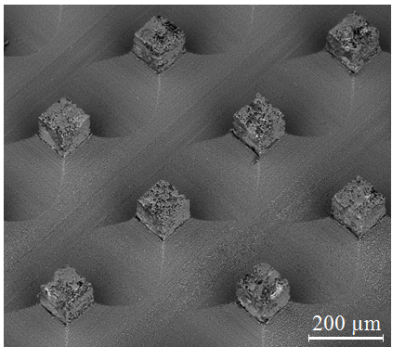

(c)

Figure 9.1: Specimens with size range of 1: 400 (a) cubic specimens with size of 5, 10, 20 ,40 mm; (b) ESEM image of sample size of 200 µm (c) ESEM image of specimens with size of 100 µm.

an unstable regime (regime 2), which signifies a rapid crack propagation and failure of the micro-cube. This unstable failure could be caused by the following: 1) the displacement control is not fast enough to measure a post-peak behaviour; 2) the behaviour of the sample might be brittle, but the system cannot capture a snap-back.

Meso-scale cubic specimens with 5 mm and 10 mm length were tested by the second instrument, a mini tension / compression stage. Two-component glue X60 consisting of a power Plex 7742 and a fluid Pleximon 801 was used to glue the sample on the test stage. A steel bar (radius: 0.5 mm) was placed between the loading stage and the specimen to impose a line load on one end. The test was performed under deformation control with a constant loading rate of 0.01 mm/s. 15 and 10 specimens were tested using this set up for the 5 mm and 10 mm cube size, respectively. Figure 9.3c and 9.3d show a cracked 10 mm cubic specimen on the stage and its load-displacement curve. The failure mode is the cube split into two halves and a relatively brittle post-peak behaviour is observed.

For testing of larger specimens (20 mm and 40 mm), an Instron 8872 loading device was used. For the sake of consistency of applied boundary conditions, the specimens were glued to the bottom steel plane using the same adhesive used in the 10 mm cubic specimen test, while a steel bar with a 2 mm radius was applied at the top (see Figrue 9.3e). A constant loading speed of 0.03 mm/s was used and 10 specimens for each size family were tested. In Figure 9.3f, a typical load-displacement curve is presented in which a similar brittle post-peak as specimens tested by the mini tension / compression stage is found.

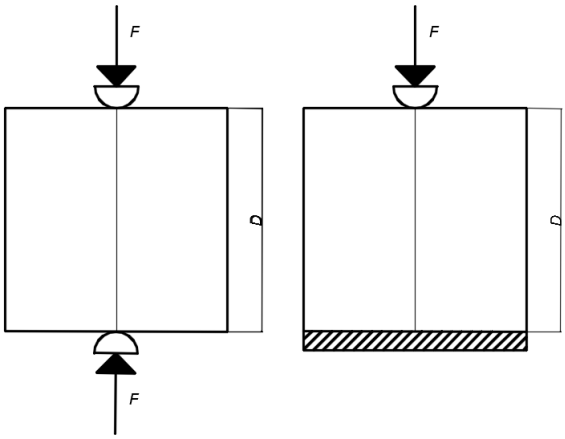

Figure 9.2: Schematics of the Brazilian splitting test (left) and the one-sided splitting test (right).

A consistent crack pattern is observed for all tested specimens. Although a brittle post peak behaviour is measured for specimens larger than 5 mm, no post peak behaviour could be measured by the nanoindenter for smaller specimens. Furthermore, it should be noticed that the displacement was measured directly from the machine. This means that the measured displacements could be affected to a certain extent by the stiffness of the loading frame, which cannot be eliminated. Thus, in this work the focus was only on the splitting strength which was calculated from the peak load P. As previously shown in Chapter 5, the strength estimation of such test can be analogous to the Brazilian splitting test using Equation 4.2:

$$f_{st} = \alpha \frac{2P}{\pi D^2} \tag{9.1}$$

where D is the dimension of the cube. α is estimated as 0.73 from a finite element model as shown in Chapter 4. Note that this parameter was used for strength estimation for all specimens over the examined size range, although the HCP specimens can hardly be considered as homogeneous at any of the size examined. The influence of heterogeneity on the mechanical behaviour at different length scale is discussed later. Therefore, Equation 4.2 was used to estimate the splitting tensile strength of all specimens along the tested range.

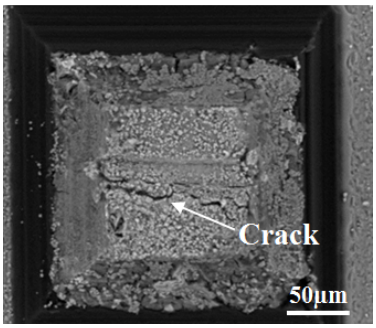

(a)

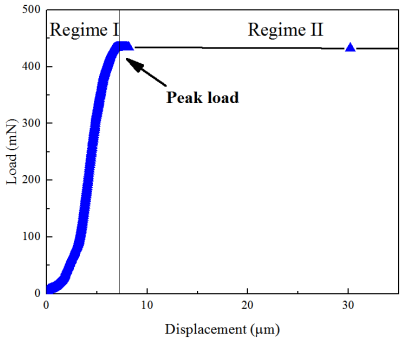

(b)

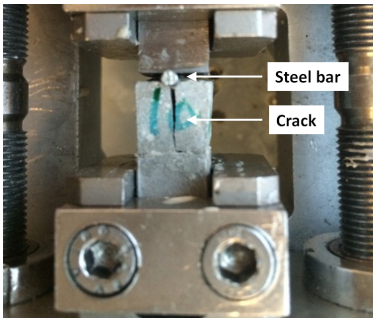

(c)

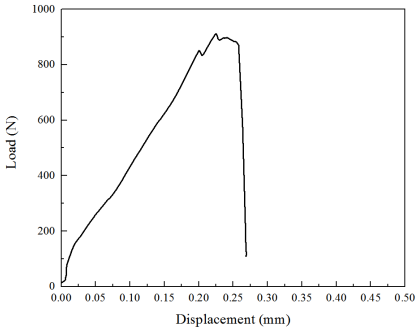

(d)

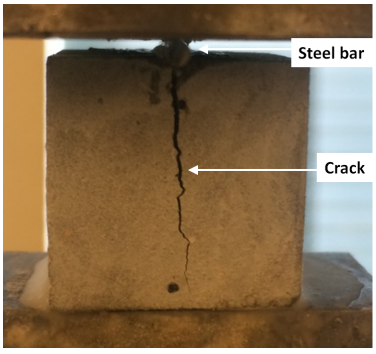

(e)

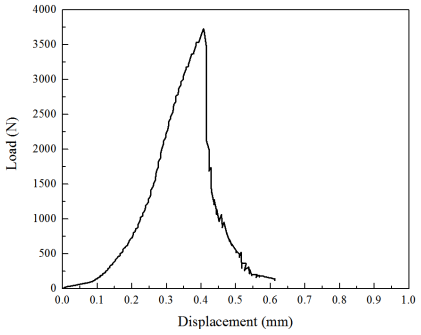

(f)

Figure 9.3: Test configurations for the one-sided splitting test: (a) a cracked 100 µm HCP cube observed by ESEM; (b) a typical load - displacement curve measured by nanoindenter; (c) a cracked 10 mm cube on the mini tension / compression stage; (d) a typical load - displacement curve measured by the mini tension / compression stage (e) a cracked 40 mm specimen on the loading device; (f) a typical load - displacement curve measured by the Instron loading device.

9.2.3. MATERIAL STRUCTURE CHARACTERIZATION

The mechanical properties of HCP are affected by various factors at different length scales. In order to understand better the influence of material structure on the decrease of strength with specimen size, the material structure informed lattice fracture simulation was performed as described in Section 9.3. As input, material structures of HCP at two levels of observation, i.e., micro- and meso-scale, were captured by X-ray computed tomography (XCT) scanning of different sized specimens. Consequentially, different voxel sizes of material structure as well as material structures were obtained.

MICRO-SCALE MATERIAL STRUCTURE

At the micro-scale, multiple hydration products and capillary pores can be observed in the HCP matrix. Therefore, a multi-phase microstructure should be considered at this scale. Herein, 10 cubic volumes consisting of anhydrous cement grains, high and low density hydration products and capillary pores with size of 100 μm (50 × 50 × 50 voxels) as reported in Chapter 4 were tested by the discrete lattice fracture model. Note that, for each cubic specimen, different relative amount of each phase is present as a result of the heterogeneous nature of HCP.

MESO-SCALE MATERIAL STRUCTURE

For the material structure at meso-scale, a cylindrical specimen with a diameter of 24 mm was scanned with a resolution of 100 μm/voxel using XCT. Voltage of 130 Kev and current of 150 μA for the X-ray source tube was used during the scanning. After image reconstruction, a binary microstructure comprising air (i.e. entrapped air void or large capillary pore) and homogenised cement paste matrix was segmented from the initial greyscale images. The first inflection point in the cumulative fraction curve of greyscale level was used for the thresholding [18, 23]. In this way, total porosity of 5.29 % (large pores only) was obtained for the scanned specimen. 5 mm cubic volume (i.e., 50 × 50 × 50 voxels) was randomly extracted from the scanned volume to be used as input in the fracture simulation (see Figure 9.4). Note that the resolution at the meso-scale was chosen to match the size of the investigated size of material volume at the micro-scale. In such a way, a multi-scale fracture modelling approach developed and validated in Chapter 8 can be implemented. The number of voxels was kept constant for the digital cubic specimens in different scales to explicitly show the influence of featured material on the predicted mechanical response. 10 cubic volumes were randomly extracted for fracture simulation to investigate the fluctuation of simulated results.

9.3. MODELLING

WITH the multi-scale modelling shceme validated in Chapter 8, material structures at different levels of observation can be implemented. By properly choosing a volume size of material structure at small scale which matches the smallest feature of the larger scale observation, the global fracture behaviour (i.e., load-displacement response under uniaxial tension) of smaller scale simulation can be used as input local mechanical properties for the fracture modelling at larger scale (see Figure 9.5). It is worth emphasizing that this methodology does not consider the representative volume element (RVE) of cement paste. This is because, for fracture of softening materials, an RVE might

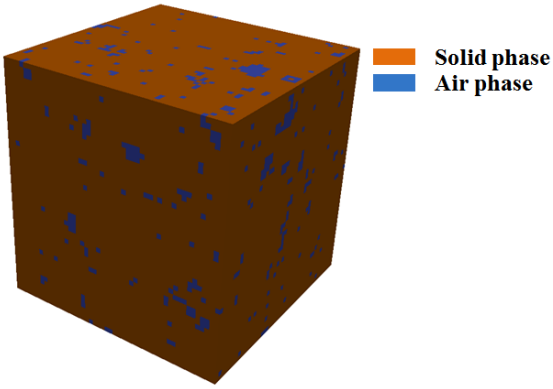

Figure 9.4: Material structure of specimen with size of 5 mm × 5 mm × 5 mm extracted from XCT experiment.

not exist due to localization issues [297]. The simulation strategy using two scale digital material structures is as follows:

For the micro-scale simulation, six types of lattice elements were determined by the three phases. Their elastic moduli and tensile strength can be found in Table 3.5.

For the meso-scale fracture simulation, 10 types of lattice elements were randomly distributed in the lattice network (after removing element corresponding to the air phase). Their mechanical properties, i.e., elastic modulus and tensile strength (see Table 9.1), were taken from the computational uniaxial tension test of the corresponding micro-scale specimens which have been reported in Chapter 5. For simplification, the average of modelling results from three directions was used to represent the specimen's micromechanical properties. In order to focus on the influence of the microstructural features on the fracture behaviour, the constitutive law of local element was assumed to be linear elastic-perfectly brittle.

The one-sided splitting boundary condition was assigned to the specimens at both length-scales, as shown in Figure 9.6. The nodes at bottom surface were clamped to represent the glued sample on the plate and a prescribed vertical displacement was applied on nodes in the two lines closed to the middle axis of the top surface to mimic the indenter load. The glue between the specimens and glass substrate was not considered in this work, as it is found in Chapter 4 that its influence on the predicted strength is negligible, although it does influence the deformation of the loading point significantly.

9.4. RESULTS AND DISCUSSION

9.4.1. EXPERIMENTAL RESULTS AND DISCUSSION

TABLE 9.2 presents the measured average strength of each size family together with their standard deviation and coefficient of variation (CoV). As a result of the small volume of material sampled, a large scatter in measured strength is found for the specimens at small scale. Clearly, the average strength of the micro cube (100 µm) is one order of magnitude larger than the strength of the laboratory (i.e. centimetre sized) sample.

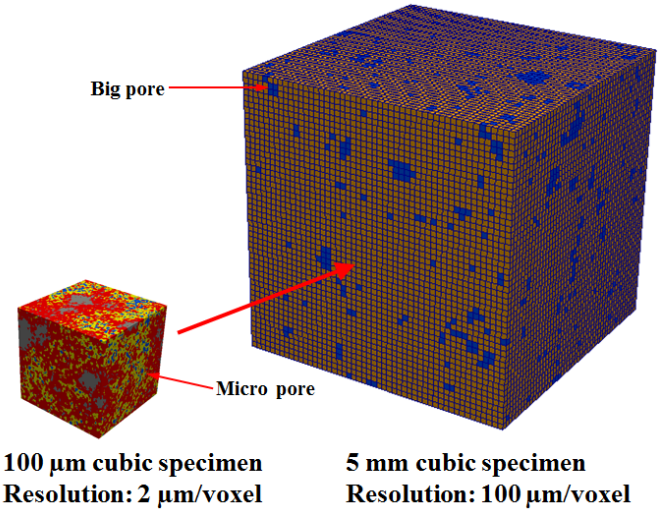

Figure 9.5: Schematic illustration of the multi-scale modelling strategy.

Table 9.1: Element types used for the fracture simulation of 5 mm specimens (obtained in Chapter 5).

Element type	Young's modulus (Gpa)	Tensile strength (MPa)
1	21.47	21.13
2	19.20	16.72
3	23.13	18.85
4	22.20	20.81
5	19.01	15.19
6	21.03	19.45
7	24.24	20.12
8	20.04	17.40
9	22.26	22.03
10	18.10	14.63

Since the size of specimens is below a few hundred micrometres, they are free from large capillary pores and air voids which significantly reduce the mechanical performance of the material. With increasing specimen size, the standard deviation and CoV decrease, as well as the measured strength. As the failure of micro-scale sized samples largely depends on the spatial distribution of micro-scale pores, a large scatter in measured data is present. In the meso-scale specimens, a relatively large population of micro-scale pores exists, therefore their distribution has less impact on the strength and potentially allows more micro-cracks to occur and coalesce before final fracture [186].

Because of the high scatter that exists in the small size ($\leqslant$ 0.5 mm) specimens, it is advised to present the strength at the small scale by its probability distribution rather than the average value. Herein, a two-parameter Weibull analysis (Equation 4.3) was performed as the fracture is mostly governed by the weakest spot, i.e., pores. As reported in Ref. [175, 176], in the absence of specific requirements, approximately 30 test specimens can provide adequate Weibull distribution parameters and more specimens contribute

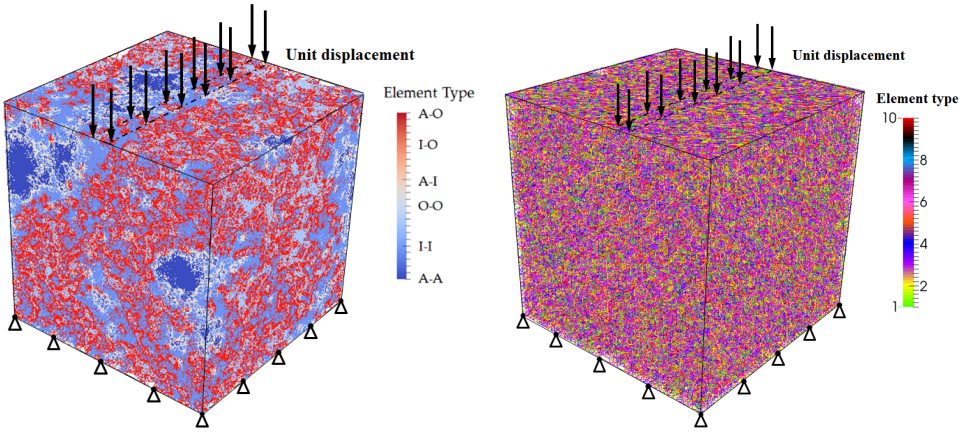

(a) (b)

Figure 9.6: Boundary conditions of one-sided splitting test on two scale specimens: (a) micro-scale specimen; (b) meso-scale specimen.

Table 9.2: Summary of test results of each specimen size.

Cubic size	Number of tested cubes	Average strength (MPa)	Standard deviation	CoV
0.1	100	18.81	3.95	0.210
0.2	60	14.84	2.71	0.182
0.5	30	10.75	1.89	0.176
5.0	15	4.92	0.82	0.170
10.0	10	3.90	0.61	0.156
20.0	10	1.80	0.26	0.144
40.0	10	1.18	0.16	0.135

little towards better uncertainty estimates. Considering the number of specimens tested in each size group (0.1 mm, 0.2 mm and 0.5 mm), a good regression can be expected if the strength of HCP at micro-scale can be represented by the two-parameter Weibull statistics. The estimated regression parameters are listed in Table 9.3 with a high determination coefficient. A similar Weibull modulus is found for the three specimen sizes considered. The small difference among the three size families could be caused by the heterogeneity of the solid phases and the interaction between cracks, or between cracks and the gradient of the stress field [298]. The fracture probabilities of three size specimens are compared in Figure 9.7. It is apparent that, on one hand, regarding the same fracture strength (below 30 MPa), the smaller specimen has a lower fracture probability. On the other hand, for the same fracture probability, the smaller specimen tends to yield a higher strength.

Table 9.3: Fitting results of the distribution of small size sample.

Family size (mm)	m	σ_0	R^2
0.1	5.376	20.27	0.9966
0.2	6.103	15.60	0.9920
0.5	6.089	11.54	0.9912

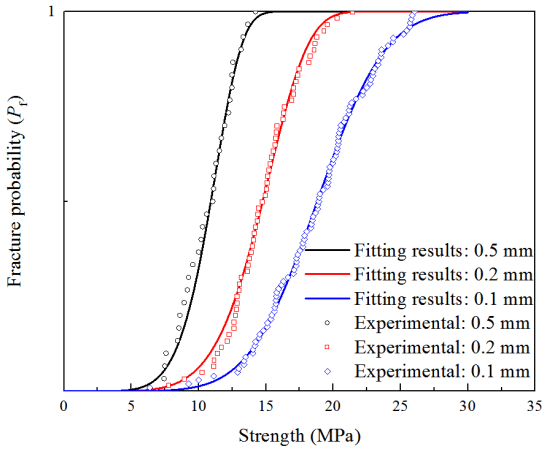

Figure 9.7: Fracture probability of cubic specimens with size of 0.1 mm, 0.2 mm and 0.5 mm.

9.4.2. FITTING OF ANALYTICAL SIZE EFFECT MODELS

The large size range (1: 400) of experimental data allows an examination of existing size effect models for brittle and quasi-brittle materials, which need to be fitted by experimental data. Among them, the most popular approaches are the Weibull statistical theory [299], multifractal scaling law (MFSL) developed by Carpinteri [289–291] and Bažant's size effect law [179].

WEIBULL SIZE EFFECT

The most well-known theory considering the statistical size effect caused by randomness of material strength is the Weibull statistical theory [299], also known as the weakest link theory. This theory assumes that the entire structure will fail once the first (i.e., the weakest) element fails. On the basis of statistics, the nominal strength σ_N shows the following relationship with the structure size D [300]:

$$\sigma_N(D) \propto D^{\frac{-n}{m}} \tag{9.2}$$

where m is the Weibull modulus which can be found by a fit on experimental data and n denotes the number of dimensions. In case of three-dimensional similarity like in the present investigation, n=3. When the nominal strength and the size are presented in a bi-logarithmic plot, the parameters can be approximated with a linear expression:

$$log\sigma_N = a - \frac{n}{m} logD \tag{9.3}$$

In the current work, the linear regression was performed using a Trust-Region method [301]. As shown in Table 9.4 and Figure 9.8, the best fit shows a high determination coefficient R^2=0.9886 and gives an estimation of the Weibull modulus m=8.1. Note that if the measurements show little variation from sample to sample, the calculated Weibull modulus will be high and a single strength value would serve as a good description of the

sample-to-sample performance. Apparently, this is not the case for HCP. Without presence of stiff aggregate which enables a more stable crack propagation, HCP is weaker and shows higher scatter, thus its Weibull modulus is lower than that of concrete (i.e., 12 as reported by Zech and Wittmann [302]). It has been shown by Van Vliet *et al.* [214] that a Weibull size effect is applicable for concrete in uniaxial tension. In their work, m=12 and n=2 were directly used to fit the Weibull size effect theory and showed good agreement with experimental data. Herein, a Weibull modulus m=6.0 was estimated from Section 9.4.1 for the HCP, which makes the slope value -0.5 in the $log\sigma_N - logD$ plot as n=3. A determination coefficient of 0.9536 is found meaning a good linear regression exists in the analytical equation and the measured nominal splitting strength. As m is assumed from the micro-scale specimens, a better agreement is found at this size range, while a relatively large discrepancy is observed at the meso-scale. This is because the complex microstructural features of specimens change with the specimen's size increasing.

Table 9.4: Fitting results of Weibull size effect.

Case number	m	a	R^2
1	8.1	8.05	0.9886
2	6.0	6.44	0.9536

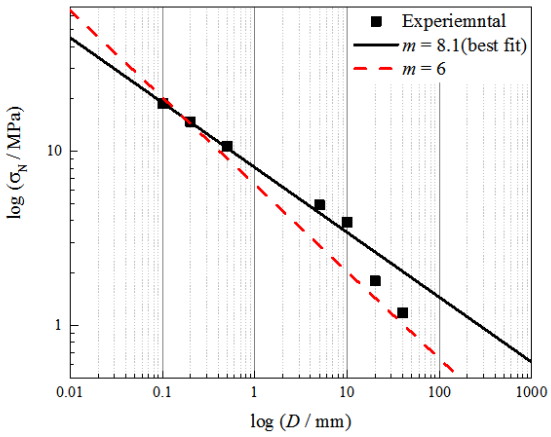

Figure 9.8: Fit of Weibull weakest link theory.

CARPINTERI'S MULTIFRACTAL SCALING LAW

Based on considerations of the fractal structure of material and its effect on mechanical behaviour, Carpinteri and his co-workers developed the multifractal scaling law (MFSL) [289–291]. According to MFSL, the nominal strength σ_N under tension decreases with increasing the characteristic structure size D, which can be expressed by the following equation:

$$\sigma_N(D) = f_t\sqrt{1+\frac{l_c}{D}} \tag{9.4}$$

where f_t and l_c are empirical constants to be determined from tests. f_t presents the tensile strength of the structure with infinitely large size and l_c denotes a characteristic length representing the influence of disorder on the mechanical behaviour. When D is below the characteristic length scale l_c, a strong size-scale effect is provided by the influence of disorder which results in a slope of -0.5 on a $\log\sigma_N - \log D$ diagram. Whereas, when D is higher than l_c, the size effect vanishes, and the MFSL grows toward a horizontal asymptote where a constant value of the strength is attained. As shown in the $\log\sigma_N$–$\log D$ plot (Figure 9.9), Equation 9.4 is fitted by the Trust-Region method. The best fitted curve with a determination coefficient (R^2) of 0.9676 predicts f_t = 2.385 MPa and l_c = 6.823 mm (Table 9.5). Although the determination coefficient is high, the tensile strength of the material for larger specimens is higher than the experimentally measured results of the largest specimens (D = 40 mm) herein. For a more reasonable fitting, the following two cases are assumed for f_t: 1) as same as the measured results of the largest specimens (1.2 MPa); 2) 70 % of the measured strength of the largest specimens (0.84 MPa) for linear regression respectively. Note that the value of 70 % strength of largest specimen is only an estimation to show the influence of f_t on the curve fitting process, as the parameter f_t cannot be measured neither estimated accordingly. A determination coefficient higher than 0.95 is observed for both regressions, while a big difference in l_c is found with decreasing f_t. Thus, a reasonable estimation of f_t is necessary for a proper fitting of such model.

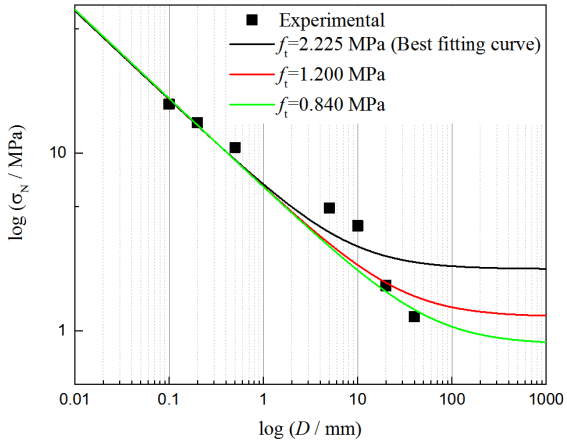

Figure 9.9: Fits of Carpinteri's MFSL with different f_t.

Table 9.5: Fitting results of MFSL.

Case number	f_t (MPa)	l_c (mm)	R^2
1	2.225	8.017	0.9676
2	1.200	28.36	0.9616
3	0.840	58.30	0.9530

BAŽANT'S ENERGETIC-STATISTICAL SIZE EFFECT THEORY

According to Bažant and his co-workers [261, 292, 303], there are two (independent) sources of size effect in brittle and quasi-brittle materials: energetic and statistical. The energetic (also known as deterministic) size effect is caused by formation of a region of intense strain localization with a certain volume, i.e., fracture process zone (FPZ). In turn, the statistical size effect is a result of the randomness of material strength as described above, which can be expressed by the Weibull weakest link theory. Combining the size effect and Weibull statistical theory, a general energetic-statistical size effect theory (ESSET) [292] can be written as:

$$\sigma_N(D) = f_r \left(\left(\frac{L_b}{D + L_0} \right)^{\frac{r \times n}{m}} + \frac{r D_b}{D + l_p} \right)^{\frac{1}{r}} \tag{9.5}$$

f_r, L_0, l_p, D_b and r are empirical constants to be determined from tests. f_r is the nominal strength for very large structures (assuming no Weibull statistical size effects). L_0 is the statistical characteristic length, controlling the transition from constant properties to local Weibull statistic via strength random field, while D_b drives it from elastic-brittle to quasi-brittle. l_p represents the characteristic length of the microstructure influencing both the size and spacing of localized zones, which is introduced to satisfy the asymptotic requirement to have a finite plastic limit when D approaches infinite size. Exponent r is a geometry-dependent factor, which controls both the curvature and the slope of the size effect and is constant when geometrically similar structures are considered.

This analytical equation is regarded as the asymptotic matching of large-size statistical and small-size deterministic size effects as it satisfies the following three asymptotic conditions: (1) for small sizes $D \to 0$, the asymptotic prediction reaches the plastic limit; (2) for large sizes $D \to \infty$, the Weibull size effect become dominant; (3) for $m \to \infty$ and $L_0 \to \infty$, the prediction leads to a deterministic size effect law. Figure 9.10 presents the best fit of Equation 9.5. Although a high determination coefficient (0.9992) is found, the Weibull modulus m is below 0.1, which is obviously unrealistic. Furthermore, although it is reported that the value of r should be close to 1 for two dimensional beams [292, 304], the value for the cubic specimen is unknown. Thus, several assumptions on m were made with r=2 (from the best fit curve in the current work) and r=1, respectively. the fitted results were listed in Table 9.6. The value of m controls the slope at the large size range and a higher value of m corresponds to a gentler decrease of strength with the size increasing which means a more disordered material has a stronger size effect on the strength decreasing. For the same m value, the cases in which r=1 predicts a higher f_r. Note that the predicted f_r in Table 9.6 is higher than the f_t (2.225 MPa) predicted in Section 4.2.2 by the MFSL, because the nominal strength for very large structures in the Bažant's ESSET does not take the statistical size effects into account. Although, it is suggested that f_r should be calculated from the finite element modelling [292], this cannot be achieved with current test technique.

GENERAL DISCUSSION

As shown above, all three analytical models are able to describe the decreasing trend of strength along the tested specimen size range. Assuming that the Weibull modulus m=6 for HCP under such one-sided splitting test, the fitting results of case 2 in Table 9.4, case

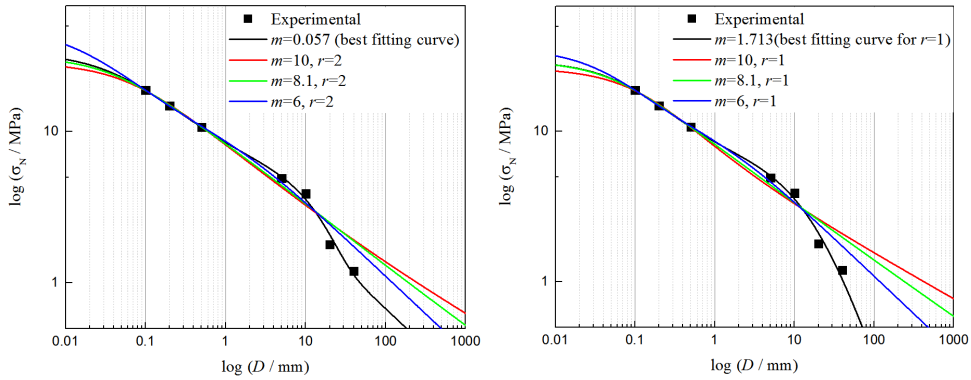

Figure 9.10: Fits of Bažant's ESSET with different m: (a) r=2; (b) r=1.

Table 9.6: Fitting results of the empirical parameters in Equation 9.5.

Case number	f_t (MPa)	L_0 (mm)	m	D_b (mm)	l_p (mm)	r	R^2
1	5.73	759.5	0.0566	0.6947	0.04214	2	0.9992
2	5.05	0.7549	10	1.083	0.06969	2	0.9934
3	6.92	0.741	8.1	0.4755	0.048	2	0.9944
4	9.02	1.133	6	0.1954	0.01371	2	0.9962
5	6.822	19.61	1.713	0.3744	0.1122	1	0.9991
6	7.097	0.6107	10	0.4386	0.1617	1	0.9936
7	9.45	0.557	8.1	0.2045	0.09583	1	0.9936
8	9.635	1.269	6	0.1558	0.05734	1	0.9963

3 in Table 9.5 and case 4 in Table 9.6 are plotted together in Figure 9.11 for comparison. In the range of tested specimen sizes, Bažant's ESSET is capable to shift to any point apart from the linear line (Weibull size effect), while MFSL gradually grows from a slope of -0.5 at small-scale asymptote towards a horizontal line for the large-scale specimen. It is interesting to mentation that both the Weibull size effect model and Carpinteri's MFSL behave linear in the small-scale asymptote with a slope of -0.5. Such slope at small-scale asymptote is inherent to the MFSL. The agreement between the Weibull size effect and MFSL might prove that the role of microstructural disorder and of self-similar features dominate the damage and fracturing processes of HCP at the micro-scale [305]. However, Bažant's ESSET gives a constant strength for small specimen sizes (plastic limit). Even with the unprecedented size range of experimental data, such plastic limit could not be captured in current work. For strength measurements of specimens smaller than 10 micrometres, it is possible to use a focused ion beam for specimen preparation and the nanoindenter for mechanical testing [45, 102]. However, when the specimens are so small, the measured strength is not representative of cement paste any more, as the material might only contain a single cement phase (for example, calcium-silicate-hydrate or Portlandite). Thus, the small-size asymptote can never be measured experimentally for HCP. In turn, the attention might be put on validation of these size effect models

at large-scale (structure size scale), which is more of practical importance. As shown in Figure 9.11, a different trend is found between the ESSET and MFSL at this size range. Specifically, Bažant's ESSET (Equation 9.5) turns to be parallel with the Weibull size effect in the large-scale asymptote with a slope value -0.5 in this case, because the parameter D_b is close to 0. Whereas Carpinteri's MFSL shifts to a horizontal line. Large sized experiments should therefore be carried out for validation. The challenges related with such large-scale experiments are the demands of the testing instruments which can operate the big size specimen and have enough load capacity, and the specimen preparation which might make it impossible use HCP as a material because of the shrinkage and eigenstress which will develop in large specimens during the hydration process.

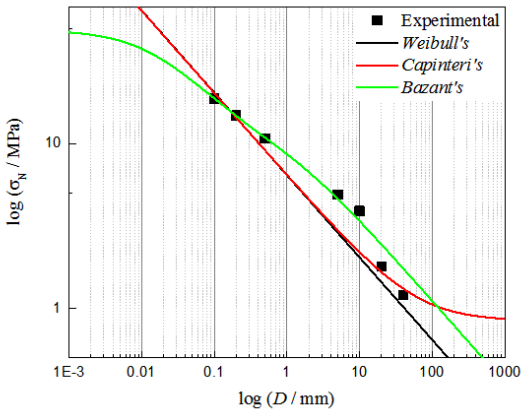

Figure 9.11: Comparison of the fitting result of three analytical models.

9.4.3. MODELLING RESULTS AND DISCUSSION

Using the multi-scale modelling strategy described in Section 3.2, the one-sided splitting test was simulated on specimens of two sizes: 0.1 mm and 5 mm. As the simulated mechanical behaviour of 0.1 mm has been validated in 4 by comparing both the load-displacement response and crack pattern with experimental data, herein the focus is on the different fracture response of specimens of different sizes. Simulated load-displacement diagrams of each size family are plotted in Figure 9.12. For each size family, 10 specimens were simulated to show the scatter. Compared with the 0.1 mm specimens, a relatively brittle post peak behaviour is found for the 5 mm specimens (note again that, due to the limitations of the tests performed, the post-peak was not measured experimentally). This is mainly because of the different material structures. For 0.1 mm specimens, a more tortuous and distributed crack pattern is found (see Figure 9.13), due to presence of the capillary pores and anhydrous cement particles. More specifically, on one hand, capillary pores introduce stress concentrations and micro cracks initialize in their vicinity. On the other hand, the anhydrous cement particles work as stiff inclusions in the matrix which disturb the crack pattern propagation path when crack localization starts. In the 5 mm specimens, the capillary pores and anhydrous cement particles are

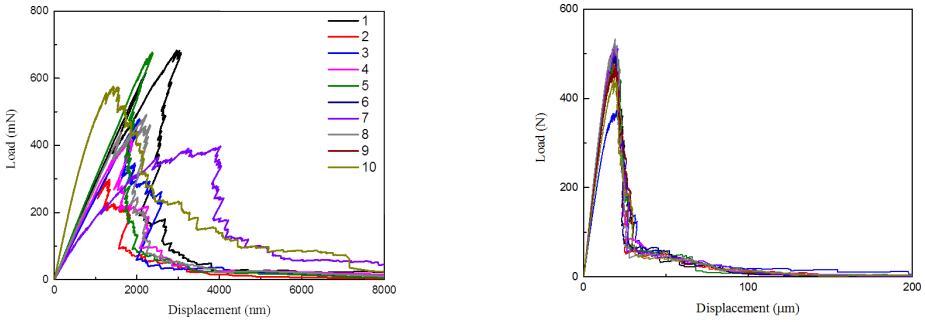

(a) (b)

Figure 9.12: Simulated load-displacement curve of the digital specimens with size of (a) 0.1 mm and (b) 5 mm.

homogenised as the cement matrix, although the distributed cracks can be found due to the presence of large capillary pores or entrapped air voids, the 'stiff inclusion effect' disappears as the particle size is only visualized within the micro length scale.

In order to assess whether the proposed microstructure-informed lattice model is capable of accurately predicting the strength of HCP at multiple scales, the nominal splitting strength was calculated from the peak load using Equation 4.2, and compared with experimental results (see Figure 9.14). The calculated average splitting strengths are 22.00 MPa for 0.1 mm size specimen and 5.27 MPa for the 5 mm specimen. The fluctuation is captured by the modelling strategy: a CoV of 0.095 is found for 5 mm size specimen, while a higher CoV value (0.260) is obtained for 0.1 mm size specimen. Note that the simulation covers a wide size range of 1: 50. Although smaller than the tested size range, it is still 6 times larger than the simulated range in previous studies [295, 296]. It is known that with a constant resolution and increasing the material size in the 3D discrete model, the computational demands are increased as a power law and thus the investigated size range was limited. A multi-scale modelling strategy as proposed herein is capable of enlarging the prediction size over several length scales to have more insight into the influence of microstructural features on the material's fracture behaviours.

As shown in Chapters 5 and 8, such model offers further insight into the relation between the microstructural features and its corresponding mechanical properties. For example, the influence of the population of micro-scale pores on the micromechanical properties has been studied in previous chapters. In this chapter, the influence of the micro pores is taken indirectly in simulations of specimens as the homogenised cement paste matrix. The relation between the meso-scale porosity ($\leqslant$ 100 μm) and simulated strength is plotted in Figure 9.15. Clearly, the nominal splitting strength decreases exponentially with increasing population of meso-scale pores. The scatter can be attributed to the variation of pore size distribution and its spatial distribution in each single specimen. Both factors are known to play an important role in the fracture process [182, 306]. Based on the modelling approach proposed herein, further studies could be carried out using advanced image analysis methods and pore structure characterization approaches (e.g., Ref. [14]) to have more quantitative investigation on the influence of the multi-scale pore structures on the fracture process.

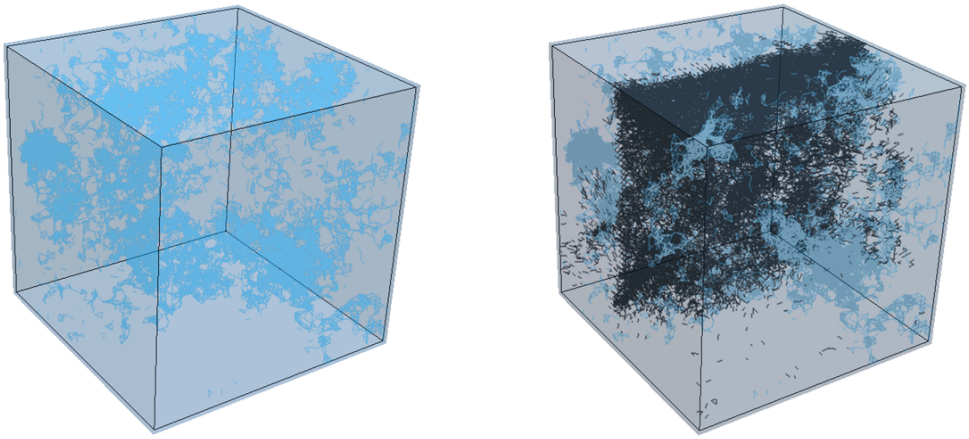

(a)

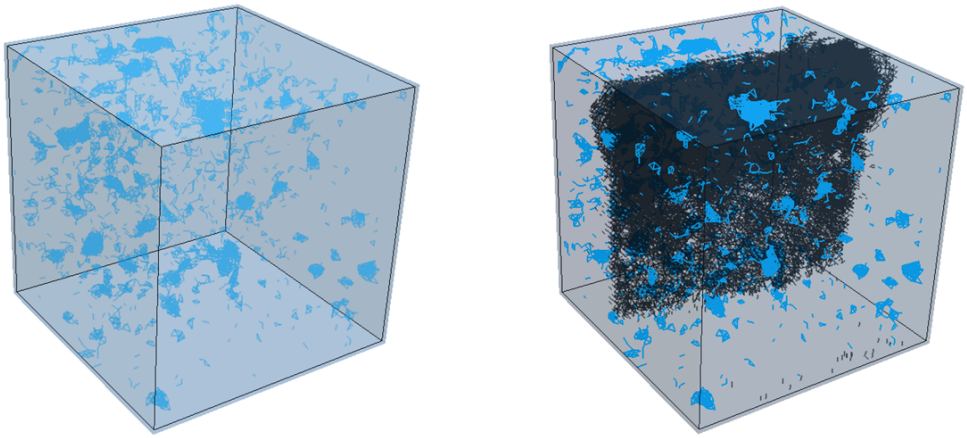

(b)

Figure 9.13: Spatial distribution of pores (left) and fracture pattern (right) of the digital specimens with size of (a) 0.1 mm and (b) 5 mm (blue–pore, black-crack).

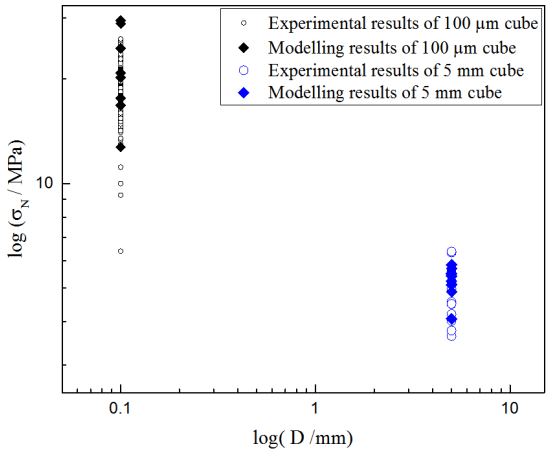

Figure 9.14: Comparison between the modelling results and experimental results in terms of the nominal splitting strength.

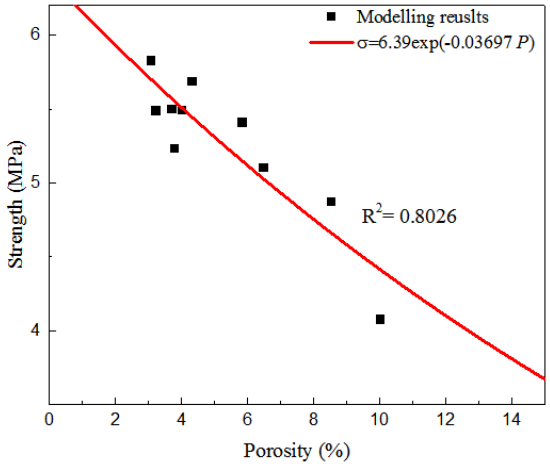

Figure 9.15: Relationship between nominal splitting strength and population of meso-pore for the 5 mm specimens.

9.5. CONCLUSIONS

THE experimental basis for the size effect (size range: 0.1–40 mm) study has been successfully extended by the present work. Based on the unprecedented size range of strength measurements, existing analytical models for size effect are critically examined. A microstructure-informed discrete model has been used to simulate the fracture of specimens at both micro and meso-scales. Based on the presented results, the following conclusions can be drawn:

- It is confirmed by the experimental measurements that the splitting tensile strength of HCP at micro-scale is significantly higher than the one measured from the laboratory (centimetre sized) scale. Together with the measured average strength, the scatter (CoV) of the measurements decreases with the specimen size increasing.

- The two-parameter Weibull analysis reveals that, on one hand, regarding the same fracture strength (below 30 MPa), the smaller specimen has a lower fracture probability, while, on the other hand, for the same fracture probability, the smaller specimen tends to yield a higher strength.

- Although all examined analytical models can be fitted with a high determination coefficient, special attention should be should be given to the physical meaning behind the empirical parameters used in these models. Controversial trends were found in both small and large size asymptotes for multifractal scaling law and energetic-statistical size effect theory, which could not be validated nor disproved by the experiments performed herein.

- The lattice model is able to predict strengths that are in good accordance with the experimental measurements for both 0.1 mm and 5 mm specimens as well as the fluctuations. With the multi-scale modelling strategy adopted herein, the size range of microstructure-informed 3D discrete model on strength prediction is significantly enlarged.

- Because of the presence of capillary pores and anhydrous cement particles, a higher degree of heterogeneity is observed in the model at the micro-scale. This results in a more tortuous and diffuse crack pattern as well as a more ductile post-peak behaviour.

The current model can provide a link between the material structure and the predicted mechanical properties. An exponential equation is proposed to express the relationship between predicted strength and porosity that is explicitly presented in the model. The dispersion between the proposed empirical strength-porosity relationship and numerical modelling results can be attributed to the variation of pore size distribution and its spatial distribution in each single specimen. By combining more advanced image analysis methods and pore structure characterization approaches, the proposed modelling approach can offer insight into the relation between the pore structure and fracture properties of materials.

10

MODELLING OF FRACTURE OF MORTAR USING OUTPUT FROM MICROMECHANICAL MODELLING

This chapter presents a validation process of the developed multi-scale modelling scheme on mortar. Special attention was paid to make the material structure of real and virtual mortar specimens comparable at the meso-scale. The input mechanical parameters of cement paste (both bulk cement paste and interfacial transition zone) at the meso-scale were derived from micromechanical modelling using the volume averaging approach. Different constitutive relations for local elements were tested. By comparing with the experiments, the model using linear-elastic constitutive relation can reproduce the experimental load-displacement response satisfactorily in terms of the elastic stage and peak load. More realistic load-displacement curve in the non-elastic stage can be simulated by considering the softening of cement paste using a step-wise approach. More importantly, the experimentally validated multi-scale modelling scheme offers the opportunity for the meso-scale model to become fully predictive.

10.1. INTRODUCTION

THE meso-scale model deals with material structures consisting of cement matrix, aggregates with different particle sizes and air voids. Numerous publications can be found in the literature to model the fracture process of concrete using both discrete lattice models [138, 162, 279, 307–312] and finite element models [313–320]. However, quantitative prediction of the fracture behaviour in terms of the crack pattern and stress-strain response is still a challenging task. This is partly because of the complex material structure: between aggregate and cement paste matrix, there exists a so-called interfacial transition zone (ITZ). This zone is a highly porous region of the cement paste with a thickness between 30 and 80 µm and appears to be the weakest spot [233–235]. Thus, a large number of micro-cracks take place in this zone before coalescence. To explicitly represent this zone in the meso-scale model is computationally expensive. Consequently, most of the studies are limited to 2D which cannot predict non-planar 3D fracture surfaces. There are several attempts using 3D discrete-element models [162, 295, 307, 311, 312, 321, 322] and finite element models [238, 316, 323–329] but mostly with rather coarse mesh discretization. Moreover, the determination of the input parameters in the models is mostly done through inverse analysis, which decreases the predictive capabilities of the models.

In light of the multi-scale modelling approach, the constitutive relation of the bulk cement paste matrix and ITZ should be preferably derived from lower-scale (i.e. micro-scale) simulations or measurements. With the aid of the micro-dicing saw and nanoindenter, micro-scale sized specimens have been successfully prepared and tested. Based on the experimental measurements, micromechanical models, for both bulk cement paste (see Chapter 3) and ITZ (see Chapter 7), have been calibrated. Therefore, reliable results can be expected from the micromechanical modelling which are competent as input for the meso-scale modelling. Another concern is related with up-scaling of micromechanical properties to the meso-scale model. This has been validated in the cement paste system (Chapters 8 and 9). However, when dealing with mortar or concrete, the modelling scheme is further complicated by the presence of ITZ. Thus, a validation is required at the meso-scale in terms of a system consisting of aggregate, ITZ and bulk cement paste matrix.

To this end, a comparison between experimental test and numerical modelling is carefully designed. As size effect [20, 305] occurs in such material, the material volume in the model and test has to be identical. Thus, herein the sample size is set to be 10 mm as a compromise between computational efficiency and experimental possibilities. Sand aggregates with realistic shape were modelled and placed using a so-called Anm particle packing model [330]. The discrete lattice fracture model is used to model the fracture process of the computational generated material structure. Uniaxial tensile test was performed experimentally and numerically. The good agreement between simulations and experiments shows the feasibility of the volume averaging approach to link the micro-scale and meso-scale models.

10.2. EXPERIMENTAL

10.2.1. MATERIALS AND SAMPLE PREPARATION

THE mortar mixture was prepared using standard CEM I 42.5 N Portland cement, deionized water and crushed quartzite sand with particle size between 1 mm and 2 mm. The specimens were prepared with a water to cement (w/c) ratio of 0.3 and sand was added at 70 % of cement mass. The amount of sand and particle size is chosen on purpose to make the comparison between numerical simulation and experimental measurement easier. Sand was mixed first with dry cement in a bowl using Hobart mixer for 30 s, and then deionized water was added into the mixture within 10 s. This was followed by mixing for 90 s at low speed. The mixer was then stopped for 30 s during which paste adhering to the wall and the bottom part of the bowl was scrapped off using a metal scraper and added to the mix. The mixing was then resumed for additional 90 s. The total mixer running time was around 3 min. After mixing, the fresh mixture was cast in a cylindrical mould (24 mm diameter, 39 mm height) and vibrated for 30 s to minimize the amount of entrapped air. The cylinders were then sealed and cured for 28 days at lab conditions (temperature: 22±2 °C). After curing, cubic specimens with size of 10 mm (see Figure 10.1) were sawn out from the cylinders. Two notches (1 mm depth and 1 mm thick) were sawn in mid-height, see Figure 10.1.

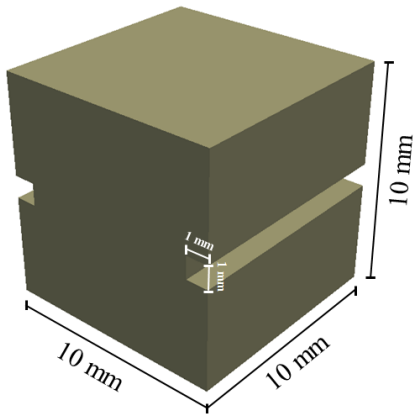

Figure 10.1: Dimension of the prepared mortar specimen fort the uniaxial tension test.

10.2.2. UNIAXIAL TENSION TEST

For the uniaxial tension test, an Instron 8872 loading device was used. The test configuration is shown in Figure 10.2. A two-component glue (X60 consisting of a power Plex 7742 and a fluid Pleximon 801) was used to bind the 10 mm mortar to the two fixed steel plates. The displacement between the two steel plates was measured continuously by two linear variable differential transformers (LVDT) at the notched sides. A loading speed of 15 nm/s constant increment was used, which was controlled by the average of two LVDT's.

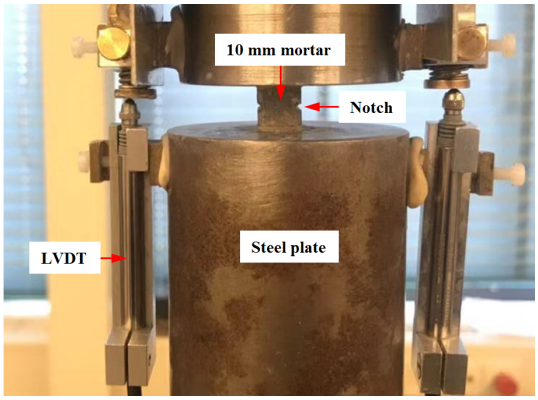

Figure 10.2: Configuration of uniaxial tension test of the 10 mm mortar.

10.2.3. EXPERIMENTAL RESULTS

Three specimens were prepared and tested. One fractured specimen is shown in Figure 10.3. It is clear that the cube fractured in the middle where two notches exist. Due to the heterogeneity of the material structure, the surface is quite tortuous. The measured load-displacement curves are shown in Figure 10.4. As the test is under displacement control using LVDT, a stable fracture process is measured. Typical quasi-brittle behaviour is observed. In the pre-peak branch, the load increases monotonically with displacement, while decreasing in the post-peak branch. A four-stage fracture model [2] can be used to describe the measured load-displacement curves. In the pre-peak branch, the material behaves linear elastic at stage I (below 0.2 kN, in this case), after which the stiffness decreases gradually (stage II). In the post-peak branch, a significant load drop (stage III) is observed after the peak. This is followed by a long shallow tail. The experimentally measured load-displacement and observed failure pattern are further used to validate the adopted modelling strategies. More details about the fracture propagation can be obtained by the simulation and used to explain the observed load-displacement response.

Table 10.1 shows the Young's modulus, strength and fracture energy calculated from the load-displacement curve. The modulus is calculated from the linear-elastic stage. Strength is derived from the peak load. Fracture energy is derived from the post-peak branch using Equation 5.1. The maximum displacement used for the calculation is 20 μm. As the specimen is 4 times larger than the biggest aggregate (2 mm), small variations occur in the measured Young's moduli and strengths [2]. A large deviation (coefficient of variation > 0.1) is observed in terms of the fracture energy, because the post-peak response is governed by the crack localization process, which can be disturbed by the flaws or stiff aggregate present in the matrix.

10.3. GEOMETRICAL MODELS

THE composite geometrical structure of mortar can be represented by a model consisting of sand, entrapped air voids and cement paste matrix at the meso-scale. In

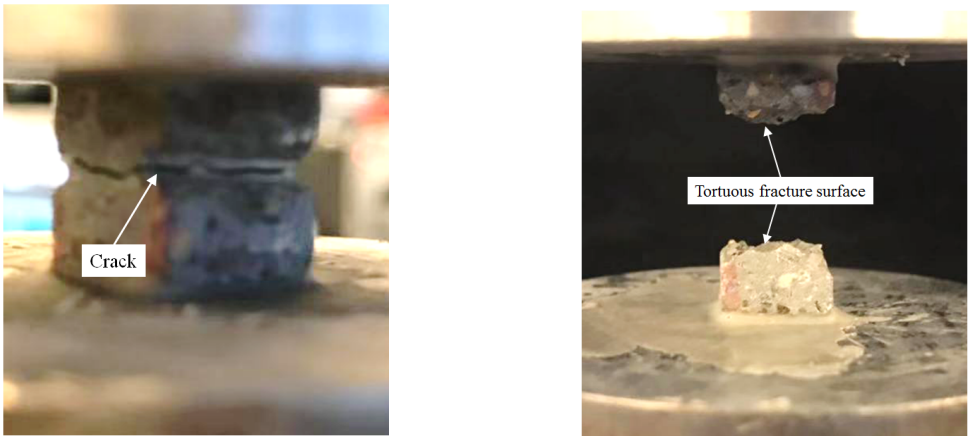

(a) (b)

Figure 10.3: Fractured specimens under uniaxial tension: (a) side of view; (b) front view.

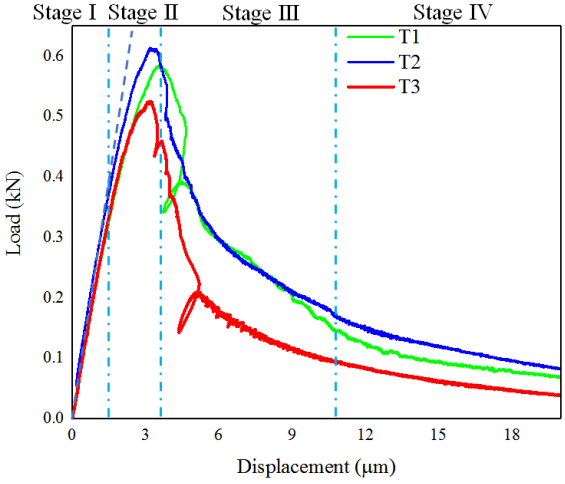

Figure 10.4: Experimentally measured load-displacement curves of the 10 mm specimens.

Table 10.1: Measured mechanical properties of the 10 mm mortar specimens.

Sample	Young's modulus (GPa)	Tensile strength (MPa)	Fracture energy (J/m^2)
T1	26.38	5.84	29.28
T2	26.85	6.14	33.38
T3	25.84	5.25	19.80
Average	26.36	5.74	27.49
Coefficient of variation	0.015	0.064	0.2069

the presented work, the real-shaped aggregates were created using a so-called Anm model [330]. Spherical shaped air voids were created on the basis of the pore size distribution obtained from XCT image analysis. After packing, the continuum geometrical model was digitalised into a microstructure with a resolution of 100 µm/ voxel. The resolution is chosen on purpose to match the size of the investigated material volume at micro-scale from the previous chapters. In such a way, the volume averaging up-scale approach can be implemented.

10.3.1. ENTRAPPED AIR VOIDS

As the entrapped air voids act as initial flaws in the material structure and have considerable influence on the mechanical properties of the specimen, it is essential to explicitly consider them in the model. The porosity and pore size distribution are commonly used to characterize the pore structure. They were determined by X-ray computed tomography (XCT) scanning and image processing techniques and used as reference to generate the spherical shaped air voids in the container.

For the XCT scanning, a cylindrical specimen (24 mm diameter, 39 mm height) as described in Section 10.2.1 was used to form a digitalized microstructure with a spatial resolution of 100 µm/voxel. During the scanning, voltage of 150 Kev and current of 150 µA for the X-ray source tube was used. After image reconstruction, the global thresholding method using the over-flow point as described in Chapter 3 was implemented to segment the pores from the initial greyscale level based images. This results in a porosity of 3.56 %, which is in accordance with Ref. [1]. Assuming spherical shape for air voids, the experimental pore size distribution can be obtained (see Figure 10.5). The experimentally characterized porosity and its pore size distributions were then used as reference to generate the database of the air voids (diameter range: 0.2 mm to 2.4 mm) which are going to be placed into a pre-defined container (10 mm × 10 mm × 10 mm).

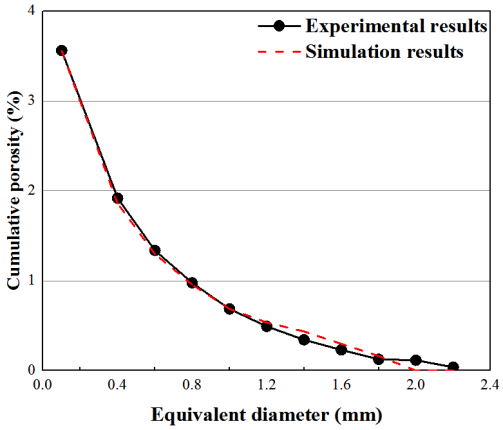

Figure 10.5: Cumulative porosities of experimental and simulated material structures.

10.3.2. IRREGULAR SAND PARTICLES

It is well-known that aggregate shape and size in the model has a significant influence on the simulated mechanical performance of mortar or concrete [238, 315, 331]. In order to have a quantitative prediction of the material behaviour, realistic aggregate shape and size should be used. Using spherical harmonic series, the Anm model can represent the irregular aggregate shape well. An example of a sand particle described by spherical harmonic expansion is shown in Figure 10.6. The aggregates were selected from a database containing 806 crushed sand particles and scaled up or down (using pseudo-random number based algorithms) to the size between 1 mm to 2 mm and placed into a pre-defined container (10 mm × 10 mm × 10 mm) one after another until reaching the prescribed volume ratio.

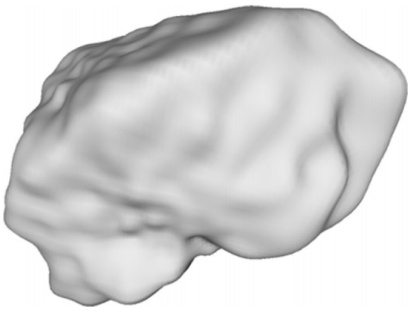

Figure 10.6: An irregular shape sand particle created by Anm model [330].

10.3.3. DIGITAL MORTAR SPECIMEN

In order to properly model the aggregate structure in mortar, the realistic volumetric ratio of sand should be considered. According to the mixture design, the volumetric ratio of sand is calculated as follows:

Given that the specific gravity of sand and cement is 2.60 kg/ m^3 and 3.15 kg/ m^3 respectively, the volumetric ratio of cement: sand: water is: (1/ 3.15): 0.7/ 2.60: 0.3 = 0.317: 0.269: 0.3. On a percentage basis, the volumes are as follows: cement (dry) = 35.803; sand = 30.363; water = 33.834. In terms of the given case, 70 % of the cement has hydrated after 28 days (Chapter 3). Consequently, continuing in percentage volume units, the volume of anhydrous cement equals 10.741 and the volume of hydrated cement 25.062. Assuming volume of combined water is 0.23 [1] of the mass of hydrated cement, i.e. 0.23 × 25.062 × 3.15 = 18.157 and the free water is 15.677. On hydration, the volume of the solid products of hydration becomes smaller than the sum of volumes of the constituent cement and water by 0.254 of the volume of combined water [1]. Hence, the volume of the solid products of hydration is: 25.062 + (1 - 0.254) × 18.157 = 38.607. Because the air content is 3.56 % as measured by XCT, the volume of the remaining materials must add up to 96.44 % of the total volume of mortar. Therefore, the volumetric ratio of sand is: 0.9644 × (30.363) / (10.741 + 38.607 + 30.363 + 15.677) = 0.307.

In terms of placing or packing air voids and sand particles in the predefined con-

tainer, no overlap was allowed. Pseudo-random number based algorithms were implemented to position and rotate the packing objects (No rotation is needed for the air voids). In order to improve the packing efficiency, large particles are placed first. Considering that the realistic specimen was sawn from the cylinder, to avoid the "wall effect" when depositing the aggregates, periodic boundary conditions are applied. This permits a particle to pass through the surface of the simulation box and the part outside the simulation box is put on the opposite surface by placing a duplicate particle with the same orientation. After packing, the simulated vector-based composite geometrical structure was digitalized into the digital specimens with a resolution of 100 µm/voxel, resulting in a 100 × 100 × 100 voxels microstructure, see Figure 10.7.

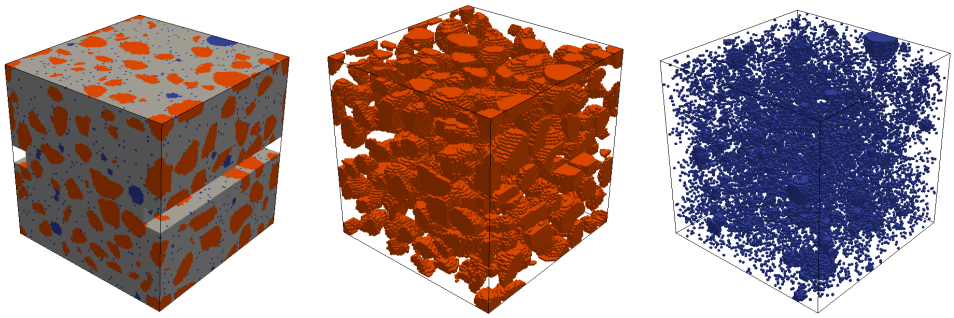

(a) (b) (c)

Figure 10.7: Simulated composite geometrical structure of 10 mm mortar specimen: (a) sand particles and air voids are embed in the continuum cement paste matrix; (b) spatial distribution of sand particles; (c) spatial distribution of air voids (orange: aggregate; grey: cement paste; blue: pore).

10.4. DEFORMATION AND FRACTURE MODELLING

10.4.1. DISCRETIZATION AND BOUNDARY CONDITIONS

The discrete lattice mesh was generated following the approach described in Chapter 3. It has 1000000 nodes and 7084561 Timoshenko beam elements. Digital material structure that generated in Section 10.3 was considered by utilizing the overlay procedure as shown in Figure 10.8. Three types of element were defined according to the location of the two ends of the element, namely: cement paste, interface and aggregate. This was used to define the properties of each lattice element. In this way, different mechanical properties can be assigned to different phases presented in the material structure. The cement paste element and aggregate element represent the cement paste and aggregate respectively. The interface element is introduced to consider the interaction between cement paste and aggregate. Additionally, no element is generated to connect the pore phase, which results in the initial flaws in the model.

As shown in Figure 10.9, the computational uniaxial tension test is performed by applying nodal displacement at one end and fixing the other. Because fixed plates are used in the experiment, the rotations at the ends are restricted in the simulation. To consider the restrictions introduced by the high stiffness of steel plates, no lateral deformation is allowed at both ends in the model.

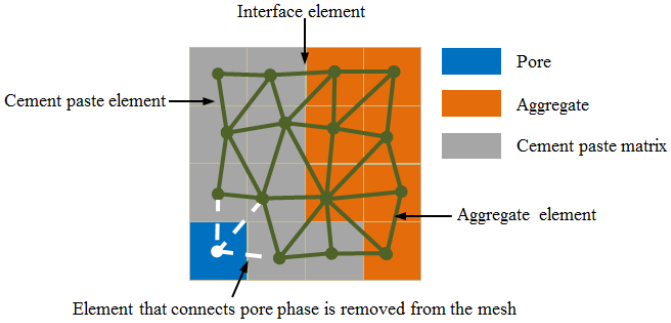

Figure 10.8: Schematic view of overlay procedure for lattice mesh.

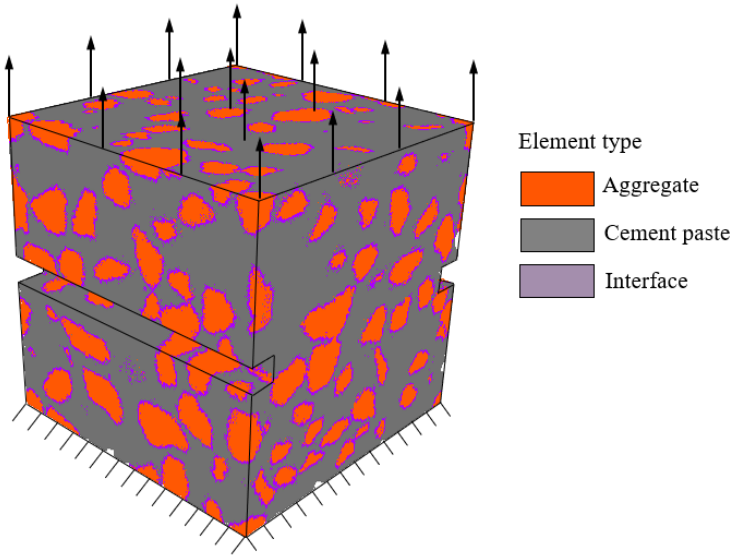

Figure 10.9: Boundary condition of the computational uniaxial tension test of the mortar.

10.4.2. USING LINEAR-ELASTIC CONSTITUTIVE RELATION

For the sake of simplification, a prefect elastic brittle constitutive relation is generally assumed at the element level [19, 161, 241, 295, 332]. The up-scaling approach presented in Chapter 9 was used to determine the input mechanical properties of all phases. The mechanical properties (Young's modulus and tensile strength) of bulk cement paste were taken from Table 5.1 and assigned randomly to the cement paste elements. With respect to ITZ, its mechanical properties are taken from Table 7.5, which are the upper bound of the predicted micromechanical properties of ITZ. For the sand aggregate, a perfect linear elastic constitutive law is assumed. Its elastic modulus is taken from [251], i.e. 70 GPa. Its tensile strength is assumed as 1/1000 of the elastic modulus. This ratio is larger than commonly observed at the meso-scale, as it is found in Chapter 5 that it increases with the length scale decreasing . Moreover, in case of the current study, no cracking is expected in the aggregate. Consequently, strength of the aggregate has no contribution to the mechanical response of the simulated mortar.

As shown in Figure 10.8, the interface element takes up a piece of aggregate and a piece of cement paste (ITZ). The strength of this type element was assumed as the bonding strength between the cement paste and aggregate, while its Young's modulus E is calculated using a Reuss (series) model:

$$\frac{2}{E_{\text{interface}}} = \frac{1}{E_{\text{ITZ}}} + \frac{1}{E_{\text{aggregate}}} \tag{10.1}$$

where E_{ITZ} and $E_{\text{aggregate}}$ are elastic moduli corresponding to ITZ and aggregate, respectively. The resulting mechanical properties of the interface elements are listed in Table 10.2.

Table 10.2: Mechanical properties of the elastic-brittle interface element up-scaled from Table 7.5.

Number	Young's modulus E (GPa)	Tensile strength f_t (MPa)
1	8.22	3.12
2	10.13	3.82
3	11.85	4.47
4	7.36	2.75
5	9.19	3.47
6	9.89	3.87
7	8.17	3.03
8	8.73	3.25
9	9.06	3.47
10	10.55	4.07

As shown in Figure 10.10, the simulated load-displacement (termed as case E) response is compared with the experimental measurements. It shows that, the model can reproduce the load-displacement response in a qualitative sense. It is worth mentioning that, without any calibration at the meso-scale, the predicted Young's modulus (27.67 MPa) and tensile strength (5.56 MPa) are in accordance with experimental measurements, except that the fracture energy (17.36 J/m^2) is much lower. Moreover, as shown in Figure 10.11, the simulated fractured specimen shows a similar crack pattern compared to the experiments.

The fracture patterns at different loading stages are plotted in Figure 10.12. Figure 10.12a shows the crack pattern at point a in Figure 10.10. Clearly, up to the end of the

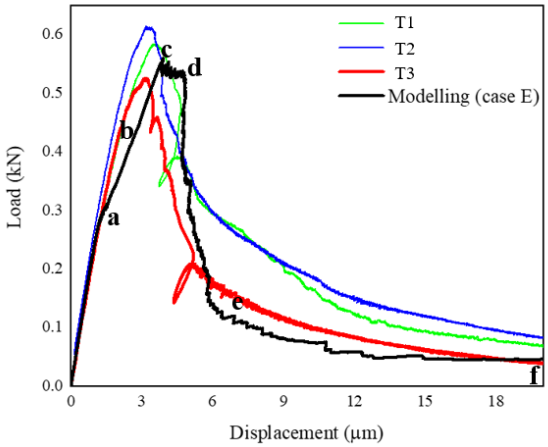

Figure 10.10: Simulated load-displacement curve using linear elastic constitutive relation (compared with experimental results).

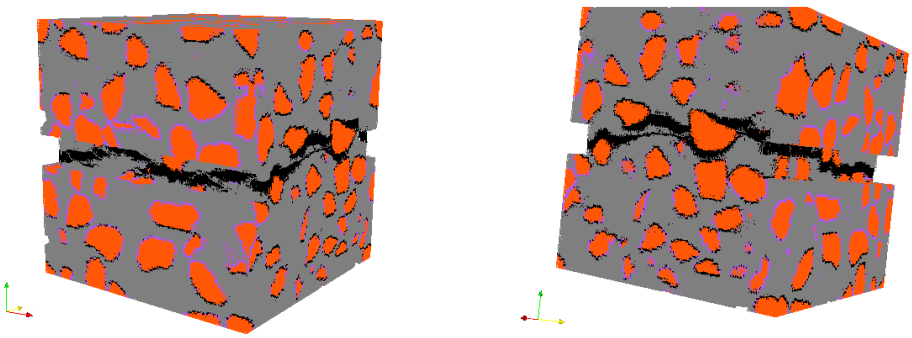

(a) (b)

Figure 10.11: Simulated fractured specimen at the failure stage of case E: (a) view from the notch side; (b) view from the non-nothced side.

linear-elastic stage, only interface elements are cracked. No crack in cement paste matrix is observed. With the load increasing, micro-cracks start to nucleate and grow in the bulk cement paste around the notches (see Figure 10.12b). This leads to the curved pre-peak load-displacement diagram. At the peak load, two macro-cracks initialized at the notches are observed (10.12c). Furthermore, a large number of interface elements are broken, which is in accordance with optical microscopy observations [333]. Two cracks are then formed as macro-cracks (see Figure 10.12d and Figure 10.12e)in stage III, leading to the significant drop of the load bearing capacity of the material. As shown in Figure 10.12f, the overlap between the two main cracks leads to the long tail before failure.

In sense of quantitative analysis, the simulated stiffness in stage II decreases more than the experimental results. As shown in Figure 10.10, a significant drop of the slope can be observed at the end of stage I, which indicates that a lot of interface elements crack at once under the same load. This is unrealistic. Furthermore, a steeper drop in stage III and a long tail with lower load are observed. In previous studies, this brittleness was explained by the relatively coarse mesh which cannot explicitly consider the influence of small aggregate and 3D effect (for a 2D model) [139, 334]. Compared with 2D model, more crack branches and overlaps can occur in 3D model. This enables a more stable crack development and more ductile post-peak behaviour. In the current study, these influences have been eliminated by using sand aggregate larger than 1 mm in both modelled material structure and real material and a 3D mesh with relatively high resolution (0.1 mm). The brittleness present in the current simulation is therefore attributed to the adopted linear-elastic constitutive relation, which neglects the softening of cement paste. Thus, the approach developed in Chapter 8 is further used to pass the post-peak information to the meso-scale model. As it has been shown in a similar type model,i.e., lattice discrete particle model, the simulated load-displacement response would be more ductile [223].

10.4.3. USING STEP-WISE SOFTENING LAW

As presented in Chapter 8, instead of removing beam element immediately from the mesh, a step-wise reduction of both the Young's modulus and strength is used. With respect to bulk cement paste, the reduction was made using the simulated stress-strain curve of 100 µm cement paste cube under uniaxial tension presented in Chapter 5. The process is schematically shown in Figure 10.13 in which a multi-linear curve with six segments is created. The points were taken at: (1) origin; (2) first cracking; (3) peak load; (4) first point in response for which load is < 75 % of the peak; (5) first point in response for which the load is < 50 % of the peak; (6) first point in response for which the load is < 25 % of the peak; (7) point for which the strain reaches 0.015. After the last point, the cement paste was regarded as failed. To consider the heterogeneity of bulk cement paste, 10 stress-strain curves simulated in Chapter 5 were schematized and listed Table 10.3. These multi-linear constitutive relations were randomly assigned to the cement paste elements.

Two sets of input constitutive relation of ITZ were considered using stress-strain curves presented respectively in Figure 7.21a and Figure 7.21b, and implemented respectively. Unlike cement paste matrix, ITZ specimens have two peaks in the simulated stress-strain response. The stress-strain curve was schematized as a multi-linear curve

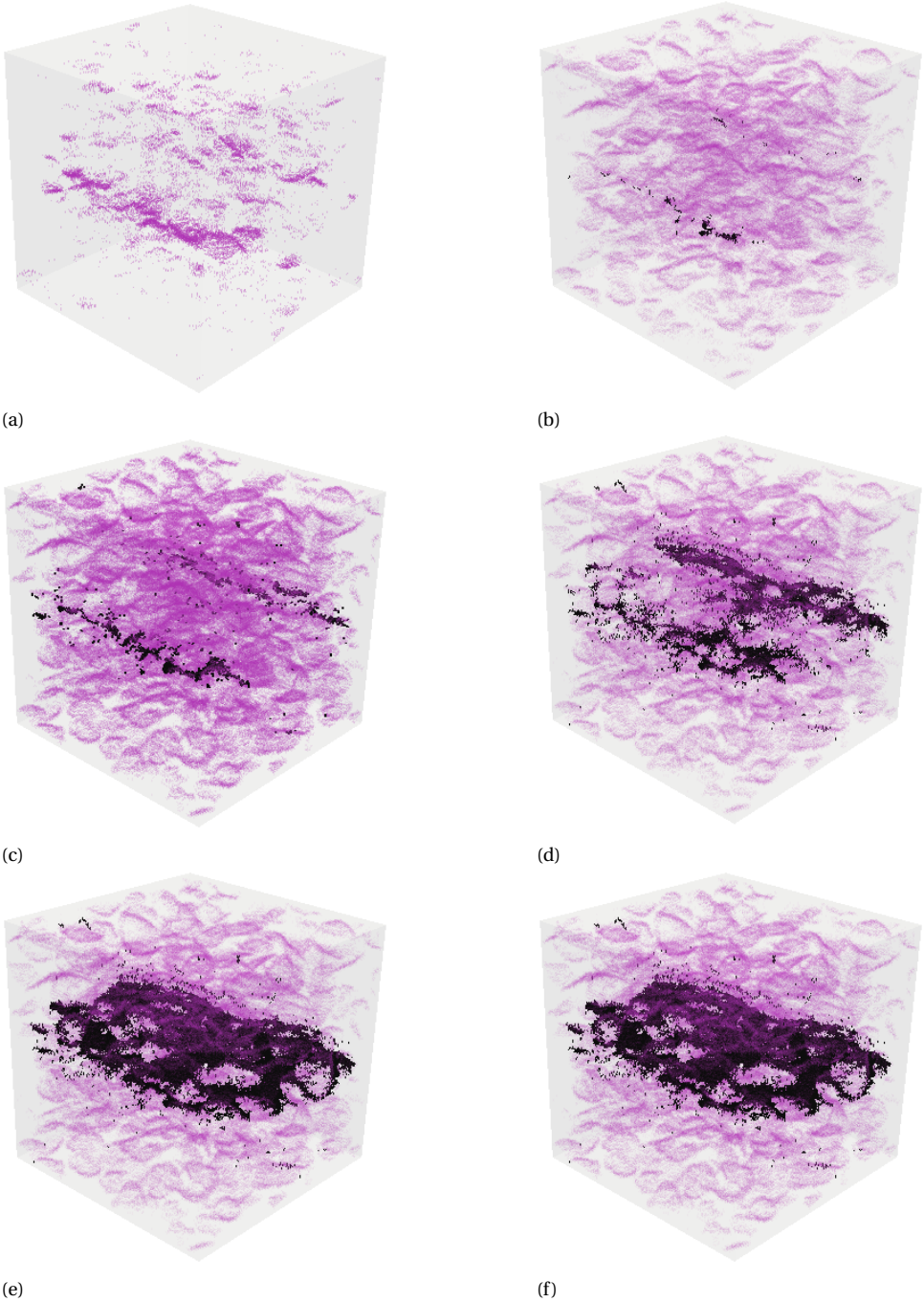

(a) (b)

(c) (d)

(e) (f)

Figure 10.12: Simulated fracture pattern of case E at different loading stage in Figure 10.10: (a) point a, end of the linear-elastic stage; (b) point b, middle point at stage II; (c) point c, peak load; (d) point d, at which load starts decreasing significantly; (e) point e, start of the long shallow tail (f) point f, material failures.(only cracked elements are plotted: violet - interface element; dark - cement paste element).

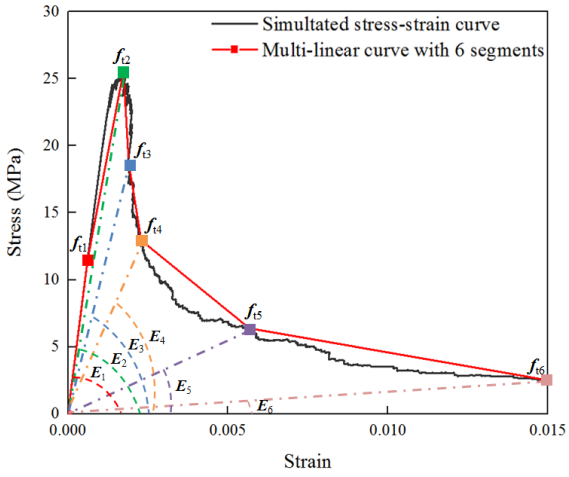

Figure 10.13: Approximation of non-linear stress-strain response of cement paste using multi-linear curve.

Table 10.3: Step-wise constitutive relation of cement paste up-scaled from the micro-scale modelling (Chapter 5, 100 µm × 100 µm × 100 µm).

Number	Mechanical parameters	Segment 1	Segment 2	Segment 3	Segment 4	Segment 5	Segment 6
1	E (GPa)	27.10	22.49	14.78	8.12	2.06	0.34
	f_t (MPa)	7.07	21.21	15.90	10.59	5.30	2.86
2	E (GPa)	29.40	24.67	16.83	10.02	2.79	0.34
	f_t (MPa)	8.23	24.67	18.50	12.34	6.14	2.38
3	E (GPa)	31.48	25.11	16.15	8.50	2.17	0.38
	f_t (MPa)	10.78	25.34	19.00	12.67	6.34	3.05
4	E (GPa)	31.86	26.63	14.60	9.52	3.26	0.22
	f_t (MPa)	6.76	22.68	17.04	11.54	5.65	1.73
5	E (GPa)	37.11	28.15	21.35	11.77	2.99	0.28
	f_t (MPa)	12.77	27.07	20.32	13.54	6.67	2.18
6	E (GPa)	35.67	28.22	18.80	10.82	2.16	0.39
	f_t (MPa)	11.49	25.55	18.66	12.94	6.39	2.81
7	E (GPa)	36.05	28.33	21.30	12.67	3.68	0.39
	f_t (MPa)	11.36	24.38	18.68	12.21	6.09	2.51
8	E (GPa)	29.92	28.37	18.86	12.48	3.98	0.38
	f_t (MPa)	11.04	25.67	19.26	12.96	6.42	2.63
9	E (GPa)	35.31	31.63	24.61	16.61	6.24	0.38
	f_t (MPa)	10.89	29.30	22.17	15.37	7.32	2.26
10	E (GPa)	33.66	32.34	27.92	14.02	4.91	0.41
	f_t (MPa)	13.36	28.07	21.44	14.27	7.03	2.56

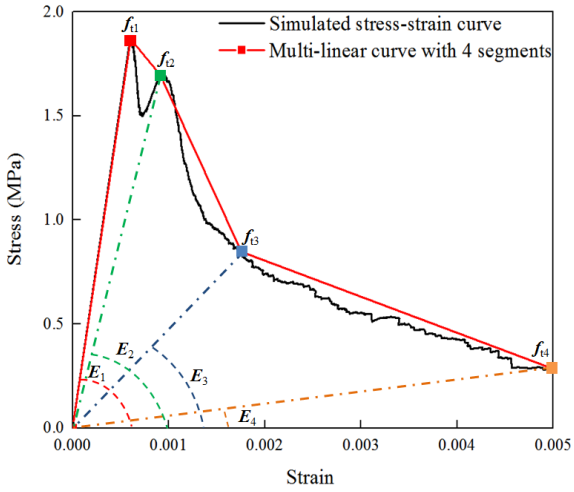

Figure 10.14: Approximation of non-linear stress-strain response of ITZ using multi-linear curve.

with four segments as shown in Figure 10.14. The five points to make the segmentation were taken at: (1) origin; (2) peak load; (3) second peak load; (4) first point in response for which the load is < 50 % of the peak; (5) point for which the strain reaches 0.005. For each set, 10 specimens that have been simulated in Chapter 7 were schematized. The constitutive relation of aggregate remains elastic brittle as in the case E. Equation 10.1 was used to calculate Young's modulus of the interface elements at all stages, while the strength at each stage equals to ITZ's. The resulting two sets of constitutive relation of the interface elements are, respectively, listed in Table 10.4 and Table 10.5 . Values in Table 10.4 were then assigned to the interface elements in simulation termed as case L, while Table 10.5 was distributed to the simulation termed as case U.

The simulated load-displacement curves of case L and case U are compared with case E and the experimental results in Figure 10.15. The calculated Young's modulus, strength and fracture energy are listed in Table 10.6. The simulated fractured specimen at failure stage is shown in Figure 10.16 and 10.17 for case L and case U respectively. Simulated crack patterns at different stages are shown in Figure 10.18 and 10.19 for case L and case U respectively.

Clearly, the simulated load-displacement curves using the step-wise approach are closer to the experimental results. As higher strengths and Young's moduli are assigned to interface elements in case U, the simulated mechanical properties of case U are higher than case L. Due to the same reason, less interface elements are cracked in case U, see Figure 10.16-10.19. The simulated Young's modulus, strength and fracture energy in Table 10.6 show a reasonable agreement with the experimental results in Table 10.1. It is worth mentioning that, in case L, the first segment of interface elements has lower moduli and strengths compared with case E. Even though, case L has higher stiffness and peak load in stage II than case E as well as a more ductile post-peak response. This is because of the fact that softening has been implemented in case L and less interface elements are removed from the mesh, see Figure 10.13 and Figure 10.18. Table 10.7 lists

Table 10.4: Step-wise constitutive relation of interface element up-scaled from the simulated lower bound of load-displacement response of ITZ (Chapter 7, 50 µm × 100 µm × 100 µm).

Number	Mechanical parameters	Segment 1	Segment 2	Segment 3	Segment 4
1	E (GPa)	5.91	3.61	0.96	0.11
	f_t (MPa)	1.87	1.69	0.85	0.29
2	E (GPa)	7.31	4.13	1.33	0.10
	f_t (MPa)	2.29	1.94	0.97	0.25
3	E (GPa)	8.58	4.74	1.48	0.01
	f_t (MPa)	2.68	2.25	1.12	0.03
4	E (GPa)	5.28	3.22	0.81	0.12
	f_t (MPa)	1.65	1.54	0.77	0.29
5	E (GPa)	6.62	3.88	1.21	0.02
	f_t (MPa)	2.08	1.82	0.91	0.06
6	E (GPa)	7.13	4.31	1.32	0.04
	f_t (MPa)	2.32	2.05	1.03	0.10
7	E (GPa)	5.87	3.48	1.03	0.03
	f_t (MPa)	1.82	1.64	0.82	0.08
8	E (GPa)	6.28	3.65	0.94	0.01
	f_t (MPa)	1.95	1.68	0.84	0.03
9	E (GPa)	6.52	3.94	1.10	0.12
	f_t (MPa)	2.08	1.87	0.93	0.29
10	E (GPa)	7.62	4.50	1.27	0.07
	f_t (MPa)	2.44	2.08	1.04	0.18

Table 10.5: Step-wise constitutive relation of interface element up-scaled from the upper bound load-displacement response of ITZ(Chapter 7, 50 µm × 100 µm × 100 µm).

Number	Mechanical parameters	Segment 1	Segment 2	Segment 3	Segment 4
1	E (GPa)	8.22	5.06	1.36	0.16
	f_t (MPa)	3.12	2.82	1.42	0.48
2	E (GPa)	10.13	5.78	1.88	0.14
	f_t (MPa)	3.82	3.23	1.62	0.42
3	E (GPa)	11.85	6.62	2.09	0.01
	f_t (MPa)	4.47	3.75	1.87	0.05
4	E (GPa)	7.36	4.52	1.14	0.17
	f_t (MPa)	2.75	2.57	1.28	0.48
5	E (GPa)	9.19	5.43	1.71	0.03
	f_t (MPa)	3.47	3.03	1.52	0.10
6	E (GPa)	9.89	6.03	1.86	0.06
	f_t (MPa)	3.87	3.42	1.72	0.17
7	E (GPa)	8.17	4.88	1.45	0.04
	f_t (MPa)	3.03	2.73	1.37	0.13
8	E (GPa)	8.73	5.11	1.33	0.01
	f_t (MPa)	3.25	2.80	1.40	0.05
9	E (GPa)	9.06	5.51	1.55	0.17
	f_t (MPa)	3.47	3.12	1.55	0.48
10	E (GPa)	10.55	6.29	1.79	0.10
	f_t (MPa)	4.07	3.47	1.73	0.30

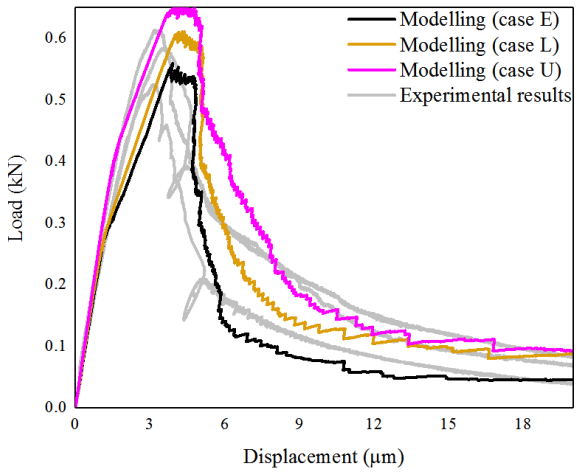

Figure 10.15: Simulated load-displacement curve using step-wise constitutive relation (compared with the experimental results).

Table 10.6: Simulated mechanical properties of the 10 mm mortar specimens.

Sample	Young's modulus (GPa)	Tensile strength (MPa)	Fracture energy (J/m^2)
Case L	25.96	6.07	25.29
Case U	27.67	6.50	31.84

the amount of cracked elements (i.e. removed from the mesh) in different stages. As expected, case U has the fewest cracked interface elements compared with the others, thus it has the least stiffness deduction in stage II and behaves more ductile in the post-peak branch. The real crack pattern would be expected in between case L and case U, as they are the two bounds for the ITZ phase derived from Chapter 7. However, it is very difficult, if not impossible, to validate these simulated crack patterns due to the technical limitations. For example, ESEM cannot be used to validate the interface cracks, as a impregnation procedure is required and the epoxy cannot go to the isolated cracks. In-situ XCT test might be a solution. However, the resolution of scanning is not high enough and there is still a challenge on the segmentation between aggregate and cement paste. Thus, the simulated crack pattern is not further validated in this thesis. More importantly, the purpose of this chapter is to show the potential of multi-scale modelling and not to have an 'exact' match. It offers the opportunity for the meso-scale model to become fully predictive as no calibration work is required at this length scale. In sense of quantitative prediction of fracture process of mortar at the meso-scale, the step-wise softening law has to be used for cement paste matrix and ITZ phase to consider the influence of heterogeneity at the micro-scale.

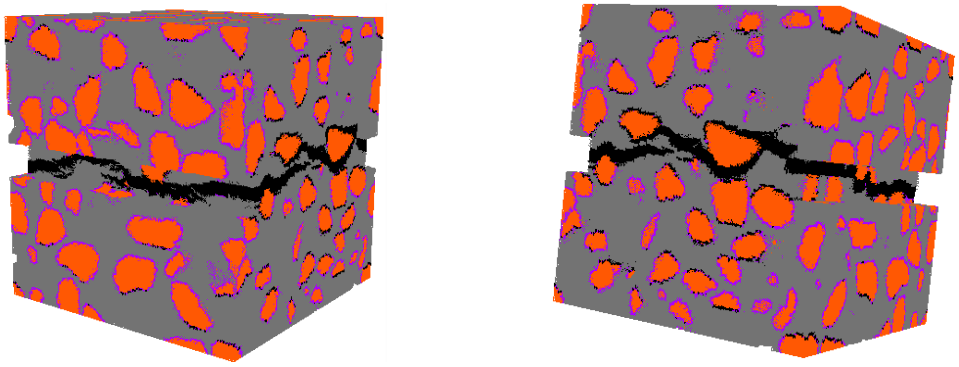

(a) (b)

Figure 10.16: Simulated fractured specimen at the failure stage of case L: (a) view from the notch side; (b) view from the non-nothced side.

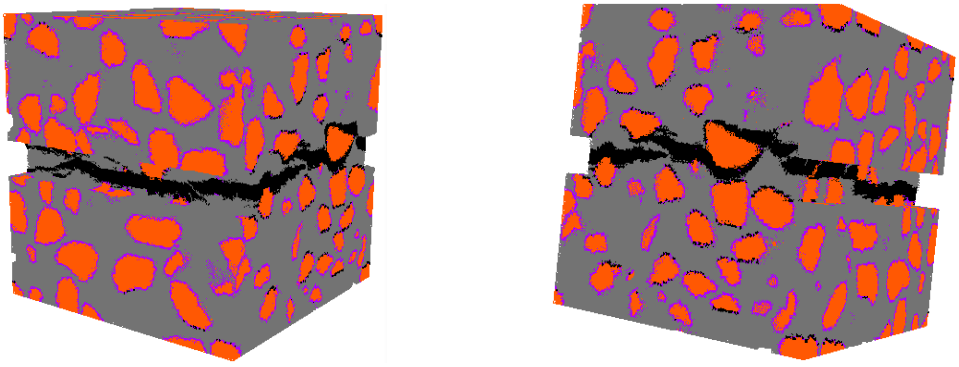

(a) (b)

Figure 10.17: Simulated fractured specimen at the failure stage of case U: (a) view from the notch side; (b) view from the non-nothced side.

Table 10.7: Summary of totally cracked element amount at different fracture stages.

Sample name	Cracked elements at peak		Cracked elements at failure stage	
	Interface	Cement paste	Interface	Cement paste
Case E	268657	1839	316769	49584
Case L	44664	877	90437	30086
Case U	23764	1304	64617	38126

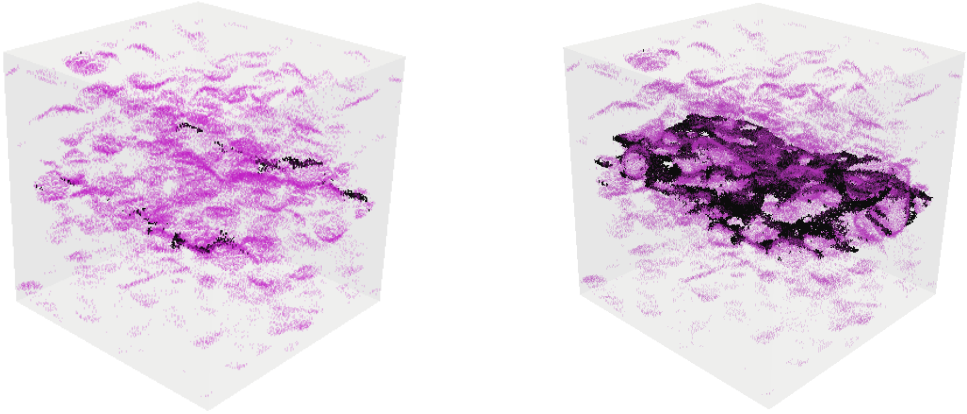

(a) (b)

Figure 10.18: Simulated fracture patterns of case L at (a) peak load and (b) failure stage.

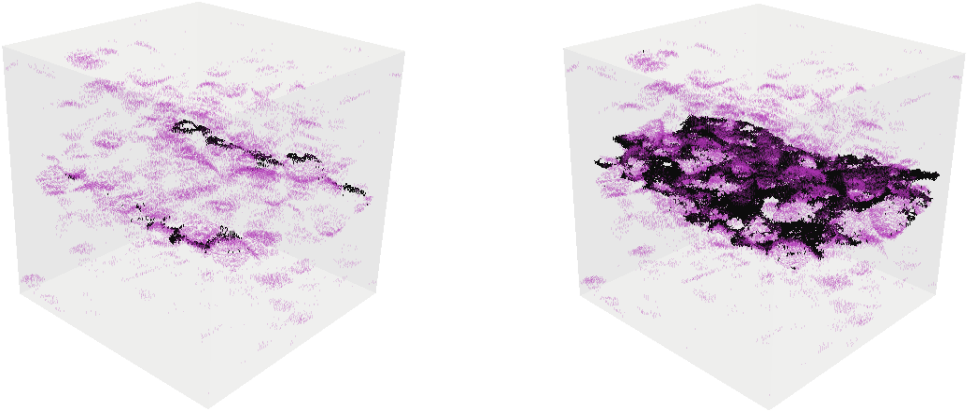

(a) (b)

Figure 10.19: Simulated fracture patterns of case U at (a) peak load and (b) failure stage.

10.5. CONCLUSIONS

IN this chapter, a comparison between numerical simulation and experimental measurement is carefully designed to validate the multi-scale modelling scheme for mortar composites at the meso-scale. Special attention was paid to make the material structure of real and virtual mortar composites comparable. Two constitutive relations (linear-elastic and step-wise softening) of local elements were assumed to up-scale the micromechanical modelling results as input for the meso-scale model. The comparison shows that the scheme using elastic constitutive relation is able to predict the realistic modulus and strength of the mortar composites. However, this does not hold for stage II and the post-peak branch. The experimental measured results behave more ductile compared with the modelling result using elastic constitutive relation. By considering the softening behaviour using the step-wise constitutive relation, the simulations show more realistic load-displacement response. In terms of crack pattern, case L has more fully cracked interface elements compared with case U. More advanced techniques are required to validate the simulated crack patterns, which is not further investigated in this thesis, because the purpose of this chapter is just to show the potential of multi-scale modelling and not to have an 'exact' match. It offers the opportunity for meso-scale model to become fully predictive as no calibration work is required at this scale.

IV

Conclusions and Prospects

11

CONCLUSION

In this chapter, a brief summary of the work presented in this PhD thesis is given. Additionally, general conclusions and findings of this research are presented and discussed. In the end, recommendations for further work are given.

11.1. RETROSPECTION

THE main aim of this PhD thesis is, starting from the micro-scale, to develop an experimentally validated multi-scale modelling scheme for cementitious materials. Discrete lattice fracture model is used as the numerical tool. Volume averaging approach is used as the upscaling approach to bridge any two adjacent scales. Two main subjects were dealt with: designing and performing micro-scale tests for the calibration and validation of the micro-scale model and sub-meso- or meso-scale experiments for the validation of adopted up-scaling approach. As developing a quantitatively sound model requires combined experimental and numerical research with different geometries under a wide variety of loading situations, the following works have been conducted in the current research.

In Chapters 3, 4, 5, and 6, the mechanical responses of hardened cement paste (HCP) micro-cube under different loading situations are studies. Micro-cube specimens are fabricated through thin-sectioning and micro-dicing, and tested by the nanoindenter. virtual micro-cubes are created by a combination of X-ray computed tomography (XCT) and image segmentation, and analysed through the discrete fracture lattice model. A set of input mechanical properties of each phase was calibrated through a so-called indentation splitting test presented in Chapter 3. The unique set of parameters was validated in Chapter 4 and Chapter 6 respectively, through the one-sided splitting and uniaxial compression tests and used to predict the stress-strain response of the micro-cube under uniaxial tension in Chapter 5.

In Appendix A, an alternative approach based on the combination of XCT and nanoindentation for micromechanical modelling of cement paste is proposed. In this approach, a link is made between the greyscale value and the micromechanical properties. Without the need for explicit identification of distinct phases, the intrinsic heterogeneity of cement paste is directly implemented using original greyscale images obtained by XCT. Compared with the approach used in Part II, the one proposed in Appendix A is more generic and direct, as no processing of the XCT images and the measured micromechanical properties is required.

Chapter 7 develops an approach to quantitatively study the interface properties between HCP and aggregates through a combined experimental and numerical approach at micro-scale. Micro-scale sized HCP-aggregate cantilever beams are fabricated and loaded by the nanoindenter. Microstructure informed lattice model is used to model the fracture process. The model is first calibrated by the experimental measurements and further used to predict the debonding process between aggregate and ITZ which is characterized by a locally more porous zone using XCT. The predicted stress-strain response is further used as input for the fracture modelling of mortar at the meso-scale in Chapter 10.

In Chapter 8, the so-called volume averaging up-scaling approach is validated by comparing the results obtained by testing and modelling respectively of a HCP beam (500 μm square cross-section) under three-point bending. Two levels of microstructure of HCP are generated by the XCT and image segmentation techniques and analysed by the lattice model. The good agreement between experimental and numerical results shows that, starting from the micro-scale and with relatively simple mechanical considerations, it is possible to reproduce the fracture behaviour of HCP at higher scale.

Based on the experimental techniques and modelling approaches that have been developed or validated in the previous chapters, the size effect is studied in Chapter 9. The size range that can be experimentally measured has been greatly extended to 1: 400, while the size range that can be numerically modelled is extended from 1:8 to 1:50. The good agreement between experimental observations and numerical results indicates that the featured material structure dominates the size effect on the measured strength in the considered size range.

Chapter 10 designs a uniaxial tension test on the 10 mm cubic specimens on the purpose of validation of fracture modelling of mortar at meso-scale. The constitutive relations of cement paste matrix and HCP-aggregate interface element are derived from the micromechanical modelling results presented in Part II through the volume averaging up-scaling approach which has been validated in Chapter 8 and 9. A good agreement is found in the linear stage and peak load when assuming elastic-brittle constitutive relations for local elements, while the relatively brittle softening branch in the modelling indicates that softening needs to be considered at the element level. This softening is further implemented using a step-wise constitutive relation derived from the results of the micro-scale simulations. When softening is considered, the simulated load-displacement become more realistic because less interface elements are broken and more crack branches are formed during the fracture process.

11.2. GENERAL CONCLUSIONS

IN every chapter of the thesis, conclusions related to that part of the work are drawn. Here, some general conclusions are given.

- *Cement paste has extremely high strength at the micro-scale*
  It is found in Part II, both tensile and compressive strengths of cement paste at micro-scale are one order of magnitude higher than meso-scale. Porosity appears to be the main factor determining the strength and stiffness of cement paste at the micro-scale, which has a high correlation with the predicted strength. The matrix prepared with higher w/c ratio results in a more porous microstructure, thus leading to a lower strength but higher variation.

- *Attention has to be given to the deviation of micromechanical properties of cementitious materials*
  In Part II, micro-cubes under different loading conditions are modelled and tested. It is found that a large deviation exists due to the heterogeneity of the microstructure. Therefore, it is suggested that the mechanical properties at the micro-scale should be given statistically, e.g. Weibull rather than a deterministic value. Therefore, a large number of tests need to be performed for the experimental measurements or numerical modelling to be statistically reliable.

- *Care has to be taken when comparing the modelling and experimental results*
  The first aspect is related with size effect. As seen in Chapter 9, the material structure of specimens at different length scales are different. Micro-scale sized specimens are free from flaws larger than the specimen size. These flaws reduce the

mechanical performance of the material significantly. Consequently, the mechanical properties predicted by the micromechanical model are not comparable with the measurements of centimetre sized specimens. The second is related with the tested boundary conditions, which has considerable influence on the response of tested material. To date, it remains a challenge to control the boundary conditions in micro-scale tests. As seen in Chapter 7, two ideal extreme loading boundaries are assumed to model the experimental loading configurations which changes with the test going on.

- *Volume averaging up-scaling approach is a valid tool to bridge two adjacent scales*
  In the volume averaging up-scaling approach, a volume size of material structure at small scale is chosen to match the smallest features in the larger scale model. In this way, the global fracture behaviour (i.e. stress- strain response) of smaller scale simulation can be used as input local constitutive relation for the fracture modelling at larger scale. It has to be remarked that the input local constitutive relation of models in sub-meso or meso-scale are directly derived from the micromechanical model in Part II, without further parameter-fitting process at the higher scale, the model can predict satisfactory stiffness, strength and crack pattern of cementitious materials under various loading boundary conditions. This enables that the model has fully predictive capabilities at the meso-scale and offers the opportunity of investigating in more detail the influence of the microstructure on the material response and engineering properties.

- *Discrete lattice model is a robust tool for fracture modelling of cementitious material at both micro- and meso-scale*
  Fracture process of specimens with different geometries and under a wide variety of loading situations are simulated using the discrete lattice model at both micro- and meso-scales. A unique set of input parameters which has been determined in Chapter 3 is consistently used in the thesis and shows a quantitatively good prediction of the mechanical performance of investigated material. The material structure can be easily implemented in the lattice model. With the development of advanced computing facilities, the model would become a powerful tool for fundamental understanding the relationship between material structure and mechanical performance.

11.3. RECOMMENDATIONS FOR FURTHER RESEARCH

AN attempt was made to construct an experimentally validated multi-scale modelling framework of cementitious material. Many issues were tackled, while others arose or were left untouched. In the future, the following experiments and numerical simulations are recommended:

- Extending the micro-scale testing and modelling approaches that have been developed in Part II to study the influence of addition of micro-particles (e.g., slag, fly ash, microcapsules, microencapsulated phase change materials), and micro or nanoparticles e.g., carbon nanotube, silica nanoparticles, titanium dioxide (TiO_2)

nanoparticles, zinc dioxide (ZnO_2) nanoparticles, calcium carbonate ($CaCO_3$) nanoparticles, and nano-clays on the micromechanical performance of the hardened pastes. This helps designing cement composites with enhanced or novel properties and functions.

- Extending the research scope to the nano-scale. At the nano-scale, atomistic simulations could be carried out to model the constitutive behaviour of each phase in HCP. With a certain packing scheme at sub-micro-scale, e.g. Jenning's model [119], hydration products with different densities can be obtained and their mechanical properties can be further analysed and used as input for the micro-scale model. Micro-scale testing techniques that has been developed in Part II can be applied to validate these input parameters as well as the modelling strategies at nano- and sub-micro-scale.

- Extending the study of size effect in Chapter 8 to the other boundary conditions (e.g. uniaxial compression and indentation splitting). Fracture of specimens with size range 1: 400 would be experimentally tested and numerical modelled. The comparison between modelling and experiment would give more insights into the origin of this phenomenon and be of practical interest.

- Extending the multi-scale modelling scheme to study the mechanisms underlying the phenomena of creep, fatigue and shrinkage at the micro-scale and their influences on the meso-scale. Experiments at both micro- and meso-scales could be carried out in case of validation of the modelling.

- Extending the developed multi-scale modelling scheme to study and design fibre reinforced concrete. At the micro-scale, the mechanical properties of the cement matrix would be studied using the approach developed in Part II. The bond between fibre and cement matrix can be studied both numerically and experimentally [335]. These micromechanical properties would be further used as input for the meso-scale modelling (consisting of matrix and packed fibres) in which a set of appropriate matrix properties and the fibre/matrix bond would lead to multiple micro cracks and increase the ductility, a strain hardening capacity can be even obtained. The developed multi-scale modelling scheme would offer a guidance and reference for designing and modifying fibre reinforced concrete.

- Coupling the fracture lattice model with lattice transport model on multiple length scales [241] to study the ions ingress in cracked cementitious materials. Starting from the material structure of cement paste at the micro-scale, both mechanical and transport properties of each phase could be numerically or experimentally determined. Through the volume averaging approach, the information from the micro-scale would be passed to the level of mortar, calculated again, and passed to the concrete scale. In this way, the influence of cracks at different length scales on the transport properties can be quantitatively studied.

V

APPENDIX

A

CORRELATION BETWEEN X-RAY COMPUTED TOMOGRAPHY AND STATISTICAL NANOINDENTATION: AN APPLICATION FOR MICROMECHANICAL MODELLING

This work proposes a method for numerically investigating the fracture mechanism of cement paste at micro-scale based on X-ray computed tomography and nanoindentation. For this purpose, greyscale level based digital microstructure was generated by X-ray microcomputed tomography with a resolution of 2 µm/voxel. In addition, statistics based micromechanical properties (i.e. Young's modulus and hardness) were derived from the grid nanoindentation test which was set to have an interaction volume the same as resolution of digital microstructure. A linear relationship between the two probability density functions of greyscale level and local Young's modulus was assumed and verified by the two-sample Kolmogorov-Smirnov (K-S) statistic. Based on this assumption, the fracture and deformation of a digital cubic volume with a dimension of 100 µm under uniaxial tension was simulated using the lattice fracture model. Furthermore, the influence of heterogeneity on fracture response was studied. The proposed method was compared with the results obtained from the approach used in the previous chapters.

Parts of this chapter have been published in Composites Part B: Engineering **157**: 109-122 (2019) [336].

A

A.1. INTRODUCTION

MICROMECHANICAL modelling of cement paste has generated considerable research interest recently as it provides an insight into the link between the material's microstructure and its global functional performance. In order to simulate the fracture behaviour of cement paste, the microstructure and micromechanical properties of its constituents need to be characterized.

Cement paste is a multi-phase material comprising several phases, most importantly calcium silicate hydrate (C-S-H), calcium hydroxide (CH), anhydrous cement clinker and pores. Consequently, micromechanical models consider, in general, a multi-phase microstructure. This microstructure can be obtained either by numerical modelling [24, 28, 29] or experiments [22, 23, 50, 51]. Both of these approaches rely heavily on the theoretical knowledge of the microstructure evolution of the material. Compared with the experiments, numerical cement hydration models have clear advantages in terms of time effort and ease of use. In such models cement clinkers are commonly modelled as spheres [24, 28]. This simplification, however, has an influence on the simulated hydration of cement [72]. Cement hydration models that consider realistic particle shapes are still rare [29, 337]. Regarding with the elasticity estimation, the simulated microstructure has a strong influence on early-age [73]. Although the microstructure has less influence in the later hydration stage, where phase volume fractions dominate the elasticity, it plays a key role in determining the material strength. On the other hand, X-ray computed tomography (XCT) is becoming a general technique for three-dimensional microstructure characterisation of cement-based materials [51–53, 338]. X-ray computed tomography can visualise the spatial distribution of cement phases with different densities by greyscale levels. The phase segmentation can then be performed to identify the spatial distribution of distinct hydration phases. However, phase segmentation is not a standardized technique: many methods exist, and it is difficult, if not impossible, to ascertain which segmentation method produces more accurate results. For example, the identified pore phase volume varies significantly depending on the applied segmentation method. In the literature [18] and [14], XCT images with similar resolution are obtained. However, a tangent-slope method merely depending on the greyscale level histogram results in a lower calculated porosity (8.65 % [18]) compared with the one from [14] using theoretical porosity from Power's model (30 %) as criteria to conduct segmentation. Since this is only the first step in micromechanical modelling, there is uncertainty already in the input. As the models are built up, there are additional sources of uncertainty, and it would be of great use to minimize the subjectivity involved in the thresholding procedure of the multi-phase material structure. To this end, this article tries to address the following question: can we avoid thresholding and use directly the greyscale material structure obtained from X-ray computed tomography as input for the micromechanical modelling of cement paste?

Another important aspect for the micromechanical modelling of cement paste are the micromechanical properties of local hydration phases. These micromechanical properties can be measured by statistical nanoindentation [16, 86, 90, 97] or calculated using molecular dynamics simulations [34, 118]. At the moment, it is difficult to directly use the data from these simulations as the real crystalline structures in cement paste are more complex compared with the ideal situation. Furthermore, the input mechani-

cal properties are resolution-dependent for the discrete micromechanics models [168]. This is because the material components and their relative amounts within the voxel (3-dimensional pixel) vary with the resolution. In the statistical nanoindentation test, a large number of indentation tests are performed in a grid without prior knowledge of the microstructure of the probed microvolume-generally termed the interaction volume [86]. The micromechanical properties (stiffness and hardness) of individual phases (anhydrous cement clinkers, inner and outer hydration products) are extracted by analysing the histograms with statistical methods such as the deconvolution method [86, 93, 94]. These values are widely used as input to perform micromechanical simulations [3, 14–16, 18, 30, 76, 135]. However, it should be noted that the scatter in the results is big and it is debated in literature whether this method can be used at all for heterogeneous materials like cement paste [19, 93–96]. A reason for this is that, although the tip-radius is very small (in case of the typically used Berkovich tip), it is almost impossible to probe a single phase; in fact, a composite made up of different phases is probed by indenting the material with a diamond tip [93]. Furthermore, when dealing with cement paste, which is a 3D heterogeneous material, the indentation outcome is always influenced by the underlying material, which can be stiffer and harder or just the opposite [19]. On the other hand, a question always arsing is how many phases should be considered in the modelling as it is still debated whether two clearly distinct phases with distinct mass densities exist [13, 16, 119, 339, 340]. Therefore, the following question is addressed: can we avoid deconvolution or averaging and use directly the micromechanical properties obtained from nanoindentation as input for the micromechanical modelling of cement paste?

This work proposes a new method for micromechanical simulations of cement paste based on a combination of statistical nanoindentation and XCT technique without the need for explicit identification of distinct phases. The material structure of cement paste was characterized by XCT and corresponding histogram of greyscale distribution. The probability density function (PDF) of micromechanical properties (i.e. histogram of micromechanical properties) was quantified using statistical nanoindentation. Without image segmentation or histogram deconvolution, micromechanical properties were directly correlated with the greyscale level by a linear equation. The linear relationship assumption was further verified by two-sample Kolmogorov-Smirnov (K-S) statistics. The influence of heterogeneity on fracture and deformation behaviour was studied by randomizing the “realistic” microstructure. Furthermore, the newly developed approach has been compared to the method considering distinct phases, previously used in the previous chapters. Strengths and drawbacks of both methods are compared and discussed.

A.2. EXPERIMENTAL

A.2.1. MATERIAL

THE tested material was a standard grade OPC CEM I 42.5 N paste with 0.4 water-to-cement ratio. First, cement was mechanically mixed with deionized water and cast into a PVA cylinder mould (diameter 24 mm, height 39 mm). After 28 days hydration, the sample was demoulded and cut into discs with thickness of 2 mm using a diamond

saw. Solvent exchange method using isopropanol was used to stop hydration of cement paste [55]. The middle portion of the slices was cut out to prepare the specimens for nanoindentation test.

A.2.2. XCT SCANNING

For acquiring greyscale based digital material structure, a small cement paste prism with cubic cross-section of 500 µm × 500 µm and length of 2 mm was produced by grinding, polishing and micro-dicing, and scanned by a Micro CT-Scanner (Phoenix Nanotom, Boston, MA, USA). The readers are referred to Chapter 3 for more details about the specimen preparation procedure. The X-ray source tube was set as 120 kev/60 µA during scanning. 2800 images with an exposure of 6 s were acquired on a digital GE DXR detector (3072 × 2400 pixels). The voxel resolution under these conditions was 2 × 2 × 2 μm^3/voxel. Reconstructed slices were carried out with Phoenix Datos|x software and a 3D stack of 8-bit cross-section images were generated in the end. A cubic region of interest (ROI) with a length of 200 µm was extracted from the specimen for the statistical analysis. To diminish the influence of beam hardening in the XCT experiment, the middle region of the specimen was chosen and analysed.

A.2.3. NANOINDENTATION

Prior to nanoindentation, the samples were ground and polished to achieve a smooth surface. For purpose of grinding, sandpapers (180, 240, 400, 600 and 800 and 1200 grit) were used in order and each sandpaper was used for 5 min-10 min. Instead of water, ethanol was used as a cooling liquid to prevent further hydration of residual cement clinkers. After grinding, samples were polished with diamond paste (6 µm, 3 µm, 1 µm, and 0.25 µm) on a lapping table in order and soaked into an ultrasonic bath to remove any residue between each polishing step. Sample preparation was performed just prior to testing to avoid carbonation of the tested surface.

KLA-Tencor G200 nano-indenter with a diamond Berkovich tip was used for nanoindentation tests. Quartz standard was indented before the test to ensure accuracy. Three specimens in total were tested. The indentation depth was 700 nm. For each specimen, a series of 25 × 20 indents were performed on a tightly spaced grid, with spacing of 20 µm between indents. This makes 1500 indents in total covering an area of 0.6 mm^2. The Continuous Stiffness Method (CSM) developed by Oliver and Pharr [81] was used. This method consists of superimposing a small oscillation on the primary loading signal and analysing the response of the system by means of a frequency-specific amplifier. As a consequence, it enables a continuous measure of contact stiffness as a function of indentation depth and not just at the point of initial unloading. Therefore, hardness and indentation modulus are obtained as a continuous function of surface penetration depth.

The nanoindentation measurements encompass mechanical properties of the local (indented) material microstructure but also the microstructure around the indent, generally with the length scale around 3–5 h_{max}, where h_{max} is the maximum indentation depth [87, 88]. This ratio between the indentation depth and interaction length (and volume) has been proposed in the literature [341–343], where correlation of micromechanical and chemical properties measured by nanoindentation and wavelength disper-

sive spectroscopy measurements was performed. In order to compare the results from nanoindentation and CT scan, it was necessary to make the interaction volume the same as the voxel size in CT scan. Therefore, the average E modulus and hardness were determined in the displacement range between 400 nm and 660 nm. For the calculation, Poisson's ratio of the indented material was taken as 0.18 in the CSM method.

A.2.4. EXPERIMENTAL RESULTS AND ASSUMPTIONS

As shown in Figure A.1a), the XCT provides visualization of the attenuation coefficients of material by greyscale level. Therefore, greyscale level of each individual voxel is determined by the attenuation coefficient of that voxel. It has been shown in the literature that the greyscale value can be correlated to the density and atomic number of the material [344]. For a constant applied voltage of the X-ray tube, there is a linear relationship between the greyscale level and the material density [345]. By virtue of this relationship, X-ray tomography can be used to measure local density variations within the material given proper calibration [346–348]. However, due to the complex material structure of cement paste, purely analytical solution mapping the attenuation to physical density has not been achieved to date. Still, greyscale level map can be assumed to represent the density distribution [18, 23, 51]. In this case, the reconstructed image is coded on 8-bit (0 to 255) greyscale level. Value 0 is black corresponding to minimum density. Value 255 is white corresponding to maximum density. A greyscale level histogram of a volume with 200 µm × 200 µm × 200 µm (100 × 100 × 100 voxels) is shown in Figure A.1b), which is expected statistically representative for cement paste at this scale. Note that this does not mean that this is a representative volume element (RVE) of cement paste. If an RVE exist depends on the process that is being considered, for fracture of softening materials an RVE might not exist due to localization issues [297].

Similar to the greyscale level, there is a relation between density and mechanical properties [349]. Therefore, an attempt is made here to correlate two values that are both density dependent: greyscale level obtained from XCT, and micromechanical properties of cement paste. With respect to bone material, elastic modulus can be linked to the CT number for the finite element model [350–352]. The CT number is represented by the Hounsfield unit and has a linear relationship with the greyscale level [353]. For cement-based materials, no published data was found defining this relationship because of the complex material structure. As the main aim of this study is to show the possibility of using a continuous model for micromechanical modelling of cement paste, a simple linear relationship between the greyscale level and elastic modulus was assumed. Nevertheless, this relationship has to be validated before it can be used as input for the modelling. The distribution of the local Young's modulus and hardness are plotted in Figure A.2 with a bin size of 1 GPa from 0 to 120 GPa. To test this approach, a two-sample Kolmogorov-Smirnov (K-S) test was performed. The K-S test is a non-parametric test, which quantifies the distance between the cumulative distribution functions of two samples [354, 355]. The null hypothesis of K-S test generally sets as that the samples are drawn from the same distribution. For two given one-dimensional PDFs, the K-S statistic is:

$$D_{n,m} = \sup \left| F_{1,n}(x), -F_{2,m}(x) \right| \tag{A.1}$$

where $F_{1,n}$ and $F_{2,m}$ are the empirical distribution functions of the first and second sam-

A

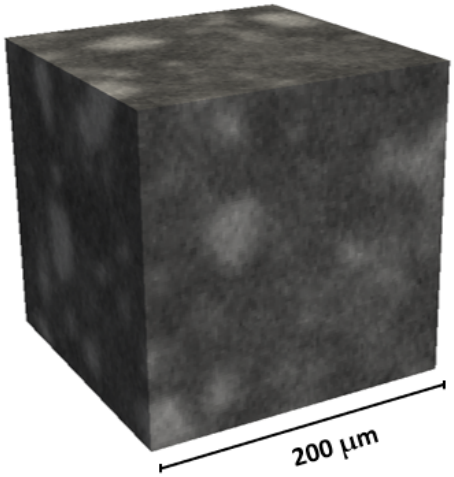

(a)

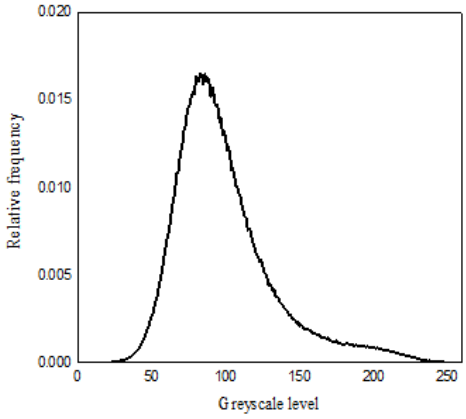

(b)

Figure A.1: Results of XCT: (a) a cubic volume of a reconstructed 3D microstructure; (b) histogram of greyscale level distribution of a volume having 10^6 voxels (8×10^6 µm^3).

ple respectively, and sup is the supremum function. The null hypothesis is rejected at level α if

$$D_{n,m} > c(\alpha)\sqrt{\frac{n+m}{nm}} \tag{A.2}$$

where n and m are the sizes of first and second sample respectively. In general, the value of c(α) is given by [356]:

$$c(\alpha) = \sqrt{-\frac{1}{2}ln(\frac{\alpha}{2})}. \tag{A.3}$$

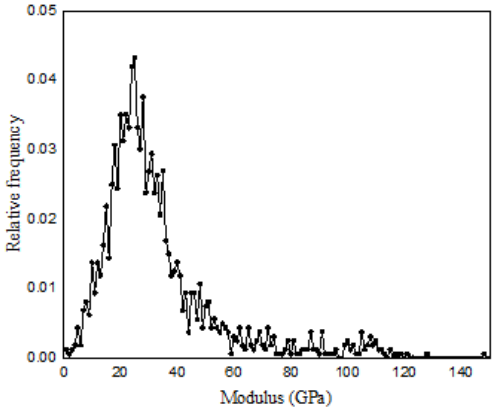

Figure A.2: Histogram of Young's modulus from nanoindentation experiments on cement paste

As shown in Figure A.3a, the two PDFs are linearly normalized to the range of 0 to 1 with a bin size of 0.01 and their cumulative probability functions are plotted in Figure A.3b. Commonly, with respect to a porous material, its stiffness approaches zero before its porosity equals 1 and a critical porosity (<100 %) always exists to represent the porosity leading to the zero stiffness [357]. In the XCT scan, voxels with porosity higher than the critical value can be detected (i.e. the air voxel with 100 % porosity has a greyscale level equals 0). However, a micro volume with zero stiffness cannot be tested by nanoindentation. Furthermore, a gap between the zero indentation modulus and minimum detected modulus between 1 and 2 GPa with a probability of 0.3 % is also observed in the PDF of elastic modulus. Therefore, to make these two distributions comparable, voxels having undetectable indentation modulus have to be eliminated from the PDF of greyscale level. For this purpose, a greyscale level (at the left tail) having the same probability as the detectable stiffness was chosen as the threshold value (T_g=42). Voxels having greyscale level lower than the threshold were then removed from the probability distribution measurements. This makes the initial greyscale level have the same probability as the minimum detected indentation modulus. Note that the probability of the minimum detected indentation modulus might change with the selected bin size. A bin size of 1 GPa was adopted herein.

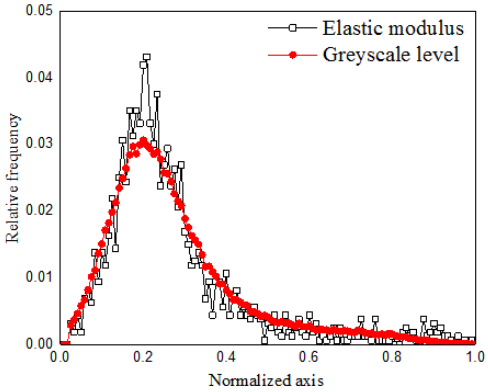

(a)

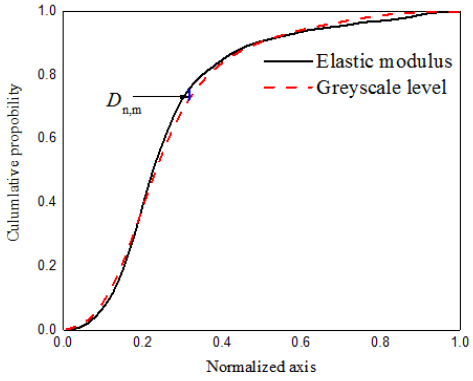

(b)

Figure A.3: Comparison of distributions of Young's modulus and greyscale level with normalized axis: (a) probability density function; (b) cumulative probability function.

In this case, $D_{n,m}$ is regarded as the maximum distance between the two cumulative probability curves which is calculated as 0.0348, and the c(α) is equal to 0.0351 with respect to a common level of α=0.05 with m=1500 and n=125000 from Equation A.3. Therefore, it is concluded from the K-S test that the null hypothesis cannot be rejected indicating that the two samples are supposed to be drawn from the same distribution with a 95 % confidence level. Therefore, for a specific greyscale level g of one voxel, its local Young's modulus can be addressed as:

$$E_{\text{local}} = \text{Min}(F(x) + (\text{Max}(F(x)) + \text{Min}(F(x))) \frac{g - T_g}{255 - T_g}, \tag{A.4}$$

where T_g is the greyscale that corresponds to the voxel having modulus equals to zero and equals 42 in this case. Min($F(x)$) and Max($F(x)$) are the minimum and maximum values that can be derived from Young's modulus histogram, and equal to 1 GPa and 120 GPa respectively. This procedure is schematically shown in Figure A.4.

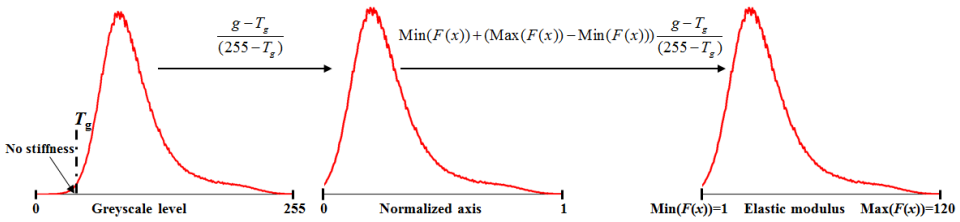

Figure A.4: A sketch of the interval conversion.

Another parameter that obtained by nanoindentation is the microhardness which can be further linked to the ultimate tensile strength of the probed micro volume. The ratio between micro hardness and tensile strength varies between 3 to 183 for different materials [358]. For cement paste, this ratio is found to be around 12 in Chapter 3. In this study, micro-cubes of cement paste were created and split using a nanoindenter. Tensile strength of individual phases in the material was then determined through inverse analysis. Since hardness of cement phases is known, a ratio between hardness and tensile strength was then obtained. The PDF of measured hardness is plotted against the greyscale level as shown in Figure A.5a. The two-sample K-S statistics as descripted above shows a maximum distance: D =0.4392 (Figure A.5b), which is greater than the critical value c(α) (0.0351) at the significance level: α = 0.05. This indicates that the microhardness cannot be correlated with the greyscale level through a linear relation. In order to determine the microhardness, an empirical model in a form of power exponent ($H_{\text{local}} = aE_{\text{local}}{}^{b}$) is proposed to correlate the hardness with its corresponding Young's modulus and shows a good fit with a determination coefficient (R^2) of 0.90 (Figure A.6). Therefore, the local tensile strength can be determined as:

$$F_{\text{local}} = \frac{aE_{\text{local}}{}^{b}}{12} \tag{A.5}$$

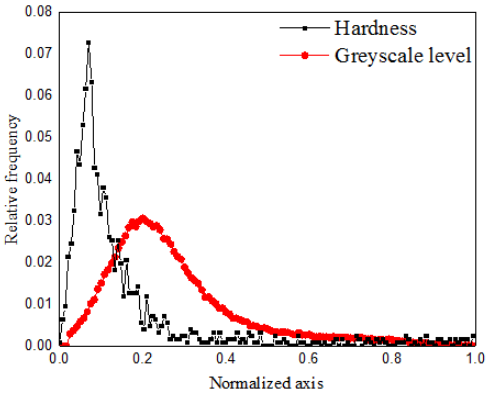

(a)

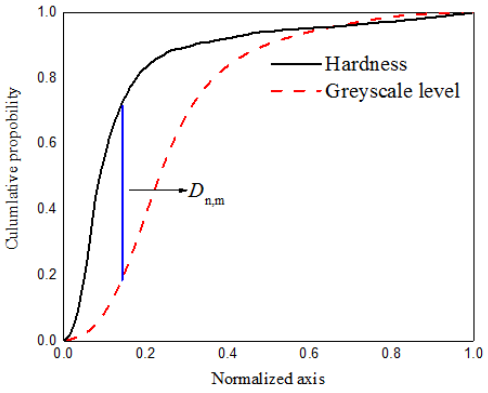

(b)

Figure A.5: Comparison of distributions of Young's modulus and greyscale level with normalized axis: (a) histogram of two distributions; (b) cumulative probability of two distributions.

where a and b are the empirical constants fitted from the experimental results. In this case, $a = 0.004288$ and $b = 1.626$. Relationships developed in this section are used in the micromechanical model as further described.

A.3. MODELLING APPROACH

FOR micromechanical modelling, the lattice-type model was used. The material heterogeneity can be easily considered by overlaying a material structure to the lattice mesh. In the current study, the digitalized greyscale level based material structure was used. The modelling details are as follows:

First, a volume of cube with length of 100 μm (50 voxels) was randomly extracted from the greyscale images obtained by XCT (Figure A.7). The red colour represents the material with highest density, while blue denotes the lowest density. For each voxel,

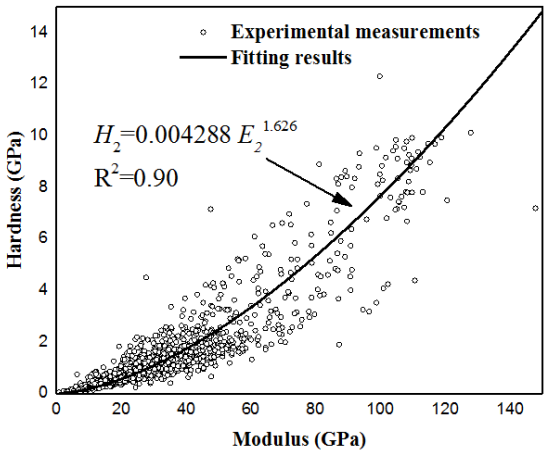

Figure A.6: Relationship between hardness and Young's modulus from nanoindentation.

its corresponding Young's modulus and tensile strength were assigned according to its greyscale level (as described in Section A.2.4). For the simulations at this scale local brittle behaviour (a linear elastic, purely brittle constitutive law at beam level) is assumed.

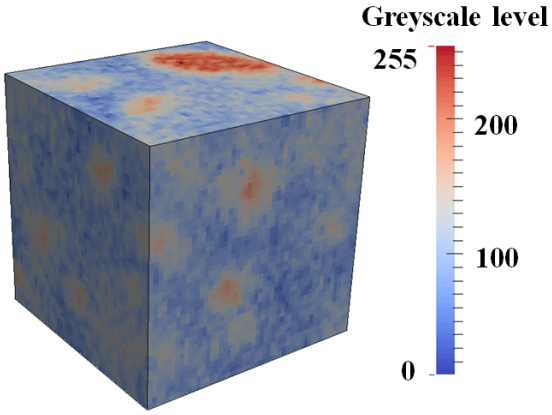

Figure A.7: A greyscale based digital material structure of cement paste with a cubic dimension of 100 µm × 100 µm × 100 µm.

The extracted volume was then used to map the heterogeneity to the mesh that has been generated in Chpater 3. Elasticity modulus of beam element was ascribed as the harmonic average of the two connected voxels, while the tensile strength was assigned as the lower value of the two. The elements connecting to the voxels with greyscale level lower than T_g (determined in Section A.2.4) were removed from the mesh as these voxels have undetectable indentation modulus. These removed elements represent the pre-

A

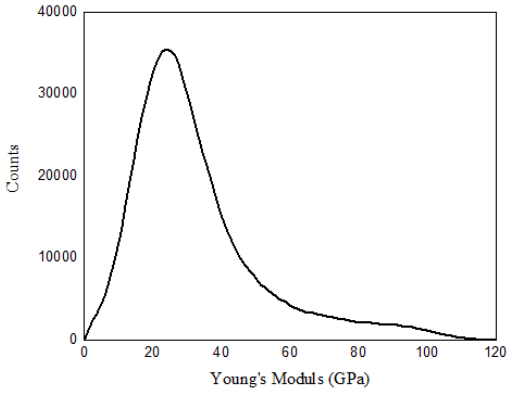

(a)

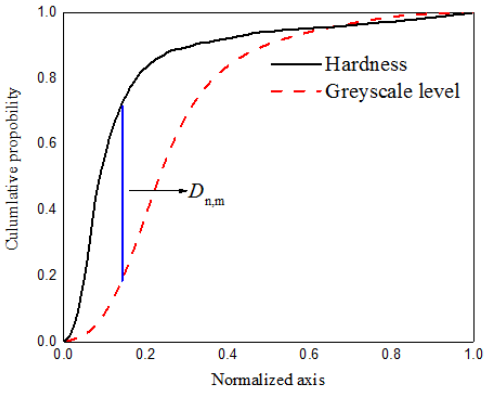

(b)

Figure A.8: Distribution of assigned mechanical properties of beam elements: (a) Young's modulus; (b) tensile strength.

existing defects in the system (see Section A.2.4). The distributions of input local mechanical properties are presented in Figure A.8.

After mapping micromechanical properties on the lattice mesh, a computational uniaxial tensile test was performed. Nodal displacement was imposed at one side while the deformation of nodes at the opposite side was completely restrained, see Figure A.9.

A.4. NUMERICAL REUSLTS AND DISCUSSION

A.4.1. RESULTS OF PROPOSED METHOD

FIGURE A.10 shows simulated stress-strain curve from where Young's modulus (E), tensile strength (f_t) and fracture energy (G_f) can be calculated. The Young's modulus can be computed from the initial slope of the curve, while tensile strength corresponds to the peak point. Fracture energy was calculated from the post-peak part of the stress-strain curve using Equation 5.1. The failure was set when displacement reaches 1 μm.

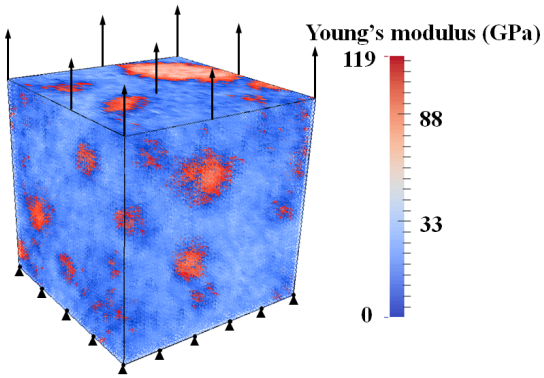

Figure A.9: Lattice system under uniaxial tension.

Note that the calculated fracture energy would be somewhat different if a different "cut-off" displacement was selected, but the main purpose of this work was to compare the fracture energy between different specimens. Herein, the simulated micromechanical properties are listed in Table A.1. Such high strength of cement paste at micro-scale was recently experimentally measured in Chapter 4. For cement paste with w/c=0.4 (prepared in the same way and using the same materials as that used in the present study), the nominal splitting strength was found to be 18.72 MPa on average with a standard deviation of 3.85 MPa. The tensile strength at this scale is almost one order of magnitude lager than the value of laboratory centimetre sized samples. This trend has been shown by the material structure informed multi-scale fracture modelling as presented in Chapter 8. Similar trend was observed in other quasi-brittle materials, e.g. nuclear graphite both experimentally [186] and numerically [106]. The value of Young's modulus obtained in the simulation (28.53 GPa) is in between the results reported by Lukovic et al. (around 33 GPa) [19] and Chapter 5 (21.07±3.01 GPa), and close to the elastic resonance measurements (around 25 GPa, Chapter [77]). The difference between the results reported in the literature could be explained by the heterogeneity nature of such material which introduces the fluctuation of its micromechanical properties.

Table A.1: Simulated micromechanical properties of Portland cement paste (w/c=0.4), corresponding with A.10.

Young's modulus (GPa)	Tensisle Strength (MPa)	Strain at peak load (%)	Fracture Energy (J/m^2)
28.53	20.01	0.08	5.89

The deformed specimen in the final failure state is presented in Figure A.11a. The red elements represent material with relatively high modulus and strength, which can be regarded as the stiff inclusion in the structure (possibly anhydrous cement clinkers). It is clear that a main crack disturbed by the stiff inclusion forms through the middle part of the volume. Similar behaviour was reported by Lukovic et al. [184]. Furthermore, crack branching and trapping are also observed. In order to have a clear look of the crack distribution and formation progress, the fracture patterns at certain failure stage are pre-

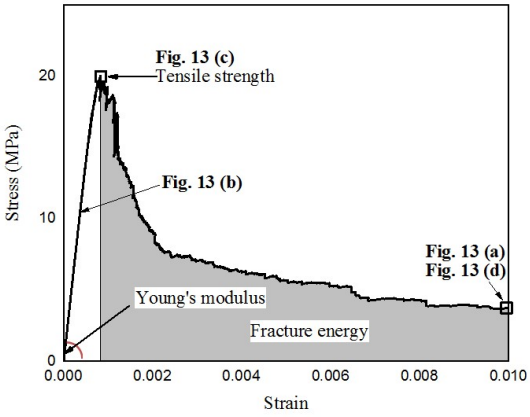

Figure A.10: Simulated stress-strain curve of cement paste under uniaxial tension test (points for which crack patterns are displayed are marked).

sented following. As shown in Figure A.11b, the distributed microcracks tend to initiate in the vicinity of the pre-existing defects where stress concentrations occur. After a certain level, the distributed micro cracks start localizing and nucleating and failure of the specimens follows (Figure A.11c). At the final stage (Figure A.11d), a main crack perpendicular to the loading direction is formed, leading to the failure of the test specimen.

A.4.2. INFLUENCE OF HETEROGENEITY

In order to investigate the influence of heterogeneity on the micromechanical performance of material structure, micromechanical properties presented in Figure A.8 were randomly distributed to the same lattice mesh, which means that each value of modulus/strength is simply randomly assigned to a lattice element in the mesh. This way, the connectivity of phases is neglected. Note that elements having no strength/stiffness are kept at the same locations. In this way, a randomized microstructure was formed and its fracture performance under uniaxial tension was computed and compared with the results considering the "realistic" microstructure. The simulated stress-strain curve and its corresponding micromechanical properties are presented in Figure A.12 and Table A.2. It is observed that the two cases have similar stiffness with difference in a range of 5%, because the input micromechanical properties have the same PDF. Unlike the elastic modulus of composite materials that is influenced by the properties of material components and their relative amounts, the (fracture) strength is governed by the weakest link in the system. Furthermore, the connectivity of weak phases (or pores) is present in the "real" system but is lost in the "random" system. As presented in Figure A.13, a completely different fracture pattern is observed. The main crack leading to the final failure shifts to the upper side. More distributed micro cracks are formed before the localization and nucleation happen in the randomized microstructure. Therefore, as expected, the randomized microstructure has significantly higher strength, enables more deformation when reaches the peak load, and releases more fracture energy. Furthermore, it is worth

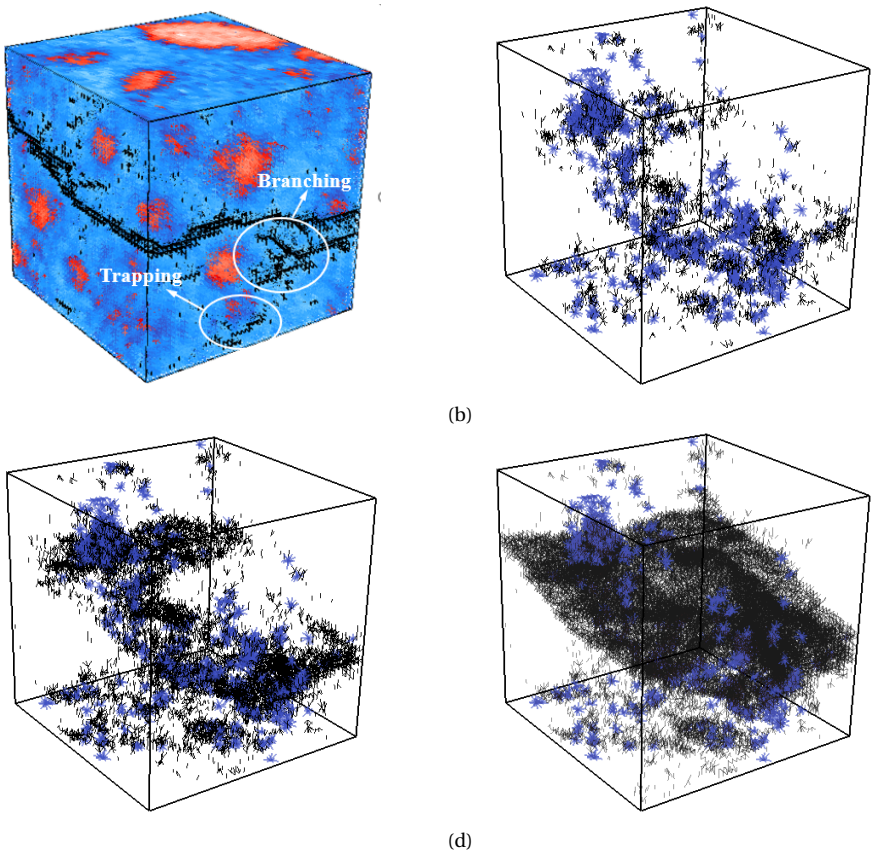

Figure A.11: Simulated fracture pattern of greyscale based microstructure: (a) deformed specimen with cracked elements at the final stage with a strain of 0.01; (b) crack pattern at elastic stage with 5000 elements cracked; (c) crack pattern at peak load with 14281 cracked elements; (d) crack pattern at the final stage with 53097 cracked elements (black represents cracked element; blue elements in the crack pattern represent elements having no strength/stiffness which are considered as the pre-existing defects in the simulation).

mentioning that a sharper decrease occurs after reaching the peak load for the randomized microstructure, which is mainly attributed to the larger amount of pre-peak micro cracks compared to the "realistic" microstructure. On the other hand, for the "realistic" microstructure, localized cracks develop around the "stiff inclusions" (mainly anhydrous clinker particles) after the initial cracking stage [19]. These cracks tend to interconnect more easily, but make more tortuous crack patterns, which enable more stable post-peak behaviour.

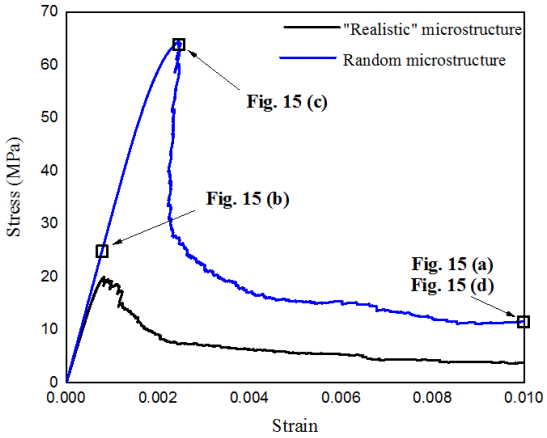

Figure A.12: Comparison of simulated stress-strain diagrams for realistic microstructure and randomized microstructure (points for which crack patterns are displayed are marked).

Table A.2: Simulated micromechanical properties of randomized material structure.

Young's modulus (GPa)	Tensisle Strength (MPa)	Strain at peak load (%)	Fracture Energy (J/m^2)
30.08	64.99	0.3	20.45

A.4.3. COMPARISON WITH METHOD CONSIDERING DISCRETE PHASES

For comparison, the method considering discrete phases (4-phase method) was performed on the same material structure. The input micromechanical properties of indu-vial phases and their relative volume amount were derived from the statistical nanoindentation as shown in Figure A.14. This was achieved by a statistical deconvolution method consisting of fitting the experimental cumulative distribution of the measured modulus as described in [92]. It is assumed in this method that the distribution of each parameter is a combination of several Gaussian distributions, each corresponding to a different phase. Three phases, namely outer hydration products (Phase 1), inner hydration products (Phase 2) and anhydrous cement clinkers (Phase 3) were determined and listed in Table A.3. It is important to notice that these hydration products are averages overall all types of hydrates (including Portlandite, Ettringite, and Calcium Silicate Hydrates (C–S–H) of different mass densities) and small capillary pores. Although it is still

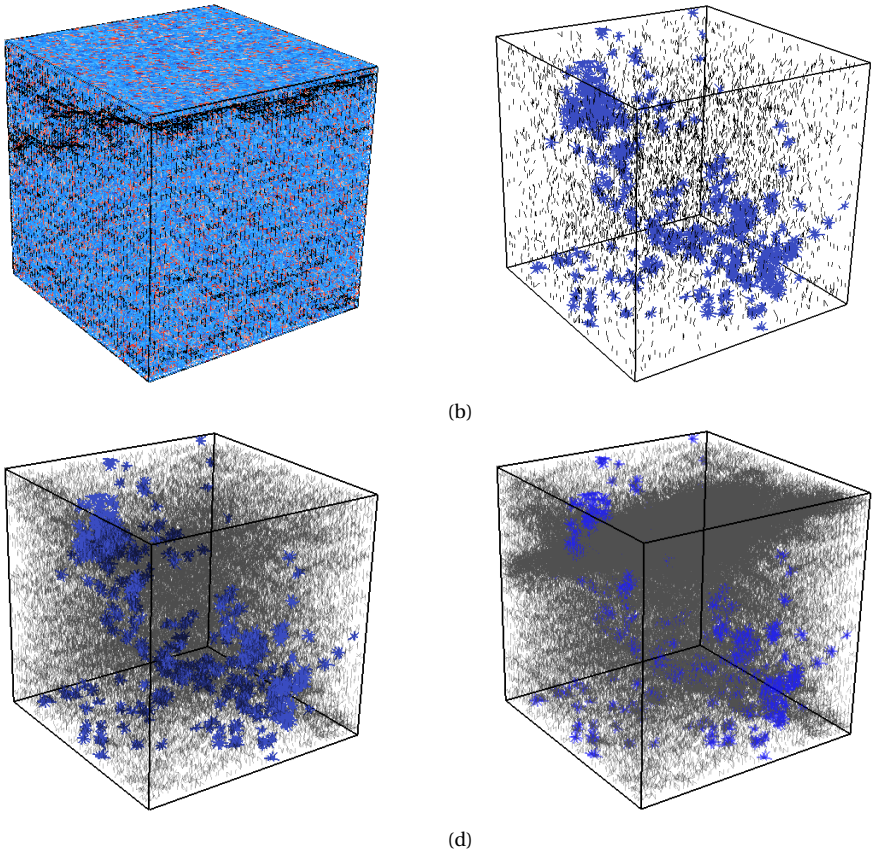

(a) (b)

(c) (d)

Figure A.13: Simulated fracture pattern of randomized microstructure: (a) deformed specimen with cracked elements at the final stage with a strain of 0.01; (b) crack pattern at initial stage with 5000 elements cracked; (c) crack pattern at peak load with 63677 cracked elements; (d) crack pattern at the final stage with 121464 cracked elements (black represents cracked element; blue elements in the crack pattern represent elements having no strength/stiffness which are considered as the pre-existing defects in the simulation).

under debate whether 3 phases should be distinguished from the statistical nanoindentation and what they indeed represent, again, the purpose of adopting this deconvolution method is to compare with the method using a continuous material structure proposed in this work. The distinction of two types of hydration products, inner and outer hydration products, is adopted here for simplification.

The elastic moduli of distinct phases (Table A.3) determined in the current work are somewhat different from those reported results in the literatures [16, 86, 97]. This is because the current results are derived from a different indentation depth, which results in a different interaction volume. The next step is related with segmentation phases from the greyscale level based microstructure. For this purpose, the global threshold method was applied. The cumulative distribution of greyscale level was used to determine the threshold value (see Figure A.15). In the current work, the upper threshold value of capillary pore (P) was determined by the tangent-slope method [43] in which greyscale value at inflection point in the cumulative distribution curve is used. This point represents the critical point where a small increment in the threshold value will cause a sharp increase in the segmented volume fraction of pores. The threshold of the rest phases were set to meet their relative amount determined by statistical nanoindentation. The determined relative amount is 0.0949, 0.6184, 0.2128 and 0.0740 for capillary pores (P), outer hydration products (O), inner hydration products (I) and anhydrous cement clinkers (A) respectively. The four intervals are then formed, and the voxel's phase can be labelled according to the interval its greyscale level falls in. The segmented material structure and its corresponding lattice mesh are presented in Figure A.16 and Figure A.17 respectively. Note that elements connecting the voxel labelled as pore were eliminated from the mesh. Therefore, six types of elements with different mechanical properties were generated (Table A.4).

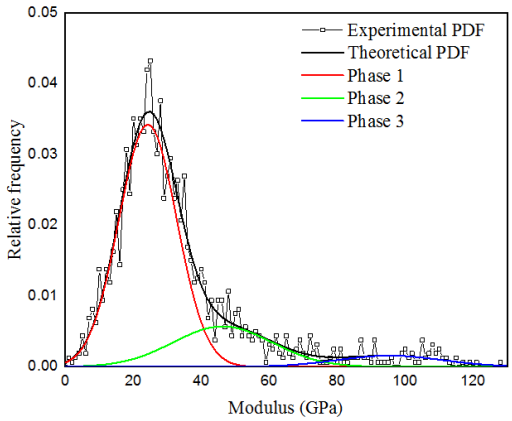

Figure A.14: Experimental and theoretical probability density function plots of Young's modulus from statistical indentation

As shown in Figure A.18, the simulated stress-strain curve of the 4-phase composite is compared with the results from greyscale level based microstructure. Although similar stress-strain response is found for the two methods, the 4-phase composite has a

Table A.3: Micromechanical properties of distinct solid phases determined by the deconvolution method and Equation A.5.

Phase name	Young's modulus (GPa)	Tensisle Strength (MPa)	Relative amount (%)
Outer hydration products	23.82	61.94	68.51
Inner hydration products	42.06	156.13	23.99
Anhydrous cement clinkers	90.30	540.78	7.5

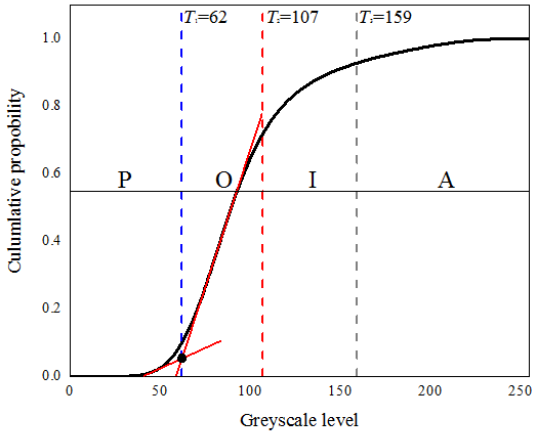

Figure A.15: Schematic view of threshold value determination.

somewhat lower stiffness but higher strength and fracture energy (Table A.5). The lower stiffness is mainly attributed to the higher porosity included in the material [182], while the higher strength is because of the big difference between assigned mechanical properties. For example, the anhydrous cement particle works as the stiff inclusion in the matrix, forcing the crack to propagate around it. This results in a more tortuous and overlapped crack pattern. Thus, a more stable crack propagation and higher strength can be expected. The higher porosity in the 4-phase method reduces the number of elements in the lattice system, which makes the main crack forms with less cracked elements, as more pre-existing defects can be localized or nucleated to form to the main crack. Figure A.19 shows the cracked 4-phase composite at final stage and the crack patterns at certain deformation levels. Although it is observed that the crack patterns at pre-peak

Table A.4: Local mechanical properties of lattice elements.

Element type	Young's modulus (GPa)	Tensisle Strength (MPa)
A-A	90.30	540.78
A-I	57.89	156.13
A-O	37.70	61.94
I-I	42.06	156.13
I-O	30.42	61.94
O-O	23.82	61.94

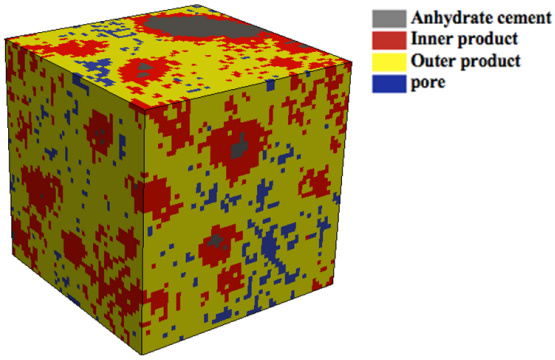

Figure A.16: 4-phase microstructure segmented from greyscale level based microstructure in A.7.

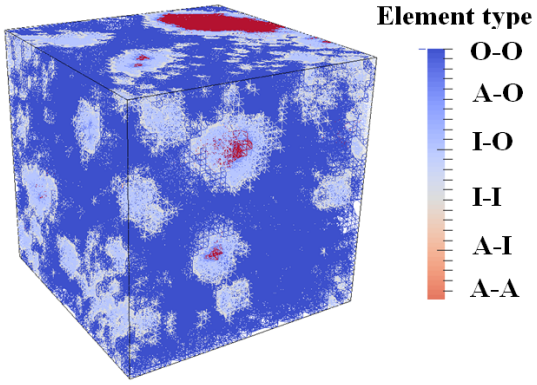

Figure A.17: Lattice discretization of 4-phase microstructure.

stage are different for these two methods because of the difference in the pre-existing defects spatial distribution, the final crack patterns at final stage are almost identical to each other. This indicates that, on one hand, the pre-peak crack propagation is mainly governed by pre-existing defects, one the hand the stiff inclusions have more influence on the post-peak crack propagation and localization. This is in accordance with expectations: the pre-peak phase is characterised by microcrack growth, which is influenced by the defects, while the post peak phase is characterised by bridging and branching, which are influenced by the inclusions.

A.5. GENERAL DISCUSSION

As shown in the comparison, a similar fracture pattern and stress-strain response is found in between the 4-phase method and greyscale level based method. It is dif-

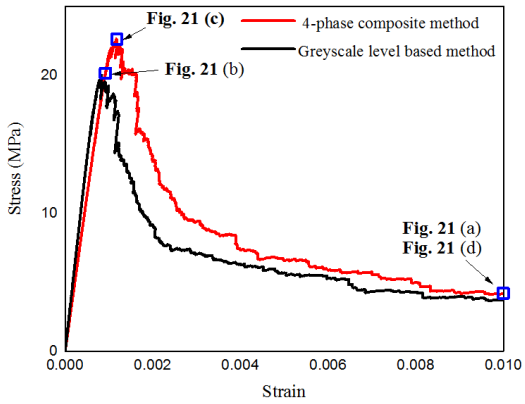

Figure A.18: Comparison of simulated stress-strain diagrams for greyscale level based microstructure and 4-phase microstructure (points for which crack patterns are displayed are marked).

Table A.5: Simulated micromechanical properties of 4-phase composite microstructure.

Young's modulus (GPa)	Tensisle Strength (MPa)	Strain at peak load (%)	Fracture Energy (J/m^2)
22.61	22.64	0.12	8.28

ficult to determine which method gives more satisfactory results on the micromechanical modelling, but the proposed approach is more generic and direct. It requires less processing steps (no need for deconvolution or averaging of properties, which might introduce errors) and can be always applied once the link is made between the greyscale value and the micromechanical properties. As the intrinsic heterogeneity of cement paste is directly implemented from the XCT scanning, no additional assumptions need to be made with regard to distribution of local micromechanical properties. The 4-phase method distinguishes four homogeneous phases with distinct material properties (no gradients are considered due to deconvolution and averaging); in reality, none of the phases considered is completely homogeneous, and a gradient of material properties in each of the phases might exist. This is probably captured better with the current model. With respect to the application, the grey-scale based method requires less prior knowledge, as no processing of the XCT images and the measured micromechanical properties is required. Therefore, the greyscale level based method shows advantages in micromechanical modelling of a composite material with limited knowledge on the microstructure and micromechanical properties of its constituents. However, it should be noted that the local micromechanical properties should be the representative of the XCT resolution. This is because, with resolution variation, different amounts of capillary porosity or defects may be included in a voxel thereby introducing different micromechanical properties of the voxel. Therefore, when this method is applied, the interaction volume probed by the nanoindenter must be kept the same as the image voxel size. It is worth mentioning that this issue should also be considered when using the 4-phase method. Furthermore, it is possible to improve the spatial resolution of current microstructure

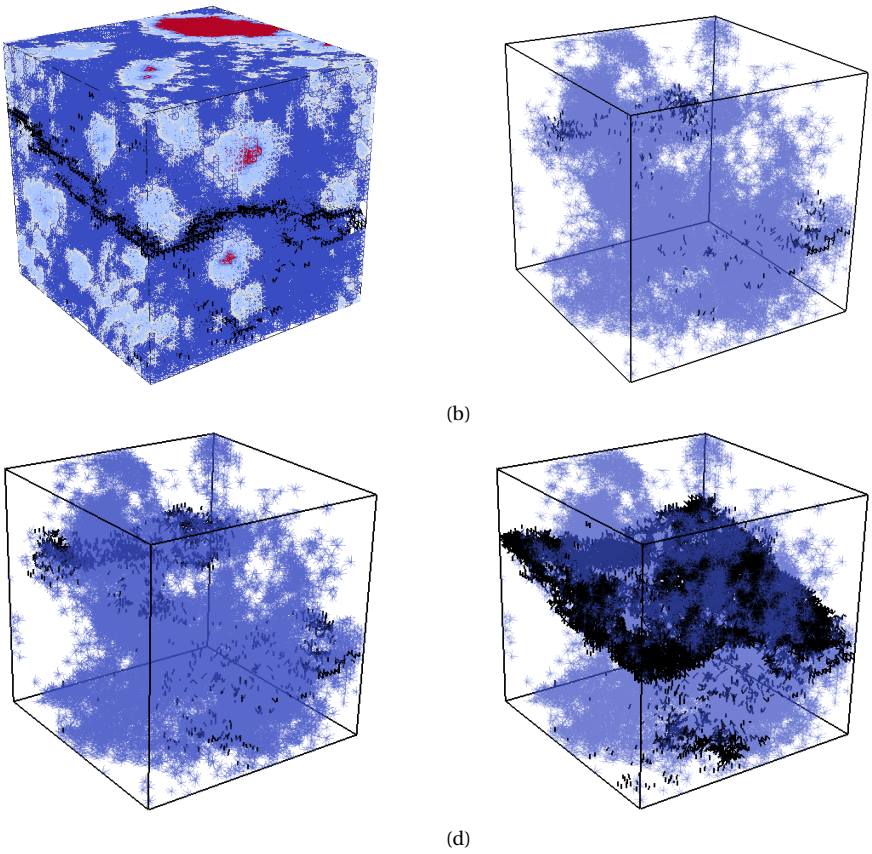

Figure A.19: Simulated fracture pattern of the 4-phase composite: (a) deformed specimen with cracked elements at the final stage with a strain of 0.01; (b) crack pattern at initial stage with 500 elements cracked; (c) crack pattern at peak load with 1848 cracked elements; (d) crack pattern at the final stage with 23917 cracked elements (black represents cracked element; blue elements in the crack pattern represent elements having no mechanical properties which are considered as the pre-existing defects in the simulation).

to 0.5 microns by XCT scanning without changing the scanned size of the specimen, or to 50 nm resolution with different setting [359, 360]. But, again, the corresponding micromechanical properties should be determined from a smaller interaction volume. This can be achieved by deriving data from a shallower depth of nanoindentation test or using other techniques such as atomic force microscopy [361]. Furthermore, current limitations of the proposed method should be addressed. As we focus on the feasibility of the proposed continuous method, the relationship between the greyscale level and local mechanical properties was determined by assumption and statistical analysis. Although a validation procedure was carried out to prove the correctness of the assumption, a physical explanation is still lacking. Therefore, a throughout understanding of the relationship between the greyscale level and local mechanical properties is expected to be gained in the future to achieve the automatic assignment of local micromechanical properties from XCT data for the micromechanical modelling.

A.6. CONCLUSIONS

In this work, a new approach for micromechanical modelling of cement paste is proposed. Without the need for explicit identification of distinct phases, the intrinsic heterogeneity of cement paste is directly implemented using original greyscale images obtained by XCT. The PDFs (i.e. histograms) of nanoindentation measurements (both Young's modulus and microhardness) and greyscale value were normalized linearly and tested by a two-sample K-S statistics, showing that a strong linear relationship exists between Young's modulus and greyscale level, while microhardness has a weak linear correlation with grayscale value. An empirical model in a form of power exponent was therefore proposed to correlate the hardness with its corresponding Young's modulus and showed a good fit. The micromechanical properties (E modulus and micro hardness) were then mapped to the voxels according to their greyscale level.

The deformation and fracture of a greyscale level based microstructure was simulated using a discrete lattice model. The influence of material heterogeneity and phase distribution on the mechanical performance is studied by comparing a "realistic" and a "randomized" microstructure. Although similar elastic moduli are obtained, much higher strength and more distributed micro cracks are observed in the "randomized" microstructure. Therefore, the distribution of heterogeneous phases in a composite quasi-brittle material like cement paste is critical when it comes to the overall mechanical behaviour. Phase connectivity plays an important role in the process of crack propagation and growth. If the phases are clustered in stiff and strong particles and weak interfaces, it will lead to a much lower strength of the composite than in the case the same properties are randomly distributed over the sample. This leads to strong limitations when use of RVE and homogenization are considered for composites with crack localization.

The fracture behaviour of greyscale level based microstructure is also compared with the method considering discrete phases. The comparison shows that the strength of material obtained by the method considering discrete phases is higher compared to the method of greyscale level based microstructure. This might be attributed to the additional processing steps that are applied in the method considering discrete phases: deconvolution and averaging. Errors and biases might occur in any of these steps.

The proposed method is promising, because it captures the gradient of material prop-

erties in cement paste that is more realistic. However, a physical understanding behind the relationship between the XCT data and local micromechanical properties is still not sufficiently understood and deserves further study. It is expected that, in the future, the fracture behaviour of different types of binders at the micro-scale possibly can be studied based only on XCT and the reliable link between the greyscale value obtained by XCT and micromechanical properties measured by nanoindentation as proposed in this study.

REFERENCES

REFERENCES

[1] A. M. Neville, Properties of concrete, Pearson, 2002.

[2] J. G. Van Mier, Concrete fracture: a multiscale approach, CRC press, 2012.

[3] O. Bernard, F.-J. Ulm, E. Lemarchand, A multiscale micromechanics-hydration model for the early-age elastic properties of cement-based materials, Cement and Concrete Research 33 (9) (2003) 1293–1309.

[4] Z. Qian, Multiscale modeling of fracture processes in cementitious materials, Ph.D. thesis, Delft University of Technology, Delft, The Netherlands (2012).

[5] Z. Qian, E. Schlangen, G. Ye, K. van Breugel, Modeling framework for fracture in multiscale cement-based material structures, Materials 10 (6) (2017) 587.

[6] F. Bernard, S. Kamali-Bernard, W. Prince, 3D multi-scale modelling of mechanical behaviour of sound and leached mortar, Cement and Concrete Research 38 (4) (2008) 449–458.

[7] V. P. Nguyen, M. Stroeven, L. J. Sluys, Multiscale failure modeling of concrete: micromechanical modeling, discontinuous homogenization and parallel computations, Computer Methods in Applied Mechanics and Engineering 201 (2012) 139–156.

[8] E. A. Rodrigues, O. L. Manzoli, L. A. Bitencourt Jr, T. N. Bittencourt, M. Sánchez, An adaptive concurrent multiscale model for concrete based on coupling finite elements, Computer Methods in Applied Mechanics and Engineering 328 (2018) 26–46.

[9] B. Sun, Z. Li, Adaptive concurrent multi-scale fem for trans-scale damage evolution in heterogeneous concrete, Computational Materials Science 99 (2015) 262–273.

[10] P. Chaudhuri, Multi-scale modeling of fracture in concrete composites, Composites Part B: Engineering 47 (2013) 162–172.

[11] V. P. Nguyen, M. Stroeven, L. J. Sluys, An enhanced continuous–discontinuous multiscale method for modeling mode-i cohesive failure in random heterogeneous quasi-brittle materials, Engineering Fracture Mechanics 79 (2012) 78–102.

[12] F. Wittmann, Structure of concrete with respect to crack formation, in: F. Wittmann (Ed.), Fracture Mechanics of Concrete, Elsevier, Amsterdam, The Netherlands, 1983, pp. 43–74.

A

[13] P. D. Tennis, H. M. Jennings, A model for two types of calcium silicate hydrate in the microstructure of portland cement pastes, Cement and Concrete Research 30 (6) (2000) 855–863.

[14] T.-S. Han, X. Zhang, J.-S. Kim, S.-Y. Chung, J.-H. Lim, C. Linder, Area of lineal-path function for describing the pore microstructures of cement paste and their relations to the mechanical properties simulated from μ-ct microstructures, Cement and Concrete Composites 89 (2018) 1–17.

[15] B. Pichler, C. Hellmich, Upscaling quasi-brittle strength of cement paste and mortar: A multi-scale engineering mechanics model, Cement and Concrete Research 41 (5) (2011) 467–476.

[16] G. Constantinides, F.-J. Ulm, The effect of two types of CSH on the elasticity of cement-based materials: Results from nanoindentation and micromechanical modeling, Cement and concrete research 34 (1) (2004) 67–80.

[17] M. Zhang, A. P. Jivkov, Microstructure-informed modelling of damage evolution in cement paste, Construction and Building Materials 66 (2014) 731–742.

[18] M. Zhang, A. P. Jivkov, Micromechanical modelling of deformation and fracture of hydrating cement paste using x-ray computed tomography characterisation, Composites Part B: Engineering 88 (2016) 64–72.

[19] M. Luković, E. Schlangen, G. Ye, Combined experimental and numerical study of fracture behaviour of cement paste at the microlevel, Cement and Concrete Research 73 (2015) 123–135.

[20] Z. P. Bažant, Size effect, International Journal of Solids and Structures 37 (1) (2000) 69–80.

[21] A. Carpinteri, B. Chiaia, G. Ferro, Size effects on nominal tensile strength of concrete structures: multifractality of material ligaments and dimensional transition from order to disorder, Materials and Structures 28 (6) (1995) 311.

[22] K. L. Scrivener, Backscattered electron imaging of cementitious microstructures: understanding and quantification, Cement and Concrete Composites 26 (8) (2004) 935–945.

[23] E. Gallucci, K. Scrivener, A. Groso, M. Stampanoni, G. Margaritondo, 3D experimental investigation of the microstructure of cement pastes using synchrotron x-ray microtomography (μct), Cement and Concrete Research 37 (3) (2007) 360–368.

[24] K. Van Breugel, Simulation of hydration and formation of structure in hardening cement-based materials, Ph.d. thesis, Delft University of Technology, Delft, The Netherlands (1991).

[25] E. A. B. Koenders, Simulation of volume changes in hardening cement-based materials, Ph.d. thesis, Delft University of Technology, Delft, The Netherlands (1997).

[26] G. Ye, Experimental study and numerical simulation of the development of the microstructure and permeability of cementitious materials, Ph.d. thesis, Delft University of Technology, Delft, The Netherlands (2003).

[27] S. Bishnoi, Vector modelling of hydrating cement microstructure and kinetics, Ph.d. thesis, École polytechnique fédérale de Lausanne, Lausanne, Switzerland (2008).

[28] S. Bishnoi, K. L. Scrivener, μic: A new platform for modelling the hydration of cements, Cement and Concrete Research 39 (4) (2009) 266–274.

[29] D. P. Bentz, Three-dimensional computer simulation of portland cement hydration and microstructure development, Journal of the American Ceramic Society 80 (1) (1997) 3–21.

[30] C. Hu, Z. Li, Micromechanical investigation of portland cement paste, Construction and Building Materials 71 (2014) 44–52.

[31] H. M. Jennings, J. J. Thomas, J. S. Gevrenov, G. Constantinides, F.-J. Ulm, A multitechnique investigation of the nanoporosity of cement paste, Cement and Concrete Research 37 (3) (2007) 329–336.

[32] J. J. Hughes, P. Trtik, Micro-mechanical properties of cement paste measured by depth-sensing nanoindentation: a preliminary correlation of physical properties with phase type, Materials characterization 53 (2) (2004) 223–231.

[33] H. Manzano, J. Dolado, A. Guerrero, A. Ayuela, Mechanical properties of crystalline calcium-silicate-hydrates: comparison with cementitious C-S-H gels, physica status solidi (a) 204 (6) (2007) 1775–1780.

[34] R. J.-M. Pellenq, A. Kushima, R. Shahsavari, K. J. Van Vliet, M. J. Buehler, S. Yip, F.-J. Ulm, A realistic molecular model of cement hydrates, Proceedings of the National Academy of Sciences 106 (38) (2009) 16102–16107.

[35] M. K. Head, N. R. Buenfeld, Confocal imaging of porosity in hardened concrete, Cement and Concrete Research 36 (5) (2006) 896–911.

[36] M. Yio, M. Mac, H. Wong, N. Buenfeld, 3D imaging of cement-based materials at submicron resolution by combining laser scanning confocal microscopy with serial sectioning, Journal of Microscopy 258 (2) (2015) 151–169.

[37] L. Holzer, P. Gasser, A. Kaech, M. Wegmann, A. Zingg, R. Wepf, B. Muench, Cryo-fib-nanotomography for quantitative analysis of particle structures in cement suspensions, Journal of Microscopy 227 (3) (2007) 216–228.

[38] P. Trtik, B. Münch, P. Gasser, A. Leemann, R. Loser, R. Wepf, P. Lura, Focussed ion beam nanotomography reveals the 3D morphology of different solid phases in hardened cement pastes, Journal of microscopy 241 (3) (2011) 234–242.

A

[39] S. R. Chae, J. Moon, S. Yoon, S. Bae, P. Levitz, R. Winarski, P. J. Monteiro, Advanced nanoscale characterization of cement based materials using x-ray synchrotron radiation: a review, International Journal of Concrete Structures and Materials 7 (2) (2013) 95–110.

[40] J. Ha, S. Chae, K. Chou, T. Tyliszczak, P. Monteiro, Effect of polymers on the nanostructure and on the carbonation of calcium silicate hydrates: a scanning transmission x-ray microscopy study, Journal of materials science 47 (2) (2012) 976–989.

[41] J. I. Goldstein, D. E. Newbury, J. R. Michael, N. W. Ritchie, J. H. J. Scott, D. C. Joy, Scanning electron microscopy and X-ray microanalysis, Springer, 2017.

[42] K. L. Scrivener, H. Patel, P. Pratt, L. Parrott, Analysis of phases in cement paste using backscattered electron images, methanol adsorption and thermogravimetric analysis, MRS Online Proceedings Library Archive 85.

[43] H. Wong, M. Head, N. Buenfeld, Pore segmentation of cement-based materials from backscattered electron images, Cement and Concrete Research 36 (6) (2006) 1083–1090.

[44] V. Shah, K. Scrivener, B. Bhattacharjee, S. Bishnoi, Changes in microstructure characteristics of cement paste on carbonation, Cement and Concrete Research 109 (2018) 184–197.

[45] J. Němeček, V. Králík, V. Šmilauer, L. Polívka, A. Jäger, Tensile strength of hydrated cement paste phases assessed by micro-bending tests and nanoindentation, Cement and Concrete Composites 73 (2016) 164–173.

[46] A. Michel, B. J. Pease, M. R. Geiker, H. Stang, J. F. Olesen, Monitoring reinforcement corrosion and corrosion-induced cracking using non-destructive x-ray attenuation measurements, Cement and Concrete Research 41 (11) (2011) 1085–1094.

[47] M. Souza, L. C. Pardini, E. C. Botelho, M. Costa, X-ray tomography applied to the void/defect measurement of hybrid cfrc/sic composites, Materials Research Express.

[48] F. Auzerais, J. Dunsmuir, B. Ferreol, N. Martys, J. Olson, T. Ramakrishnan, D. Rothman, L. Schwartz, Transport in sandstone: A study based on three dimensional microtomography, Geophysical Research Letters 23 (7) (1996) 705–708.

[49] E. Rosenberg, J. Lynch, P. Gueroult, M. Bisiaux, R. F. De Paiva, High resolution 3D reconstructions of rocks and composites, Oil & Gas Science and Technology 54 (4) (1999) 497–511.

[50] C. Hall, S. L. Colston, A. C. Jupe, S. D. Jacques, R. Livingston, A. O. Ramadan, A. W. Amde, P. Barnes, Non-destructive tomographic energy-dispersive diffraction imaging of the interior of bulk concrete, Cement and Concrete Research 30 (3) (2000) 491–495.

[51] T. Chotard, M. Boncoeur-Martel, A. Smith, J. Dupuy, C. Gault, Application of x-ray computed tomography to characterise the early hydration of calcium aluminate cement, Cement and Concrete Composites 25 (1) (2003) 145–152.

[52] M. A. B. Promentilla, T. Sugiyama, T. Hitomi, N. Takeda, Quantification of tortuosity in hardened cement pastes using synchrotron-based x-ray computed microtomography, Cement and Concrete Research 39 (6) (2009) 548–557.

[53] M. Z. Zhang, Y. J. He, G. Ye, D. A. Lange, K. van Breugel, Computational investigation on mass diffusivity in portland cement paste based on x-ray computed microtomography (mu ct) image, Construction and Building Materials 27 (1) (2012) 472–481.

[54] D. P. Bentz, S. Mizell, S. Satterfield, J. Devaney, W. George, P. Ketcham, J. Graham, J. Porterfield, D. Quenard, F. Vallee, The visible cement data set, Journal of Research of the National Institute of Standards and Technology 107 (2) (2002) 137.

[55] M. Zhang, G. Ye, K. Van Breugel, Microstructure-based modeling of water diffusivity in cement paste, Construction and Building Materials 25 (4) (2011) 2046–2052.

[56] K. Van Breugel, Modelling of cement-based systems—the alchemy of cement chemistry, cement and concrete research 34 (9) (2004) 1661–1668.

[57] C. Pignat, P. Navi, K. Scrivener, Simulation of cement paste microstructure hydration, pore space characterization and permeability determination, Materials and structures 38 (4) (2005) 459–466.

[58] J. S. Dolado, K. Van Breugel, Recent advances in modeling for cementitious materials, Cement and concrete research 41 (7) (2011) 711–726.

[59] J. J. Thomas, J. J. Biernacki, J. W. Bullard, S. Bishnoi, J. S. Dolado, G. W. Scherer, A. Luttge, Modeling and simulation of cement hydration kinetics and microstructure development, Cement and concrete research 41 (12) (2011) 1257–1278.

[60] P. Gao, Simulation of hydration and microstructure development of blended cements, Thesis, Delft University of Technology, Delft, The Netherlands (2018).

[61] H. M. Jennings, S. K. Johnson, Simulation of microstructure development during the hydration of a cement compound, Journal of the American Ceramic Society 69 (11) (1986) 790–795.

[62] P. Navi, C. Pignat, Simulation of cement hydration and the connectivity of the capillary pore space, Advanced Cement Based Materials 4 (2) (1996) 58–67.

[63] R. Nothnagel, H. Budelmann, Model for the formation of microstructure in cement paste during hydration, in: International RILEM Symposium on Concrete Modelling-ConMod'08, RILEM Publications SARL, 2008, pp. 361–368.

[64] X.-Y. Wang, H.-S. Lee, K.-B. Park, Simulation of low-calcium fly ash blended cement hydration, ACI materials journal 106 (2) (2009) 167.

A

[65] K. Maekawa, R. Chaube, T. Kishi, Modeling of concrete performance: hydration, microstructure formation and mass transport, E and FN SPON, London 1.

[66] J. W. Bullard, A three-dimensional microstructural model of reactions and transport in aqueous mineral systems, Modelling and Simulation in Materials Science and Engineering 15 (7) (2007) 711.

[67] J. W. Bullard, Approximate rate constants for nonideal diffusion and their application in a stochastic model, The Journal of Physical Chemistry A 111 (11) (2007) 2084–2092.

[68] L. Liu, X. Wang, H. Chen, C. Wan, Microstructure-based modelling of drying shrinkage and microcracking of cement paste at high relative humidity, Construction and Building Materials 126 (2016) 410–425.

[69] R. Chamrova, Modelling and measurement of elastic properties of hydrating cement paste, Ph.d. thesis, École polytechnique fédérale de Lausanne, Lausanne, Switzerland (2010).

[70] Q. H. Do, Modelling properties of cement paste from microstructure, Ph.d. thesis, École polytechnique fédérale de Lausanne, Lausanne, Switzerland (2013).

[71] S. Bishnoi, S. Joseph, A. Kaur, Microstructural modelling of the strength of mortars containing fly ash using μic, Construction and Building Materials 163 (2018) 912–920.

[72] J. W. Bullard, E. J. Garboczi, A model investigation of the influence of particle shape on portland cement hydration, Cement and Concrete Research 36 (6) (2006) 1007–1015.

[73] B. Pichler, C. Hellmich, J. Eberhardsteiner, Spherical and acicular representation of hydrates in a micromechanical model for cement paste: prediction of early-age elasticity and strength, Acta Mechanica 203 (3) (2009) 137–162.

[74] E. J. Garboczi, J. W. Bullard, Shape analysis of a reference cement, Cement and Concrete Research 34 (10) (2004) 1933–1937.

[75] M. Hain, P. Wriggers, Numerical homogenization of hardened cement paste, Computational Mechanics 42 (2) (2008) 197–212.

[76] J. Sanahuja, L. Dormieux, G. Chanvillard, Modelling elasticity of a hydrating cement paste, Cement and Concrete Research 37 (10) (2007) 1427–1439.

[77] C.-J. Haecker, E. Garboczi, J. Bullard, R. Bohn, Z. Sun, S. P. Shah, T. Voigt, Modeling the linear elastic properties of portland cement paste, Cement and Concrete Research 35 (10) (2005) 1948–1960.

[78] D. P. Bentz, O. M. Jensen, K. K. Hansen, J. F. Olesen, H. Stang, C.-J. Haecker, Influence of cement particle-size distribution on early age autogenous strains and stresses in cement-based materials, Journal of the American Ceramic Society 84 (1) (2001) 129–135.

[79] J. Von Neumann, A. W. Burks, Theory of self-reproducing automata, IEEE Transactions on Neural Networks 5 (1) (1966) 3–14.

[80] F. Bernard, S. Kamali-Bernard, Predicting the evolution of mechanical and diffusivity properties of cement pastes and mortars for various hydration degrees–a numerical simulation investigation, Computational Materials Science 61 (2012) 106–115.

[81] W. C. Oliver, G. M. Pharr, An improved technique for determining hardness and elastic modulus using load and displacement sensing indentation experiments, Journal of materials research 7 (6) (1992) 1564–1583.

[82] H. Hertz, D. E. Jones, G. A. Schott, Miscellaneous papers, Macmillan and Company, 1896.

[83] C. Hu, Z. Li, A review on the mechanical properties of cement-based materials measured by nanoindentation, Construction and Building Materials 90 (2015) 80–90.

[84] J. Woirgard, C. Tromas, J. Girard, V. Audurier, Study of the mechanical properties of ceramic materials by the nanoindentation technique, Journal of the European Ceramic Society 18 (15) (1998) 2297–2305.

[85] A. Shimamoto, K. Tanaka, Y. Akiyma, H. Yoshizaki, Nanoindentation of glass with a tip-truncated berkovich indenter, Philosophical Magazine A 74 (5) (1996) 1097–1105.

[86] C. Hu, Y. Gao, Y. Zhang, Z. Li, Statistical nanoindentation technique in application to hardened cement pastes: Influences of material microstructure and analysis method, Construction and Building Materials 113 (2016) 306–316.

[87] H. Bückle, Use of the hardness test to determine other material properties, The Science of Hardness Testing and Its Research Applications (1973) 453.

[88] J. J. Chen, L. Sorelli, M. Vandamme, F.-J. Ulm, G. Chanvillard, A coupled nanoindentation/SEM-EDS study on low water/cement ratio portland cement paste: evidence for C-S-H/$Ca(OH)_2$ nanocomposites, Journal of the American Ceramic Society 93 (5) (2010) 1484–1493.

[89] G. Constantinides, F.-J. Ulm, The nanogranular nature of C-S-H, Journal of the Mechanics and Physics of Solids 55 (1) (2007) 64–90.

[90] G. Constantinides, F. J. Ulm, K. Van Vliet, On the use of nanoindentation for cementitious materials, Materials and structures 36 (3) (2003) 191–196.

[91] F. Ulm, M. Vandamme, C. Bobko, J. Alberto Ortega, K. Tai, C. Ortiz, Statistical indentation techniques for hydrated nanocomposites: concrete, bone, and shale, Journal of the American Ceramic Society 90 (9) (2007) 2677–2692.

A

[92] M. Miller, C. Bobko, M. Vandamme, F.-J. Ulm, Surface roughness criteria for cement paste nanoindentation, Cement and Concrete Research 38 (4) (2008) 467–476.

[93] D. Davydov, M. Jirásek, L. Kopecký, Critical aspects of nano-indentation technique in application to hardened cement paste, Cement and Concrete Research 41 (1) (2011) 20–29.

[94] P. Lura, P. Trtik, B. M(̈U)nch, Validity of recent approaches for statistical nanoindentation of cement pastes, Cement and Concrete Composites 33 (4) (2011) 457–465.

[95] F.-J. Ulm, M. Vandamme, H. M. Jennings, J. Vanzo, M. Bentivegna, K. J. Krakowiak, G. Constantinides, C. P. Bobko, K. J. Van Vliet, Does microstructure matter for statistical nanoindentation techniques?, Cement and Concrete Composites 32 (1) (2010) 92–99.

[96] P. Trtik, B. Münch, P. Lura, A critical examination of statistical nanoindentation on model materials and hardened cement pastes based on virtual experiments, Cement and Concrete Composites 31 (10) (2009) 705–714.

[97] K. Velez, S. Maximilien, D. Damidot, G. Fantozzi, F. Sorrentino, Determination by nanoindentation of elastic modulus and hardness of pure constituents of portland cement clinker, Cement and Concrete Research 31 (4) (2001) 555–561.

[98] W. Zhu, J. J. Hughes, N. Bicanic, C. J. Pearce, Nanoindentation mapping of mechanical properties of cement paste and natural rocks, Materials characterization 58 (11) (2007) 1189–1198.

[99] M. Vandamme, F.-J. Ulm, Nanogranular origin of concrete creep, Proceedings of the National Academy of Sciences 106 (26) (2009) 10552–10557.

[100] M. Vandamme, F.-J. Ulm, Nanoindentation investigation of creep properties of calcium silicate hydrates, Cement and Concrete Research 52 (2013) 38–52.

[101] T. Howind, J. Hughes, W. Zhu, F. Puertas, S. Goñi Elizalde, M. S. Hernandez, A. Guerrero Bustos, M. Palacios, J. S. Dolado, Mapping of mechanical properties of cement paste microstructures, in: Proceedings of 13th International Congress on the Chemistry of Cement, Caminos, 2011, p. 39.

[102] S. J. Chen, W. H. Duan, Z. J. Li, T. B. Sui, New approach for characterisation of mechanical properties of cement paste at micrometre scale, Materials & Design 87 (2015) 992–995.

[103] R. Shahrin, C. P. Bobko, Characterizing strength and failure of calcium silicate hydrate aggregates in cement paste under micropillar compression, Journal of Nanomechanics and Micromechanics 7 (4) (2017) 06017002.

[104] J. Němeček, J. Maňák, T. Krejčí, Effect of vacuum and focused ion beam generated heat on fracture properties of hydrated cement paste, Cement and Concrete Composites.

[105] M. J. Pfeifenberger, M. Mangang, S. Wurster, J. Reiser, A. Hohenwarter, W. Pfleging, D. Kiener, R. Pippan, The use of femtosecond laser ablation as a novel tool for rapid micro-mechanical sample preparation, Materials & Design 121 (2017) 109–118.

[106] B. Šavija, D. Liu, G. Smith, K. R. Hallam, E. Schlangen, P. E. Flewitt, Experimentally informed multi-scale modelling of mechanical properties of quasi-brittle nuclear graphite, Engineering Fracture Mechanics 153 (2016) 360–377.

[107] H. Manzano, J. Dolado, A. Ayuela, Elastic properties of the main species present in portland cement pastes, Acta Materialia 57 (5) (2009) 1666–1674.

[108] D. Tavakoli, A. Tarighat, Molecular dynamics study on the mechanical properties of portland cement clinker phases, Computational Materials Science 119 (2016) 65–73.

[109] H. Manzano, J. S. Dolado, A. Ayuela, Structural, mechanical, and reactivity properties of tricalcium aluminate using first-principles calculations, Journal of the American Ceramic Society 92 (4) (2009) 897–902.

[110] D. Grigoratos, J. Knowles, Y. Ng, K. Gulabivala, Effect of exposing dentine to sodium hypochlorite and calcium hydroxide on its flexural strength and elastic modulus, International endodontic journal 34 (2) (2001) 113–119.

[111] A. G. Kalinichev, R. J. Kirkpatrick, Molecular dynamics modeling of chloride binding to the surfaces of calcium hydroxide, hydrated calcium aluminate, and calcium silicate phases, Chemistry of Materials 14 (8) (2002) 3539–3549.

[112] A. G. Kalinichev, J. Wang, R. J. Kirkpatrick, Molecular dynamics modeling of the structure, dynamics and energetics of mineral–water interfaces: Application to cement materials, Cement and Concrete Research 37 (3) (2007) 337–347.

[113] S. V. Churakov, Hydrogen bond connectivity in jennite from ab initio simulations, Cement and concrete research 38 (12) (2008) 1359–1364.

[114] S. V. Churakov, Structural position of H_2O molecules and hydrogen bonding in anomalous 11 Å tobermorite, American Mineralogist 94 (1) (2009) 156–165.

[115] S. V. Churakov, Structure of the interlayer in normal 11 Å tobermorite from an ab initio study, European journal of mineralogy 21 (1) (2009) 261–271.

[116] R. Shahsavari, M. J. Buehler, R. J.-M. Pellenq, F.-J. Ulm, First-principles study of elastic constants and interlayer interactions of complex hydrated oxides: Case study of tobermorite and jennite, Journal of the American Ceramic Society 92 (10) (2009) 2323–2330.

A

[117] H. Manzano, R. González-Teresa, J. Dolado, A. Ayuela, X-ray spectra and theoretical elastic properties of crystalline calcium silicate hydrates: comparison with cement hydrated gels, Materiales de ConstrucciÓn 60 (299) (2010) 7–19.

[118] D. Hou, T. Zhao, P. Wang, Z. Li, J. Zhang, Molecular dynamics study on the mode I fracture of calcium silicate hydrate under tensile loading, Engineering Fracture Mechanics 131 (2014) 557–569.

[119] H. M. Jennings, Refinements to colloid model of CSH in cement: CM-II, Cement and Concrete Research 38 (3) (2008) 275–289.

[120] H. M. Jennings, A model for the microstructure of calcium silicate hydrate in cement paste, Cement and concrete research 30 (1) (2000) 101–116.

[121] R. Gonzalez-Teresa, V. Morales-Florez, H. Manzano, J. S. Dolado, Structural models of randomly packed tobermorite-like spherical particles: A simple computational approach, Materiales de construccion 60 (298) (2010) 7–15.

[122] V. Morales-Florez, F. Brunet, Structural models of random packing of spheres extended to bricks: simulation of the nanoporous calcium silicate hydrates, Molecular Simulation 35 (12-13) (2009) 1001–1006.

[123] V. Morales-Flórez, N. De La Rosa-Fox, M. Piñero, L. Esquivias, The cluster model: a simulation of the aerogel structure as a hierarchically-ordered arrangement of randomly packed spheres, Journal of sol-gel science and technology 35 (3) (2005) 203–210.

[124] D. P. Bentz, D. A. Quenard, V. Baroghel-Bouny, E. J. Garboczi, H. M. Jennings, Modelling drying shrinkage of cement paste and mortar part 1. structural models from nanometres to millimetres, Materials and Structures 28 (8) (1995) 450–458.

[125] M. Q. Chandler, J. F. Peters, D. Pelessone, Modeling nanoindentation of calcium silicate hydrate, Transportation Research Record 2142 (1) (2010) 67–74.

[126] F. Sanchez, K. Sobolev, Nanotechnology in concrete–a review, Construction and building materials 24 (11) (2010) 2060–2071.

[127] R. M. Jones, Mechanics of composite materials, CRC press, 1999.

[128] Y. Benveniste, A new approach to the application of mori-tanaka's theory in composite materials, Mechanics of materials 6 (2) (1987) 147–157.

[129] B. Budiansky, On the elastic moduli of some heterogeneous materials, Journal of the Mechanics and Physics of Solids 13 (4) (1965) 223–227.

[130] B. Pichler, S. Scheiner, C. Hellmich, From micron-sized needle-shaped hydrates to meter-sized shotcrete tunnel shells: micromechanical upscaling of stiffness and strength of hydrating shotcrete, Acta Geotechnica 3 (4) (2008) 273.

[131] M. Hlobil, V. Šmilauer, G. Chanvillard, Micromechanical multiscale fracture model for compressive strength of blended cement pastes, Cement and Concrete Research 83 (2016) 188–202.

[132] E. J. Garboczi, A. Day, An algorithm for computing the effective linear elastic properties of heterogeneous materials: three-dimensional results for composites with equal phase poisson ratios, Journal of the Mechanics and Physics of Solids 43 (9) (1995) 1349–1362.

[133] C.-J. Haecker, E. Garboczi, J. Bullard, R. Bohn, Z. Sun, S. Shah, T. Voigt, Modeling the linear elastic properties of portland cement paste, Cement and Concrete Research 35 (10) (2005) 1948–1960.

[134] P. Wriggers, M. Hain, Micro-meso-macro modelling of composite materials, in: Computational Plasticity, Springer, 2007, pp. 105–122.

[135] V. Šmilauer, Z. Bittnar, Microstructure-based micromechanical prediction of elastic properties in hydrating cement paste, Cement and Concrete Research 36 (9) (2006) 1708–1718.

[136] E. Stora, Q. C. He, B. Bary, Influence of inclusion shapes on the effective linear elastic properties of hardened cement pastes, Cement and Concrete Research 36 (7) (2006) 1330–1344.

[137] B. Bary, M. B. Haha, E. Adam, P. Montarnal, Numerical and analytical effective elastic properties of degraded cement pastes, Cement and Concrete Research 39 (10) (2009) 902–912.

[138] E. Schlangen, E. Garboczi, Fracture simulations of concrete using lattice models: computational aspects, Engineering fracture mechanics 57 (2) (1997) 319–332.

[139] E. Schlangen, Experimental and numerical analysis of fracture processes in concrete, Ph.D. thesis, Delft University of Technology, Delft, The Netherlands (1993).

[140] C. Lee, X. Wei, J. W. Kysar, J. Hone, Measurement of the elastic properties and intrinsic strength of monolayer graphene, science 321 (5887) (2008) 385–388.

[141] A. A. Griffith, The phenomena of rupture and flow in solids, Philosophical transactions of the royal society of london. Series A, containing papers of a mathematical or physical character 221 (1921) 163–198.

[142] I. Gitman, H. Askes, L. Sluys, Coupled-volume multi-scale modelling of quasi-brittle material, European Journal of Mechanics-A/Solids 27 (3) (2008) 302–327.

[143] S. Eckardt, Adaptive heterogeneous multiscale models for the nonlinear simulation of concrete, Ph.D. thesis, Bauhaus-Universität Weimar, Weimar, Germany (2009).

A

[144] P. J. Sánchez, P. J. Blanco, A. E. Huespe, R. Feijóo, Failure-oriented multi-scale variational formulation: micro-structures with nucleation and evolution of softening bands, Computer Methods in Applied Mechanics and Engineering 257 (2013) 221–247.

[145] H. Yamashita, R. Hart, T. Sharma, A. Samanta, Q. Wang, S. Xiao, A review of multiscale methods and their applications in modeling and simulation of engineering problems, Int. J. Recent Technol. Mech. Electr. Eng. 3 (2016) 42–47.

[146] F. Wittmann, Structure of concrete with respect to crack formation, Fracture mechanics of concrete 43 (5) (1983) 6.

[147] J. Zheng, X. Zhou, L. Shao, X. Jin, Simple three-step analytical scheme for prediction of elastic moduli of hardened cement paste, Journal of Materials in Civil Engineering 22 (11) (2010) 1191–1194.

[148] X.-H. Zhao, W. Chen, The effective elastic moduli of concrete and composite materials, Composites Part B: Engineering 29 (1) (1998) 31–40.

[149] O. Lloberas-Valls, D. Rixen, A. Simone, L. Sluys, On micro-to-macro connections in domain decomposition multiscale methods, Computer Methods in Applied Mechanics and Engineering 225 (2012) 177–196.

[150] T. J. R. Hughes, G. R. Feijóo, L. Mazzei, J.-B. Quincy, The variational multiscale method-a paradigm for computational mechanics, Computer Methods in Applied Mechanics and Engineering 166 (1) (1998) 3–24.

[151] O. Lloberas-Valls, F. Everdij, D. Rixen, A. Simone, B. Sluys, Concurrent multiscale analysis of heterogeneous materials, Delft University of Technology 2 (2012) 3mE.

[152] H. Zhang, B. Šavija, S. Chaves Figueiredo, M. Lukovic, E. Schlangen, Microscale testing and modelling of cement paste as basis for multi-scale modelling, Materials 9 (11) (2016) 907.

[153] J. Zhang, G. W. Scherer, Comparison of methods for arresting hydration of cement, Cement and Concrete Research 41 (10) (2011) 1024–1036.

[154] R. H. Poelma, B. Morana, S. Vollebregt, E. Schlangen, H. W. van Zeijl, X. Fan, G. Q. Zhang, Tailoring the mechanical properties of high-aspect-ratio carbon nanotube arrays using amorphous silicon carbide coatings, Advanced Functional Materials 24 (36) (2014) 5737–5744.

[155] E. Schlangen, M. Lukovic, B. Šavija, O. Copuroglu, Nano-indentation testing and modelling of cement paste, in: Proceedings of the 10th International Conference on Mechanics and Physics of Creep, Shrinkage, and Durability of Concrete and Concrete Structures, Vienna, Austria, 2015, pp. 21–23.

[156] P. D. Tennis, H. M. Jennings, A model for two types of calcium silicate hydrate in the microstructure of Portland cement pastes, Cement and Concrete Research 30 (6) (2000) 855–863.

[157] H. Ma, Z. Li, Realistic pore structure of portland cement paste: experimental study and numerical simulation, Computers and Concrete 11 (4) (2013) 317–336.

[158] H. Ma, D. Hou, Y. Lu, Z. Li, Two-scale modeling of the capillary network in hydrated cement paste, Construction and Building Materials 64 (2014) 11–21.

[159] T. C. Powers, T. L. Brownyard, Studies of the physical properties of hardened portland cement paste, in: Journal Proceedings, Vol. 43, 1946, pp. 101–132.

[160] R. A. Cook, K. C. Hover, Mercury porosimetry of hardened cement pastes, Cement and Concrete research 29 (6) (1999) 933–943.

[161] G. Lilliu, J. G. Van Mier, 3D lattice type fracture model for concrete, Engineering Fracture Mechanics 70 (7-8) (2000) 855–863.

[162] G. Lilliu, 3D analysis of fracture processes in concrete, Ph.D. thesis, Delft University of Technology, Delft, The Netherlands (2007).

[163] Y. GAO, Y. ZHANG, C. HU, Z. LI, Nanomechanical properties of individual phases in cement mortar analyzed using nanoindentation coupled with scanning electron microscopy, Journal of The Chinese Ceramic Society 40 (11) (2012) 1559–1563.

[164] B. Pichler, C. Hellmich, J. Eberhardsteiner, J. Wasserbauer, P. Termkhajornkit, R. Barbarulo, G. Chanvillard, Effect of gel–space ratio and microstructure on strength of hydrating cementitious materials: An engineering micromechanics approach, Cement and Concrete Research 45 (2013) 55–68.

[165] C. Hellmich, H. Mang, Shotcrete elasticity revisited in the framework of continuum micromechanics: From submicron to meter level, Journal of materials in civil engineering 17 (3) (2005) 246–256.

[166] S. Scheiner, C. Hellmich, Continuum microviscoelasticity model for aging basic creep of early-age concrete, Journal of engineering mechanics 135 (4) (2009) 307–323.

[167] M. Königsberger, M. Irfan-ul Hassan, B. Pichler, C. Hellmich, Downscaling based identification of nonaging power-law creep of cement hydrates, Journal of Engineering Mechanics 142 (12) (2016) 04016106.

[168] H. Zhang, B. Šavija, E. Schlangen, Combined experimental and numerical study on micro-cube indentation splitting test of cement paste, Engineering Fracture Mechanics 199 (2018) 773–786.

[169] D. Liu, P. E. Flewitt, Deformation and fracture of carbonaceous materials using in situ micro-mechanical testing, Carbon 114 (2017) 261–274.

[170] BS-EN 12390-6: 2009. Testing of hardened concrete - Part 6: Split tensile strength of test specimens, British Standards Institution-BSI and CEN European Committee for Standardization, 2009.

A

[171] C. Rocco, G. V. Guinea, J. Planas, M. Elices, Size effect and boundary conditions in the brazilian test: experimental verification, Materials and Structures 32 (3) (1999) 210.

[172] S. Nilsson, The tensile strength of concrete determined by splitting tests on cubes, Rilem Bulletin 11 (1961) 63–67.

[173] G. N. FEMMASSE B.V., FEMMASSE MLS 8.5 User manual Finite element modules for material science and structural engineering, Technical Report, 2006.

[174] P. Pizette, C. Martin, G. Delette, P. Sornay, F. Sans, Compaction of aggregated ceramic powders: From contact laws to fracture and yield surfaces, Powder technology 198 (2) (2010) 240–250.

[175] J. B. Quinn, G. D. Quinn, A practical and systematic review of weibull statistics for reporting strengths of dental materials, dental materials 26 (2) (2010) 135–147.

[176] D. R. Thoman, L. J. Bain, C. E. Antle, Inferences on the parameters of the weibull distribution, Technometrics 11 (3) (1969) 445–460.

[177] M. Röβler, I. Odler, Investigations on the relationship between porosity, structure and strength of hydrated portland cement pastes i. effect of porosity, Cement and Concrete Research 15 (2) (1985) 320–330.

[178] R. Kumar, B. Bhattacharjee, Porosity, pore size distribution and in situ strength of concrete, Cement and concrete research 33 (1) (2003) 155–164.

[179] Z. P. Bažant, Size effect in blunt fracture: concrete, rock, metal, Journal of engineering mechanics 110 (4) (1984) 518–535.

[180] J. Eliáš, M. Vořechovskỳ, J. Skoček, Z. P. Bažant, Stochastic discrete meso-scale simulations of concrete fracture: Comparison to experimental data, Engineering Fracture Mechanics 135 (2015) 1–16.

[181] M. Salviato, V. T. Chau, W. Li, Z. P. Bažant, G. Cusatis, Direct testing of gradual post-peak softening of fracture specimens of fiber composites stabilized by enhanced grip stiffness and mass, Journal of Applied Mechanics 83 (11) (2016) 111003.

[182] D. Liu, B. Šavija, G. E. Smith, P. E. Flewitt, T. Lowe, E. Schlangen, Towards understanding the influence of porosity on mechanical and fracture behaviour of quasi-brittle materials: experiments and modelling, International Journal of Fracture 205 (1) (2017) 57–72.

[183] H. Zhang, B. Šavija, E. Schlangen, Towards understanding stochastic fracture performance of cement paste at micro length scale based on numerical simulation, Construction and Building Materials 183 (2018) 189–201.

[184] M. Luković, B. Šavija, H. Dong, E. Schlangen, G. Ye, Micromechanical study of the interface properties in concrete repair systems, Journal of Advanced Concrete Technology 12 (9) (2014) 320–339.

[185] I. Odler, M. Rößler, Investigations on the relationship between porosity, structure and strength of hydrated portland cement pastes. ii. effect of pore structure and of degree of hydration, Cement and Concrete Research 15 (3) (1985) 401–410.

[186] D. Liu, K. Mingard, O. T. Lord, P. Flewitt, On the damage and fracture of nuclear graphite at multiple length-scales, Journal of Nuclear Materials 493 (2017) 246–254.

[187] E. Schlangen, Crack development in concrete, part 1: Fracture experiments and ct-scan observations, in: Key Engineering Materials, Vol. 385, Trans Tech Publ, 2008, pp. 69–72.

[188] E. Schlangen, Crack development in concrete, part 2: modelling of fracture process, in: Key Engineering Materials, Vol. 385, Trans Tech Publ, 2008, pp. 73–76.

[189] H. W. Chandler, I. Merchant, R. Henderson, D. Macphee, Enhanced crack-bridging by unbonded inclusions in a brittle matrix, Journal of the European Ceramic Society 22 (1) (2002) 129–134.

[190] M. Y. Corapcioglu, Advances in porous media, Vol. 3, Elsevier, 1996.

[191] C. Lian, Y. Zhuge, S. Beecham, The relationship between porosity and strength for porous concrete, Construction and Building Materials 25 (11) (2011) 4294–4298.

[192] X. Chen, S. Wu, J. Zhou, Influence of porosity on compressive and tensile strength of cement mortar, Construction and Building Materials 40 (2013) 869–874.

[193] D. M. Roy, G. R. Gouda, Porosity-strength relation in cementitious materials with very high strengths, Journal of the American Ceramic Society 56 (10) (1973) 549–550.

[194] Y.-X. Li, Y.-M. Chen, J.-X. Wei, X.-Y. He, H.-T. Zhang, W.-S. Zhang, A study on the relationship between porosity of the cement paste with mineral additives and compressive strength of mortar based on this paste, Cement and Concrete Research 36 (9) (2006) 1740–1743.

[195] M. RELIS, I. SOROKA, Compressive strength of low-porosity hydrated portland cement, Journal of the American Ceramic Society 63 (1980) 690–694.

[196] D. Hasselman, Relation between effects of porosity on strength and on young's modulus of elasticity of polycrystalline materials, Journal of the American Ceramic Society 46 (11) (1963) 564–565.

[197] M. Balshin, Relation of mechanical properties of powder metals and their porosity and the ultimate properties of porous metal-ceramic materials, Doklady Akademii Nauk SSSR 67 (5) (1949) 831–834, cited By 141.

[198] W. Duckworth, Discussion of ryshkewitch paper by winston duckworth, Journal of the American Ceramic Society 34 (1953) 68–78.

A

[199] K. Schiller, Strength of porous materials, Cement and Concrete Research 1 (4) (1971) 419–422.

[200] G. McAdam, Some relations of powder characteristics to the elastic modulus and shrinkage of sintered ferrous compacts, Journal of the Iron and Steel Institute 168 (4) (1951) 346–358, cited By 54.

[201] R. Spriggs, Expression for effect of porosity on elastic modulus of polycrystalline refractory materials, particularly aluminum oxide, Journal of the American Ceramic Society 44 (12) (1961) 628–629.

[202] F. Knudsen, Dependence of mechanical strength of brittle polycrystalline specimens on porosity and grain size, Journal of the American Ceramic Society 42 (8) (1959) 376–387.

[203] A. Maitra, K. Phani, Ultrasonic evaluation of elastic parameters of sintered powder compacts, Journal of materials science 29 (17) (1994) 4415–4419.

[204] A. Griffith, The phenomena of rupture and flow in solids, Philosophical transactions of the royal society of london. Series A, containing papers of a mathematical or physical character 221 (1921) 163–198.

[205] C. Lee, X. Wei, J. W. Kysar, J. Hone, Measurement of the elastic properties and intrinsic strength of monolayer graphene, Science 321 (5887) (2008) 385–388.

[206] S. Harsh, Z. Shen, D. Darwin, Strain-rate sensitive behavior of cemet paste and mortar in compression, ACI Materials Journal (1990) 508–516.

[207] M. Abreu, J. Lemos, J. Carmeliet, E. Schlangen, Modelling compressive cracking in concrete by a modified lattice model, in: Proceedings of the 6th International Conference on Fracture Mechanics of Concrete and Concrete Structures, New trends in Fracture Mechanics of Concrete, Vol. 1, 2007, pp. 453–460.

[208] M. Kotsovos, Effect of testing techniques on the post-ultimate behaviour of concrete in compression, Materiaux et construction 16 (1) (1983) 3–12.

[209] M. A. van Vliet, J. M. van Mier, Experimental investigation of concrete fracture under uniaxial compression, Mechanics of Cohesive-frictional Materials: An International Journal on Experiments, Modelling and Computation of Materials and Structures 1 (1) (1996) 115–127.

[210] K. H. Gerstle, D. L. Linse, P. Bertacchi, Strength of concrete under multiaxial stress states, Special Publication 55 (1978) 103–132.

[211] J. G. M. Van Mier, Strain-softening of concrete under multiaxial loading conditions, Phd thesis, Eindhoven University of Technology, Eindhoven, The Netherlands (1984).

[212] P. Tumidajski, L. Fiore, T. Khodabocus, M. Lachemi, R. Pari, Comparison of weibull and normal distributions for concrete compressive strengths, Canadian Journal of Civil Engineering 33 (10) (2006) 1287–1292.

[213] F. W. Zok, On weakest link theory and weibull statistics, Journal of the American Ceramic Society 100 (4) (2017) 1265–1268.

[214] M. R. Van Vliet, J. G. Van Mier, Experimental investigation of size effect in concrete and sandstone under uniaxial tension, Engineering Fracture Mechanics 65 (2) (2000) 165–188.

[215] T.-f. Wong, R. H. Wong, K. Chau, C. Tang, Microcrack statistics, weibull distribution and micromechanical modeling of compressive failure in rock, Mechanics of Materials 38 (7) (2006) 664–681.

[216] W. G. Cochran, The χ^2 test of goodness of fit, The Annals of Mathematical Statistics (1952) 315–345.

[217] P. Monteiro, Concrete: microstructure, properties, and materials, McGraw-Hill Publishing, 2006.

[218] H. Fu, M. Erki, M. Seckin, Review of effects of loading rate on concrete in compression, Journal of structural engineering 117 (12) (1991) 3645–3659.

[219] Z. P. Bažant, R. Gettu, Rate effects and load relaxation in static fracture of concrete, ACI Materials Journal 89 (5) (1992) 456–468.

[220] C. Mazzotti, M. Savoia, Nonlinear creep damage model for concrete under uniaxial compression, Journal of engineering mechanics 129 (9) (2003) 1065–1075.

[221] M. F. Ruiz, A. Muttoni, P. G. Gambarova, Relationship between nonlinear creep and cracking of concrete under uniaxial compression, Journal of Advanced Concrete Technology 5 (3) (2007) 383–393.

[222] J. Němeček, Creep effects in nanoindentation of hydrated phases of cement pastes, Materials Characterization 60 (9) (2009) 1028–1034.

[223] G. Cusatis, A. Mencarelli, D. Pelessone, J. Baylot, Lattice discrete particle model (ldpm) for failure behavior of concrete. ii: Calibration and validation, Cement and Concrete composites 33 (9) (2011) 891–905.

[224] H. Zhang, Y. Gan, Y. Xu, S. Zhang, E. Schlangen, B. Šavija, Experimentally informed fracture modelling of interfacial transition zone at micro-scale, Cement and Concrete Composites 104 (2019) 103383.

[225] L. Struble, J. Skalny, S. Mindess, A review of the cement-aggregate bond, Cement and concrete research 10 (2) (1980) 277–286.

[226] B. Barnes, S. Diamond, W. Dolch, The contact zone between portland cement paste and glass “aggregate” surfaces, Cement and Concrete Research 8 (2) (1978) 233–243.

[227] K. L. Scrivener, A. K. Crumbie, P. Laugesen, The interfacial transition zone (itz) between cement paste and aggregate in concrete, Interface Science 12 (2004) 411–421.

A

[228] S. Diamond, J. Huang, The itz in concrete–a different view based on image analysis and sem observations, Cement and concrete composites 23 (2-3) (2001) 179–188.

[229] A. Delagrave, J. Bigas, J. Ollivier, J. Marchand, M. Pigeon, Influence of the interfacial zone on the chloride diffusivity of mortars, Advanced Cement Based Materials 5 (3-4) (1997) 86–92.

[230] B. Nyame, Permeability of normal and lightweight mortars, Magazine of Concrete Research 37 (130) (1985) 44–48.

[231] A. Princigallo, K. van Breugel, G. Levita, Influence of the aggregate on the electrical conductivity of portland cement concretes, Cement and Concrete Research 33 (11) (2003) 1755–1763.

[232] Q.-f. Liu, G.-l. Feng, J. Xia, J. Yang, L.-y. Li, Ionic transport features in concrete composites containing various shaped aggregates: a numerical study, Composite Structures 183 (2018) 371–380.

[233] T. Akçaoğlu, M. Tokyay, T. Çelik, Effect of coarse aggregate size and matrix quality on itz and failure behavior of concrete under uniaxial compression, Cement and Concrete Composites 26 (6) (2004) 633–638.

[234] G. Ramesh, E. Sotelino, W. Chen, Effect of transition zone on elastic moduli of concrete materials, Cement and Concrete Research 26 (4) (1996) 611–622.

[235] A. R. Mohamed, W. Hansen, Micromechanical modeling of crack-aggregate interaction in concrete materials, Cement and Concrete Composites 21 (5-6) (1999) 349–359.

[236] F. Grondin, M. Matallah, How to consider the interfacial transition zones in the finite element modelling of concrete?, Cement and Concrete Research 58 (2014) 67–75.

[237] S. Zhang, C. Zhang, L. Liao, C. Wang, Numerical study of the effect of itz on the failure behaviour of concrete by using particle element modelling, Construction and Building Materials 170 (2018) 776–789.

[238] S.-M. Kim, R. K. Abu Al-Rub, Meso-scale computational modeling of the plastic-damage response of cementitious composites, Cement and Concrete Research 41 (3) (2011) 339–358.

[239] X. F. Wang, Z. J. Yang, J. R. Yates, A. P. Jivkov, C. Zhang, Monte carlo simulations of mesoscale fracture modelling of concrete with random aggregates and pores, Construction and Building Materials 75 (2015) 35–45.

[240] L. Snozzi, A. Caballero, J.-F. Molinari, Influence of the meso-structure in dynamic fracture simulation of concrete under tensile loading, Cement and Concrete Research 41 (11) (2011) 1130–1142.

[241] B. Šavija, J. Pacheco, E. Schlangen, Lattice modeling of chloride diffusion in sound and cracked concrete, Cement and Concrete Composites 42 (2013) 30–40.

[242] K. L. Scrivener, P. L. Pratt, Characterization of interfacial microstructure, Interfacial transition zone in concrete 2 (1996) 3–18.

[243] M. Jebli, F. Jamin, E. Malachanne, E. Garcia-Diaz, M. S. El Youssoufi, Experimental characterization of mechanical properties of the cement-aggregate interface in concrete, Construction and Building Materials 161 (2018) 16–25.

[244] T. Thomas, F. O. Slate, Tensile bond strength between aggregate and cement paste or mortar, in: Journal Proceedings, Vol. 60, 1963, pp. 465–486.

[245] R. Zimbelmann, A contribution to the problem of cement-aggregate bond, Cement and Concrete Research 15 (5) (1985) 801–808.

[246] J. Wang, A. Maji, Experimental studies and modeling of the concrete/rock interface, ACI Special Publication on Interface Fracture and Bond 156 (1994) 45–68.

[247] E. Tschegg, H. Rotter, P. Roelfstra, U. Bourgund, P. Jussel, Fracture mechanical behavior of aggregate–cement matrix interfaces, Journal of Materials in Civil Engineering 7 (4) (1995) 199–203.

[248] K. Alexander, Strength of the cement aggregate bond, in: Journal Proceedings, Vol. 56, 1959, pp. 377–390.

[249] C. Perry, J. Gillott, The influence of silica fume on the strength of the cement-aggregate bond, Special Publication 156 (1995) 191–212.

[250] W. Dong, Z. Wu, X. Zhou, N. Wang, G. Kastiukas, An experimental study on crack propagation at rock-concrete interface using digital image correlation technique, Engineering Fracture Mechanics 171 (2017) 50–63.

[251] M. Hassanzadeh, Fracture mechanical properties of rocks and mortar/rock interfaces, MRS Online Proceedings Library Archive 370.

[252] O. Buyukozturk, B. Hearing, Crack propagation in concrete composites influenced by interface fracture parameters, International Journal of Solids and Structures 35 (31) (1998) 4055–4066.

[253] S. Caliskan, Aggregate/mortar interface: influence of silica fume at the micro-and macro-level, Cement and Concrete Composites 25 (4-5) (2003) 557–564.

[254] K. Mitsui, Z. Li, D. Lange, S. Shah, 13 a study of properties of the paste-aggregate interface, Interfaces in Cementitious Composites (1993) 119.

[255] A. Abu-Tair, S. Rigden, E. Burley, Testing the bond between repair materials and concrete substrate, Materials Journal 93 (6) (1996) 553–558.

A

[256] E. Garboczi, Stress, displacement, and expansive cracking around a single spherical aggregate under different expansive conditions, Cement and concrete research 27 (4) (1997) 495–500.

[257] D. Bentz, E. Garboczi, Computer modelling of interfacial transition zone: microstructure and properties, Engineering and Transport Properties of the Interfacial Transition Zone in Cementitious Composites-State-of-the-Art Report of RILEM TC 159-ETC and 163-TPZ (1999) 349–385.

[258] Z. Sun, E. J. Garboczi, S. P. Shah, Modeling the elastic properties of concrete composites: Experiment, differential effective medium theory, and numerical simulation, Cement and Concrete Composites 29 (1) (2007) 22–38.

[259] Y. Gan, H. Zhang, B. Šavija, E. Schlangen, K. van Breugel, Static and fatigue tests on cementitious cantilever beams using nanoindenter, Micromachines 9 (12) (2018) 630.

[260] BS-EN 196-3:2005+A1:2008. Methods of testing cement. Determination of setting times and soundness., British Standards Institution-BSI and CEN European Committee for Standardization, 2008.

[261] Z. P. Bažant, S.-D. Pang, Activation energy based extreme value statistics and size effect in brittle and quasibrittle fracture, Journal of the Mechanics and Physics of Solids 55 (1) (2007) 91–131.

[262] C. Z. Yuan, W. J. Guo, Bond between marble and cement paste, Cement and Concrete Research 17 (4) (1987) 544–552.

[263] X. Zhang, G. Groves, S. Rodger, The microstructure of cement aggregate interfaces, MRS Online Proceedings Library Archive 114.

[264] P. J. Monteiro, C. P. Ostertag, Analysis of the aggregate-cement paste interface using grazing incidence x-ray scattering, Cement and Concrete Research 19 (6) (1989) 987–988.

[265] X. Ping, J. Beaudoin, R. Brousseau, Flat aggregate-portland cement paste interfaces, i. electrical conductivity models, Cement and Concrete Research 21 (4) (1991) 515–522.

[266] X. Ping, J. J. Beaudoin, R. Brousseau, Effect of aggregate size on transition zone properties at the portland cement paste interface, Cement and concrete research 21 (6) (1991) 999–1005.

[267] X. Ping, J. Beaudoin, Effects of transition zone microstructure on bond strength of aggregate-portland cement paste interfaces, Cement and concrete research 22 (1) (1992) 23–26.

[268] W. Tasong, C. Lynsdale, J. Cripps, Aggregate-cement paste interface. ii: Influence of aggregate physical properties, Cement and Concrete Research 28 (10) (1998) 1453–1465.

[269] H. Zhang, B. Šavija, S. C. Figueiredo, E. Schlangen, Experimentally validated multi-scale modelling scheme of deformation and fracture of cement paste, Cement and Concrete Research 102 (2017) 175–186.

[270] J. Ollivier, J. Maso, B. Bourdette, Interfacial transition zone in concrete, Advanced cement based materials 2 (1) (1995) 30–38.

[271] X. Zhao, R. Langford, J. Tan, P. Xiao, Mechanical properties of sic coatings on spherical particles measured using the micro-beam method, Scripta Materialia 59 (1) (2008) 39–42.

[272] H. Bei, S. Shim, E. P. George, M. K. Miller, E. Herbert, G. M. Pharr, Compressive strengths of molybdenum alloy micro-pillars prepared using a new technique, Scripta Materialia 57 (5) (2007) 397–400.

[273] M. Sebastiani, K. Johanns, E. G. Herbert, F. Carassiti, G. M. Pharr, A novel pillar indentation splitting test for measuring fracture toughness of thin ceramic coatings, Philosophical Magazine 95 (16-18) (2015) 1928–1944.

[274] S. Timoshenko, Strength of materials. part. 1 and part. 2 (1955).

[275] D. A. Lange, H. M. Jennings, S. P. Shah, Relationship between fracture surface roughness and fracture behavior of cement paste and mortar, Journal of the American Ceramic Society 76 (3) (1993) 589–597.

[276] T. Ficker, D. Martišek, H. M. Jennings, Roughness of fracture surfaces and compressive strength of hydrated cement pastes, Cement and Concrete Research 40 (6) (2010) 947–955.

[277] A. Makishima, J. D. Mackenzie, Calculation of bulk modulus, shear modulus and poisson's ratio of glass, Journal of Non-crystalline solids 17 (2) (1975) 147–157.

[278] J. E. Bolander, N. Sukumar, Irregular lattice model for quasistatic crack propagation, Physical Review B 71 (9) (2005) 094106.

[279] P. Grassl, M. Jirásek, Meso-scale approach to modelling the fracture process zone of concrete subjected to uniaxial tension, International Journal of Solids and Structures 47 (7-8) (2010) 957–968.

[280] R. Torrent, A general relation between tensile strength and specimen geometry for concrete-like materials, Matériaux et construction 10 (4) (1977) 187–196.

[281] Z. P. Bazant, J. Planas, Fracture and size effect in concrete and other quasibrittle materials, Vol. 16, CRC press, 1997.

[282] J. Birchall, A. Howard, K. Kendall, Flexural strength and porosity of cements, Nature 289 (5796) (1981) 388.

[283] H. Zhang, B. Šavija, Y. Xu, E. Schlangen, Size effect on splitting strength of hardened cement paste: Experimental and numerical study, Cement and Concrete Composites 94 (2018) 264–276.

A

[284] P. Chindaprasirt, C. Jaturapitakkul, T. Sinsiri, Effect of fly ash fineness on compressive strength and pore size of blended cement paste, Cement and Concrete Composites 27 (4) (2005) 425–428.

[285] P. Gu, J. J. Beaudoin, E. G. Quinn, R. E. Myers, Early strength development and hydration of ordinary portland cement/calcium aluminate cement pastes, Advanced cement based materials 6 (2) (1997) 53–58.

[286] P. J. Sandberg, F. Doncaster, On the mechanism of strength enhancement of cement paste and mortar with triisopropanolamine, Cement and concrete research 34 (6) (2004) 973–976.

[287] T. C. Powers, T. L. Brownyard, Studies of the physical properties of hardened portland cement paste, in: Journal Proceedings, Vol. 43, 1946, pp. 101–132.

[288] M. F. Pantano, H. D. Espinosa, L. Pagnotta, Mechanical characterization of materials at small length scales, Journal of Mechanical Science and technology 26 (2) (2012) 545–561.

[289] A. Carpinteri, B. Chiaia, Multifractal scaling laws in the breaking behaviour of disordered materials, Chaos, Solitons & Fractals 8 (2) (1997) 135–150.

[290] A. Carpinteri, B. Chiaia, G. Ferro, Size effects on nominal tensile strength of concrete structures: multifractality of material ligaments and dimensional transition from order to disorder, Materials and Structures 28 (6) (1995) 311.

[291] A. Carpinteri, B. Chiaia, P. Cornetti, S. Puzzi, Comments on "is the cause of size effect on structural strength fractal or energetic-statistical?" by bažant & yavari [engng fract mech 2005; 72: 1–31], Engineering Fracture Mechanics 74 (17) (2007) 2892–2896.

[292] Z. P. Bažant, M. Vořechovskỳ, D. Novák, Asymptotic prediction of energetic-statistical size effect from deterministic finite-element solutions, Journal of engineering mechanics 133 (2) (2007) 153–162.

[293] R. Ince, A. Arslan, B. Karihaloo, Lattice modelling of size effect in concrete strength, Engineering Fracture Mechanics 70 (16) (2003) 2307–2320.

[294] J. Van Mier, M. Van Vliet, Influence of microstructure of concrete on size/scale effects in tensile fracture, Engineering fracture mechanics 70 (16) (2003) 2281–2306.

[295] H.-K. Man, J. Van Mier, Damage distribution and size effect in numerical concrete from lattice analyses, Cement and Concrete Composites 33 (9) (2011) 867–880.

[296] H.-K. Man, J. G. van Mier, Size effect on strength and fracture energy for numerical concrete with realistic aggregate shapes, International journal of fracture 154 (1-2) (2008) 61–72.

[297] I. Gitman, H. Askes, L. Sluys, Representative volume: existence and size determination, Engineering fracture mechanics 74 (16) (2007) 2518–2534.

[298] P. Milella, N. Bonora, On the dependence of the weibull exponent on geometry and loading conditions and its implications on the fracture toughness probability curve using a local approach criterion, International journal of fracture 104 (1) (2000) 71–87.

[299] W. Weibull, A statistical theory of the strength of materials, Ing. Vet. Ak. Handl.

[300] Z. Bazant, Y. Xi, Statistical size effect in quasi-brittle structures: Ii. nonlocal theory, J. Eng. Mech 117 (11) (1991) 2623–2640.

[301] J. J. Moré, D. C. Sorensen, Computing a trust region step, SIAM Journal on Scientific and Statistical Computing 4 (3) (1983) 553–572.

[302] B. Zech, F. Wittmann, Part ii probabilistic approach to describe the behaviour of materials, Nuclear Engineering and Design 48 (2-3) (1978) 575–584.

[303] Z. P. Bažant, A. Yavari, Is the cause of size effect on structural strength fractal or energetic–statistical?, Engineering Fracture Mechanics 72 (1) (2005) 1–31.

[304] Z. P. Bažant, S. Pang, M. Vořechovský, D. Novák, Energetic–statistical size effect simulated by sfem with stratified sampling and crack band model, International Journal for Numerical Methods in Engineering 71 (11) (2007) 1297–1320.

[305] A. Carpinteri, S. Puzzi, Fractals, statistics and size-scale effects on concrete strength, Fracture Mechanics of Concrete Structures (2007) 31–37.

[306] H. Chandler, I. Merchant, R. Henderson, D. Macphee, Enhanced crack-bridging by unbonded inclusions in a brittle matrix, Journal of the European Ceramic Society 22 (1) (2002) 129–134.

[307] D. Asahina, E. Landis, J. Bolander, Modeling of phase interfaces during pre-critical crack growth in concrete, Cement and Concrete Composites 33 (9) (2011) 966–977.

[308] J. Bolander Jr, S. Saito, Fracture analyses using spring networks with random geometry, Engineering Fracture Mechanics 61 (5-6) (1998) 569–591.

[309] E. Prado, J. Van Mier, Effect of particle structure on mode i fracture process in concrete, Engineering fracture mechanics 70 (14) (2003) 1793–1807.

[310] E. Schlangen, J. Van Mier, Experimental and numerical analysis of micromechanisms of fracture of cement-based composites, Cement and concrete composites 14 (2) (1992) 105–118.

[311] G. Cusatis, D. Pelessone, A. Mencarelli, Lattice discrete particle model (ldpm) for failure behavior of concrete. i: Theory, Cement and Concrete Composites 33 (9) (2011) 881–890.

[312] G. Cusatis, A. Mencarelli, D. Pelessone, J. Baylot, Lattice discrete particle model (ldpm) for failure behavior of concrete. ii: Calibration and validation, Cement and Concrete composites 33 (9) (2011) 891–905.

A

[313] W. Ren, Z. Yang, R. Sharma, C. Zhang, P. J. Withers, Two-dimensional x-ray ct image based meso-scale fracture modelling of concrete, Engineering Fracture Mechanics 133 (2015) 24–39.

[314] X. Wang, M. Zhang, A. P. Jivkov, Computational technology for analysis of 3d meso-structure effects on damage and failure of concrete, International Journal of Solids and Structures 80 (2016) 310–333.

[315] W. Trawiński, J. Tejchman, J. Bobiński, A three-dimensional meso-scale modelling of concrete fracture, based on cohesive elements and x-ray μct images, Engineering Fracture Mechanics 189 (2018) 27–50.

[316] O. Yılmaz, J.-F. Molinari, A mesoscale fracture model for concrete, Cement and Concrete Research 97 (2017) 84–94.

[317] I. Carol, C. M. López, O. Roa, Micromechanical analysis of quasi-brittle materials using fracture-based interface elements, International Journal for Numerical Methods in Engineering 52 (1-2) (2001) 193–215.

[318] P. Wriggers, S. Moftah, Mesoscale models for concrete: Homogenisation and damage behaviour, Finite elements in analysis and design 42 (7) (2006) 623–636.

[319] M. Tijssens, L. Sluys, E. Van der Giessen, Simulation of fracture of cementitious composites with explicit modeling of microstructural features, Engineering Fracture Mechanics 68 (11) (2001) 1245–1263.

[320] L. Snozzi, A. Caballero, J.-F. Molinari, Influence of the meso-structure in dynamic fracture simulation of concrete under tensile loading, Cement and Concrete Research 41 (11) (2011) 1130–1142.

[321] G. Lilliu, J. Van Mier, On the relative use of micro-mechanical lattice analysis of 3-phase particle composites, Engineering Fracture Mechanics 74 (7) (2007) 1174–1189.

[322] J. Kozicki, J. Tejchman, Modelling of fracture process in concrete using a novel lattice model, Granular Matter 10 (5) (2008) 377–388.

[323] G. Ruiz, A. Pandolfi, M. Ortiz, Three-dimensional cohesive modeling of dynamic mixed-mode fracture, International Journal for Numerical Methods in Engineering 52 (1-2) (2001) 97–120.

[324] A. Caballero, C. López, I. Carol, 3D meso-structural analysis of concrete specimens under uniaxial tension, Computer Methods in Applied Mechanics and Engineering 195 (52) (2006) 7182–7195.

[325] A. Caballero, I. Carol, C. López, A meso-level approach to the 3D numerical analysis of cracking and fracture of concrete materials, Fatigue & Fracture of Engineering Materials & Structures 29 (12) (2006) 979–991.

[326] J. M. Sancho, J. Planas, A. M. Fathy, J. C. Galvez, D. A. Cendon, Three-dimensional simulation of concrete fracture using embedded crack elements without enforcing crack path continuity, International Journal for Numerical and Analytical Methods in Geomechanics 31 (2) (2007) 173–187.

[327] X. Su, Z. Yang, G. Liu, Finite element modelling of complex 3d static and dynamic crack propagation by embedding cohesive elements in abaqus, Acta Mechanica Solida Sinica 23 (3) (2010) 271–282.

[328] S. Shahbeyk, M. Hosseini, M. Yaghoobi, Mesoscale finite element prediction of concrete failure, Computational Materials Science 50 (7) (2011) 1973–1990.

[329] Y. Huang, Z. Yang, W. Ren, G. Liu, C. Zhang, 3D meso-scale fracture modelling and validation of concrete based on in-situ x-ray computed tomography images using damage plasticity model, International Journal of Solids and Structures 67 (2015) 340–352.

[330] Z. Qian, E. Garboczi, G. Ye, E. Schlangen, Anm: a geometrical model for the composite structure of mortar and concrete using real-shape particles, Materials and Structures 49 (1-2) (2016) 149–158.

[331] C. Du, L. Sun, S. Jiang, Z. Ying, Numerical simulation of aggregate shapes of three-dimensional concrete and its applications, Journal of Aerospace Engineering 26 (3) (2011) 515–527.

[332] L.-Y. Lv, H. Zhang, E. Schlangen, Z. Yang, F. Xing, Experimental and numerical study of crack behaviour for capsule-based self-healing cementitious materials, Construction and Building Materials 156 (2017) 219–229.

[333] P. Stroeven, Some aspects of the micromechanics of concrete, Ph.D. thesis, Delft University of Technology, Delft, The Netherlands (1973).

[334] A. Vervuurt, E. Schlangen, J. G. Van Mier, Tensile cracking in concrete and sandstone: Part 1—basic instruments, Materials and Structures 29 (1) (1996) 9–18.

[335] M. Luković, H. Dong, B. Šavija, E. Schlangen, G. Ye, K. van Breugel, Tailoring strain-hardening cementitious composite repair systems through numerical experimentation, Cement and Concrete Composites 53 (2014) 200–213.

[336] H. Zhang, B. Šavija, M. Luković, E. Schlangen, Experimentally informed micromechanical modelling of cement paste: an approach coupling x-ray computed tomography and statistical nanoindentation, Composites Part B: Engineering 157 (2019) 109–122.

[337] C. Liu, R. Huang, Y. Zhang, Z. Liu, M. Zhang, Modelling of irregular-shaped cement particles and microstructural development of portland cement, Construction and Building Materials 168 (2018) 362–378.

[338] E. N. Landis, D. T. Keane, X-ray microtomography, Materials characterization 61 (12) (2010) 1305–1316.

[339] A. C. Muller, K. L. Scrivener, A. M. Gajewicz, P. J. McDonald, Densification of c–s–h measured by 1h nmr relaxometry, The Journal of Physical Chemistry C 117 (1) (2012) 403–412.

[340] M. Königsberger, C. Hellmich, B. Pichler, Densification of csh is mainly driven by available precipitation space, as quantified through an analytical cement hydration model based on nmr data, Cement and Concrete Research 88 (2016) 170–183.

[341] J. Vanzo, A nanochemomechanical investigation of carbonated cement paste, Ph.D. thesis, Massachusetts Institute of Technology, Cambridge, Cambridge, The United States of America (2009).

[342] K. J. Krakowiak, J. J. Thomas, S. Musso, S. James, A.-T. Akono, F.-J. Ulm, Nano-chemo-mechanical signature of conventional oil-well cement systems: Effects of elevated temperature and curing time, Cement and Concrete Research 67 (2015) 103–121.

[343] A. Deirieh, J. Ortega, F.-J. Ulm, Y. Abousleiman, Nanochemomechanical assessment of shale: a coupled wds-indentation analysis, Acta Geotechnica 7 (4) (2012) 271–295.

[344] D. Phillips, J. Lannutti, Measuring physical density with x-ray computed tomography, Ndt & E International 30 (6) (1997) 339–350.

[345] E. I. Jussiani, C. R. Appoloni, Effective atomic number and density determination of rocks by x-ray microtomography, Micron 70 (2015) 1–6.

[346] I. Sinka, S. Burch, J. Tweed, J. Cunningham, Measurement of density variations in tablets using x-ray computed tomography, International Journal of Pharmaceutics 271 (1-2) (2004) 215–224.

[347] H. Kariem, C. Hellmich, T. Kiefer, A. J ager, J. F ussl, Micro-ct-based identification of double porosity in fired clay ceramics, Journal of Materials Science 53 (13) (2018) 9411–9428.

[348] R. Blanchard, C. Morin, A. Malandrino, A. Vella, Z. Sant, C. Hellmich, Patient-specific fracture risk assessment of vertebrae: A multiscale approach coupling x-ray physics and continuum micromechanics, International journal for numerical methods in biomedical engineering 32 (9) (2016) e02760.

[349] N. Douarche, D. Rouby, G. Peix, J. Jouin, Relations between x-ray tomography, density and mechanical properties in carbon–carbon composites, Carbon 39 (10) (2001) 1455–1465.

[350] J. Rho, M. Hobatho, R. Ashman, Relations of mechanical properties to density and ct numbers in human bone, Medical engineering & physics 17 (5) (1995) 347–355.

[351] A. Edidin, D. Taylor, D. Bartel, Automatic assignment of bone moduli from ct data: a 3-d finite element study, Trans. Annu. Meet.-Orthop. Res. Soc 16 (1991) 491.

[352] J. Keyak, J. Meagher, H. Skinner, C. Mote Jr, Automated three-dimensional finite element modelling of bone: a new method, Journal of biomedical engineering 12 (5) (1990) 389–397.

[353] T. Shapurian, P. D. Damoulis, G. M. Reiser, T. J. Griffin, W. M. Rand, Quantitative evaluation of bone density using the hounsfield index, International Journal of Oral & Maxillofacial Implants 21 (2).

[354] F. J. Massey Jr, The kolmogorov-smirnov test for goodness of fit, Journal of the American statistical Association 46 (253) (1951) 68–78.

[355] R. Cao, I. Van Keilegom, Empirical likelihood tests for two-sample problems via nonparametric density estimation, Canadian Journal of Statistics 34 (1) (2006) 61–77.

[356] M. H. Gail, S. B. Green, Critical values for the one-sided two-sample kolmogorov-smirnov statistic, Journal of the American Statistical Association 71 (355) (1976) 757–760.

[357] A. Day, K. Snyder, E. Garboczi, M. Thorpe, The elastic moduli of a sheet containing circular holes, Journal of the Mechanics and Physics of Solids 40 (5) (1992) 1031–1051.

[358] P. Zhang, S. Li, Z. Zhang, General relationship between strength and hardness, Materials Science and Engineering: A 529 (2011) 62–73.

[359] M. A. Le Gros, G. McDermott, C. A. Larabell, X-ray tomography of whole cells, Current opinion in structural biology 15 (5) (2005) 593–600.

[360] P. Trtik, A. Diaz, M. Guizar-Sicairos, A. Menzel, O. Bunk, Density mapping of hardened cement paste using ptychographic x-ray computed tomography, Cement and Concrete Composites 36 (2013) 71–77.

[361] P. Trtik, J. Kaufmann, U. Volz, On the use of peak-force tapping atomic force microscopy for quantification of the local elastic modulus in hardened cement paste, Cement and concrete research 42 (1) (2012) 215–221.

CURRICULUM VITÆ

Hongzhi ZHANG

08-07-1990 Born in Jinan, China.

EDUCATION

2009–2015	BSc and MSc sutdent Harbin Institute of Technology, China
2015–2019	PhD. student Delft University of Technology, The Netherlands
2020–present	Professor Shandong University, China
Thesis:	Experimentally validated multi-scale fracture modelling scheme of cementitious materials
Promotor:	Prof. dr. ir. E. Schlangen
Copromotor:	Dr. B. Šavija

LIST OF PUBLICATIONS

JOURNAL PUBLICATIONS

1. **H. Zhang**, B. Šavija, S. Chaves Figueiredo, M. Lukovic, E. Schlangen *Microscale testing and modelling of cement paste as basis for multi-scale modelling*, Materials **9** (11), 907 (2016).

2. **H. Zhang**, B. Šavija, S. Chaves Figueiredo, E. Schlangen *Experimentally validated multi-scale modelling scheme of deformation and fracture of cement paste*, Cement and Concrete Research **102** : 175-186 (2017).

3. **H. Zhang**, B. Šavija, E. Schlangen *Combined experimental and numerical study on micro-cube indentation splitting test of cement paste*, Engineering Fracture Mechanics **199**: 773-786 (2018).

4. **H. Zhang**, B. Šavija, E. Schlangen *Towards understanding stochastic fracture performance of cement paste at micro length scale based on numerical simulation*, Construction and Building Materials **183**: 189-201 (2018).

5. **H. Zhang**, B. Šavija, Y. Xu, E. Schlangen *Size effect on splitting strength of hardened cement paste: Experimental and numerical study*, Cement and Concrete Composites **94**: 264-276 (2018).

6. **H. Zhang**, B. Šavija, M. Lukovic, E. Schlangen *Experimentally informed micromechanical modelling of cement paste: an approach coupling X-ray computed tomography and statistical nanoindentation*, Composites Part B: Engineering **157**: 109-122 (2019).

7. **H. Zhang**, Y. Gan, Y. Xu, Z. Chang, E. Schlangen B. Šavija, *Experimentally informed fracture modelling of interfacial transition zone at micro-scale*, Cement and Concrete Composites **104**: 103383 (2019).

8. **H. Zhang**, Y. Xu, Y. Gan, Z. Chang, E. Schlangen B. Šavija, *Combined experimental and numerical study of uniaxial compression failure of hardened cement paste at micrometre length scale*, under review.

9. L. Lv, **H. Zhang**, E. Schlangen, Z. Yang, F. Xing *Experimental and numerical study of crack behaviour for capsule-based self-healing cementitious materials*, Construction and Building Materials **156**: 219-229 (2017).

10. B. Šavija, **H. Zhang**, E. Schlangen *Influence of microencapsulated phase change material (PCM) addition on (micro) mechanical properties of cement paste*, Materials **10** (8), 863 (2017).

11. H. Dong, **H. Zhang**, Y. Zuo, P. Gao, G. Ye *Relationship between the size of the aamples and the interpretation of the mercury intrusion results of an artificial sandstone*, Materials **11** (2), 201 (2018).

12. Y. Gan, **H. Zhang**, B. Šavija, E. Schlangen, K. van Breugel *Static and fatigue tests on cementitious cantilever beams using nanoindenter*, Micromachines **9**(12), 630 (2018).

13. Y. Xu, **H. Zhang**, B. Šavija, S. Chaves Figueiredo, E. Schlangen *Deformation and fracture of 3D printed disordered lattice materials: Experiments and modeling*, Materials & Design **162**: 143-153 (2019).

14. B. Šavija, **H. Zhang**, E. Schlangen *Assessing hydrated cement paste properties using experimentally informed discrete models*, Journal of Materials in Civil Engineering **31**,9(2019).

BOOK EDITORSHIP

1. E. Schlangen,G. de Schutter, B. Šavija, **H. Zhang**, C. Romero Rodriguez *Proceedings of the Symposium on Concrete Modelling, CONMOD2018,* RILEM Publications S.A.R.L., 2018.

2. G. Ye, Y. Yuan, C. Romero Rodriguez, **H. Zhang**, B. Šavija *Proceedings of the 4th International Conference on Service Life Design for Infrastructures, SLD4,* RILEM Publications S.A.R.L., 2018.

CONFERENCE PROCEEDINGS

1. **H. Zhang**, B. Šavija, E. Schlangen. *Fracture test and simulation of cement paste cubes and beams at microscale.* Proceedings of 2016 Engineering Mechanics Institute Conference, Metz, France, 2016.

2. **H. Zhang**, B. Šavija, E. Schlangen. *Application of X-ray computed tomography on fracture behaviour study of cement paste at micro-scale.* Proceedings of 7th GACM Colloquium on Computational Mechanics, Stuttgart, Germany, 2017.

3. **H. Zhang**, B. Šavija, E. Schlangen. *Testing and modelling of micro cement paste cube under indentation splitting.* Proceedings of the Conference on Computational Modelling of Concrete and Concrete Structures, Bad Hofgastein, Austria, 2018.

4. **H. Zhang**, B. Šavija, E. Schlangen. *Micromechanical modelling of cement paste using X-ray computed tomography and statistical nanoindentation.* Proceedings of the Symposium on Concrete Modelling-CONMOD2018, Delft, The Netherlands, 2018.

5. C. Justino de Lima, F. Veer, O. Çopuroglu, **H. Zhang**, R. Nijsse. *Fracture analysis of phosphate and silicate glasses by microscopy and nanoindentation: comparison of different glasses utilized for building engineering.* Proceedings of 17th Euroseminar on Microscopy Applied to Building Materials, Toronto, Canada, 2019.

6. **H. Zhang**, E. Schlangen, B. Šavija. *Use of X-ray computed tomography as input for fracture modelling of cement paste-aggregate interface.* 10th International Conference on Fracture Mechanics of Concrete and Concrete Structures, Bayonne, France, 2019.

7. Y. Gan,**H. Zhang**, B. Šavija, E. Schlangen K. van Breugel. *Micro-cantilever testing of cementitious materials under various loading conditions.* 10th International Conference on Fracture Mechanics of Concrete and Concrete Structures, Bayonne, France, 2019.

8. Z. Chang,**H. Zhang**, E. Schlangen B. Šavija. *Lattice model for numerical analysis of fracture process of concrete material under various loading conditions.* 10th International Conference on Fracture Mechanics of Concrete and Concrete Structures, Bayonne, France, 2019.

9. **H. Zhang**, E. Schlangen, B. Šavija. , *Fracture testing and modelling of cement paste at micrometre length scale.* Proceedings of International Conference on Innovative Materials for Sustainable Civil Engineering, Nanjing, China, 2019.

ACKNOWLEDGEMENTS

PhD is a lonely journey. Luckily, I am not alone. At the end of this journey, I would like to take this opportunity to express so many appreciations to those who are along with me.

First of all, a special gratitude goes to China Scholarship Council for offering me the scholarship to start my PhD journey in the Microlab, Section of Materials and Environment at the Faculty of Civil Engineering and Geosciences, Delft University of Technology.

I would like to express my sincere gratitude to my Promotor Prof. Erik Schlangen. It is really my good fortune to be his student. He can always help me find the right direction easily using his own way. I really enjoyed all the discussions we had in the office, lab and corridor. Although, as a full professor, his hands are always tied, I could just knock at the door and start asking questions whenever I see him in the office. I truly appreciate his persistent support, patient guidance. No matter how dark around me, I know he would always be there lighting a candle for me. Most importantly, he is not only teaching me how to do good research but also showing me how to be a good person, and how to enjoy the research life.

My special appreciation extends to my Copromotor Dr. Branko Šavija. How lucky I am to work with both Erik and him! How can you image we could have discussions almost in every working day! He is always friendly, patient, high-efficiency and ready to help others. Whenever I sent him my first version of manuscript, it would always come back within one or two days with full of valuable comments and revisions. Even though there is a period of time that he has to leave the Microlab without known whether he would be able to come back, his help to me has never been stopped.

I would like to take a moment to express my special gratitude to Dr. Zhiwei Qian for introducing Erik to me and continuous help both at and outside of the work. I am very thankful to all the members of my doctoral committee: Prof. Eric Landis, Prof. Jan Rots, Prof. Zili Li and Dr. Bernhard Pichler for taking the time and effort to carefully review the preliminary version of this work. Their insightful comments and suggestions helped me improve this thesis significantly.

People from Harbin Institute of Technology are always important for me. I would like to express my deepest appreciation to Prof. Xinchun Guan. He brought me into the research field of cementitious materials encourage to pursue a PhD study at TU Delft. Special gratitude also goes to Prof. Yingzi Yang. The first lesson I had for testing cementitious materials was given by her. She is always elegant and amiable to students. During my PhD journey, she has visited the Microlab for half year. It is so good to have her walking with me in this journey.

The starting period of a journey is always tough. Deep appreciation goes to Hua Dong, Tianshi Lu, Peng Gao, Leyang Lv and Xu Ma. Thank you for taking care of me! A special gratitude goes to Dr. Ye, thanks for always organizing parties for the Chinese festivals, which makes me feel at home. I owe my gratitude to Dr. Oguzhan Copuroglu for all the questions and suggestions during the group meeting and all the helps after the

meeting. Many thanks goes to Dr. Mladena Luković. Thank you for all the friendly and inspiring discussions since the first beginning of this project.

Special thanks also goes to my office mates: Shi Xu (Qilin Wang), Wenjuan Lyu, Xuhui Liang, Kamel Arbi. Our office is perhaps the most quietest but efficient one in the 6th floor. It is my true pleasure to share my research life day and night with all of you.

I would like to thank Yading Xu and Yidong Gan. Thanks for walking with me in the journey. Thanks to them, I am not alone in the lab. I remember every moment when we sit in the chairs waiting for the results of laboratory tests. It is my honour to work with these two brilliant and unselfish young PhD researchers.

I am very thankful to those who make our lab work possible: Arjan Thijssen for his helping in ESEM and XCT scanning, Maiko van Leeuwen for operating the Instron machine and making such enjoyable atmosphere of the lab, Johon van den Berg and Ton Blom for their kind helps. Many thanks goes to Paul Vermeulen, who always helps me with repairing the small tension/compression stage. I also want to thank our secretaries: Jacqueline, Iris, Claire, Nynke. Thanks for all their kind helps with all these "little things". Without them, these "little things" would become big troubles for me.

My gratitude also goes to Stefan Chaves Figueiredo and Bianca Fraga Silva, Yu Chen, Claudia Romero Rodríguez and Fernando Franca de Mendonca Filho, Marija Nedeljković and Patrick Holthuizen, Ze Chang and Lu Cheng, Martin Megalla. Thanks for the friendship, the lunch time, coffee break and all the great times that we have shared.

I would like to thank all the other colleagues and former colleagues of Microlab for their friendship, support and interesting discussions over the years. They are Prof. Klaas van Breugel, Dr. Henk Jonkers, Dr. Damian Palin, Dr. Amir Tabakovic, Dr.Bahman Ghiassi, Renée Mors, Jakub Pawłowicz, Luiz Lima, Clarissa Justino de Lima, Jeannette van den Bos, Albina Kostiuchenko, Agus Susanto, Emanuele Rossi, Bart Hendrix. Deepest appreciation also goes to all my Chinese colleagues for all the great time we have shared together. They are Yong Zhang, Hao Huang (Niha), Bei Wu, Jiayi Chen (Wenqin Shi), Xuliang Hou (Ying Yang), Zhipei Chen, Xiaowei Ouyang (Cui Wei), Yibing Zuo, Zhenming Li, Shizhe Zhang, Boyu Chen, Zhiyuan Xu, Yu Zhang. It would not be such a wonderful journey without any of them.

I am also very grateful to all the friends that I met in the Netherlands. Thanks for making my monotonous life vivid. They are Yushi Huang, Yi Xia and Mengmeng Gao, Qingpeng Li, Ruxin Jing, Hongxiao Guo, Wei Fang, Yiming Wang, Zhou Zhang, Langzi Chang, Hong Zhang and Haopeng Wang.

A special note of appreciation goes to Prof. Zhi Ge from Shandong University. He helped me get the opportunity that I dare not dream of to start a new journey after PhD in my hometown. I am also very thankful to Prof. Shucai Li, Prof. Jian Liu, Prof. Liping Li, Mr. Long Chen, Dr. Renjuan Sun, Dr. Yanhua Guan, Dr. Honglei Chang for their help and support.

At the end, I would like to express the love from the bottom of my heart to my parents for their unconditional love, endless support and encouragement. It is because of you that I could always follow my heart and go for my dreams bravely. After such a long long journey, your son is back!

Hongzhi Zhang
Delft, 2019

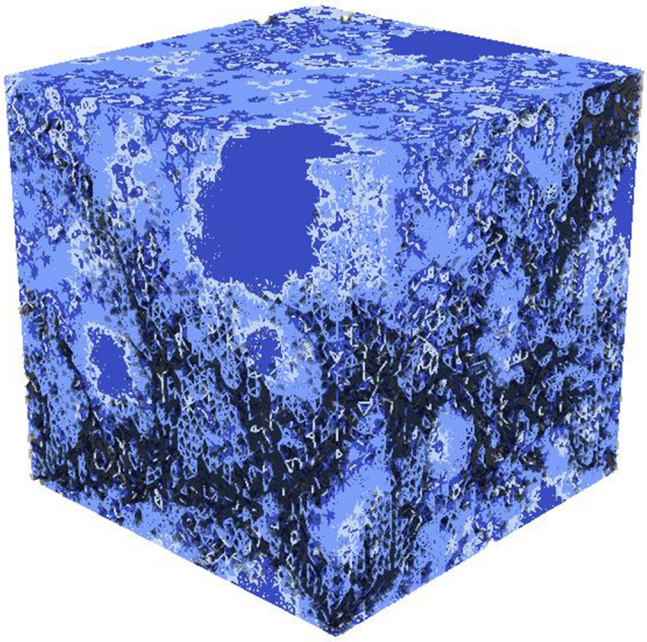

ISBN 978-94-6384-071-2

TU Delft Delft University of Technology